



PhD-FSTM-2023-058
The Faculty of Science, Technology and Medicine

DISSERTATION

Defence held on 20/07/2023 in Esch-sur-Alzette, Luxembourg

to obtain the degree of

DOCTEUR DE L'UNIVERSITÉ DU LUXEMBOURG

EN PHYSIQUE

by

Longfei SONG

Born on 01 March 1994 in Dongying, (China)

**PROCESSING OF PIEZOELECTRIC OXIDE FILMS FOR
SURFACE HAPTICS**

Dissertation defence committee

Dr Emmanuel DEFAY, dissertation supervisor
Unit Leader, Luxembourg Institute of Science and Technology

Dr Maël GUENNOU, Chairman
Associate Professor, Université du Luxembourg

Dr Sohini KAR-NARAYAN, Vice Chairman
Professor, University of Cambridge

Dr Frédéric GIRAUD
Associate Professor, Université de Lille

Dr Nazanin BASSIRI-GHARB
Professor, Georgia Institute of Technology

Dr Sebastjan GLINSEK, Observer
Senior Research and Technology Associate, Luxembourg Institute of Science and Technology

Abstract

Human-machine interaction (HMI) relies mainly on vision and hearing, but touch is essential for perceiving the environment, especially for those who are visually impaired. To incorporate touch into HMI systems, haptic technologies have been developed, with piezoelectric actuators being a promising solution. However, challenges exist in integrating these actuators into touch screens due to their thickness and lack of transparency. Researchers have turned to piezoelectric PZT thin films that provide acceptable haptic performance and optical transparency. Depositing these films onto glass substrates presents challenges, requiring a low-temperature process to enable cost-effective and large-scale production. Transparent electrodes, particularly indium tin oxide, are necessary for creating transparent actuators, but their production process is complex and costly. Chemical solution deposition (CSD) based on inkjet printing technology is a low-cost and large-scale deposition method, enabling direct film patterning without expensive lithography. In this thesis these challenges were addressed by developing a low-temperature flash-lamp process for PZT film growth, low-temperature combustion processed and inkjet printed ITO electrodes, and an all inkjet printed haptic device. Additionally, we proposed the use of thick piezoelectric films for low-power consumption and large deflection in haptic applications that do not require transparency.

Acknowledgements

The Luxembourg National Research Fund (FNR) is acknowledged for funding this thesis work via project PACE (PRIDE17 12246511).

First of all, I am deeply grateful to my supervisor Dr. Emmanuel Defay and my tutor Dr. Sebastjan Glinsek, for not only affording me the opportunity to pursue this research but also for providing consistent and invaluable guidance through weekly supervisions over the course of four years. They always provide me valuable suggestions and help throughout my four years, which make my life easier. Their unwavering dedication and passion for his field served as a constant wellspring of inspiration for me. Without their help and encouragement, I could not study here and could not perform these works.

I would like to express my gratitude to the members of my CET committee, Prof. Mael Guennou and Prof. Sohini Kar-Narayan, for following my work during these four years. I am grateful for their continuous interest in my work, and for their time to read my manuscript. I also would like to extend my appreciation to the external members of the jury, Prof. Nazanin Bassiri-Gharb and Prof. Frederic Giraud, for their time to read and evaluate my manuscript.

I would like to express my heartfelt gratitude to all the co-authors for their valuable contributions to the presented works. I extend my sincere thanks to my colleagues and former colleagues in our groups: Alfredo Blazquez Martinez, Dr. Nicolas Godard, Dr. Veronika Kovacova, Dr. Stephanie Girod, Dr. Junning Li, Dr. Juliette Cardoletti, Dr. Cosme Milesi-Brault, Ashwath Aravindhana, Barnik Mandal, Dr. Uros Prah, Dr. Naveen Aruchamy, Dr. Tony Schenck, and everyone else who has been part of this journey. Furthermore, I would like to acknowledge and thank my colleagues in our department for their support and guidance.

I would also like to express my appreciation to our colleagues in Jozef Stefan Institute: Prof. Barbara Malic, Prof. Hana Ursic, Prof. Andreja Bencan, Silvo Drnovsek, Dr. Matej Sadl, Victor Regis... Thanks also for their help during my secondment in Slovenia.

I would also like to take this opportunity to express my deep appreciation to all my

friends in Luxembourg. The time we have spent together has been truly memorable, and I am grateful for the wonderful experiences we have shared.

In particular, I would like to extend a special thank you to Alfredo Blazquez Martinez, Poorani Gnanasambandan, and Diana Elisa Murillo Navarro. Your unwavering support and assistance have been invaluable to me, and I am sincerely grateful for everything you have done.

I would also like to express my appreciation to Prof. Phillip Dale, the head of our project. I am grateful for the opportunities he has provided, including the organization of trips and training sessions that have been beneficial to our development. Additionally, I would like to extend my thanks to all the other students involved in the PACE project.

Finally, I would like to take a moment to express my thanks to my family for their support. My last thoughts are dedicated to my beloved girlfriend, dear Rong, for her constant love and encouragement.

Contents

1	Introduction	14
2	Background	20
2.1	Piezoelectric films and applications	21
2.1.1	Piezoelectricity	21
2.1.2	Lead zirconate titanate	21
2.1.3	PZT thin films	24
2.1.4	PZT thick films	26
2.1.5	Applications	26
2.2	Transparent conductive oxides	28
2.2.1	Electrical conductivity	28
2.2.2	Optical Transparency	31
2.2.3	Opto-electrical performance	32
2.3	Chemical solution processing of oxides films	33
2.3.1	Solution chemistry	33
2.3.2	General steps	34
2.3.3	Solution deposition technologies	35
2.4	Surface haptic technology	41
2.4.1	Fingerpad contact mechanics in a sliding contact	41
2.4.2	Overview of surface haptic device	47
2.4.3	Squeezed-air film theory	50
2.4.4	Vibration model in ultrasonic haptics	52
3	State of the art of low-temperature process of PZT thin films	55
4	Low-temperature flash lamp process of PZT films	88
4.1	Introduction, experimental results and discussions	89

4.2	Chapter conclusion	144
4.3	Challenges	144
5	Inkjet printing of indium tin oxides top electrodes	146
5.1	Motivation	146
5.2	Materials and methods	148
5.2.1	Processing of PZT thin films	148
5.2.2	Inkjet printing of ITO top electrodes	148
5.3	Experimental results	150
5.3.1	XRD and SEM of PZT thin film	150
5.3.2	Optical transparency of ITO film	151
5.3.3	Electrical conductivity of ITO film	151
5.3.4	SIMS of ITO/PZT stacks	153
5.3.5	Ferroelectric properties of ITO/PZT/Pt stacks	154
5.4	Chapter conclusion	158
5.5	Challenges	159
5.6	Outlook	159
6	All inkjet-printed haptic actuators on platinised Si substrate	161
6.1	Motivation	161
6.2	Chosen films deposition technologies and thickness	162
6.3	Ink synthesis and jetting parameters	163
6.4	Inkjet printing and thermal annealing process	164
6.5	Device design and finite element modelling	165
6.6	Printing design	166
6.7	Characterizations of inkjet printed actuators	167
6.7.1	Phase composition	167
6.7.2	Microstructure characterization	167
6.7.3	Electrical measurement	168
6.8	Acoustic measurements	169
6.9	Chapter conclusion	170
6.10	Challenges	171
6.11	Outlook	171

7	Power efficient haptic devices based on piezoelectric thick films	173
7.1	Piezoelectric thick film for power efficient haptic actuator	173
7.2	Screen-printed power-efficient haptic device with large deflection	195
7.3	Challenges	208
7.4	Outlook	208
8	Conclusion and perspectives	209
8.1	Conclusion	209
8.2	Perspectives	210
9	Publications, Conferences and Activities	213
A	Characterization techniques	216
A.1	X-ray diffraction	216
A.1.1	θ - 2θ and grazing incidence configurations	216
A.1.2	$\sin^2\Psi$ approach for estimating strain and stress in thin film	217
A.2	Secondary ions mass spectrometry	218
A.3	Scanning electron microscope	219
A.4	Electrical measurements	220
A.4.1	Four-probe conductivity measurement	220
A.4.2	Polarization-electric field hysteresis loop	221
A.4.3	Relative permittivity and loss tangent versus electrical field	222
A.4.4	Converse piezoelectric coefficient measurement	223
A.5	Setup for Acoustic measurement	223

List of Figures

1.1	Schematic diagram of acoustic haptic device with a transparent structure.[1]	17
2.1	(a) Cubic perovskite structure above T_C and (b) Noncentrosymmetric structures below T_C caused by the distortions of the cubic cell of PZT . . .	22
2.2	(a) Original temperature-composition phase diagram of the PZT solid solution. (b) Electromechanical properties versus composition of PZT ceramic.[2]	23
2.3	Typical ferroelectric polarization versus electric field hysteresis loop.[2]	24
2.4	Transverse piezoelectric response in $\{111\}$ and $\{100\}$ textured PZT films as a function of composition. All of the films were deposited on platinized Si substrates.[3]	25
2.5	Piezoelectric coefficient versus film thickness.[4] Note that in PZT thick films or ceramics, doping was performed to improve their piezoelectric properties.	27
2.6	Actuators with two different working mode.	28
2.7	Electrical conductivity of semiconductors, TCOs and metals.[5]	29
2.8	Sorting (Conducting) solids: materials space for semimetals, good metals, transparent conductors and semiconductors based on $n - \mu$ correlations (electron carrier density and electron mobility, respectively). Data shown are for room-temperature measurements.Constant conductivity contours are shown as straight lines.[6]	30
2.9	Resistivity, carrier density and hall mobility of pulse laser deposited ITO films versus (a) Sn doping concentration; (b) growth temperature; (c) oxygen pressure.[7]	31
2.10	Typical transmittance spectrum of TCOs.[5]	31
2.11	T in the visible range as a function of R_s for TCOs films.[8] SWNTs represent single-wall carbon nanotubes.	33
2.12	Different solution deposition technologies.[9]	35

2.13	Schematic diagram of continuous mode and drop-on-demand mode inkjet printing.	37
2.14	Schematic diagrams of (a) thermal DOD inkjet printing and (b) piezoelectric DOD inkjet printing.[10]	38
2.15	Derby diagram that indicates the range of Z values that enables stable printing ($Z = 1/Oh$).[10]	39
2.16	Flow of ink during solvent evaporation (left) and formed coffee ring after drying (right).	40
2.17	Graspable, wearable and touchable haptic devices.[11]	42
2.18	Schematics diagrams of sensorial properties of softness, warmth, roughness and slipperiness.[12] δ_{sur} and δ_{skin} stand for deformation of the object surface and the deformation of the fingerpad skin, respectively. d_{finger} , Q , v and τ_{max} are the displacement of a finger, the heat, the moving speed of a finger and the max. interfacial shear strength, respectively.	43
2.19	Schematic overview of the sliding contact between the fingerpad and a rough surface.[12]	44
2.20	Schematic diagram of rigid spherical probe sliding on soft countersurface.[13]	45
2.21	Structure of fingertip with a gradient of elasticity across the skin depth.[14]	46
2.22	Schematic diagram of the interaction between the surface and the finger. Different mechanoreceptors units are sensitive to different vibration frequency.[15]	46
2.23	Classification of current surface haptic technologies.[16]	48
2.24	The implementation of electro-adhesion-based surface haptics in a standard display assembly requires only the addition of a patterned ITO layer on the cover glass. Source: Tanvas	49
2.25	Squeezed-air film effect in a ultrasonic transparent haptic device.[17] . . .	50
2.26	Approximation of the finger pad ridges.[18]	51
2.27	Comparison of experimental results with the analytical model for the relative friction coefficients versus vibration amplitude (Sednaoui et al., 2015)[19]	52
2.28	Half-wavelength beam which bends by contracting the piezoceramics.[18]	53
5.1	Jetting of ITO ink with a nozzle voltage of 26 V and a nozzle temperature of 30 °C.	149
5.2	Schematic diagram of annealing processes of inkjet printed ITO. . . .	149

5.3	Optical appearance of inkjet-printed ITO rectangular patterns on silicon substrate.	150
5.4	Characterizations of PZT film. a) X-ray diffraction (XRD) of PZT film deposited on platinised silicon substrate (SINTEF wafer, 100 nm Pt/20 nm TiO ₂ /500 nm SiO ₂ /Si). b) Cross-sectional scanning electron microscope (SEM) image of PZT film deposited on platinised silicon substrate. Note that in order to promote PZT film to grow along {100} orientation, a 10 nm-thick PTO nucleation was used.	150
5.5	Optical transparency. Transmittance of 1×1 cm ⁻² -large and 120 nm-thick inkjet printed 400 °C-processed ITO film on fused silica glass. . . .	151
5.6	Thickness profile of printed ITO film on fused silica substrate.	152
5.7	Sheet resistance measurements of inkjet printed ITO film on fused silica glass. In the measurements, current was set as 100μA. ITO film contacted with probe is marked by red box.	152
5.8	Electrical conductivity. a) Sheet resistance of inkjet printed ITO film after annealing and after exposed in air for one day, obtained by measuring 10 points in the center of printed ITO pattern. b) corresponding calculated conductivity.	153
5.9	SIMS analysis of a) inkjet printed ITO electrode on PZT film. b) Sputtered ITO electrode on PZT film. Note that sputtered ITO was annealed at 300 °C for 20 min in air.	154
5.10	Thickness of electrode. a) Optical appearance of inkjet printed ITO dots as top electrodes on PZT film. b) Thickness profile of one of inkjet printed ITO electrode, which was scanned along the black dash line in a). 15 layers were printed in total.	155
5.11	Ferroelectric property. Polarization P and current I versus electric field E loops measured at 100 Hz.	155
5.12	Ferroelectric property. $P(E)$ and $I(E)$ loops measured at a) 1 kHz and b)10 Hz.	156

5.13	Ferroelectric property comparison. a) $P(E)$ and b) $J(E)$ loops of PZT capacitors with inkjet printed 200 nm-thick ITO, sputtered 100 nm-thick ITO, and sputtered 100 nm-thick Pt as top electrodes, respectively, were measured at 100 Hz. The sputtered ITO and Pt electrodes were deposited in-house. The conductivity of sputtered ITO was enhanced by post-annealing at 300 °C for 20 minutes in air, resulting in a conductivity of 3000 S cm ⁻¹ . The dimension of sputtered ITO and Pt circular electrodes are 200 μm and 100 μm, respectively. It is important to note that PZT films were deposited on platinised silicon substrate (SINTEF Wafer) in all cases, whose information has been introduced earlier.	156
5.14	Dielectric property. Relative permittivity ϵ_r and dielectric loss $\tan\delta$ versus electric field measured via applying an ac signal at 1 kHz frequency and 100 mV amplitude.	157
5.15	Ferroelectric property of devices with big ITO electrode. a) $P(E)$ b) $I(E)$ loops of PZT capacitors using 4 mm ² and 90 nm-thick electrodes. PZT film used in this measurement is 900 nm-thick and deposited on platinised silicon substrate using a standard CSD process.	158
5.16	Dielectric property of devices with big ITO electrode. $\epsilon_r(E)$ and $\tan\delta(E)$ loops of PZT capacitors using large ITO electrodes. The sample is same with ones used for the measurements in Figure 5-15.	158
5.17	Image that shows inkjet-printed large ITO electrodes (2×2 mm ² , 2×4 mm ² , and 2×6 mm ²) on a 500 nm-thick PZT film. Upon applying voltage to these electrodes, the ITO films exhibit cracking. The inset depicts a cross-sectional SEM image of a PZT thin film.	159
5.18	Photograph shows the sample with large ITO electrodes after immersion in acetone, resulting in the lifting off of both the ITO and PZT films. . .	160
5.19	The thickness profile of the lifted-off area depicted in Figure 5.18.	160
6.1	Depiction of the jetting process for a) PZT ink and b) ITO ink, utilizing the conditions outlined in Table 6.3.	164
6.2	Finite element modelling. Schematic diagram of haptic design based on 0.3 mm Si plate, used in the modelling.	165
6.3	Mode shape obtained from the modelling, at its resonance.	166
6.4	Schematic diagram of the design of all inkjet printed haptic device. .	166

6.5	1D and 2D profilometry of the printed device.	167
6.6	XRD pattern of inkjet printed actuator, identified via PZT and In_2O_3 powder diffraction file (PDF) No 01-070-4264 and No. 71-2194, respectively. 168	168
6.7	SEM. Cross-sectional SEM images of all inkjet-printed haptic actuator (low-resolution image (left) and zoomed-in image (right)).	168
6.8	Electrical measurement of inkjet printed haptic actuator: a) polarization versus voltage loop measured at 100 Hz, b) capacitance and dielectric loss versus electric field, measured at 1 kHz.	169
6.9	Line scans: a) Frequency-dependent displacement line scan with a unipolar $22 V_{pp}$ applied voltage to each actuator. b) Displacement line scan at 21.23 kHz excitation frequency, showing voltage dependence. Note: the presence of noisy data points resulting from noise interference caused by soiled points on the back surface of the device.	170
6.10	2D map of out-of-plane displacement of the fabricated haptic device, at 44 V unipolar and total voltage (22 V for each actuator) and at its resonant frequency of 21.23 kHz. Note that all the values of voltage are read from oscilloscope.	171
A.1	$\theta/2\theta$ configuration (left) and grazing incidence configuration (right). . . .	217
A.2	Schematic diagram of Φ - and Ψ -rotations in XRD.[20]	217
A.3	Schematic diagram of the principle of SIMS.	219
A.4	Schematic diagram of scanning electron microscope.	220
A.5	Schematic diagram of the principle of four-probe conductivity measurement. 220	220
A.6	Photo of aixACCT TF-3000 system (aixACCT Systems GmbH).	221
A.7	The applied triangular waveform at a frequency. Source: axiACCT manual 221	221
A.8	a) Current and polarization versus time. b) Polarization versus electric field hysteresis loop.	222
A.9	Measurement of relative permittivity by applying a staircase DC bias with a small amplitude. Source: axiACCT manual	222
A.10	Cantilever structure for converse piezoelectric coefficient measurement. . .	223
A.11	Schematic diagram of the built set-up used for haptic measurement. . . .	224

List of Tables

2.1	State-of-the-art electromechanical properties of PZT thin films with morphotropic phase boundary (MPB) composition. Polycrystalline {100} oriented 1 μm -thick film deposited on platinized Si substrates and annealed at 700 °C.[21]	25
2.2	Electrical properties of Ag, Si:P and ITO	30
6.1	Layer thickness and deposition methods	163
6.2	PTO, PZT and ITO inks formula, developed in this work.	163
6.3	Conditions set in inkjet printer to print these films, and their crystallization temperature.	164

Chapter 1

Introduction

Currently, human-machine interaction (HMI) predominantly depends on sight and sound. Nevertheless, the sense of touch is a crucial means for people to perceive and navigate their environment, particularly for individuals with impaired vision. By running our fingers over objects, we gain a tactile sensation, which results from the mechanical properties of our skin altering in response to interactions with external stimuli. Regrettably, this feature remains absent in current HMI technology.

Haptic technology involves the study of touch in modern electronics and provides a means of conveying subtle tactile sensations through display screens.[22, 23] To achieve this, it utilizes a variety of actuating technologies that complement the friction modulation of fingers to simulate texture, as discussed in the Background section. One of the most promising solutions among the available actuators is the piezoelectric actuator, which is capable of generating ultrasonic vibrations in a haptic plate.[16] As a finger moves across the vibrating haptic plate, a thin film of squeezed air is created in between the vibrating plate and the finger.[24] This squeezed air film reduces friction, allowing for modification of the friction coefficient of a finger, which makes it possible to simulate artificial textures. To create a haptic effect, the haptic devices must generate a deflection of 1 μm at their resonant frequencies.

Great strides have been made in the development of haptic technology. For instance, in 2020, the French company Hap2U created the world's first prototype of a haptic smartphone display. They employed piezoelectric ceramic actuators to produce the haptic effect, specifically lead zirconate titanate (PZT) ceramic actuators. However, PZT ceramic actuators, which are several hundred micrometers thick, are difficult to make thinner. They must be glued onto the haptic surface, which results in additional production costs and prevents the use of collective deposition methods. Moreover, they are not transparent,

making it impossible to integrate them directly into touchscreens made of glass. Additionally, the operating voltage of these actuators in mobile phone is typically in the range of 50 V to 150 V (Information source: <https://www.powerelectronicstips.com/haptics-components-pt-2-lra-erm-and-piezo-drivers/>). An application-specific integrated circuit (ASIC) designed for voltage amplification is utilized to increase the output voltage to a level of 100 V.

To address these challenges, transparent actuators are being developed using piezoelectric PZT thin films on glass wafers, which provide both acceptable haptic performance and optical transparency. PZT films are considered superior materials among piezoelectric films, owing to their exceptional piezoelectric properties.[25] They are widely used in various piezoelectric microelectromechanical systems (MEMS), such as pressure sensors,[26, 27] accelerometers,[28, 29] energy harvesters,[30, 31] μ mirrors,[32] μ pumps,[33] μ switches,[34] piezoelectric haptic device,[17, 35] and inkjet printheads. The successful formation of the piezoelectric perovskite phase is critical to the effectiveness of these thin films. Achieving a phase transition from amorphous to crystalline requires high-temperature annealing. A well-crystalline PZT thin film is typically processed at temperatures between 550-650 °C using physical vapor deposition (PVD) and 650-750 °C using chemical solution deposition (CSD).[36, 37] If the temperature is lower than this range, the PZT films will crystallize into non-ferroelectric pyrochlore or fluorite phases rather than the desired ferroelectric perovskite phase.

However, the maximum processing temperature of most glass wafers is 400 °C, presenting a challenge for conventional processing methods. These methods typically rely on using glasses that can withstand high temperatures, or transfer technologies such as chemical etching[38] and laser lift off[39]. The former requires an additional buffer layer (such as HfO_2 and TiO_2) to prevent lead diffusion into the glass, which adds extra cost and process complexity. The latter is a complex process and not suitable for large-scale production. Therefore, a low-temperature process is necessary for a large-scale and cost-effective production of PZT films on glass. To overcome this obstacle, an efficient low-temperature process must be developed.

In recent decades, various approaches have been investigated to develop low-temperature processes, including the photochemical method,[40] annealing under high-pressure O_2 and O_3 ,[41] microwave annealing,[42] combustion synthesis,[43] and laser annealing.[44] Although successful in lowering the temperature, these methods often require long annealing times, sometimes several hours, or annealing in a reactive atmosphere, which limits their

use in large-scale and high-throughput production. Additionally, the PZT films produced using these methods suffer from poor piezoelectric properties. Although laser annealing can produce films with good piezoelectric properties through fast crystallization, the small size of the laser spot (typically in the $\mu\text{m}^2\text{-mm}^2$ range) necessitates raster scanning of the laser beam, which can lead to inhomogeneities in the film.

On the other hand, transparent electrodes are a crucial component for transparent actuators. Transparent conducting oxide (TCO) films are the preferred electrode materials due to their outstanding optical transparency and conducting properties.[5, 45–49] Among the available TCOs, ITO films have been commercialized and are widely used in display devices,[50–52] solar cell windows,[53–55] sensors,[56–58] actuators,[1, 59, 60] and security systems[61] as transparent electrodes. They are typically deposited by sputtering, which requires expensive ITO targets and deposition tools. Chemical solution deposition (CSD) is an attractive deposition approach due to its exceptional advantages, including low cost, high efficiency, and flexible composition adjustments. However, high-temperature annealing (typically $> 400\text{ }^\circ\text{C}$) is necessary to obtain conductive ITO.[62–67] This high processing temperature results in indium diffusion into PZT films, which degrades device performance. Therefore, a low-temperature process must be developed to overcome this difficulty.

Efforts have been dedicated to lowering the crystallization temperature of metal oxide films. Two solutions have been proposed: (a) using specific annealing technologies, such as deep UV photo annealing,[68–72] flash lamp annealing,[61, 73, 74] annealing with ozone[75–77] or in high-pressure O_2 or H_2O atmosphere[78–82], and (b) modifying the solutions, such as combustion synthesis[83–86] and using solution made of crystalline nanoparticles. Among these methods, combustion synthesis is a simple process that only requires adding a fuel (such as urea, acetylacetone, or glycine) and an oxidizer (typically metal nitrates) into conventional solutions to induce an exothermic combustion reaction upon heating.[87] This method allows for low-temperature annealing in the air and yields films with smooth surfaces, unlike the rough films typically prepared from nanoparticle-based solutions.

In microelectronics fabrication, the process of patterning is crucial. Traditionally, PZT films are patterned using wet or dry etching methods, while lithography is used to pattern ITO electrodes. However, these methods are either complex or expensive. A more cost-effective and direct approach to patterning is inkjet printing using CSD, which enables the deposition of ink droplets based on computer-assisted design (CAD)

without the need for lithography. In addition to being waste-free, inkjet printing has been successfully used for the large-scale production of electronic circuits and OLED displays.[88, 89][90]

For haptic applications that do not require transparency but prioritize low power consumption and large deflection, our developed metal-insulator-metal (MIM) thin film actuator (specifically d_{31} or e_{31} mode) is not the ideal solution due to its high power consumption of several watts, resulting from its large capacitance and driving current. An alternative solution is a d_{33} or e_{33} mode actuator with interdigitated electrodes (IDE), which offers low power consumption but requires a high actuation voltage of over 100 V.

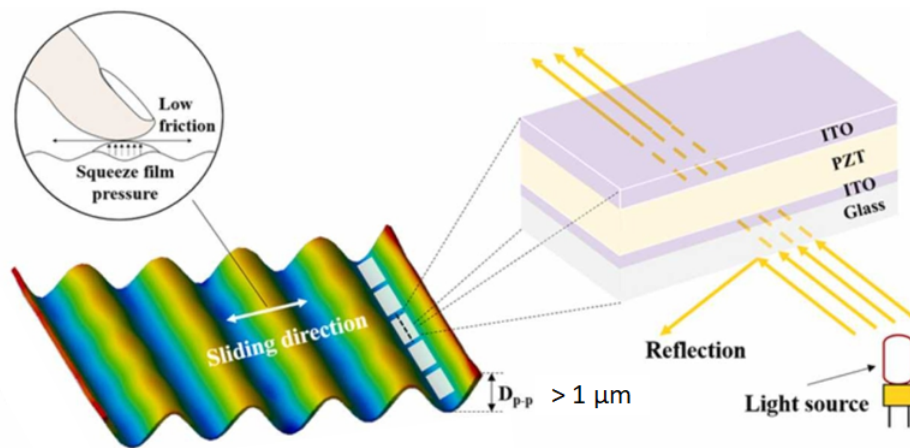


Figure 1.1: Schematic diagram of acoustic haptic device with a transparent structure.[1]

In summary, my goal is to create transparent piezoelectric haptic actuators that can be directly patterned onto glass, as shown in Figure 1.1. To achieve this, there are several requirements: (1) Deposition of piezoelectric thin films onto glass is necessary; (2) Transparent electrodes are required; (3) A fully inkjet-printing process for patterning the whole actuator is needed; (4) The fabricated haptic devices must be operated at a resonant frequency exceeding 20 kHz and be able to generate a deflection of over 1 μm .

In the abovementioned context, we have addressed these challenges in a manner that has not yet been accomplished by the current state of the art. Except Introduction and Background chapters, the thesis consists of four key chapters, each of which will try to address an abovementioned challenge and attempt to answer a scientific question from the perspective of materials science, as follows:

1. Can we directly deposit PZT thin films on glass?

(I) In Chapter 3, I have reviewed current low-temperature processes of PZT films, which includes their strategies, advances and applications. This review is helpful to guide

us to develop and design an efficient low-temperature process of PZT films, allowing for the direct deposition of PZT thin films on glasses. This work has been published as a review paper in *Applied Physics Reviews* 8 (4), 041315, and selected as featured article.

(II) In Chapter 4, I have further developed a flash-lamp process to achieve direct and low-temperature growth of PZT films on glass in seconds. The prepared PZT films reveal rather good piezoelectric property with a $e_{33,f}$ of -5 C m^{-2} . They were used to fabricate a haptic device, whose performance fulfills the specification for commercialization. This work has been submitted to *arXiv preprint arXiv:2303.13103* and *Nature Communications* (under review now).

2. Is it possible to deposit and pattern transparent electrodes using inkjet printing?

In Chapter 5, I have developed an ITO ink involving a simple combustion reaction. $400 \text{ }^\circ\text{C}$ -processed 120 nm -thick printed ITO film on fused silica glass shows a conductivity up to 1200 S cm^{-1} and a transmittance as high as 89% . Printed ITO film was used as top electrodes in PZT capacitors, and the results are comparable to those obtained with platinum top electrodes, which exhibit a remanent polarization of $14 \text{ } \mu\text{C cm}^{-2}$ and a coercive field of 80 kV cm^{-2} .

3. Is it possible to fabricate and pattern piezoelectric haptic actuators using a fully printing process?

In Chapter 6, based on inkjet-printed ITO electrodes depicted in Chapter 5 and our inkjet printed PZT films previously demonstrated in ref.[61], I have developed all-inkjet printed haptic actuators on platinised silicon substrate. At 22 V and 21.23 kHz , all-printed haptic device shows an out-of-plane deflection of $1.2 \text{ } \mu\text{m}$, beyond the specification that enables a finger to feel it ($1 \text{ } \mu\text{m}$). This work provides a strategy to directly pattern actuators without using lithography or etching.

4. Is it possible to reduce power consumption in haptic actuators with a MIM structure for those that require a low operating voltage?

(I) In Section 7.1 of Chapter 7, a proof of concept was proposed that the use of piezoelectric thick film actuators would enable comparable deflection and low power consumption. Finite element modelling indicated that the induced lateral force is dependent on voltage rather than film thickness, assuming that their piezoelectric coefficient is same. Additionally, capacitance decreases linearly with increasing thickness, leading to a decrease in power consumption. To confirm this concept experimentally, we compared the power consumption of a sol-infiltrated $10 \text{ } \mu\text{m}$ PZT actuator with a sol-gel processed

0.5 μm PZT actuator. The former consumed 15 times less power than the latter. This work has been published in *Applied Physics Letters* 121 (21), 212901.

(II) In Section 7.2, I further continued this work by constructing an 80 μm PZT actuator via screen printing to achieve significantly lower power consumption of a few mW. At 20 V and 17.8 kHz, the printed thick PZT haptic device produces 1 μm of deflection with only 5 mW of power. At 150 V, it produces a 9 μm deflection. This work has been published in *Sensors and Actuators A: Physical*, 2023, 356, 114346. This approach offers a promising solution for reducing the power consumption of a haptic device when transparency is not required.

Chapter 2

Background

To achieve the goal proposed in the Introduction, it is crucial to acquire a comprehensive understanding of the foundational principles of the related fields, from materials to devices. This involves studying the properties of piezoelectric oxide films and transparent conductive oxide films, the film deposition process, and the working principles of surface haptics.

In Section 2.1, I started with the introduction of piezoelectric films. This section delves into piezoelectricity and covers the basics of PZT materials, from bulk to thin and thick films. Furthermore, the applications of these films in sensors and actuators are briefly introduced.

Moving on to Section 2.2, I provided an overview of transparent conductive oxide films, which are employed as electrodes. This section explains the fundamental aspects of their electrical conductivity and optical transparency, along with strategies for optimizing their optical and electrical performance.

Once the fundamental knowledge of piezoelectric and conductive films is established, Section 2.3 introduces the chemical solution deposition (CSD) approach used in this thesis for film deposition. This section includes a concise introduction to solution chemistry, outlines the general steps involved in a CSD process, and specifically covers solution deposition technologies such as spin coating and inkjet printing.

Ultimately, the deposited films will be utilized in the fabrication of surface haptic devices. Section 2.4 briefly presents the fundamentals of surface haptic technologies, encompassing fingerpad contact mechanics, an overview of various surface haptic technologies, the squeezed air film theory, and the vibration model in an ultrasonic haptic device developed by Biet et al.[\[18\]](#).

2.1 Piezoelectric films and applications

2.1.1 Piezoelectricity

Applying a mechanical force to a dielectric crystal can induce charges at their surfaces. Materials with this property are named piezoelectric materials. This property is well-known as direct piezoelectric effect, first discovered in 1880 by Pierre and Jacques Curier. One year later, Gabriel Lippmann and Curier brothers discovered that applying an electric field across both sides of a crystal leads to the deformation of a crystal, known as converse piezoelectric effect.

Piezoelectric equations are developed to qualify the relationship between electrical and mechanical parameters. These parameters include electric displacement (D), electric field (E), strain (S) and stress (T). Four forms of piezoelectric equations can be written by considering any of the two above-mentioned parameters as independent variables. Eq. (2.1 and 2.2) represents the most common form (strain-charge form):

$$D = dT + \epsilon^T E \quad (2.1)$$

$$S = s^E T + d^t E \quad (2.2)$$

where d is the piezoelectric coefficient, ϵ^T is the dielectric constant measured at a constant stress, s^E is the elastic compliance coefficient at a constant electric field, the superscript t stands for the transpose, respectively.

Typically, a cantilever structure is employed for measuring the converse piezoelectric coefficient of piezoelectric thin films, as described in Appendix A4.4 on Page 193.

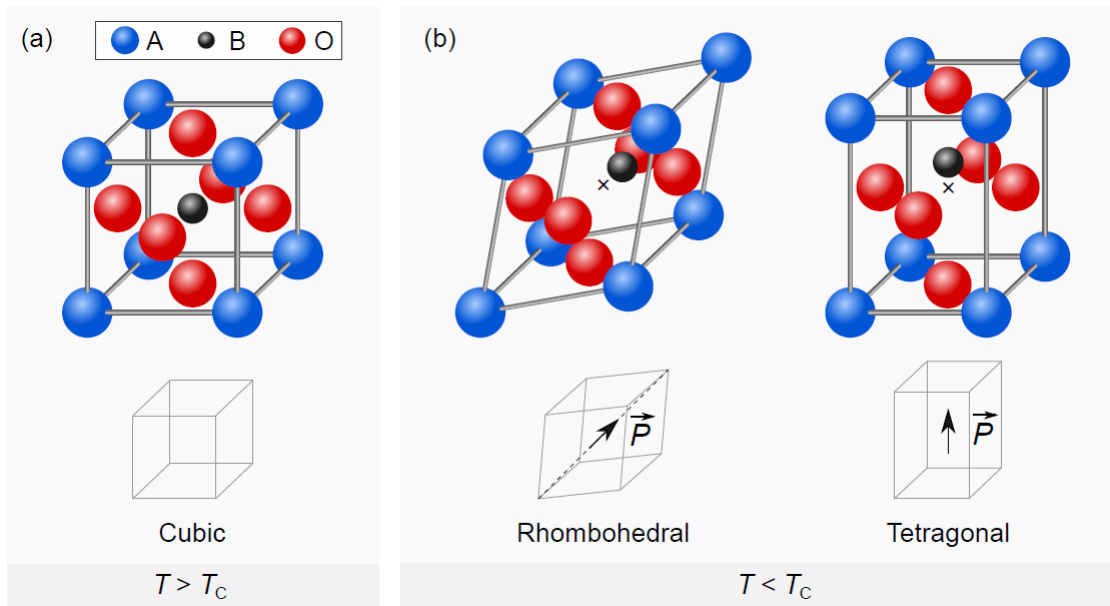
2.1.2 Lead zirconate titanate

Lead zirconate titanate (PZT) is one of the most widely used piezoelectric materials, thanks to its large piezoelectric response at the specific composition. In this section, its crystal structure, phase compositions, ferroelectricity and piezoelectricity are briefly introduced.

Perovskite PZT

PZT with a typical perovskite structure (refer to Figure 2.1), is an important crystal in piezoelectric materials. The perovskite structure is described by the chemical formula of ABO_3 , where A represents a large cation with a coordination number of 12, B represents

a small cation, and O represents oxygen. In the crystal structure of PZT, A is lead, B can be Zr or Ti. PZT exhibits an ideal cubic perovskite structure at temperatures above its Curie temperature T_c , but it is not piezoelectric at these temperatures. Below T_c , the perovskite structure undergoes different structural distortions (see Figure 2.1b), which break the centrosymmetry and lead to spontaneous polarization. This is the origin of the ferroelectricity and piezoelectricity in PZT. Commercial PZT typically has a T_c of around 200-400°C,[91] but its recommended maximum operating temperature is 150-250 °C. [92]



[93]

Figure 2.1: (a) Cubic perovskite structure above T_C and (b) Noncentrosymmetric structures below T_C caused by the distortions of the cubic cell of PZT

Phase diagram of PZT and the morphotropic phase boundary

The chemical formula of PZT is typically written as $\text{PbZr}_{1-x}\text{Ti}_x\text{O}_3$. x is a crucial parameter in determining the crystal and physical properties of PZT. Figure 2.2 shows the phase diagram of PZT as a function of temperature and Zr:Ti ratio. The morphotropic phase boundary (MPB), which occurs at $x=0.46-0.51$, separates the Ti-rich and Zr-rich regions, where PZT has tetragonal and rhombohedral structures, respectively. The MPB is almost temperature-independent within 350 °C and is nearly a vertical line. In 1999, Noheda et al. discovered a monoclinic phase in the MPB region,[94] which acts as a structural bridge in the phase transition from the rhombohedral to tetragonal phase.

The co-existence of multiple phases in PZT at MPB composition allows for the pres-

ence of more ferroelectric domain variants. In Figure 2.2b, the piezoelectric coefficients d_{31} and d_{33} and the electromechanical coupling factor (k_r) that characterizes the energy conversion efficiency between electrical energy and mechanical energy are plotted against the PZT ceramic compositions. The best electromechanical properties are observed at the MPB composition.

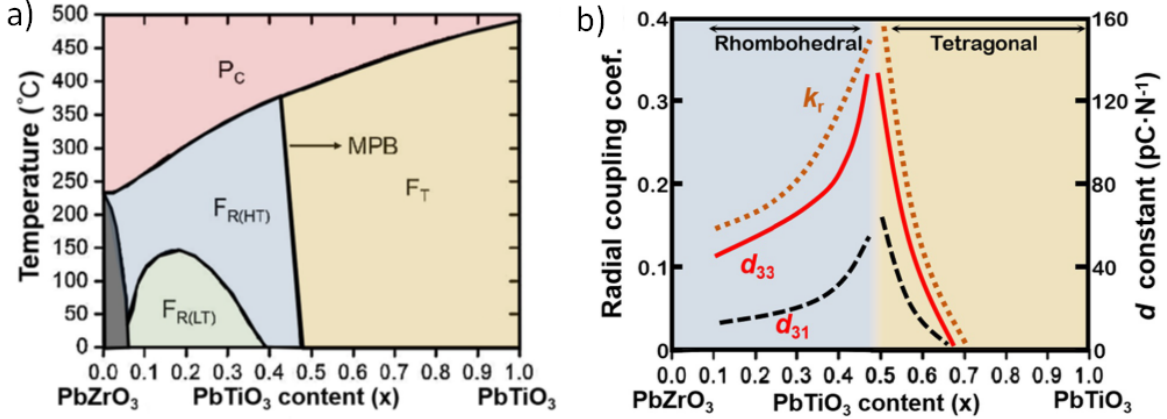


Figure 2.2: (a) Original temperature-composition phase diagram of the PZT solid solution. (b) Electromechanical properties versus composition of PZT ceramic.[2]

Ferroelectricity in PZT

Piezoelectricity in PZT is a result of its ferroelectric nature, which can be characterized by measuring the polarization (P) loop as a function of the electric field (E) at a specific frequency, exhibiting hysteresis behavior. This relationship is represented by a P - E loop that demonstrates the reorientation of the polarization in response to a changing electric field, as depicted in Figure 2.3. Prior to the application of an electric field, the polarization is nearly zero due to the compensation between the various orientations of polarization. However, when an electric field is applied, the polarization is reoriented in a specific direction, reaching a maximum value known as the saturation value, either P_{max} or P_s , depending on the strength of the applied electric field. When the electric field is reduced to zero, the polarization remains at a non-zero value, referred to as the remanent polarization P_r . To return the polarization to zero, an opposite electric voltage must be applied, known as the coercive field E_c . The switching of the polarization is achieved through the movement of domain walls and domain nucleation.

The P-E hysteresis loop is commonly measured by applying a triangular waveform at a specific frequency, as extensively described in Appendix A4.2.

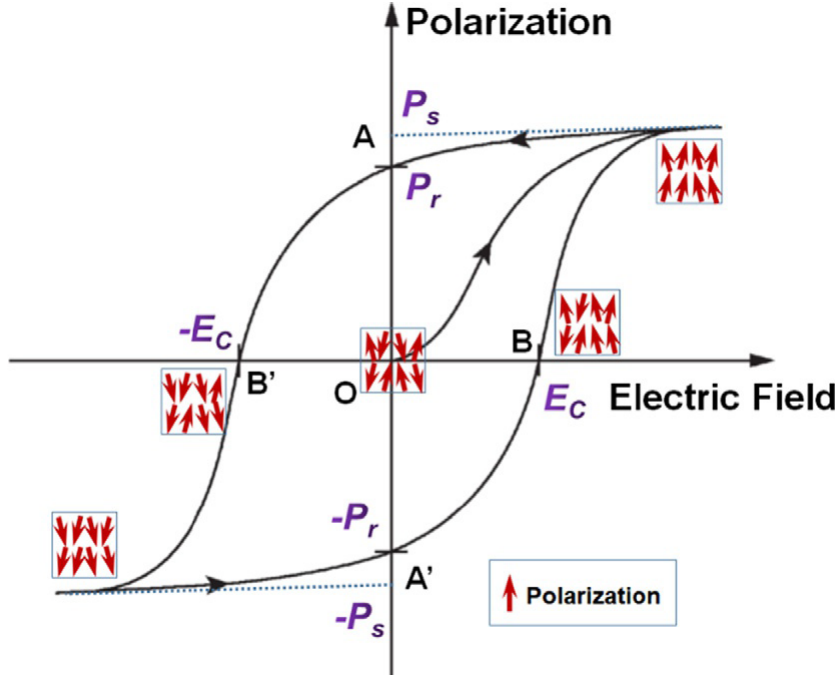


Figure 2.3: Typical ferroelectric polarization versus electric field hysteresis loop.[2]

2.1.3 PZT thin films

The high piezoelectricity of PZT films makes them a popular choice for use in MEMS sensors and actuators. However, the electromechanical properties of PZT thin films are highly dependent on various factors, including composition, microstructure, crystallographic orientation, process conditions, and residual stress. When measuring the effective piezoelectric coefficients of thin films, it is important to consider the substrate clamping effect. The piezoelectric coefficients that are commonly used are $d_{33,f}$ and $e_{31,f}$, which are defined as:

$$d_{33,f} = d_{33} - 2d_{31}s_{13}^E(s_{11}^E + s_{12}^E) \quad (2.3)$$

$$e_{31,f} = e_{31} + e_{33}s_{13}^E(s_{11}^E + s_{12}^E) \quad (2.4)$$

where s_{ij}^E , d_{33} and e_{31} are, respectively, compliances at constant electric field and pure piezoelectric coefficients.

Figure 2.4 illustrates the relationship between the effective transverse piezoelectric coefficient $e_{31,f}$ and the composition of PZT thin films that are oriented in the $\{100\}$ and $\{111\}$ directions. Similar to PZT ceramics, PZT thin films that are deposited on platinised silicon and positioned at the MPB exhibit the highest values of $e_{31,f}$. Additionally, it is worth noting that, for the same composition, PZT thin films oriented in the $\{100\}$ direction demonstrate superior piezoelectric properties compared to those in the $\{111\}$ direction.

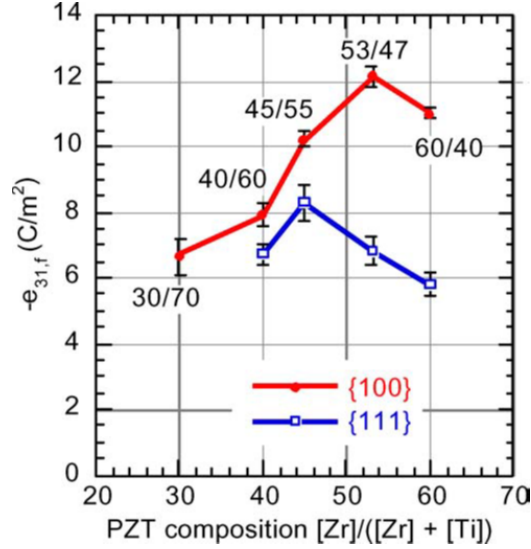


Figure 2.4: Transverse piezoelectric response in $\{111\}$ and $\{100\}$ textured PZT films as a function of composition. All of the films were deposited on platinized Si substrates.[3]

The properties of PZT thin films with regard to piezoelectricity can be significantly affected by the processing conditions employed. Different techniques for depositing thin films, such as physical vapor deposition, chemical vapor deposition, and chemical solution deposition, are commonly utilized to create PZT thin films on substrates. Once the films are deposited, a thermal annealing process is required to transform the initially amorphous PZT into the piezoelectrically active perovskite phase, typically requiring annealing temperatures in excess of 650 °C. If the temperature used is below this threshold, the PZT thin films crystallize into the non-ferroelectric pyrochlore phase.

Table 2.1 presents the state-of-the-art electromechanical properties of sol-gel PZT thin films deposited on platinized Si substrates and crystallized at the standard temperature of 700 °C for PZT films.

Table 2.1: State-of-the-art electromechanical properties of PZT thin films with morphotropic phase boundary (MPB) composition. Polycrystalline $\{100\}$ oriented 1 μm -thick film deposited on platinized Si substrates and annealed at 700 °C.[21]

Property	dielectric permittivity	dielectric loss	Remanent polarization	Longitudinal piezoelectric coefficient	Transversal piezoelectric coefficient
symbol	ϵ_r	$\tan\delta$	P_r	$d_{33,f}$	$e_{31,f}$
Unit	-	-	$\mu\text{C cm}^{-2}$	pm V^{-1}	C m^{-2}
Value	1400	0.05	20	150	-17

The crystallographic orientation of PZT thin films is heavily influenced by the choice

of substrate or bottom electrode. Platinized silicon substrates (Pt/Ti/SiO₂/Si) are among the most commonly used substrates due to the formation of Pt₃Pb resulting from the diffusion of Pb into Pt. Normally, solution-processed PZT film on platinized silicon growth along the {111} orientation, which has been demonstrated in previous literature.[95] Note also that this situation also depends on the deposition technologies and deposition conditions. However, on LaNiO₃/SiO₂/Si substrates, films tend to preferentially orient along {100}.[96] These outcomes can be altered by incorporating an additional nucleation layer. For instance, Godard et al. utilized a lead titanate oxide (PTO) nucleation layer to facilitate film growth along the {100} orientation instead of the {111} orientation.[95]

2.1.4 PZT thick films

Thin films are films that have a thickness of less than 1 μm, while thick films are those with a thickness ranging from 1 to 100 μm. As mentioned previously, film thickness plays a significant role in the electromechanical properties of PZT films. Typically, the piezoelectric coefficient of PZT films improves with increasing film thickness, as illustrated in Figure 2.5. The deposition of thick films depends on powder-based deposition technologies, such as screen printing and aerosol deposition. The initially deposited thick films are often porous, which is a common characteristic of powder-based films. To densify the films, high-temperature annealing (up to 1000 °C) is required. Such high processing temperatures necessitate the use of ceramic substrates, such as Al₂O₃ ceramic. Aerosol deposition offers a low-temperature process for creating thick films on temperature-sensitive substrates like glass and polymers. However, this technique requires powder with small size and high quality, and it is generally necessary to dry and sieve the powder before each deposition.[97]

2.1.5 Applications

Piezoelectric devices utilize PZT films in various applications, including sensors, actuators, and energy harvesters. The direct piezoelectric effect is employed in piezoelectric sensors to convert mechanical energy into electrical signals, which are commonly used for measuring force or pressure. PZT sensors have been utilized in pressure sensors,[26] wearable sensors,[98] accelerometers,[28] and gyroscopes,[99] among others. Similarly, piezoelectric energy harvesters operate on the same principle, converting mechanical energy into electrical energy, which can then power portable electronic devices. Flexible

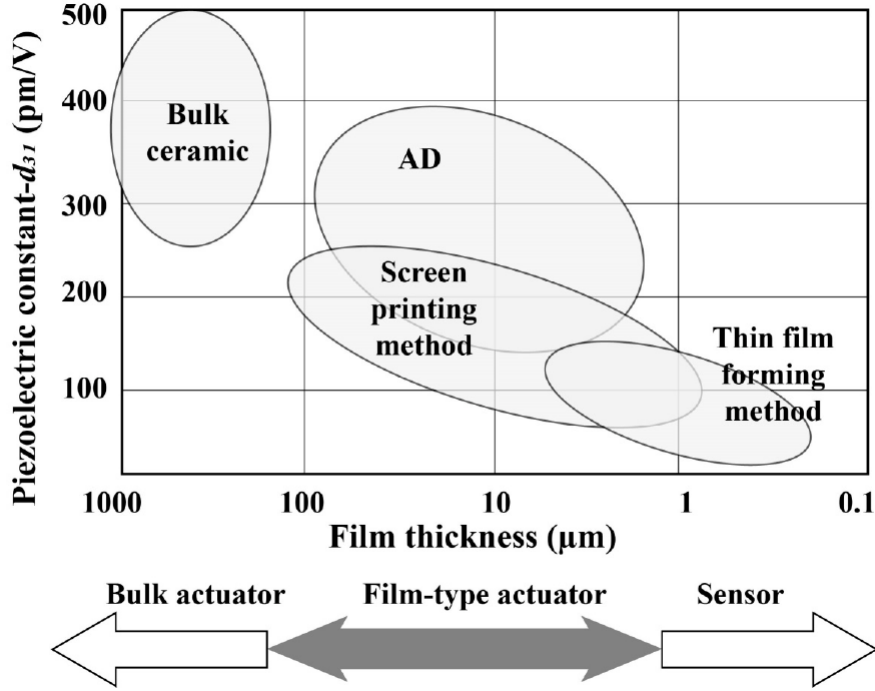


Figure 2.5: Piezoelectric coefficient versus film thickness.[4] Note that in PZT thick films or ceramics, doping was performed to improve their piezoelectric properties.

piezoelectric energy harvesters have attracted interest in the fields of electronic skin, implantable/wearable systems, and body sensor networks.[39]

In contrast to piezoelectric sensors, piezoelectric actuators utilize the converse piezoelectric effect, which converts electrical energy into mechanical energy. They are widely used to create various devices such as micropumps,[33] inkjet printer heads,[100] micromirrors, [101] and haptic devices,[17] among others.

As our studies focus on acoustic haptics based on piezoelectric actuators, more information about piezoelectric actuators is introduced here. Typically, there are two working modes of actuator, as shown in Figure 2.6. One uses metal-insulator-metal structure (MIM), which utilizes the piezoelectric coefficient d_{31} or e_{31} . Another one uses interdigitated structure electrode (IDE), which uses the piezoelectric coefficient d_{33} or e_{33} . d_{31} mode actuator usually works at a low voltage but has a large capacitance. d_{33} mode actuator usually operates at a high voltage but has a low capacitance, because the effective film thickness depends on the finger gap, which is in the range of several to tens of μm (cf. Figure 2.6). d_{33} mode actuator is, in general, used in those devices that require low current or low power consumption. These two types of actuators provide different technological solutions to add haptic effects to different electronic devices.

In order to incorporate actuators directly onto glass screens, a transparent structure is essential, which requires the utilization of transparent electrodes. In the following section,

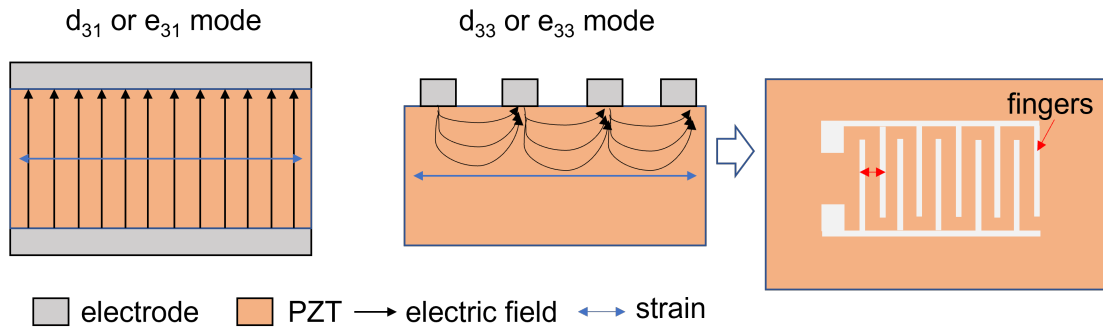


Figure 2.6: Actuators with two different working mode.

I will provide an introduction to the fundamentals of transparent conductive oxides.

2.2 Transparent conductive oxides

Among the various transparent electrodes, transparent conductive oxides (TCOs) are a class of materials that exhibit both electrical conductivity and optical transparency.[102, 103] These films have found widespread use as transparent electrodes in various electronic devices, including flat panel displays, solar cell windows, thin-film transistors, and haptic devices, among others. TCOs typically possess high transmittance in the visible range owing to their large band gap, which is greater than 3.3 eV.[103] High conductivity is achieved through a combination of high carrier density, which is usually enhanced by doping with donor elements, and high carrier mobility, which is dependent on the intrinsic properties of the TCO material. The most commonly used TCO electrode materials include aluminum-doped zinc oxide (ZAO), tin-doped indium oxide (ITO), and fluorine-doped tin oxide (FTO). In the following subsections, we will discuss their electrical conductivity, optical transparency, and methods for designing highly conductive TCOs. Specifically, we will focus on ITO, which is still considered the "gold standard" among TCOs.

2.2.1 Electrical conductivity

One of the key factors that determine the suitability of TCOs as electrode materials is their electrical conductivity (σ). Figure 2.7 provides a comparison of the (σ) values of semiconductors, TCOs, and metals, revealing that the current state-of-the-art TCOs have conductivity values that lie between those of semiconductors and metals. This is consistent with the fact that TCOs are produced by doping donor elements into oxide semiconductors. Furthermore, such conductivity values satisfy the requirements of most electronic devices. Physical vapor deposited TCOs are known to exhibit the highest

benchmark conductivity values among TCOs (5000-10000 Scm^{-1}).

To fabricate highly conductive TCOs, it is crucial to comprehend the nature of conductivity in these materials. The electrical conductivity of TCOs can be expressed through the equation:

$$\sigma = ne\mu \quad (2.5)$$

Here, n , e , and μ represent carrier density, elementary electric charge, and carrier mobility, respectively. This equation demonstrates that σ is dependent on the carrier density and carrier mobility of the material. The respective values for semiconductors (P-doped Si, heavily P-doped Si), silver, and ITO are listed in Table 2.2. Among these materials, silver exhibits the highest conductivity, with a value of approximately 10^6 Scm^{-1} , owing to its high carrier density of around 10^{22} cm^{-3} . Although P-doped Si has a much lower conductivity due to its low carrier density, it has a significantly higher mobility than silver. Its carrier density can be substantially increased by heavily doping with phosphorus, but this also decreases its mobility. This indicates that doping with a donor element can enhance conductivity, but there is a trade-off between carrier density and mobility. In the case of TCOs, ITO exhibits a high carrier density comparable to that of silver, but a low mobility in the range of $20\text{-}80 \text{ cm}^2\text{V}^{-1}\text{s}^{-1}$. This can be attributed to the fact that ITO is prepared by doping Sn into In_2O_3 , which is a semiconductor material.

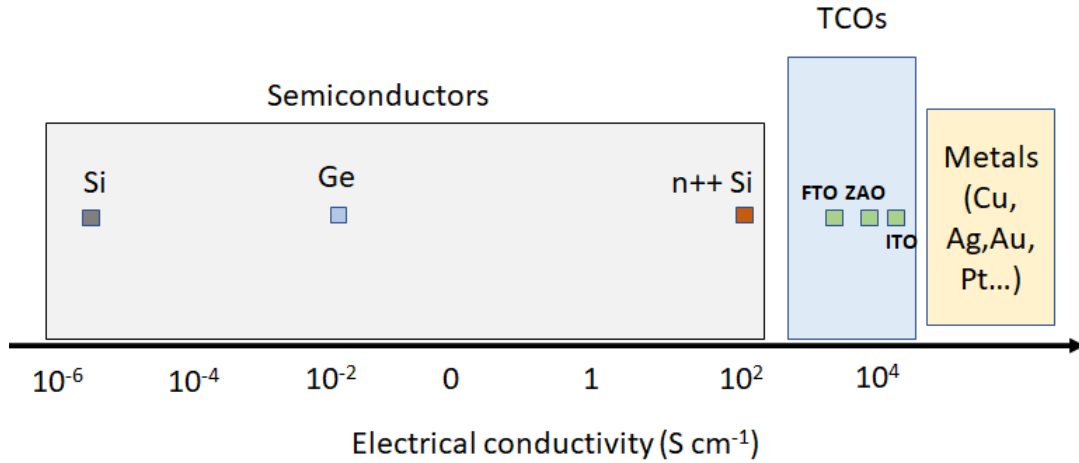


Figure 2.7: Electrical conductivity of semiconductors, TCOs and metals.[5]

Equation 2.6 describes the mobility μ in terms of the free carrier resistivity relaxation time τ and the carrier effective mass m^* , as follows:

$$\mu = \frac{e\tau}{m^*} \quad (2.6)$$

Table 2.2: Electrical properties of Ag, Si:P and ITO

Materials	$\sigma(Scm^{-1})$	$n (cm^{-3})$	$\mu (cm^2V^{-1}s^{-1})$
Ag	6.80×10^5	5.76×10^{22}	72
Si:P n	10^{-2}	10^{14}	1500
Si:P n++	100	10^{19}	100
ITO	10^4	10^{20} - 10^{21}	20-80

According to Equation 2.6, μ is directly proportional to τ . Researchers such as Edwards et al.[6] have developed an "n- μ " diagram, shown in Figure 2.8, which establishes a "sorting map" of electrical conductors. The constant conductivity contours shown in the diagram are straight lines. Electrical conductors can be classified as semimetals (up-left region), metals (up-right region), TCOs (middle region), and semiconductors (bottom-right region) based on their distribution in various regions. The diagram confirms that TCOs exhibit intermediate characteristics between (semi)metals and semiconductors. When compared to SnO_2 , In_2O_3 has a higher electron density and mobility. Doping Sn into In_2O_3 increases its electron density, but slightly decreases its electron mobility.

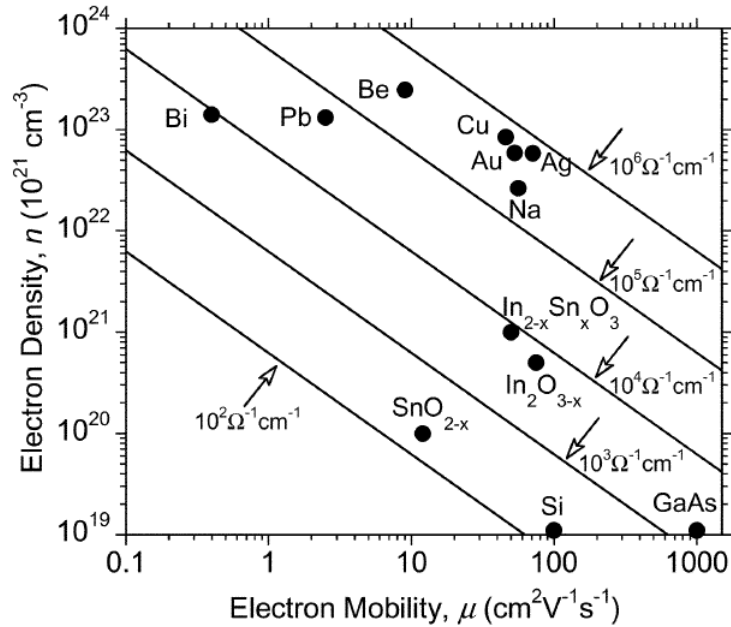


Figure 2.8: Sorting (Conducting) solids: materials space for semimetals, good metals, transparent conductors and semiconductors based on $n - \mu$ correlations (electron carrier density and electron mobility, respectively). Data shown are for room-temperature measurements. Constant conductivity contours are shown as straight lines.[6]

Various factors affect the conductivity of ITO films, including the doping concentra-

tion of Sn, film thickness, growth temperature, and processing conditions, as illustrated in Figure 2.9. [7, 104] Figure 2.9a confirms that increasing Sn doping concentration enhances carrier density but decreases carrier mobility, thus indicating an optimal doping range of 5-10%. Higher growth temperatures lead to larger grain sizes, reducing the number of grain boundaries and improving electrical properties. On the other hand, increasing oxygen pressure in the growth environment reduces conductivity due to the reduction of oxygen vacancies, which act as donors in metal oxides (Figure 2.9c). In some cases, post-annealing in a reduction atmosphere may be necessary to further enhance conductivity.

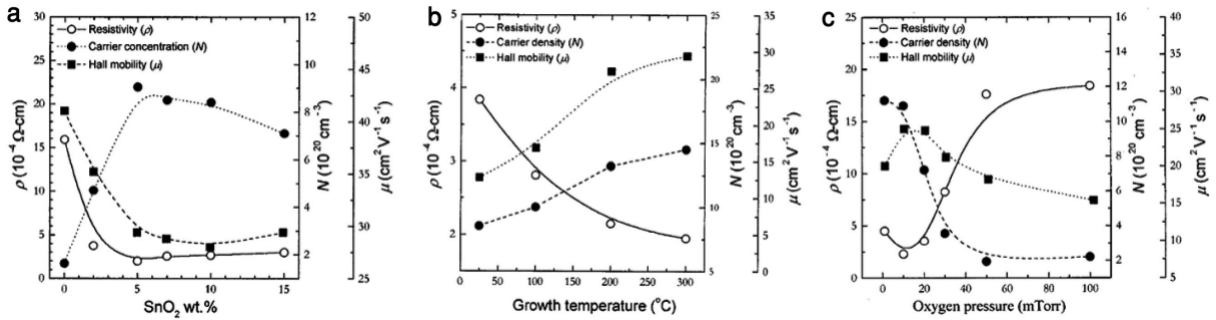


Figure 2.9: Resistivity, carrier density and hall mobility of pulse laser deposited ITO films versus (a) Sn doping concentration; (b) growth temperature; (c) oxygen pressure. [7]

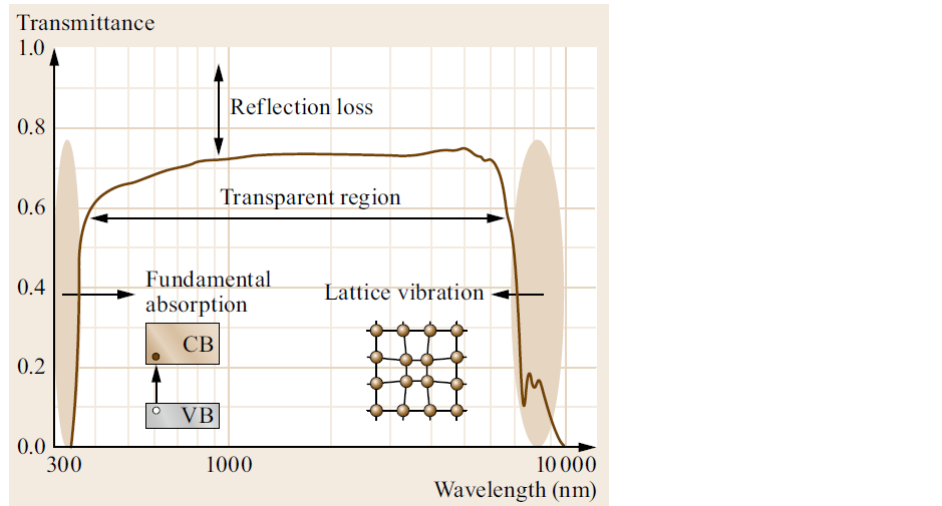


Figure 2.10: Typical transmittance spectrum of TCOs. [5]

2.2.2 Optical Transparency

Optical transparency is the property of a material to allow visible light to pass through it, typically in the range of 380-700 nm. The transmittance spectrum of TCOs is shown in Figure 2.10, where two absorption edges are observed in the infrared and ultraviolet regions, respectively. The infrared absorption is caused by lattice vibrations, while the

ultraviolet absorption results from electron transitions from the valence to the conduction band, which is related to the band gap of the material. TCOs exhibit high transmittance ($T\%$) in the visible region, with a typical value of over 80% at 550 nm wavelength, which is the wavelength our eyes are most sensitive to. ITO films have a wide band gap of 3.75 eV, which contributes to their high transmittance.[5]

2.2.3 Opto-electrical performance

To ensure a TCO film is of good quality, it must possess both satisfactory transparent and conducting properties. Typically, the conducting property of a thin film is evaluated by measuring sheet resistance (R_s) through a four-probe method. The corresponding resistivity ρ and conductivity σ can then be calculated using the equations: $\rho = R_s \times t$ and $\sigma = 1/\rho$, where t is the thickness of the film. In principle, ρ and σ are intrinsic properties of materials, meaning that R_s is dependent on the thickness of the film. Increasing the thickness of the film can lead to an improvement in σ since the grains become larger, which occurs in physical vapor deposition. Therefore, in some applications, a thicker film can benefit as an electrode, but this may come at the cost of reduced transparency.

Light is fundamentally an electromagnetic wave, and when it interacts with an electron gas, it generates a plasma oscillation that has the same frequency as the incident light. Consequently, the surface of conductors reflects the light. Conversely, when the frequency of the light is high, the carriers are unable to keep up with the rapid oscillation of the electric field, resulting in the light passing through the conductors without inducing a plasma oscillation or surface reflection. The oscillation frequency can be obtained through classical Drude theory, described as following:

$$\omega = \left(\frac{ne^2}{m^* \epsilon_r \epsilon_0} \right) \quad (2.7)$$

where ω is the oscillation frequency, n is electron concentration, m^* is the effective mass of electron, ϵ_r is the relative permittivity, and ϵ_0 is the vacuum permittivity constant. In this consideration, there is a trade-off between electron concentration and $T\%$.

Their relation between the sheet resistance and transmittance is qualified using the following equation:[8]

$$T = \left(1 + \frac{188.5\sigma_{opt}}{R_s\sigma_{DC}} \right)^{-2} \quad (2.8)$$

where σ_{opt} and σ_{DC} are the optical conductivity and the direct current conductivity, respectively. σ_{DC} is frequency dependent and can be calculated through the following

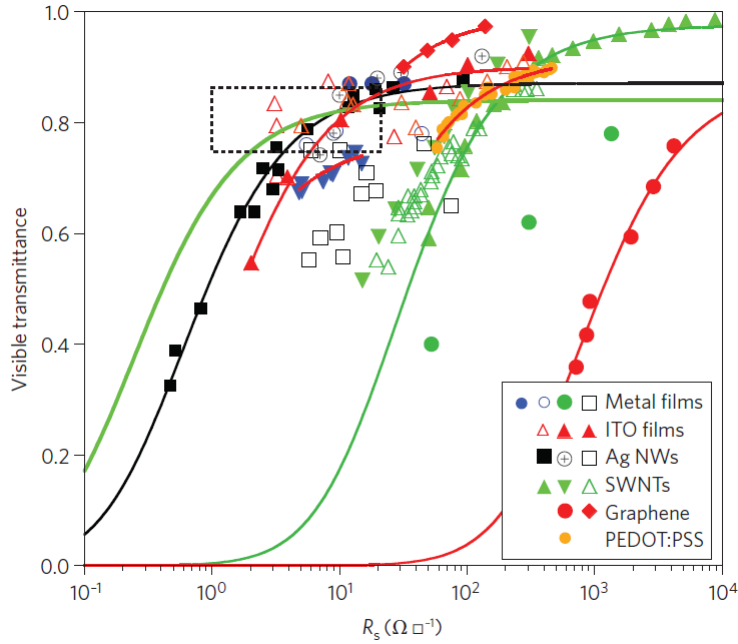


Figure 2.11: T in the visible range as a function of R_s for TCOs films.[8] SWNTs represent single-wall carbon nanotudes.

equation: $\mathbf{j} = \sigma_{DC}\mathbf{E}$, where \mathbf{j} is the current density and \mathbf{E} is the applied static electric field at frequency $\omega = 0$.

Figure 2.11 plots the $T\%$ as a function of R_s to optimize various TCOs. Materials located within the dashed box region are suitable for TCO electrodes as they offer both acceptable transparency and electrical conductivity.

2.3 Chemical solution processing of oxides films

In order to fabricate both piezoelectric films and TCO films, an efficient and cost-effective process are necessary in the large-scale production. Chemical solution deposition (CSD) is a favored method for producing thin films of functional oxides due to its simplicity, cost-effectiveness, and flexibility in adjusting composition compared to vacuum-based deposition methods.

2.3.1 Solution chemistry

The critical initial step in CSD is to prepare a solution, and the solution chemistry plays a vital role in this process. There are multiple techniques to synthesize solutions from various precursors, such as dissolving the starting material in a suitable solvent or converting it into a more soluble or stable derivative through refluxing and distillation. All of these methods involve a common initial step of dissolving metal precursors into a solvent. The choice of solvent is critical to ensure that all starting precursors are fully

dissolved and a uniform solution is formed.

2-methoxyethanol (2-MOE) has been often used as a solvent in the production of ferroelectric and conductive oxides. As long as solutions are well prepared based on 2-MOE, they exhibit remarkable stability, with no precipitation occurring for up to 2 years. Moreover, they provide precise control and reproducibility of process chemistry, and demonstrate minimal aging effects. Despite its effectiveness, the use of 2-MOE as a solvent is problematic due to its toxicity. Consequently, researchers have endeavored to identify alternative, safer solvents to replace 2-MOE.[105] One such solvent is 1-methoxy-2-propanol, which has been identified by Godard et al. as a suitable substitute for 2-MOE in the production of lead titanate solutions. Unlike 2-MOE, 1-methoxy-2-propanol is non-toxic.[95]

The choice of synthesis strategy is not solely dependent on the dissolution of the educts. Other factors such as wettability, chemical stability, and flowability of the resulting precursor solution must also be considered. Additionally, appropriate solubility combined with pyrolysis that leaves only the cations (and oxygen) as a residue is a significant limitation in the selection of educts. Metallo-organic compounds are typically preferred due to their ability to tune solubility in polar or non-polar solvents by modifying the organic part of the molecule. Moreover, the organic moiety pyrolyzes without residue in an oxidizing ambient atmosphere, making them a suitable choice.

On the other hand, the compatibility of solution to deposition technology should also be considered, which will be discussed in the following subsection.

2.3.2 General steps

The fabrication of oxide thin films through CSD follows a four-stage process. Firstly, the precursor solution is deposited onto the substrate using solution deposition techniques. Secondly, the deposited wet film is heated at a low temperature to remove the solvent, which is typically performed on a hot plate. Thirdly, the dried gel film is subjected to further heating at a medium temperature to eliminate the organic components and form an amorphous oxide film, which is also carried out on a hot plate. Finally, the amorphous film is densified and crystallized into the desired phase through high-temperature heat annealing. In some cases, the second and third steps are combined into a single step.

2.3.3 Solution deposition technologies

Various solution deposition technologies have been developed, which are described in Figure 2.12. Each of them has their own advantages and disadvantages, which has been comprehensively reviewed in Pasquarelli et al.[9]

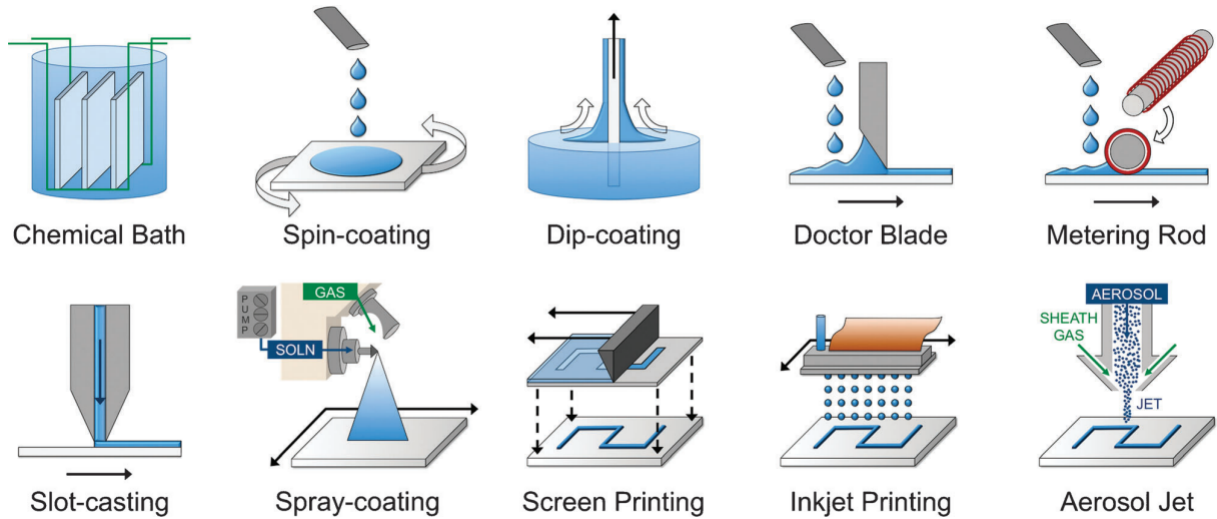


Figure 2.12: Different solution deposition technologies.[9]

Among them, spin coating is the one often used in the deposition of oxides films in the lab and industry, which enables to deposit uniform film with a surface roughness of only a few nanometer. Printing technologies is emerging to achieve the direct pattern of oxides thin films. In these considerations, we will specifically introduce spin coating and inkjet printing in this subsection.

Spin coating

Spin coating deploys centrifugal force to create uniform thin films. The method involves placing a uniformly flat substrate onto a spindle and dispensing solution onto the center of the substrate using a syringe with a filter. The substrate is then rapidly accelerated toward the center, causing the liquid to spread over the surface through centrifugal force. As a result, any extra solution is thrown off the rotating substrate's edge, leaving a consistent thin film on the surface.

Ensuring the appropriate wetting property of the substrate is crucial to achieve a uniform film. Sometimes, surface cleaning is necessary to enhance the substrate surface's wetting properties. Generally, there are three methods for cleaning the substrate surface: plasma cleaning, ozone cleaning, and preheating the substrate to high temperatures.

Apart from wet property of substrate surface, spin speed is another factor to influence the film thickness. As long as the solution concentration is unchanged, the relationship between the film thickness and spin speed can be described as:

$$t \propto \frac{1}{\sqrt{\omega}} \quad (2.9)$$

Moreover, the thickness of the resulting film is affected by various properties of the prepared solution, including density, viscosity, and solvent evaporation rate. Meyerhofer's equation, as expressed in [106], takes these factors into account and quantifies the final dried film thickness as follows:

$$t_f = \left(\frac{3\eta_0 E}{2(1 - C_0)\rho\omega_0^2} \right)^{\frac{1}{3}} \quad (2.10)$$

Here, C_0 represents the initial concentration of the solution, ρ represents the density, η_0 represents the viscosity, ω_0 represents the angular velocity, and E represents the evaporating rate.

Following the film deposition step as previously mentioned in the subsection, the functional oxide films are obtained through drying, pyrolysis, and crystallization processes. To achieve a thicker and denser film, layer-by-layer deposition is required, which involves repeating these steps multiple times.

Spin coating is the preferred technique for producing high-quality films, however, it generates significant material waste as more than 90% of the solution is spun off. This not only has cost implications, but also raises concerns about the potential environmental impact of disposing of these chemical wastes.

Inkjet printing

Unlike spin coating, inkjet printing allows for direct patterning of the film and waste-less production. This technique involves producing and patterning films by arranging and merging drops.

In general, there are two types of inkjet printers, namely continuous inkjet and drop-on-demand inkjet printers, as schematically shown in Figure 2.13.

(1) Continuous inkjet printing (CIJ)

In CIJ printing a continuous stream of drops is created through the Rayleigh instability of a liquid column. This liquid stream is forced out through a small nozzle by pressure. In general, the drop size is larger than nozzle size. The minimum size of drop can reach around 100 μm . A small pressure fluctuation on the liquid behind the nozzle via

a piezoelectric actuator is imposed to synchronize drop formation, when multiple nozzles are operating in parallel. When printing is not needed, drops are deflected through a deflector to recycling gutter. CIJ printing produces drops at a frequency of 20-60 kHz with a drop velocity $> 10 \text{ ms}^{-1}$. The disadvantage of CIJ is that deflecting drops to recycling gutter wastes ink, which induces extra cost.

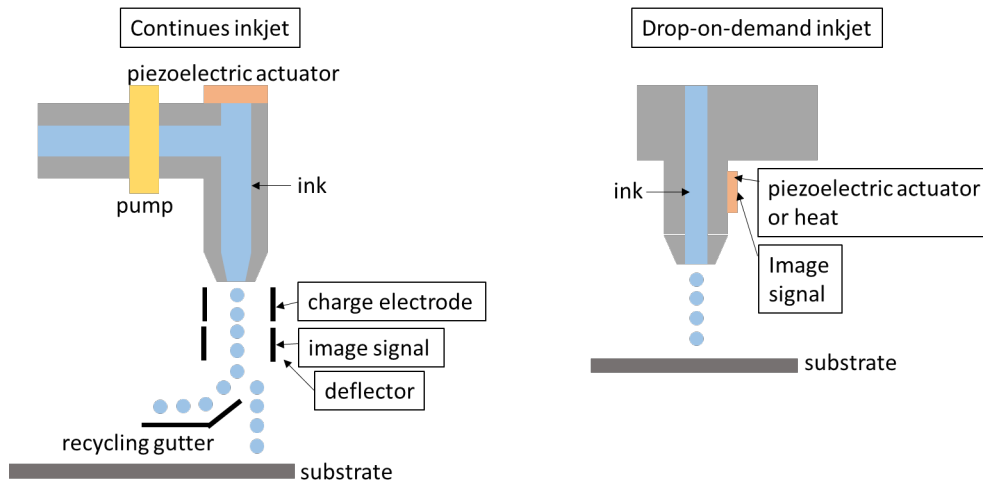


Figure 2.13: Schematic diagram of continuous mode and drop-on-demand mode inkjet printing.

(2) Drop-on-demand (DOD) inkjet printing

I. Basics of DOD printing:

DOD printing is a more cost-efficient printing method compared to CIJ printing, as it produces drops based on demands. In DOD printing, computer-assisted design (CAD) is used to generate and position drops, which are then printed onto the substrate. This process results in the expected design being achieved through the merging of the printed drops on the substrate.

Ink at the nozzle is held in place by surface tension in the absence of a pressure pulse. To maintain stability of the meniscus at the nozzle, it is customary to regulate the static pressure. In DOD systems, drops are produced at frequencies of around 1-20 kHz and the resonances occurring within the chamber behind the nozzle significantly affect the propagation of pressure pulses and the creation of drops. The size of the drops is usually similar to the size of the nozzle, but it is possible to manage the pressure pulse used to form the drops to control both the size of the drops and their ejection velocity within a specific range.

DOD inkjet printing can be classified into two types, thermal DOD inkjet printing and piezoelectric DOD inkjet printing, based on the method used to generate the pressure

pulse that expels the drop, as illustrated in Figure 2.14. In a thermal inkjet printing, a pressure pulse is created by rapidly heating a small volume of ink using a small heater located within the ink chamber, as shown in Figure 2.14a. Piezoelectric DOD inkjet printing employs a piezoelectric actuator that generates a pressure pulse when an applied pulse energy is used.

In practice, piezoelectric DOD inkjet printing is more widely used in the industry because it is relatively simple to adjust the actuation pulse, allowing for control of drop size and velocity for any type of fluid.

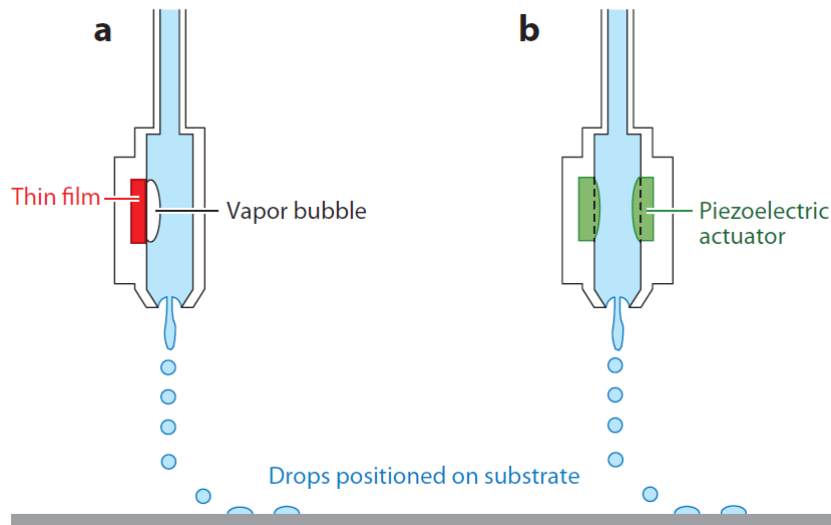


Figure 2.14: Schematic diagrams of (a) thermal DOD inkjet printing and (b) piezoelectric DOD inkjet printing.[10]

II. Ink synthesis

The first and most critical step in inkjet printing is to prepare the ink for printing. Unlike solutions used for spin coating, ink used for inkjet printing has higher viscosity or density. A good ink enables a stable jetting behaviour, which depends on the ink properties, such as viscosity η , density ρ , velocity of drop ν and surface tension γ . Given the parameters of an ink and the nozzle size (a) of the cartridge, the jetting property of the ink can generally be predicted using the Reynolds number (**Re**) and Weber number (**We**). The Reynolds number is the ratio between the inertial and viscous forces of the fluid and characterizes its flow, and can be calculated using the equation:

$$\mathbf{Re} = \frac{\rho\nu a}{\eta} \quad (2.11)$$

The Weber number is the ratio between inertial and surface tension forces, and is defined as:

$$\mathbf{We} = \frac{\rho\nu^2 a}{\eta} \quad (2.12)$$

In 1984, Fromm discovered that the $\frac{Re}{\sqrt{We}}$ ratio, also known as the Z -parameter, could be used to predict the formation of drops in inkjet printing, which is the inverse of the Ohnesorge number (Oh). [107] According to equations (2.11) and (2.12), the Z -parameter can be written as:

$$Z = \frac{1}{Oh} = \frac{Re}{\sqrt{We}} = \frac{\sqrt{\alpha\gamma\rho}}{\eta} \quad (2.13)$$

Reis and Derby found that an ink capable of forming a stable jet has a Z parameter within the range of 1 to 10, as demonstrated in Figure 2.15. This relations are true for Newtonian fluids. Inks with low values of the Z parameter exhibit excessive viscosity, making them

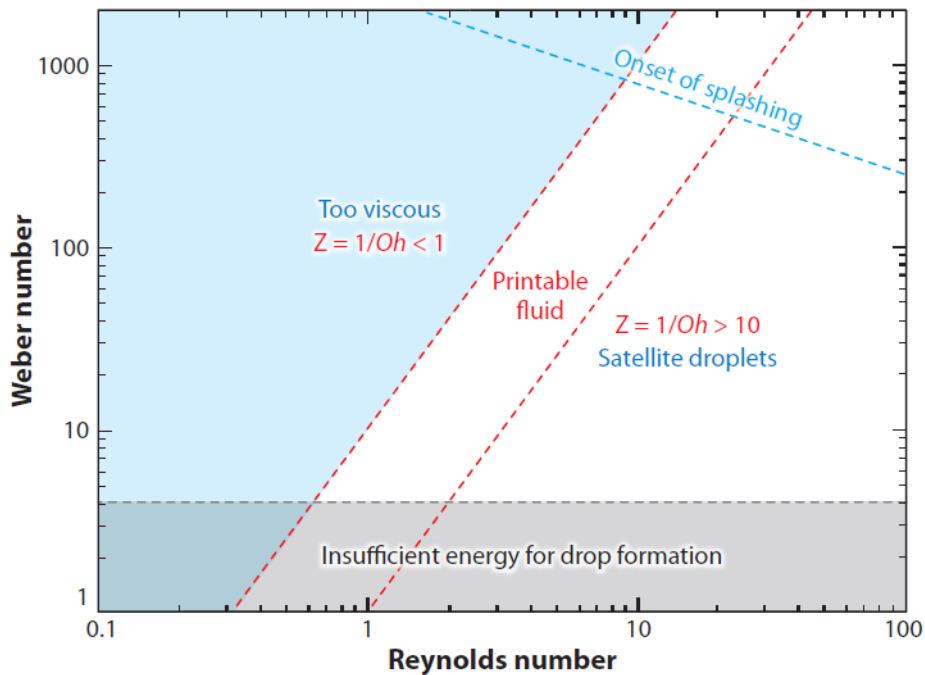


Figure 2.15: Derby diagram that indicates the range of Z values that enables stable printing ($Z = 1/Oh$). [10]

unsuitable for jetting. Conversely, inks with high Z values produce unstable satellite drops that are difficult to control and prevent the printing of precise patterns. Therefore, the Z parameter serves as an important criterion for selecting inks with optimal fluid properties for achieving high-quality inkjet printing. [10]

One feasible approach to produce a printable ink is by altering the concentration and viscosity of the spin coating solution. To enhance the printability of the spin coating solution, which commonly has a Z value greater than 10, high viscosity organic materials are employed to boost the solution's viscosity. In general, ethylene glycol and glycol are usually used.

III. surface property of substrate

In addition to the ink formulation, the surface characteristics of the substrate are also a crucial factor in influencing the properties of the printed films. Generally, a substrate with high surface energy results in a large spread drop with a greater size, making it challenging to print fine patterns. Conversely, a substrate with low surface energy leads to a smaller spread drop, causing inhomogeneity in the printed films.

One potential solution to the first issue involves utilizing an appropriate self-assembled monolayer. A study by Godard et al. [108] demonstrated this approach by using alkanethiolate-based templates to directly pattern PZT films on a high surface energy substrate. The second issue can be addressed by pre-treating the substrate with argon or oxygen plasma treatment.

Apart from above approaches, surface energy of the substrate can be also modified through controlling the substrate temperature (typically in the range of 25-50 °C).

IV. Coffee ring effect

After printing, the printed wet film undergoes a drying process as the ink solvent evaporates. In this stage, a coffee ring effect is often observed. This effect is characterized by the formation of ridge-like deposits at the edges of the printed structures (as shown in Figure 2.16). It occurs because the evaporation rate of the solvent is higher at the edge of the liquid film due to enhanced vapor transport caused by the dry substrate's proximity. As a consequence, the solute precipitates preferentially at the contact line, causing it to become pinned. In order to restore the evaporating solvent, a capillary-driven outward flow of liquid is generated, thereby sustaining the phenomenon.

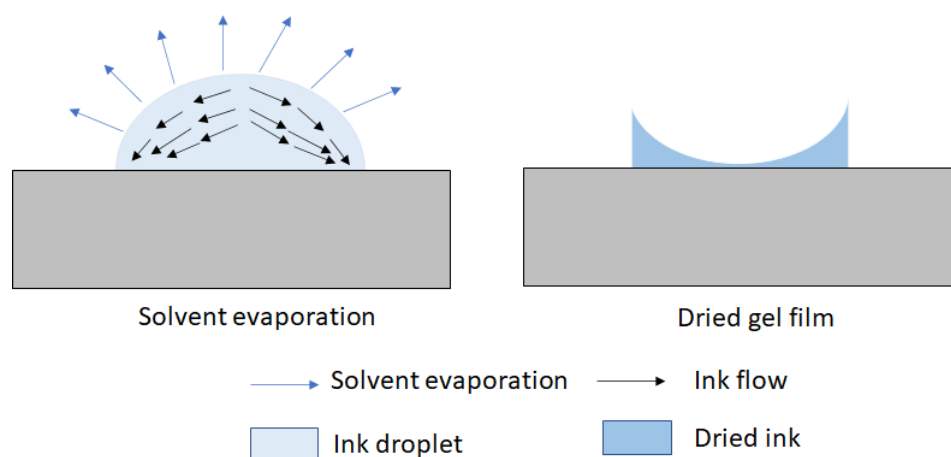


Figure 2.16: Flow of ink during solvent evaporation (left) and formed coffee ring after drying (right).

The result of the coffee ring effect is that the film at the edge of the printed pattern is significantly thicker than the film in the center, leading to non-homogeneous printed film.

To reduce this phenomenon, several approaches can be employed, including increasing the amount of solute, printing at high contact angles, and most notably, using a binary mixture of solvents.[109]

2.4 Surface haptic technology

The term “haptics” originates from the Greek word “haptesthai”, meaning to touch. Its essence lies in the transmission and comprehension of information through the sense of touch. The sense of touch arises from the interaction between materials and skin, providing our brain with information about the material properties of objects. It is crucial for humans to feel the objects in their surroundings since without haptics, we would be unable to grasp or manipulate them. In the realm of virtual reality, haptic technology is necessary to simulate the sense of touch by applying force, vibration, or motion to the human skin.

The field of haptic technology is a multidisciplinary field that encompasses knowledge from various domains such as tribology, biology, psychophysics, mechanical engineering, material science, computer science, and more. To tackle the challenges presented by this field, a comprehensive understanding of the principles underlying tactile perception and fingerpad contact mechanics in sliding contact is essential.

There is a wide range of haptic devices that have been developed for various applications based on different mechanisms. Typically, these devices can be classified into three main categories, namely graspable haptics, wearable haptics, and touchable haptics, as shown in Figure 2.17 [11]. Among these categories, surface haptics is a relatively new area of research in the field of haptics. The primary goal of surface haptics is to provide tactile feedback on touch surfaces, such as those found on display screens and front panels of new-generation home appliances. Actuation technologies are fundamental in surface haptics, and in subsection 2.1.2, we will provide an overview of surface haptics based on different mechanisms.

2.4.1 Fingerpad contact mechanics in a sliding contact

Tactile refers to the mechanical interaction between objects and skin. When a fingerpad touches an object’s surface, it stimulates thermal and mechanical receptors to generate tactile perceptions, such as softness, roughness, and warmth. This provides source information to our brain for decoding the material based on our memories. Additionally, this sensorial response also leads to a psychophysical response, resulting in emotional

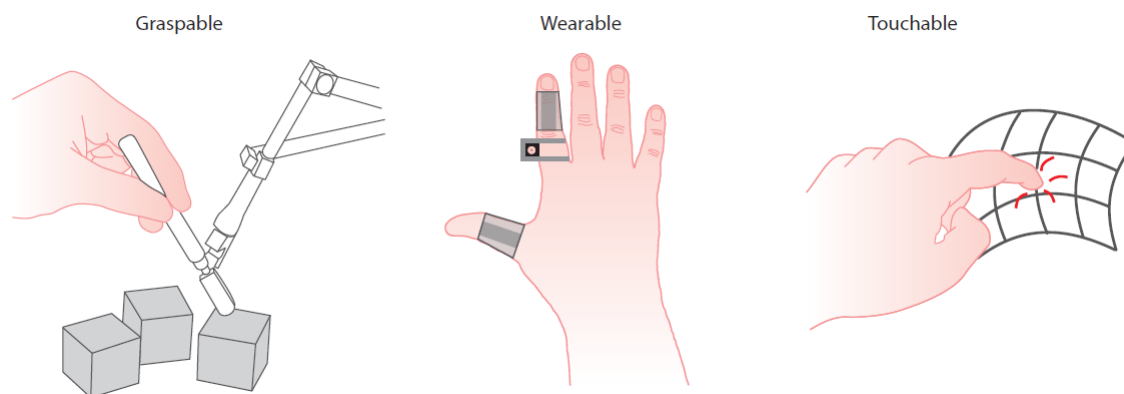


Figure 2.17: Graspable, wearable and touchable haptic devices.[11]

changes. Barnes et al.'s study showed that touching a glass surface rougher than fingers generates a negative feeling, while touching a smoother glass surface generates a positive feeling.

These sensorial and psychophysical responses are directly linked to touch surface properties, as shown in Figure 2.18. Softness is related to materials' compliance, roughness is related to the height difference of material surface, and warmth is related to the temperature difference between fingers and the surface. Mechanoreceptive afferents (sensory receptors) in the skin detect roughness, softness, and warmth, and respond to spatiotemporal stimuli such as strain and vibration. This is where contact mechanics comes into play. In the case of sliding contact, friction plays a strong role. For example, Hamilton demonstrated that in sliding contact, the maximum tensile stress at the surface and maximum shear stress beneath the surface are both proportional to friction.[110] Skeduang et al. found a negative correlation between finger friction and surface roughness in a sliding contact between a finger and paper.[111]

Friction is not only important in perceiving roughness and softness but also warmth. Choi et al. showed that a 20 K temperature change in the surface results in a 50% increase in tactile friction.[112]

Finger friction

The friction behavior of a material in mechanical engineering is described by the coefficient of friction μ , which is influenced by surface properties like compliance, roughness, temperature difference, and more. The coefficient of friction is determined using the following equation:

$$\mu = F_{\mu}/F \quad (2.14)$$

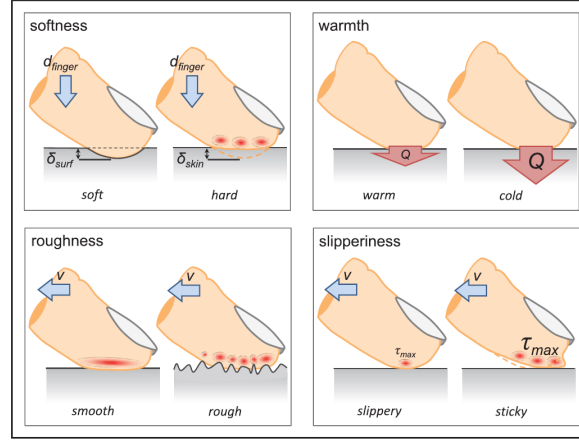


Figure 2.18: Schematics diagrams of sensorial properties of softness, warmth, roughness and slipperiness.[12] δ_{surf} and δ_{skin} stand for deformation of the object surface and the deformation of the fingerpad skin, respectively. d_{finger} , Q , v and τ_{max} are the displacement of a finger, the heat, the moving speed of a finger and the max. interfacial shear strength, respectively.

where F_{μ} is the measured friction force, and F is the normal load which is generally in the order of several N in a sliding contact.

It should be noted that the equation 2.14 provides the mean coefficient of friction in mechanical engineering to describe the friction behavior of a material, which is determined by various surface properties. However, Smith et al. have shown that the rate of change of friction is more significant than the mean coefficient of friction in describing the friction behavior. To describe the friction force, David Tabor and Frank Philip Bowden have proposed a two-term model comprising of an adhesion term F_{adh} and a deformation term F_{def} , which can be seen in equation 2.15.

$$F_{\mu} = F_{\mu,adh} + F_{\mu,def} \quad (2.15)$$

Figure 2.19 is the schematic of adhesion and deformation in a sliding contact between the fingerpad and surface. $F_{\mu,adh}$ term describes the interfacial component of friction force. It is calculated by the equation as following:

$$F_{\mu,adh} = \tau \cdot A_{real} \quad (2.16)$$

where τ is shear strength of the interface (cf. Figure 2.19) and A_{real} is the contact area. Adams et al. demonstrated that for countersurface on which there is a thin organic film such as skin, τ is a linear function of the mean contact pressure P : [13]

$$\tau = \tau_0 + \alpha \cdot P \quad (2.17)$$

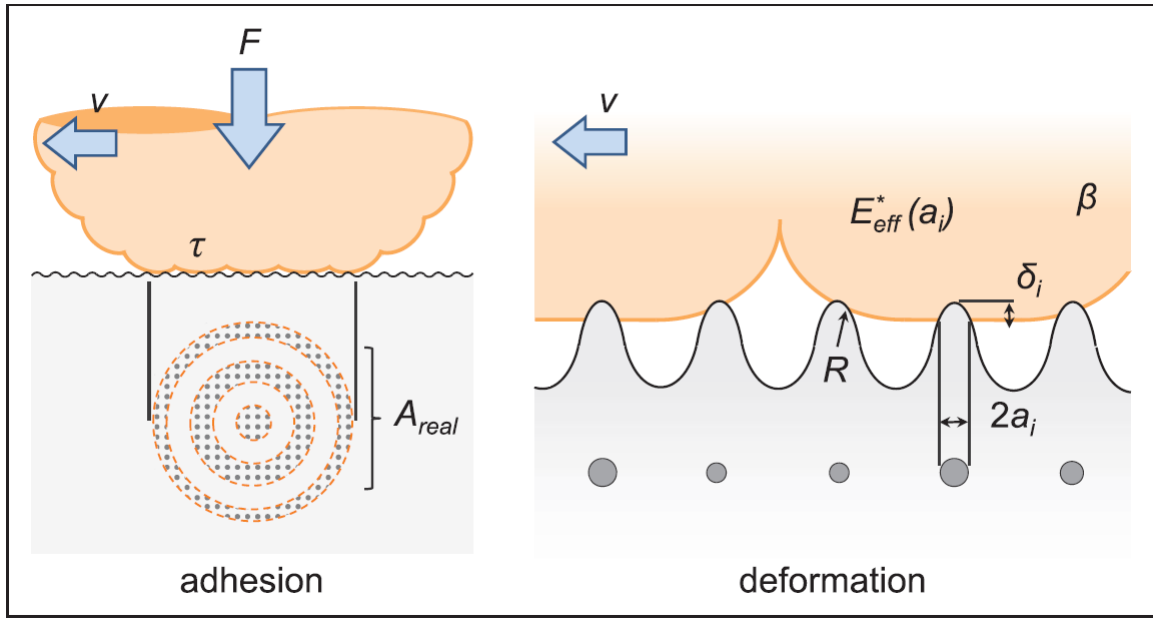


Figure 2.19: Schematic overview of the sliding contact between the fingerpad and a rough surface.[12]

where τ_0 is the intrinsic interfacial shear strength, α is a pressure coefficient.

$F_{\mu,def}$ describes the deformation component that arises from the incomplete recovery of the energy dissipated by viscoelastic deformation of skin, which is expressed as:

$$F_{\mu,def} = \frac{3}{16} \beta \frac{\delta_i}{a_i} F \quad (2.18)$$

where β is the viscoelastic hysteresis loss fraction, δ_i is the indentation, $2a_i$ is the diameter of the contact and F is the normal load (cf. Figure 2.19). β should be measured at a deformation rate that is comparable to the loading/unloading rate of the sliding contact. They may be conveniently measured using a sinusoidal deformation by using the following equation:

$$\beta = \pi \cdot \tan \delta \quad (2.19)$$

where $\tan \delta$ is viscoelastic loss tangent that is defined as the ratio between the storage and loss modulus.

Fingertip contact mechanics

Tribologists in the field of tribology engineering utilize a spherical contact model to experimentally investigate elastic-solid (skin-solid) contact mechanics. This is accomplished by sliding a rigid spherical tip, as illustrated in Figure 2.20. For human skin-solid contact, it can be approximated as the sum of many spherical contacts, as depicted in Figure 2.19. This approach is used to better understand the mechanics of tactile perception.

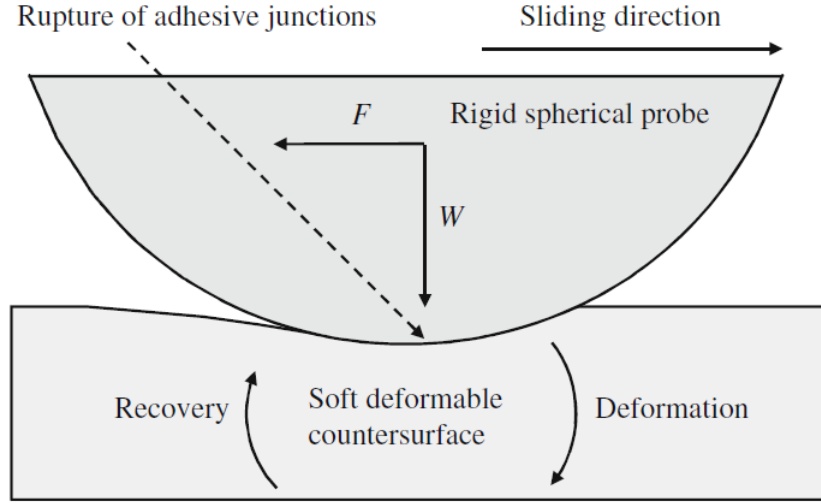


Figure 2.20: Schematic diagram of rigid spherical probe sliding on soft countersurface.[13]

Based on Hertz's theory,[113, 114] the contact radius a_H and deformation δ_H in a spherical contact are described as following:

$$a_H = \left(\frac{3}{4} \cdot \frac{RF}{E^*} \right)^{\frac{1}{3}} \quad (2.20)$$

$$\delta_H = \left(\frac{9}{16} \cdot \frac{F^2}{RE^{*2}} \right)^{\frac{1}{3}} \quad (2.21)$$

where R is the radius of curvature of spherical solid (cf. Figure 2.3), F is the normal load as mentioned earlier. E^* is the reduced elastic modulus, defined as following:

$$\frac{1}{E^*} = \frac{1 - \nu_1^2}{E_1} + \frac{1 - \nu_2^2}{E_2} \quad (2.22)$$

where E_1 and E_2 are the respective elastic moduli of contacting materials, and ν_1 and ν_2 are the respective Poisson's ratio of contacting materials. Considering that our fingerpad is much softer than touch surface in a sliding contact, this equation is simplified to be:

$$\frac{1}{E^*} = \frac{1 - \nu_{skin}^2}{E_{skin}} \quad (2.23)$$

therefore, $E^* = E_{skin}/(1 - \nu_{skin}^2)$. It should be taken into account that the skin on the fingerpad has a complex and non-uniform structure (see Figure 2.21). Consequently, there is a gradient of elasticity across the skin depth. To address this issue, Van Kuilenburg et al. introduced a new concept of effective elastic modulus $E_{eff}^* = f(a)$, which allows for the description of skin elasticity on the volar forearm as a function of the length scale a . (equal to the contact radius in a spherical contact, i.e., a_H as previously defined).

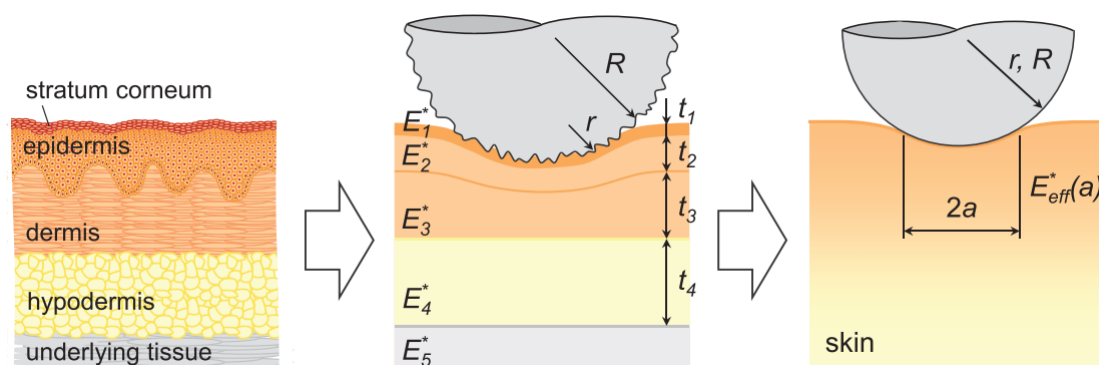


Figure 2.21: Structure of fingertip with a gradient of elasticity across the skin depth.[14]

Friction-induced vibrations at the finger contact surface

As a finger slides across the surface of an object, the resulting friction produces oscillations that travel through the skin of the finger and convey information regarding the object's properties to mechanoreceptors. These mechanoreceptors translate the vibrations into electrical signals, which are then transmitted to the brain (as has been mentioned earlier).

Mechanoreceptive units can be classified into two main categories: rapidly adapting units and slowly adapting units. In the context of the hand, there are four types of units that are particularly relevant: Meissner's corpuscles, and Pacinian corpuscles, which are both rapidly adapting, as well as Merkel cells, and Ruffini corpuscles, which are both slowly adapting (see Figure 2.22).[15] They are sensitive to different frequency, as shown in Figure 2.22.[15]

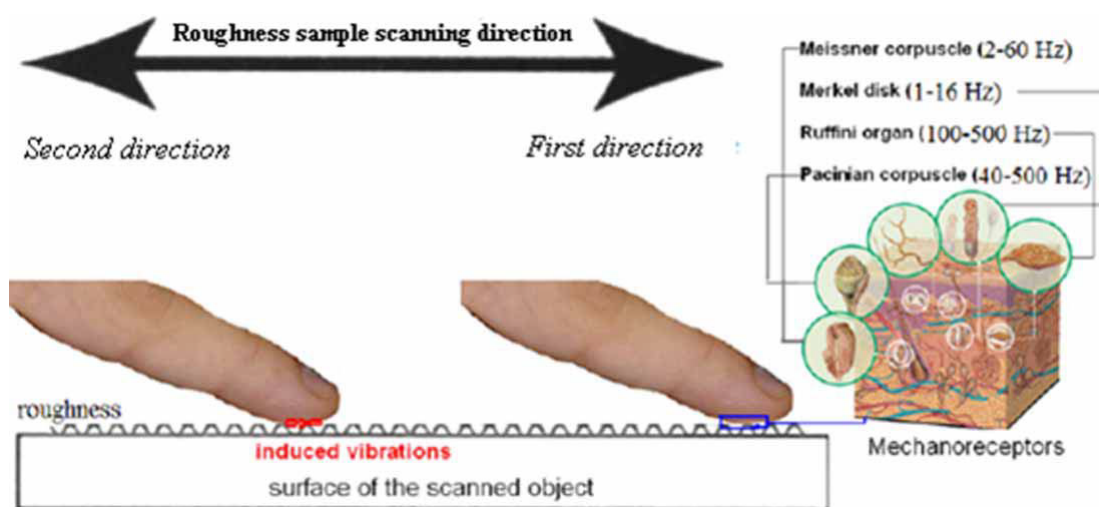


Figure 2.22: Schematic diagram of the interaction between the surface and the finger. Different mechanoreceptors units are sensitive to different vibration frequency.[15]

Specifically, Pacinian corpuscles are the most substantial mechanoreceptors, situated

in the deeper dermis layer at a depth of 1.5-2.0 mm. They are highly responsive to mechanical transients and vibrations of elevated frequencies, exhibiting sensitivity within the 40-500 Hz range, with the most elevated sensitivity occurring around 300 Hz. These corpuscles are primarily responsible for detecting acceleration vibrations, contributing to the sensation of vibrations.

As a result of the sensitivity of mechanoreceptors such as Pacinian corpuscles, haptic technologies that rely on vibration typically operate within the 10-500 Hz range. For instance, haptic actuators developed by KEMET, a US company, operate within a frequency range of 4-500 Hz, whereas those manufactured by TDK, a Japanese company, operate at a frequency of 200 Hz. In ultrasonic haptic devices, voltage amplitude modulation is necessary to create a tactile sensation on the user's finger.

2.4.2 Overview of surface haptic device

Surface haptics refer to the technologies that enable the creation of interactive touch surfaces by generating tactile effects on surfaces like display screens on mobile phones and tablets, front panels of new generation home appliances and cars, and more. The implementation of surface haptic technology has the potential to bring significant changes in various fields, including automotive, virtual reality, medical, education, online shopping, gaming, and others. As a result, the development of haptic technology has been gaining momentum, and the global market for surface haptics is projected to reach a value of approximately \$47 billion by 2030, with a compound annual growth rate (CAGR) of around 13.7% during the forecast period (Infor source: <https://www.researchandmarkets.com/reports/2832340/haptics-global-strategic-business-report>).

The modulated interaction force of a finger in a sliding contact is the key to generating haptic effects using surface haptic technology. This is achieved through the use of actuation technology, of which there are three alternatives: vibrotactile, electrostatic, and ultrasonic.

The direction of the force in force modulation can either be normal or tangential. Figure 2.23 presents the current classification of surface haptic technologies according to the method of force modulation.[16] This section provides a brief review of different surface haptic technologies and introduces their mechanisms based on the aforementioned classification.

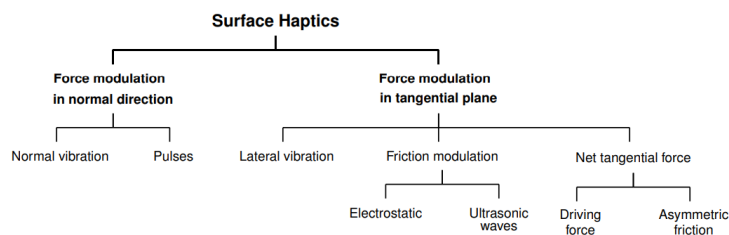


Figure 2.23: Classification of current surface haptic technologies.[16]

Normal Force modulation

The modulation of force in the normal direction involves using vibration motors or actuators to add vibrations to the touch screen. Our mobile phones have already incorporated some basic vibrations, such as when we receive a call or press virtual buttons during gaming. These haptic buttons provide a tactile feedback that simulates pressing a physical button. The localized sensations on the touch surface are created using piezoelectric actuators.

Force modulation in tangential direction

The modulation of forces in the tangential direction involves creating lateral vibrations or friction modulation. Lateral vibrations cause the skin to deflect, generating the same forces as those produced by sliding against a rough surface, and creating a sensation of roughness for a virtual surface. The advantage of lateral vibrations is that the actuators, such as electromagnetic and piezoelectric ones, can be placed at the edge of the touched surface and do not need to be transparent.

Surface haptic technologies that rely on friction modulation are designed to simulate texture and generate subtle tactile feedback. Two common methods used to achieve this are electro-adhesion and ultrasonic vibration.

1) Electro-adhesion

Johnsen and Rahbek discovered electrostatic attraction between a charged surface and human finger,[115] known as “electro-adhesion”. In 1953, Mallinckrodt et al. observed an alternating electrostatic force that attracts and releases the finger from the surface by applying voltage to insulated metal electrodes, which is known as “electrovibration”. [116] Electro-adhesion is the basis for electro-adhesion based surface haptics, which creates the sensation of texture when a user slides the finger across the surface by applying an electric charge to the display surface. The haptic effect can be controlled in real-time by adjusting the voltage. Tanvas, a US start-up company, has developed haptic

screens based on electro-adhesion, and added haptic effect to flexible TFT-LCD touch screen monitors.[117] Transparent haptic devices integrated into display screens have been developed by Tanvas, as shown in Figure 2.24, by controlling the voltage applied to a transparent indium tin oxide (ITO) matrix, which amplifies and modulates the naturally occurring friction force between the finger and smooth glass, leading to the sensation of various textures.

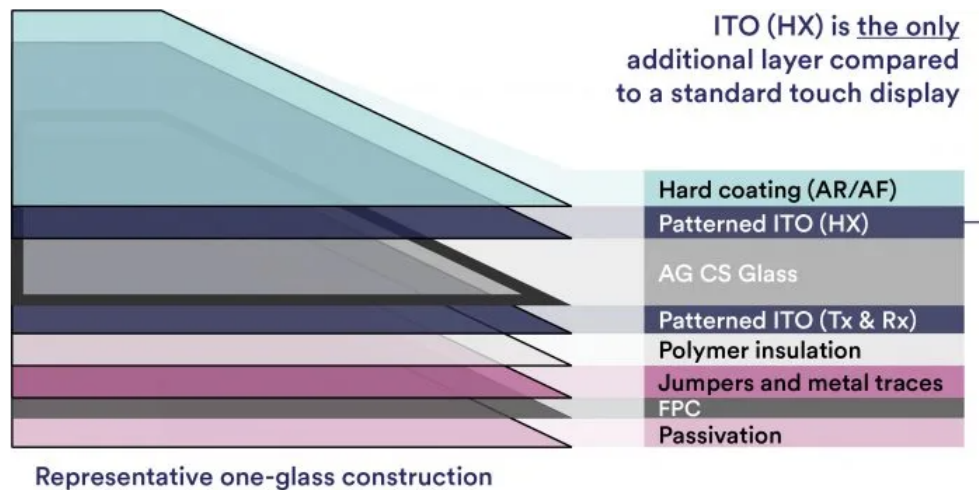


Figure 2.24: The implementation of electro-adhesion-based surface haptics in a standard display assembly requires only the addition of a patterned ITO layer on the cover glass. Source: Tanvas

2) Acoustic haptics (Ultrasonic vibration)

Ultrasonic vibrations can be generated on touch surfaces using piezoelectric actuators. As a finger slides across a haptic plate, high-speed compression and decompression of air creates a thin squeezed-air film in the contact region between the touch surface and the finger. This film reduces finger friction and simulates textures on the touch surface, as demonstrated in Figure 2.25. To form a squeezed-air film, haptic devices must operate at an A0 Lamb mode and generate a 1 μm out-of-plane amplitude at the resonance of the plate.

Hap2U, a French start-up company, has developed the world's first haptic mobile phone named "Hap2Phone" by utilizing piezoelectric actuators to generate ultrasonic vibrations. These actuators are attached to the edges of the touch screen to induce a standing wave and vibrate the screen.

Piezoelectric ceramic actuators, with a thickness of several hundred μm , have the capability to generate large deflection. However, their integration with the touch surface is restricted due to gluing, which hinders collective deposition means and adds additional

cost. To avoid such issues, piezoelectric films are used as actuators which not only offer acceptable deflection, but also allow direct integration onto the touch surface. To demonstrate this, Glinsek et al. have developed a fully transparent haptic device with piezoelectric thin film actuators and transparent interdigitated electrodes made of ITO (see Figure 2.25).

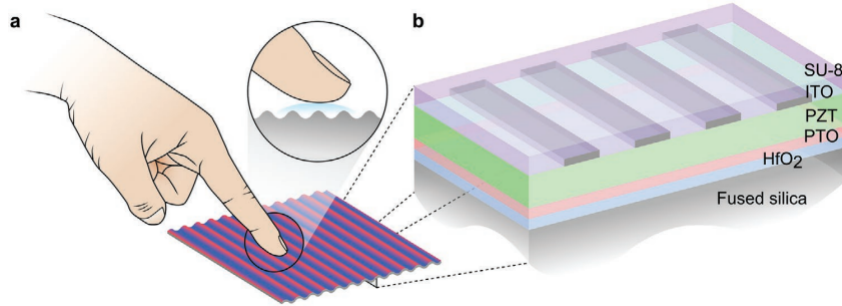


Figure 2.25: Squeezed-air film effect in a ultrasonic transparent haptic device.[17]

2.4.3 Squeezed-air film theory

The friction between two solid surfaces in contact can be significantly reduced by the application of ultrasonic vibration, which creates a squeeze film. The flow of a thin air film between two surfaces in haptics can be mathematically described using the Reynolds equation, which is a partial differential equation. In haptics, the two surfaces are the haptic surface and the fingertip of the user. In this brief introduction, we will outline how to estimate the reduction in fingertip friction due to the squeezed-air film effect, based on the models proposed by Sednaoui et al. [19] and Biet et al.[18] from L2EP lab in University of Lille .

The Reynolds equation can be written as:

$$\frac{\partial}{\partial x} \left(\rho \frac{h^3}{\eta} \frac{\partial p}{\partial x} \right) + \frac{\partial}{\partial y} \left(\rho \frac{h^3}{\eta} \frac{\partial p}{\partial y} \right) = 6U \frac{\partial(h\rho)}{\partial x} + 12 \frac{\partial(h\rho)}{\partial t} \quad (2.24)$$

where $h(x, y, t)$ is the height of the squeezed air film (see Figure 2.26), $p(x, y, t)$ is the pressure, ρ is the air density, η is the viscosity of the air and U is the tangential velocity of the surface. The left-side of the equation represents the balance of forces acting on the air film, while the right-side represents the velocity of the surface.

The given equation can be expressed in a normalized form by using the variables X , Y , H , P , and T , where X and Y are normalized lengths with respect to the active length l_0 , H is the normalized air gap height with respect to the mean air gap h_0 , P is

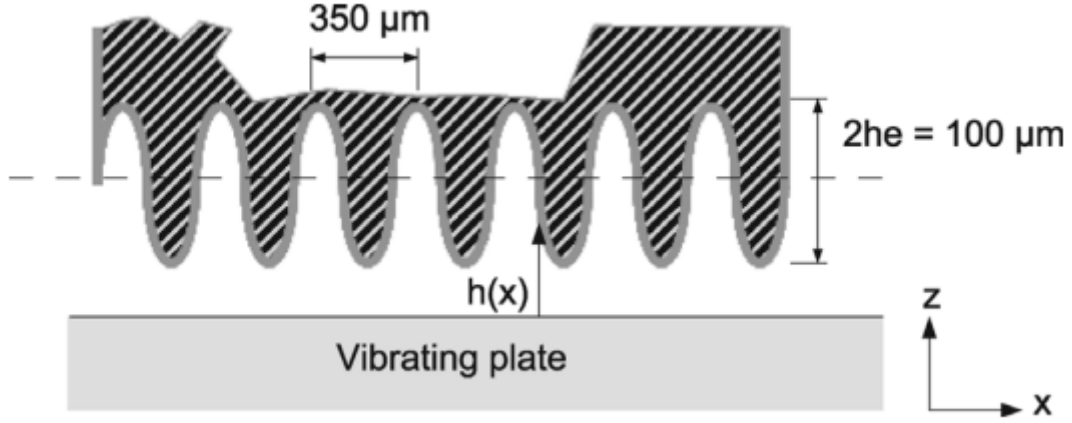


Figure 2.26: Approximation of the finger pad ridges.[18]

normalized with respect to the ambient pressure p_0 , and T is normalized with respect to the frequency ω_0 . The normalized equation is given as:

$$\frac{\partial}{\partial X} \left(H^3 P \frac{\partial P}{\partial X} \right) + \frac{\partial}{\partial Y} \left(H^3 P \frac{\partial P}{\partial Y} \right) = \Lambda \frac{\partial(HP)}{\partial X} + \sigma \frac{\partial(HP)}{\partial T} \quad (2.25)$$

Here, the squeeze number Λ and the bearing number σ are defined as:

$$\Lambda = \frac{6\eta U l_0}{h_0^2 p_0} \quad (2.26)$$

$$\sigma = \frac{12\eta \omega_0 l_0^2}{h_0^2 p_0} \quad (2.27)$$

In comparison to the out-of-plane velocity of the surface, the velocity of a sliding finger can be ignored, specifically $U=0$. According to the approximate analytical solution proposed by [19], σ is assumed to $\rightarrow \infty$. This way, the nondimensional average squeeze force F_s per unit length at steady state can be expressed by:[18, 19]

$$F_s = \iint_{\Omega} (P_{\infty} - 1) d\Omega = \frac{1}{2\pi} \int_0^{2\pi} \left(\int_{-\frac{1}{2}}^{\frac{1}{2}} (P_{\infty} - 1) dX \right) dT. \quad (2.28)$$

where P_{∞} is the the normalized pressure inside the airgap for an infinite value of the squeeze number σ , and $T = \omega_0 t$ where ω_0 is the vibrating frequency and t is time.

The typical friction model can be figured out by combining the Reynolds squeeze film theory and the Coulomb friction theory. The coefficient of friction under actuation can be quantified as:

$$\mu_r = \frac{\mu'}{\mu} = 1 - \frac{P_{\infty} - P_0}{P_f} \quad (2.29)$$

where p_f is the fingertip pressure.

Son et al. [118] compared the friction model described via eq.2.16 to the experimental results obtained by Sednaoui et al.[19] According to the friction model, an increase in the amplitude of vibration results in a decrease in the friction experienced by the fingertip, and at high enough amplitudes, the friction can be completely eliminated, reducing to zero. However, this model does not align with experimental findings, as shown in Figure 2.27. Further studies have indicated that using a two-term Herschel-Bulkley rheological equation, instead of the one-term Coulomb friction equation, could provide a solution to this problem. The adapted model has been presented in the works of Son et al.[118] and Ahmadkhanlou et al.[119].

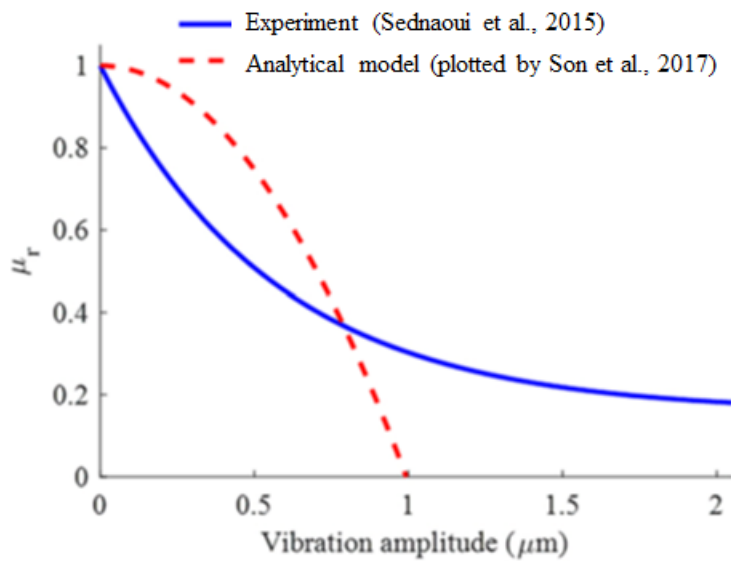


Figure 2.27: Comparison of experimental results with the analytical model for the relative friction coefficients versus vibration amplitude (Sednaoui et al., 2015)[19]

Michael et al. in J. Edward Colgate's group demonstrated that a vibration amplitude of $3 \mu\text{m}$ on an ultrasonically vibrating touch screen enables a 95% reduction in the friction force experienced by a sliding finger.[24]

2.4.4 Vibration model in ultrasonic haptics

1) Static and dynamic deflection

Euler-Bernoulli (E-B) beam theory, developed by Leonhard Euler and Jacob Bernoulli, is commonly used to construct vibration models in ultrasonic haptics. Based on E-B theory, Biet et al., developed a model of tactile plate.[18] They studied a half-wavelength portion of the plate, $\lambda/2$, modeled as a simply supported beam, as shown in Figure 2.28. The plate is vibrated by piezoelectric ceramic actuator, whose thickness is represented by h_p .

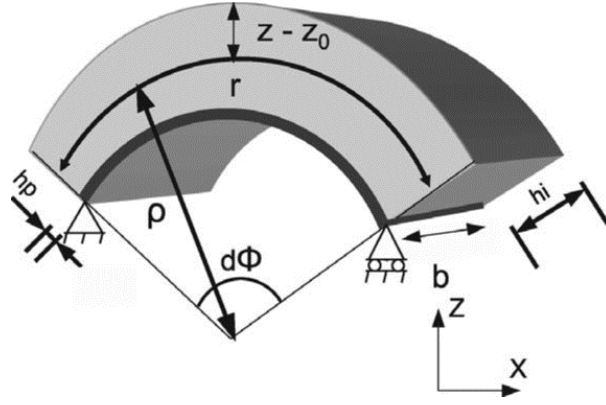


Figure 2.28: Half-wavelength beam which bends by contracting the piezoceramics.[18]

Combining E-B beam equations with the piezoelectric equations, the static deflection at $\lambda/4$ is obtained to be:

$$\omega_{max} = w(\lambda/4) = \frac{-3 d_{31} V_z (\lambda/2)^2}{16 h_p^2 a} \quad (2.30)$$

where d_{31} is the piezoelectric constant and V is the applied voltage. a can be described via the following equation:

$$\frac{1}{a} = \frac{1 - 2f_0}{1 - 3f_0 + 3f_0^2 + \alpha(3\beta + 3\beta^2 + \beta^3 - 6\beta f_0 - 3\beta^2 f_0 + 3\beta f_0^2)} \quad (2.31)$$

and:

$$\alpha = \frac{E_i}{C_{11p}^E}, \beta = \frac{h_i}{h_p}, f_0 = \frac{z_0}{h_p} \quad (2.32)$$

where E_i is the Young's modulus of the plate, C_{11p}^E is the elastic constant, h_i is the plate, h_p is the thickness of piezoelectric material, and z_0 is the neutral line ordinate.

Typically, in order to achieve maximum displacement, the device is operated at its resonance frequency. This is why it is necessary to determine the dynamic deflection, which is the static deflection times the dynamic amplification factor (Q). The ratio of the strain energy of the entire monomorph U_{mono} to the strain energy of the piezoelectric layer U_{piezo} balances with the mechanical quality factor Q_m of the piezoceramics to determine the dynamic amplification factor, which is written as:

$$Q = Q_m \frac{U_{mono}}{U_{piezo}} = Q_m \frac{a(1 - 2f_0)}{1 - 3f_0 + 3f_0^2} \quad (2.33)$$

Therefore, the dynamic displacement is described as:

$$\omega_{dyna} = Q\omega(\lambda/4) = -Q_m \frac{3 d_{31} V_z}{16 h_p^2} \left(\frac{\lambda}{2}\right)^2 \frac{(1 - 2f_0)}{1 - 3f_0 + 3f_0^2} \quad (2.34)$$

Not only the parameters of the vibration plate, but also the piezoelectric materials are observed to be linked with the dynamic deflection.

Note that in Biet's model, they used piezoelectric ceramic actuator, meaning its thickness cannot be ignored. As $f_0 = z_0/h_p$, equation 2.34 can be written as:

$$\omega_{dyna} = Q\omega(\lambda/4) = -Q_m \frac{3}{16} d_{31} V_z \left(\frac{\lambda}{2}\right)^2 \frac{(h_p - 2z_0)}{h_p^3 - 3z_0 h_p^2 + 3z_0^2} \quad (2.35)$$

This equation tells that if thickness of piezoelectric element is much smaller than plate thickness ($h_p \ll z_0$, specifically in the case of actuator made of films), its influence to the deflection amplitude can be ignored.

2) Resonance frequency

Controlling the frequency of operation is crucial when designing a haptic device. This section introduces equations that can be used to estimate the resonances of a device and identify the factors that influence the resonance frequency.

Torres et al., from University of Lille in France, conducted a recent study on the resonance frequency of longitudinal and transverse mode vibrations in an ultrasonic surface haptic device, based on E-B beam theory.[120] Transverse vibration is caused by flexural strains, resulting in an out-of-plane vibration. Longitudinal vibration is caused by extension-compression strains, resulting in an in-plane vibration. The resonance frequency of the transverse mode, which has been widely studied, can be calculated using the following equation:

$$f_{rN} = \left(\frac{1}{2\pi}\right) \left(\frac{\beta_n}{L}\right)^2 h \sqrt{\frac{E_e}{12\rho}} \quad (2.36)$$

Here, E_e represents the Young's modulus of the plate, ρ represents the density of the plate, L is the length of the haptic plate, and β_n represents the wave number. The wave number can be defined as $\beta_n = (2k_N + 1)(\pi/2)$, where $k_n \in \mathbb{N}$ denotes the number of resonance frequency. The resonance frequency of longitudinal mode vibrations is computed using the equation:

$$f_{rL} = \left(\frac{1}{2\pi}\right) \beta_l \sqrt{\frac{E_e}{12\rho}} \quad (2.37)$$

where β_l is the wave number, defined via $k_l\pi/L$. k_l represents the number of resonance frequency. According to their studies, it is possible to enhance the energetic performance of surface haptic devices by controlling the resonances of two modes.

Chapter 3

State of the art of low-temperature process of PZT thin films

This chapter provides a comprehensive overview of the current state-of-the-art low-temperature processes for PZT films, including their strategies, recent advances, and applications. The advantages and disadvantages of these processes are compared and summarized in this chapter. The purpose of this review is to offer guidance for the development and design of efficient low-temperature processes for PZT films. This has been published as a review paper titled “Toward low-temperature processing of lead zirconate titanate thin films: Advances, strategies, and applications” (Applied Physics Reviews, 2021, 8 (4), 041315), which has been attached in this chapter. The paper was written under the supervision of Dr. Emmanuel Defay and Dr. Sebastjan Glinsek.


Toward low-temperature processing of lead zirconate titanate thin films: Advances, strategies, and applications

Cite as: Appl. Phys. Rev. **8**, 041315 (2021); <https://doi.org/10.1063/5.0054004>

Submitted: 13 April 2021 • Accepted: 05 October 2021 • Published Online: 09 November 2021

 Longfei Song,  Sebastjan Glinsek and  Emmanuel Defay

COLLECTIONS

 This paper was selected as Featured



View Online



Export Citation



CrossMark

ARTICLES YOU MAY BE INTERESTED IN

[Next generation ferroelectric materials for semiconductor process integration and their applications](#)

Journal of Applied Physics **129**, 100901 (2021); <https://doi.org/10.1063/5.0037617>

[Epitaxial ferroelectric interfacial devices](#)

Applied Physics Reviews **8**, 041308 (2021); <https://doi.org/10.1063/5.0060218>

[BaTiO₃-based piezoelectrics: Fundamentals, current status, and perspectives](#)

Applied Physics Reviews **4**, 041305 (2017); <https://doi.org/10.1063/1.4990046>



Applied Physics Reviews

Special Topic: Materials and Technologies for Bioimaging and Biosensing

Submit Today!

Toward low-temperature processing of lead zirconate titanate thin films: Advances, strategies, and applications

Cite as: Appl. Phys. Rev. **8**, 041315 (2021); doi: [10.1063/5.0054004](https://doi.org/10.1063/5.0054004)

Submitted: 13 April 2021 · Accepted: 5 October 2021 ·

Published Online: 9 November 2021



View Online



Export Citation



CrossMark

Longfei Song,^{1,2,a)}  Sebastjan Glinsek,¹  and Emmanuel Defay^{1,a)} 

AFFILIATIONS

¹Materials Research and Technology Department, Luxembourg Institute of Science and Technology, rue du Brill 41, L-4422 Belvaux, Luxembourg

²University of Luxembourg, 41 rue du Brill, L-4422 Belvaux, Luxembourg

^{a)}Authors to whom correspondence should be addressed: longfei.song@list.lu and emmanuel.defay@list.lu

ABSTRACT

Lead zirconate titanate (PZT) thin films stand for a prominent technological brick in the field of microsystems. The recent improvements of their manufacturability combined with excellent piezoelectric properties have enabled their introduction in industrial clean rooms all around the world. These films require annealing temperatures beyond 600 °C to crystallize in the desired perovskite phase, which exhibits outstanding piezoelectric coefficients. This temperature requirement forbids large application fields such as flexible electronics, smart glass but also system-on-chip approaches. Decreasing the annealing temperature of PZT films would therefore spread further their potential usage to other applications. The purpose of this paper is to provide the reader with a comprehensive review of the different techniques available in the literature to process piezoelectric PZT thin films at temperatures compatible with semiconductors (450 °C), smart glass (400 °C), or flexible electronics (350 °C). We first present the typical ferroelectric and piezoelectric properties of PZT films. The different deposition techniques and growth mechanisms of these films are then reviewed with a focus on thermodynamics. Then, all the low temperature processes are detailed, such as seeding effects, the modification of deposition parameters in vapor-phase deposition, special annealing technologies assisted with UV, lasers, flash lamps, microwave radiations or high-pressure, a focus on the hydrothermal method, and finally what is called solution chemistry design with notably combustion synthesis. Transfer processing is also detailed, as an alternative way to this low temperature approach. An outlook of future applications enabled by these innovative techniques is finally provided.

© 2021 Author(s). All article content, except where otherwise noted, is licensed under a Creative Commons Attribution (CC BY) license (<http://creativecommons.org/licenses/by/4.0/>). <https://doi.org/10.1063/5.0054004>

TABLE OF CONTENTS

I. INTRODUCTION	2	1. UV photo-annealing	9
II. FERROELECTRIC AND PIEZOELECTRIC PROPERTIES OF PZT FILMS	3	2. Laser annealing	13
III. GROWTH OF PZT THIN FILMS	3	3. Flash lamp annealing	14
A. Deposition technologies	3	4. Microwave annealing	16
B. Thermodynamics and kinetics of nucleation and growth	5	5. High-pressure annealing	19
IV. LOW-TEMPERATURE PROCESSING	7	D. Hydrothermal method	20
A. Seeding effect	7	E. Solution chemistry design	22
1. Bottom electrode influence on crystallization	7	1. Controlling the compositions and homogeneity in PZT solutions	22
2. Effect of the seed layer and nano-seeds	8	2. Solution combustion synthesis (SCS)	22
B. Modification of deposition parameters for vapor-phase deposition	9	V. TRANSFER PROCESSING	24
C. Special annealing technologies	9	VI. APPLICATIONS OF LOW-TEMPERATURE PROCESSING	25
		A. MEMS-CMOS integration	25

B. Flexible piezoelectric energy harvesters 27
 VII. CONCLUSION AND OUTLOOK. 27

I. INTRODUCTION

Thanks to their large piezoelectric response, ferroelectric oxide films are considered as one of the most promising approaches to achieve small-scale integration into piezoelectric microelectromechanical systems (MEMS) for high-sensitivity sensors and low-power actuators, such as pressure sensors,^{1–7} accelerometers,^{5,8–15} energy harvesters,^{16–23} micromirrors,^{24–29} micropumps,^{30–32} microswitches,³³ piezoelectric haptics,^{34,35} and inkjet printheads.³⁶ Piezo-MEMS exhibit high performance in both sensing and actuating devices, with large amplitudes, linear responses, and large energy conversion. On the basis of a market analysis performed by “Yole Development,” Pb(Zr, Ti)O₃ (PZT) thin films now stand for more than 95% of the market share of ferroelectric thin films, thanks to their high ferroelectric properties.³⁷

PZT-based MEMS are one of the most interesting MEMS devices available today. More and more semiconductor companies are devoting efforts to the development of PZT-based MEMS (observed in Fig. 1).^{30,37–43} However, the technological bottleneck for integration of MEMS devices directly on CMOS devices is the high-temperature processing of PZT films.⁴⁴ Unfortunately, there is a trade-off between piezoelectric properties and deposition/crystallization temperature. A typical processing temperature for a desired well-crystalline PZT thin film is 550–650 °C with physical vapor deposition (PVD) and 650–750 °C with chemical solution deposition (CSD). This is substantially higher than the maximum thermal budget of CMOS devices (450 °C).^{45–47} When annealed below this specific processing temperature, PZT typically crystallizes into a non-ferroelectric undesired

pyrochlore or fluorite phase, instead of the ferroelectric (and therefore piezoelectric) perovskite structure. The current solution to MEMS-CMOS integration is that a stand-alone CMOS “application specific integrated circuit” (ASIC) chip is utilized to control the associated MEMS. The maximum temperature currently suggested to manufacture CMOS devices is 450 °C.⁴⁴ The use of stand-alone ASICs results in cost and footprint increase. The direct microfabrication of PZT MEMS on the top of ASICs requires PZT processing temperature compatible with CMOS devices, which means below 450 °C.

On the other hand, transparent and flexible devices associated with PZT thin films have recently been investigated in the fields of flexible energy harvesters,^{48,49} memory transistors,^{50,51} sensors,^{52–54} and wearable e-skin.^{55,56} The market of flexible electronics is expected to reach \$87.21 billion by 2024.⁵⁷ To satisfy the consumer needs, efforts have been made to integrate PZT thin film-based devices on flexible plastic substrates, such as polyimide (PI),^{54,58,59} polyethylene terephthalate (PET),^{49,53,60} polyethylene-2, 6-naphthalate (PEN),^{61,62} and polydimethyl siloxane (PDMS).^{63–65} Various types of flexible plastic substrates and their glass transition temperatures are shown in Fig. 2. Polymer substrates are temperature-sensitive. They allow maximum processing temperatures lower than 400 °C, which is incompatible with the high-temperature processing of PZT films (typically 650–700 °C). Apart from polymer substrates, standard glass substrates also exhibit maximum processing temperatures below 400 °C. Consequently, the main obstacle for developing flexible PZT-integrated devices remains the high temperature processing of PZT films.

To address such an issue, two strategies have been considered, namely, low-temperature processing and transfer processing. Low-temperature processing is the direct way to achieve *in situ* deposition on CMOS wafer or polymer substrate. The main obstacle is how to

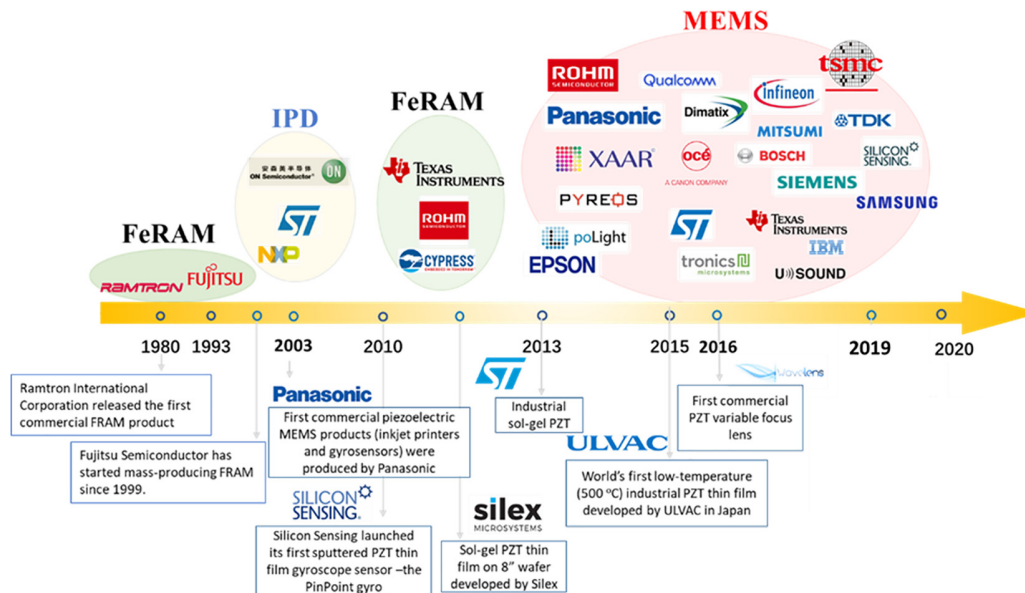


FIG. 1. Year of electronic devices based on PZT films produced by microelectronics companies. This figure was drawn based on the market report made by the company Yole Development, entitled “Status of the Mems Industry 2018.” IPD: integrated passive devices; FeRAM: ferroelectric random-access memory.

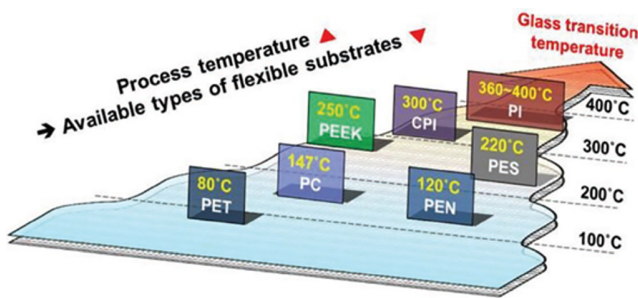


FIG. 2. Various types of flexible plastic substrates and their glass transition temperatures. PI: polyimide; PET: polyethylene terephthalate; PEN: polyethylene-2, 6-naphthalate; PDMS: polydimethylsiloxane; PC: polycarbonate; PES: polyethersulfone; PEEK: polyether ether ketone; CPI: colorless and transparent polyimide. Reproduced with permission from J. W. Park, B. H. Kang, and H. J. Kim, *Adv. Funct. Mater.* **30**, 1904632 (2020). Copyright 2019 John Wiley and Sons.⁶⁷

decrease deposition and/or crystallization temperatures. Over the past decade, significant research efforts have been made to develop such a low-temperature process. On the other hand, transfer processing is another approach to fabricate PZT films on polymer/glass substrates, which enables an independent optimization of PZT thin films.^{49,54,66}

In this article, we aimed to provide readers with a comprehensive overview of low-temperature processing of PZT films (<500 °C). We started with a short discussion on piezoelectric and ferroelectric properties. The current deposition technologies and nucleation growth mechanisms have then been reviewed. We thus covered well established strategies as well as recent progress in low-temperature processing of PZT films. Afterwards, transfer technologies for the fabrication of flexible PZT devices fabrication have been detailed. Then, we introduced the main applications in MEMS-CMOS integration and flexible energy harvesters. Finally, some insights about new challenges and future prospects have been exposed.

II. FERROELECTRIC AND PIEZOELECTRIC PROPERTIES OF PZT FILMS

The electromechanical properties of PZT thin films are strongly dependent on different factors, such as processing conditions (e.g., type and temperature of deposition), chemical composition, thickness, crystallographic orientation, microstructure, and residual stress. In this paper, we are interested in PZT thin films processed at low temperature and more specifically in their piezoelectric properties. PZT is a ferroelectric material, meaning that its piezoelectric properties stem from its ferroelectric nature and therefore from the presence of a remanent polarization P_r in the absence of electric field. It is generally

easier to characterize polarization rather than piezoelectric properties. When preparing this paper, we observed that there are much more papers reporting on polarization than on piezoelectric coefficients. This explains why we chose polarization as our main figure of merit to qualify the presence of the desired perovskite phase in the different PZT films. Note that we nonetheless reported on piezoelectric coefficients when those were available. **Table I** displays the state-of-the-art electromechanical properties of sol-gel PZT thin films deposited on platinized Si substrates and crystallized at 700 °C, which is PZT film standard crystallization temperature.^{68,69} In **Table I**, $d_{33,f}$ and $e_{31,f}$ are the effective piezoelectric coefficients of thin films, modified by the mechanical boundary conditions imposed by the substrate on the films (no in plane strain and no out of plane stress). As detailed in Ref. 70, they are defined such as $d_{33,f} = d_{33} - 2d_{31}s_{13}^E / (s_{11}^E + s_{12}^E)$ and $e_{31,f} = e_{31} + e_{33}s_{13}^E / (s_{11}^E + s_{12}^E)$, where s_{ij}^E , d_{33} and e_{31} are, respectively, compliances at constant electric field and pure piezoelectric coefficients.

III. GROWTH OF PZT THIN FILMS

A. Deposition technologies

Two competing technologies are generally employed in PZT thin film deposition: vapor-phase deposition and CSD. Vapor-phase deposition encompasses PVD and chemical vapor deposition (CVD). In PVD, materials are vaporized from a solid or liquid source in the form of atoms or molecules and transported in the form of a vapor through low-pressure gases or a plasma to a substrate in vacuum.^{71–75} PVD is the earliest technology adopted in the production of PZT thin films, thanks to its apparent simplicity—one step only—and high throughput production. However, it strongly relies on expensive pieces of equipment and a complicated process control.^{76–78}

In the case of sputtered PZT thin films, high-energy plasma species tend to remove material that has been previously deposited on the substrate.⁷⁹ Hence, PbO is preferentially re-sputtered in Ar or O₂ plasma.⁸⁰ This leads to a different composition of the PZT target in use and eventually of the sputtered PZT films.⁸¹ A 10%-lead excess is generally implemented in PZT sputtering targets to compensate for this Pb loss.

In the case of sputtered thin films, Thornton's Structure Zone model demonstrated that the temperature is not the only parameter influencing the films growth. The incident ions' energy and gas pressure play also a strong role.^{82,83} This model points out that the film growth depends on the T/T_m ratio, T and T_m being, respectively, the substrate temperature and the material's melting temperature. This ratio defines three different zones displayed in **Fig. 3(a)** (Zone 1: $T/T_m < 0.1$; Zone 2: $0.3 < T/T_m < 0.5$; and Zone 3: $0.5 < T/T_m < 1$). Thornton extended the model by adding the influence of the pressure

TABLE I. State-of-the-art electromechanical properties of PZT thin films with morphotropic phase boundary (MPB) composition. Polycrystalline {100} oriented 1 μm -thick film deposited on platinized Si substrates and annealed at 700 °C.^{68,69}

Property	Dielectric permittivity	Dielectric losses	Remanent polarization	Longitudinal piezoelectric coefficient	Transversal piezoelectric coefficient
Symbol	ϵ_r	$\tan \delta$	P_r	$d_{33,f}$	$e_{31,f}$
Unit	/	/	$\mu\text{C cm}^{-2}$	pm V^{-1}	C m^{-2}
Value	1400	0.05	20	150	-17

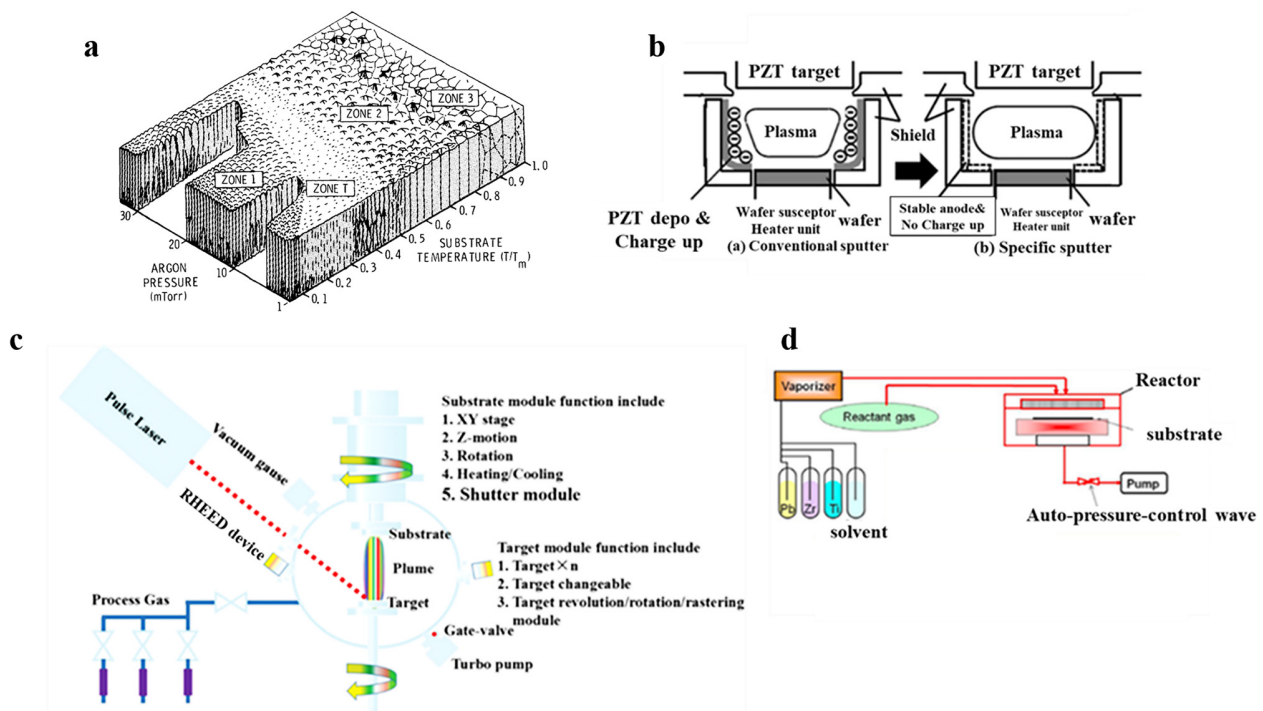


FIG. 3. (a) Thornton structure-zone diagram for films deposited by magnetron sputtering. Reproduced with permission from J. A. Thornton, *J. Vac. Sci. Technol.* **11**, 666 (1974). Copyright 1974 American Vacuum Society.⁵³ (b) Specific sputtering system for low-temperature processed PZT films developed by ULVAC. Reproduced with permission from Kobayashi *et al.*, 2020 IEEE 33rd International Conference on Micro Electro Mechanical Systems (MEMS) (2020). Copyright 2020 IEEE.⁸⁴ (c) Schematic of a PLD system. Reproduced with permission from Zhang *et al.*, *J. Mater. Chem. C* **7**, 4760 (2019). Copyright 2019 Royal Society of Chemistry.⁵⁵ (d) Main features of an MOCVD module. Reproduced with permission from K. Suu, *Advances in Ferroelectrics* (IntechOpen, 2012), Vol. 369. Copyright 2021 Author, licensed under a Creative Commons Attribution (CC BY) license.⁵²

of the sputtering chamber. As seen in Fig. 3(a), the structure in Zone 1 is promoted by high gas pressure, which has little influence on the film's structure when T/T_m is high (Zone 3). This suggests that other conditions like sputtering power can also strongly influence the structure of the film. Hence, low temperature crystallization could be achieved through the optimization of sputtering parameters such as pressure and sputtering power. Besides, Thornton's model has also been used in pulsed laser deposition (PLD) to develop low-temperature PZT thin films, which is discussed in detail in Sec. IV B.

Wilke *et al.* reported that 3 μm -thick sputtered MPB PZT thin films were deposited on a thin glass substrate (Schott D263). Here are the sputtering parameters: radio frequency (RF) power density = 2 W cm^{-2} , substrate temperature = 25°C , and pressure = 2.5–10 mTorr in Ar. The sputtered films were then crystallized at 550°C with rapid thermal annealing (RTA) for 1 min. The crystallized PZT thin films were finally annealed at 550°C in a box furnace for 24 h to reduce lead excess.⁸¹ ULVAC, as one of the main players in the market of PZT films deposition tools, recently developed the world's first low-temperature ($<500^\circ\text{C}$) PZT sputtering system. A stable anode preventing charge-up due to the adhesion of the insulating PZT films is used to stabilize the sputtering plasma [see Fig. 3(b)].⁸⁴ ULVAC claims that their sputtered 2 μm -thick PZT films on 8 in. wafer at 500°C exhibit a piezoelectric constant $e_{31,f} = 15 \text{ C m}^{-2}$ and a breakdown voltage of 200 V.⁸⁴

Pulsed laser deposition [shown in Fig. 3(c)] is an alternative PVD technique where a focused high-power laser is used to vaporize materials from a target, transport them, and deposit them on a substrate. The processing temperature is generally lower than that of any other PVD technologies because of the large kinetic energy of the ablated species. The deposition temperature and pressure are critical parameters impacting on the quality of the deposited PZT films.

CVD, and in particular, metal-organic CVD (MOCVD), enables epitaxial, uniform and pinhole-free films.^{85–91} As depicted in Fig. 3(d), MOCVD is performed on heated substrates by chemical reactions between source gases. Besides, it enables uniform deposition on three-dimensional structures thanks to its excellent step coverage.⁹²

On the top of displaying good uniformity, low cost, and an accurate control on chemical stoichiometry, CSD generally delivers films with very good properties; nonetheless, this technique is limited in high volume production throughput because of time-consuming multi-deposition and annealing steps. CSD typically includes four fundamental steps: (1) preparation of precursor solutions; (2) depositions using solution-based technologies [the current solution-based technologies are listed in Fig. 4(a)]; (3) pyrolysis step at intermediate temperature; and (4) densification and crystallization at high temperature. Several reviews have detailed solution compositions, deposition strategies, and film growth mechanisms in the fabrication of CSD-derived

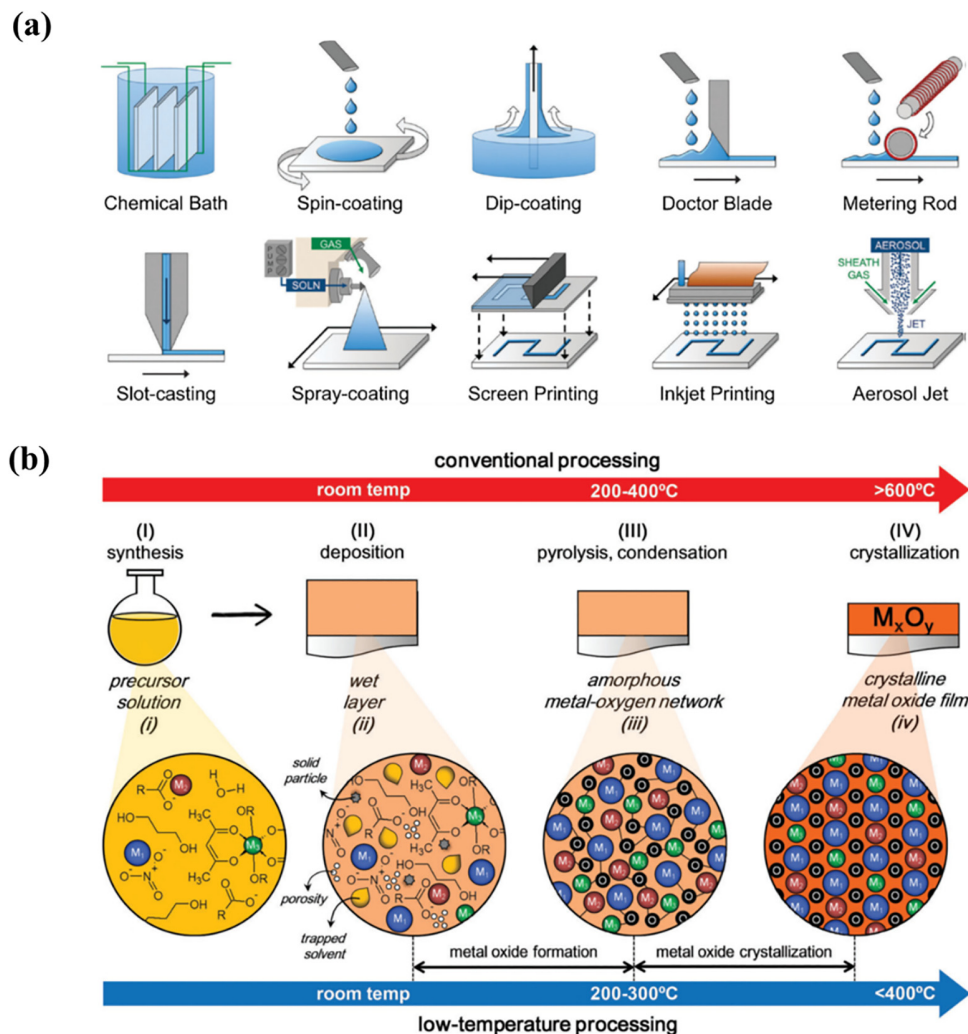


FIG. 4. (a) Various solution-based technologies for film deposition. Reproduced with permission from R. M. Pasquarelli, D. S. Ginley, and R. O'Hayre, *Chem. Soc. Rev.* **40**, 5406 (2011). Copyright 2011 Royal Society of Chemistry.³⁶ (b) Schematic diagram of basic steps of CSD in conventional processing and low-temperature processing. Bretos *et al.*, *Chem. Soc. Rev.* **47**, 291 (2018). Copyright 2018 Authors, licensed under a Creative Commons Attribution (CC BY) license.⁹⁴

ferroelectric films.^{93–95} In conventional processes, the pyrolysis step typically occurs at 300–400 °C on a hotplate and the subsequent crystallization step is achieved at temperatures higher than 600 °C, generally with RTA. Very few studies report on low-temperature processing pyrolysis steps occurring below 300 °C and crystallization completed at a temperature lower than 400 °C [cf. Fig. 4(b)].⁹⁴

B. Thermodynamics and kinetics of nucleation and growth

When deposition is performed close to room temperature, which is often the case in CSD processes, understanding the phase transition from amorphous to crystalline states is important to design low-temperature processing routines. The transition is understood as an

initial crystal nucleation followed by a growth step. The driving force of this phase transition is proportional to the difference ΔG of the free energies of the amorphous and crystalline states, which is expressed as

$$\Delta G = G_{\text{crystl}} - G_{\text{am}}, \quad (1)$$

where G_{crystl} and G_{am} are the Gibbs free energies of the crystalline and amorphous phases, respectively. This driving force plays a crucial role in the type of nucleation step that is active, which in turn impacts on the final microstructure of the films. The evolution with temperature of these Gibbs free energies is depicted in Fig. 5(a). Crystallization normally stems from the formation of crystalline nuclei at the bottom interface (i.e., heterogeneous nucleation) or inside the film (i.e., homogeneous nucleation) as shown in Fig. 5(b). The energy barriers for

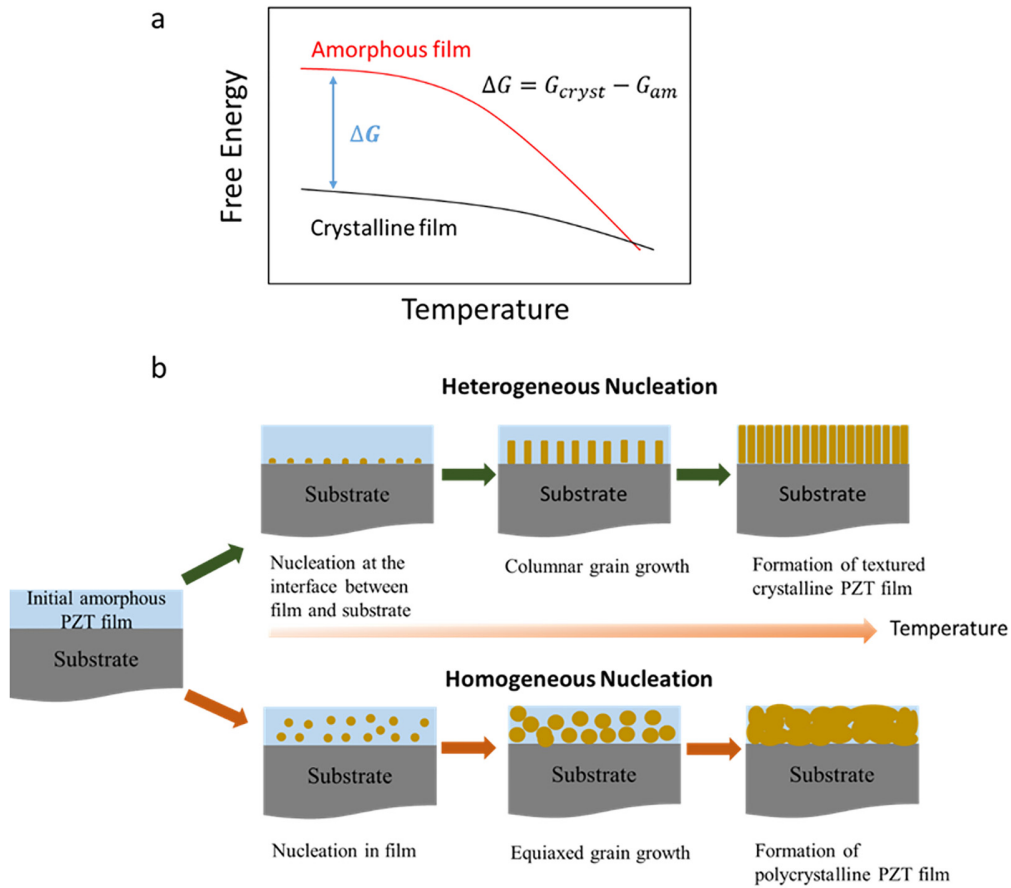


FIG. 5. (a) Schematic diagram of the free energies of a solution-derived amorphous film and the corresponding crystalline perovskite phase. (b) Homogeneous and heterogeneous nucleation and growth with respect to temperature for solution-derived thin films.

homogeneous (ΔG_{homo}^*) and heterogeneous (ΔG_{hetero}^*) nucleations are defined as^{94,97}

$$\Delta G_{homo}^* = \frac{16\pi\gamma^3}{3(\Delta G)^2}, \quad (2)$$

$$\Delta G_{hetero}^* = \frac{16\pi\gamma^3}{3(\Delta G)^2} f(\theta), \quad (3)$$

where γ is the interfacial energy and $f(\theta)$ is a function related to the contact angle θ :

$$f(\theta) = \frac{2 - 3 \cos \theta + (\cos \theta)^3}{4}. \quad (4)$$

The existence of $f(\theta)$ means that heterogeneous nucleation has a lower free energy barrier than homogeneous nucleation. Once created, a given nucleus grows larger and larger until it forms a grain that reaches the top of the film.

The kinetics of grain growth can be estimated through the Johnson–Mehl–Avrami–Kolmogorov (JMAK) equation that reads^{98,99}

$$X(t) = 1 - \exp(-Kt^n), \quad (5)$$

where $X(t)$ is the volume fraction of the transformed phase, K is the reaction rate constant depending on temperature, t is the reaction time, and n is an exponent determined by the growth mode. K is defined by the Arrhenius equation such as

$$K = K_0 \exp\left(-\frac{E_a}{k_B T}\right), \quad (6)$$

where K_0 is a vibration frequency, E_a is the activation energy, k_B is the Boltzmann constant, and T is temperature. According to Planck's equation ($E = h\nu$ where h and ν are Planck's constant and vibration frequency, respectively), K_0 is approximately $k_B T/h$. Hence, the phase transition from amorphous to crystalline states can only occur if the supplied thermal energy surpasses E_a for a duration longer than the reaction time. In the case of sputtered MPB PZT (53/47), the initial nucleation from the amorphous phase has a higher activation energy (441 kJ mol^{-1}) than the crystal growth (112 kJ mol^{-1}).¹⁰⁰ It indicates that crystal nucleation is kinetically limited at low temperature because of the insufficient thermal energy supplied.

IV. LOW-TEMPERATURE PROCESSING

Crystallization in the desired ferroelectric perovskite phase is the most critical process step in low temperature synthesis. Four routines have been investigated to succeed in the low-temperature deposition of functional PZT films: (1) reduction of the activation energy E_{a} , via, e.g., seeding processes, high-pressure annealing, or specific design of chemical reaction routines; (2) supplying thermal energy through other types of energies, such as UV photo annealing, laser annealing, microwave annealing, or solution combustion synthesis; (3) modification of the deposition parameters and heating processes; and (4) usage of technologies that can induce high kinetics energy, such as PLD or MOCVD. Some experiments showed that the combination of different approaches can end up in a lower crystallization temperature than the ones based on one single routine. Hence, several approaches have been attempted successfully. Figure 6 shows the remanent polarization P_r of PZT films as a function of processing temperature and technology. It is worth noting that in some cases, notably on Si substrates, P_r reaches values beyond $40 \mu\text{C cm}^{-2}$, which is a rather large value. This indicates either the underestimation of the actual electrode area or a high current leakage contribution. However, high P_r is realistic for Ti-rich PZT films or when MPB films are grown under compressive in-plane stress. It is also worth mentioning that it is very challenging to precisely

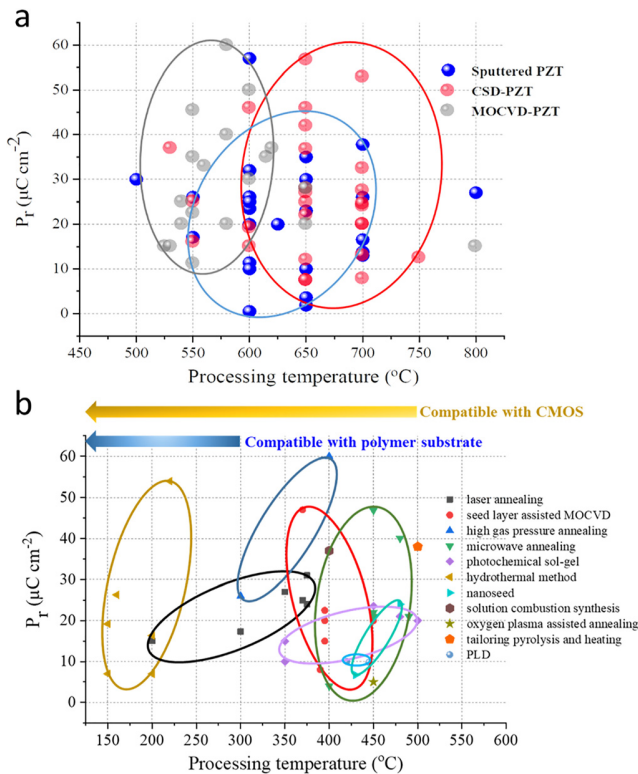


FIG. 6. (a) Temperature range typically used for the crystallization of PZT thin films with respect to different fabrication technologies. The different colors and symbols denote the different processing techniques. The results taken into account were the ones reported during the last decade. (b) Progress in the relevant technologies used for synthesizing MPB PZT thin films at low temperature ($<500^{\circ}\text{C}$).

measure temperature in vacuum, and temperature errors of 50–100 $^{\circ}\text{C}$ are common.

The majority of CSD-based PZT films have a higher crystallization temperature (650–700 $^{\circ}\text{C}$) than MOCVD (550 $^{\circ}\text{C}$) and sputtering (600–650 $^{\circ}\text{C}$). This is mainly due to residual organics in the as-deposited gel films, residues that need to be thermally removed prior to PZT crystallization [see Fig. 5(b)]. Figure 6(b) shows P_r as a function of processing temperature (below 500 $^{\circ}\text{C}$) and according to different low-T processing techniques. Hydrothermal method, flashlamp annealing, and laser annealing enable very low processing temperatures ($<300^{\circ}\text{C}$). Microwave annealing with a typical frequency of ~ 2.45 GHz enables a processing temperature at 450 $^{\circ}\text{C}$. Technologies such as photochemical sol-gel, combustion processing, high-pressure annealing, seeding method, and seed-layer assisted MOCVD allow for reducing the thermal budget of PZT thin films down to 350–500 $^{\circ}\text{C}$. In Secs. IV A–IV E, the mechanisms and latest advances of these techniques are detailed and discussed.

A. Seeding effect

1. Bottom electrode influence on crystallization

In general, there are two alternative structures for capacitors, namely, interdigitated electrodes (IDE) and metal-insulator-metal (MIM). Figure 7(a) displays a schematic diagram of an IDE capacitor with two interpenetrating comb electrodes on a layer/substrate. In this case, there is no need for a bottom electrode. Figure 7(b) is the standard geometry configuration of a MIM PZT capacitor, composed of a substrate, an adhesion layer, a bottom electrode, PZT and a top electrode. The adhesion layer is used to improve the interfacial adhesion between the bottom electrode and the substrate; its presence depends on the nature of the bottom electrode and the substrate. Besides, PZT crystalline orientation is affected by the adhesion layer material. A well-thought selection of the bottom electrode is necessary because the interface between the film and the bottom electrode plays a key role in the film growth (heterogeneous nucleation mechanism inferring preferential crystalline orientation). For example, sputtered PZT films on Pt/Ti/SiO₂/Si usually crystallize along the {111} orientation, whereas on LaNiO₃/SiO₂/Si they orient preferably along {100}.¹⁰¹ Note that several companies can produce {100}-oriented sputtered PZT on Pt-coated Si, such as ULVAC in Japan¹⁰² and SINTEF in Norway.¹⁰³

Pt is generally considered as the best bottom electrode for PZT films. Nittala *et al.* studied the growth mechanism of CSD-PZT thin films on Pt by *in situ* synchrotron x-ray diffraction (XRD).¹⁰⁴ They proposed a mechanism schematically described in Fig. 8. The formation of Pt₃Pb is caused by the diffusion of Pb in Pt [shown in Figs. 8(a)–8(c)], which stems from the reduction of Pb²⁺ in a very

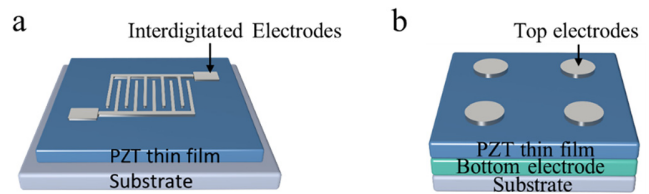


FIG. 7. Typical structures of PZT thin film capacitors: (a) interdigitated electrodes (IDE) and (b) metal-insulator-metal (MIM).

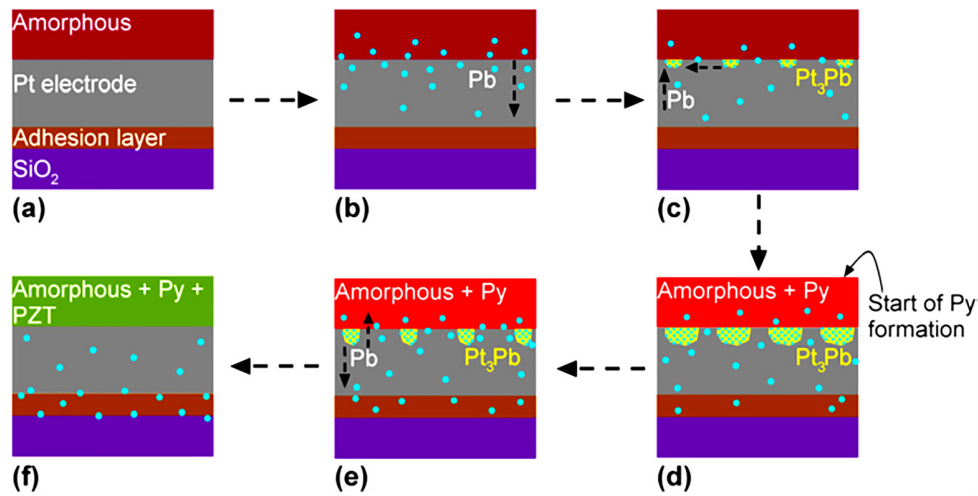


FIG. 8. Schematic diagram of the mechanism of formation and disappearance of Pt_3Pb during the crystallization of solution-deposited PZT thin films, after Nittala *et al.* (Py: pyrochlore phase). Reproduced from Nittala *et al.*, *J. Appl. Phys.* **113**, 244101 (2013). Copyright 2013 AIP Publishing.¹⁰⁴

reductive atmosphere, inducing a volume increase with time [Fig. 8(d)]. When an intermediate pyrochlore phase starts to grow, the volume of the Pt_3Pb phase rapidly decreases as oxidizing conditions promote the incorporation of Pb^{2+} into the crystallizing pyrochlore phase [Figs. 8(e)–8(f)]. In the last step, pyrochlore converts into perovskite.

A suitable bottom electrode coupled with special deposition technologies or parameters can enable low-temperature synthesis of PZT films. For instance, perovskite PZT films were crystallized at 475 °C by sputtering in an oxygen-free environment on an oxygen-doped iridium [Ir(O)] bottom electrode. PZT deposited at 475 °C on Ir(O) showed better ferroelectric properties than on Pt, Ir, or IrO_2 electrodes.¹⁰⁵ In a recent report, Kang *et al.* found that in the case of laser-annealed PZT, a crystalline structure can occur at 200 °C, though only in the presence of the LaNiO_3 bottom electrode. Crystalline LaNiO_3 has similar lattice parameters to PZT. Therefore, it plays the role of a seed nucleation layer, which reduces PZT nucleation activation energy as well as crystallization temperature.⁵⁸

2. Effect of the seed layer and nano-seeds

The insertion of a crystalline metal-oxide-based seed layer between the initial film and its bottom electrode has been widely studied in low-temperature processed MOCVD. Figure 9 discloses the recent advances of functional PZT thin films grown by MOCVD with the assistance of various metal-oxide seed layers. The utilization of seed layers enables obtaining desired crystalline orientations, and it enhances PZT ferroelectric properties in the case of low-temperature processes. However, seed layers are not able to significantly reduce the total thermal budget of PZT stacks because their own crystallization temperature is generally beyond 500 °C. The growth of seed layer assisted PZT is described in Fig. 10(a). In the case of MOCVD growth, perovskite PZT thin films can be obtained without the seed layer at temperature as low as 390 °C, although crystallinity is better when a PbTiO_3 seed layer is used.⁸⁷ Lattice parameters close to PZT and good ferroelectric properties are interesting features of seed layers.

As observed in Fig. 9, SrTiO_3 enables the growth of PZT films via MOCVD at lower temperature than with PbTiO_3 , which is attributed to a good lattice matching with PZT.⁸⁸

In the case of CSD, another strategy is to add PZT nanoparticles as seeds into the solution. This way, these nanoparticles behave like heterogeneous nuclei and crystalline PZT grows from the surrounding amorphous phase on the nanoparticles [see Fig. 10(b)]. The latter reduce the activation energy of the nucleation step, which in turn reduces the final crystallization temperature. For instance, Wu *et al.* demonstrated that the overall activation energy of sol-gel processed PZT (52/48) was decreased from 219 kJ mol^{-1} (unseeded) to 174 kJ mol^{-1} for 1 wt. % of seeds in PZT solution and down to 146 kJ mol^{-1} for 5 wt. % seeded solutions.^{106,107} Based on this seeding

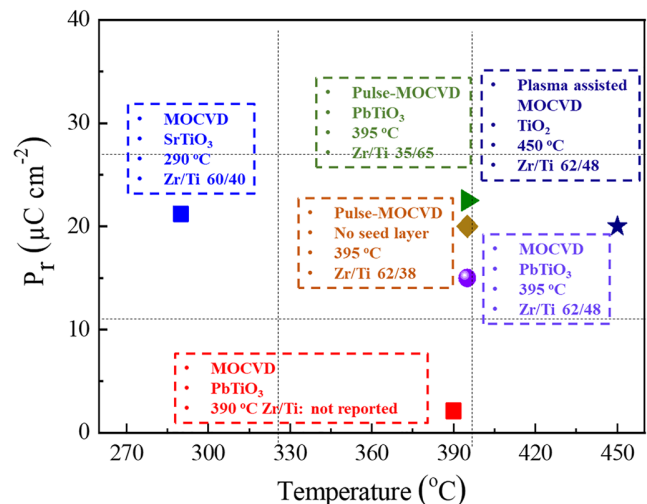


FIG. 9. Reported values of P_r as a function of temperature (<500 °C) for seed-layer-assisted MOCVD and pulsed-MOCVD technologies.

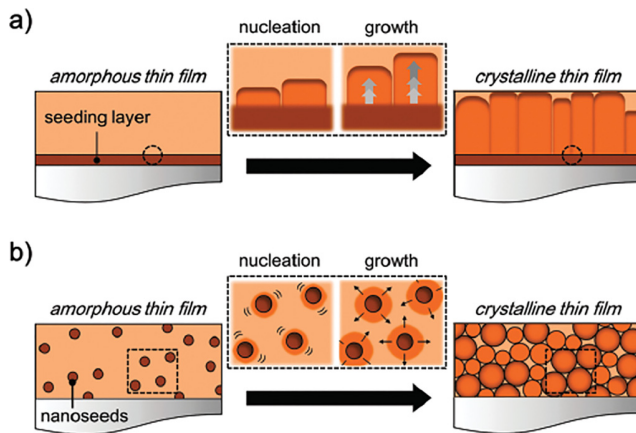


FIG. 10. Schematic illustration of the nucleation and growth phenomena in metal-oxide thin films assisted by the seeding effect, via (a) a seeding layer previously grown on the substrate and (b) crystalline nanoseeds previously introduced within the bulk film.⁹⁴ Bretos *et al.*, Chem. Soc. Rev. **47**, 291 (2018). Copyright 2018 Authors, licensed under a Creative Commons Attribution (CC BY) license.

method, Wu *et al.* reported the successful fabrication of perovskite PZT (52/48) using a sol-gel process with an annealing step at 410 °C for 30 h assisted with a 10 nm PbO nucleation layer.¹⁰⁸ Later, they reported that CSD-PZT thin films with 1% nanoseeds crystallized at 430 °C for 40 h. They exhibited a P_r and E_c of 6.7 $\mu\text{C cm}^{-2}$ and 80 kV cm^{-1} at 100 Hz, respectively.¹⁰⁹ However, the main handicap of this strategy is the need for long annealing steps. Bretos *et al.* reported a new strategy combining UV photo annealing and nano-seeds processing, which combination enables a shorter processing time as well as a lower crystallization temperature.¹¹⁰ This shows that the combination of special annealing technologies and nano-seeds is an efficient way to decrease the processing temperature.

B. Modification of deposition parameters for vapor-phase deposition

In the case of PZT films grown by PVD, deposition parameters such as gas pressure, gas atmosphere, and deposition temperature play a strong role on the final crystallization temperature. As mentioned earlier, sputtering in an oxygen-free atmosphere can promote the formation of the desired perovskite phase and delay the formation of non-ferroelectric phases. Schatz *et al.* investigated the effect of pressure and temperature on the low temperature deposition of 0.9 μm PZT thin films using PLD.^{111,112} Statistical design of experiment (DoE) methods were used to determine the main influencing growth parameters and to derive empirical models for the transverse piezoelectric coefficient $e_{31,f}$ and leakage current density J_{leak} with respect to the growth conditions (oxygen pressure and temperature), as shown in Fig. 11(a).¹¹² In this case, a cantilever fixture (single side clamping) and measurement hardware from Aixacct were used. The applied AC electric field was 100 kV cm^{-1} at 10 Hz. $e_{31,f}$ of -12.5 C m^{-2} was obtained at a deposition temperature as low as 445 °C. This high $e_{31,f}$ value is a clear indicator of the decent quality of these PZT films. It illustrates that optimized values of T_{dep} and P_{O_2} [regimes I and IV in Fig. 11(a)] lead to good PZT properties. Following this, experimental

results shown in Figs. 11(b) and 11(c) confirm that low temperature is beneficial to obtain high-crystallinity and better dielectric properties when depositing at low pressure (experiments A and C). Permittivity was measured at 1 kHz and a small AC voltage of 50 mV_{rms}. Conversely, when deposition pressure is high (experiments D and E), a high temperature is preferable to obtain functional PZT films. Sample A (445 °C, 0.05 mbar) displays a P_r of $\sim 13.4 \mu\text{C cm}^{-2}$ [Fig. 11(b)]. Leakage current density J_{leak} is below $10^{-6} \text{ A cm}^{-2}$ at low electric field (200 kV cm^{-1}).

C. Special annealing technologies

Various annealing technologies have been developed to lower PZT crystallization temperature. The most common techniques are UV photo annealing, laser annealing, flashlamp annealing, microwave annealing, and high-pressure annealing. Detailed information of low-temperature processed PZT films in recent publications based on those annealing technologies has been collected in Table II. They reveal that the coercive field E_c of low-temperature processed PZT films is higher than that in high-temperature processed films, which indicates the incomplete crystallization of PZT thin films. Note also that the frequency of the P-E measurements has not been provided in most cases. It was 100 Hz when provided and lower frequency measurements were not performed. One could think that the value of 100 Hz has been deliberately chosen to screen potential high leakage currents in the films that would prevent a proper polarization measurement.

1. UV photo-annealing

CSD processes combined with UV photo-annealing (typically with a wavelength below 250 nm) have been utilized to achieve low-T processing, thanks to the efficient elimination of organic compounds and the formation of metal-oxide-metal (M-O-M) lattices.¹¹³ The mechanism behind UV photo-annealing has been described in many reports.^{94,114,115} Under UV-treatment, the elimination of organic species in the precursor film includes two different dissociation processes. First, the treatment using UV irradiation can excite electrons to higher energy levels. The photo-excitation of organics due to $\pi \rightarrow \pi^*$ transitions promotes the dissociation of alkyl group-O bonds, as well as the activation of metal and oxygen atoms to form M-O-M bonds at low temperature, meaning the formation of crystalline PZT at this stage.⁹⁴ On the other hand, ozone (O_3) and oxygen radicals (O^*) are generated because of UV-irradiation in air, which is described by $\text{O}_2 + h\nu \rightarrow \text{O} + \text{O}$, $\text{O}_2 + \text{O} \rightarrow \text{O}_3$, and $\text{O}_3 + \text{O} \rightarrow 2\text{O}^* + \text{O}_2$. The strong oxidant character of the generated O_3 promotes chemical bond cleavage of the organic compounds in the precursor film by ozonolysis.

Photosensitivity strongly relies on the chemical components of the precursor solutions. An appropriate design of photosensitive solution chemistry coupled with suitable light wavelength is important to optimize the efficiency of reactions.⁹⁴ To do so, specific organics are employed to form photosensitive coordination complexes through reactions between metals and these organic compounds.¹¹⁶ In the case of the solution chemistry of PZT thin films, the photosensitive solution is usually synthesized using titanium and zirconium alkoxides modified by β -diketonate groups, such as acetylacetonone.^{94,117} Significant progress has been made over the past decade. For instance, Yue *et al.* reported {110}-predominated PZT (40/60) thin films fabricated using UV photo annealing ($\lambda = 185 \text{ nm}$ and 254 nm treatment) at 480 °C,

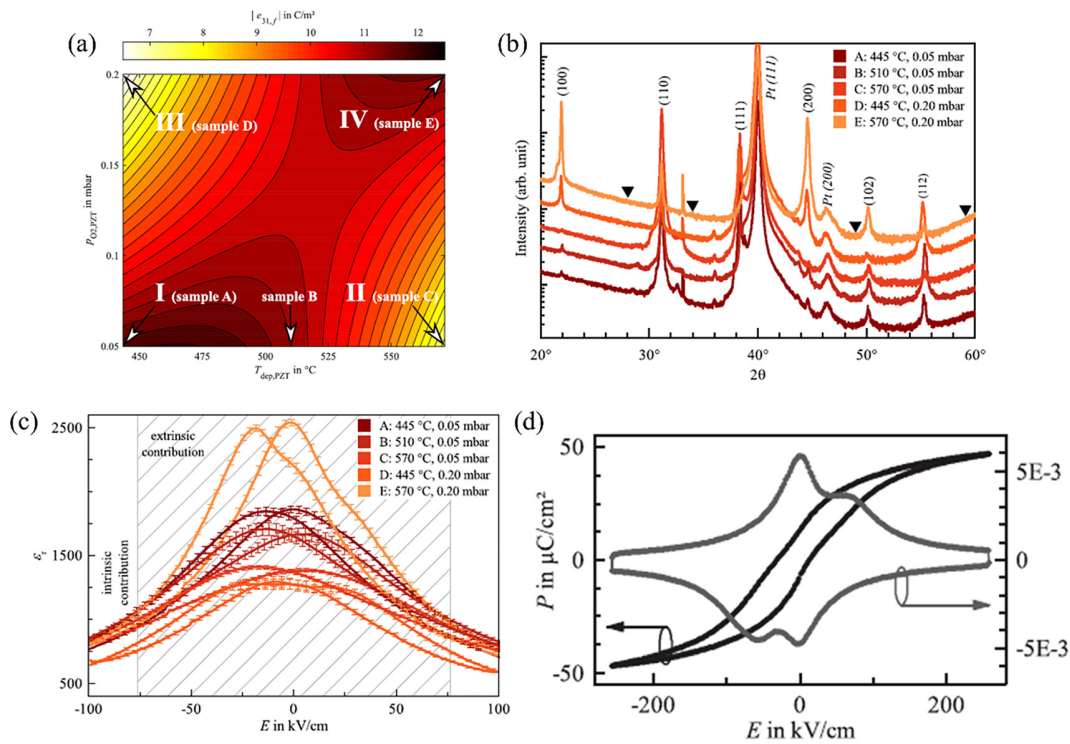


FIG. 11. Contour plot of the empirical design of experiments (DoE) model response of the transverse piezoelectric coefficient $e_{31,f}$ of a PZT thin film deposited by PLD with variable PZT deposition temperature T_{dep} and pressure P_{O_2} , maintaining all other DoE parameters (i.e., PLD deposition parameters) constant. (b) XRD patterns of PZT thin films deposited under different conditions. (c) Corresponding permittivity as a function of electric field. (d) Polarization P and current density J vs electric field E of sample A. Reproduced with permission from A. Schatz, D. Pantel, and T. Hanemann, *Thin Solid Films* **636**, 680 (2017). Copyright 2017 Elsevier.¹¹²

exhibiting a P_r of $21 \mu\text{C cm}^{-2}$, E_c of 100 kV cm^{-1} , and a leakage current of $9.7 \times 10^{-8} \text{ A cm}^{-2}$ at 100 kV cm^{-1} .¹¹⁸ However, there is no presence of PZT peaks in XRD diagrams when the films were heated at 450°C for 2 h without UV. There were no piezoelectricity measurements provided in this case.

Bretos *et al.* have made several significant contributions to explore the design of photosensitive precursors solutions.^{94,110,119,120} A new strategy, which combines seeded diphasic precursors and a photoactivated sol-gel process coupled with UV annealing, was used to reach a much lower crystallization temperature (350°C) of randomly oriented 190 nm -thick MPB PZT (52/48) films, enabling their direct deposition on flexible substrates.¹¹⁰ The growth process with a seeded photochemical solution is depicted in Fig. 12(a). Figure 12(b) shows the absorption spectrum of the photoactivated solution (Ph) and the inset is the photograph of Ph solution, which displays high absorption in the UV region. The seeded diphasic photoactive PZT sol-gel [defined as PhS, see Fig. 12(d)] was prepared by adding a suspension of nanometric PZT (52/48) powder [see Fig. 12(c)] to the photoactive PZT sol [see Fig. 12(b)], which was carried out by a typical diol-sol-gel route.^{109,121,122} PZT films were synthesized through dip-coating, followed by UV-irradiation at 250°C and rapid thermal processing at 400°C . Compared with seed-free Ph processing, PhS processing can reach lower crystallization temperature around 300°C (400°C with Ph). Figure 12(e) is a photograph of a PZT (52/48) film on flexible

polyimide at 350°C , which exhibits a P_r of $15 \mu\text{C cm}^{-2}$ but very large E_c of 500 kV cm^{-1} , indicating the incomplete crystallization of this as-synthesized PZT film [see Fig. 12(f)]. Permittivity is 80 and $\tan \delta$ is 0.03 at 1 kHz. The lab-scale equipment for UV annealing uses a high-density excimer lamp ($\lambda \sim 222 \text{ nm}$). This approach gives the opportunity to go to even lower temperatures with the assistance of nano-seeds, enabling direct deposition on a flexible substrate. Note that piezoelectric properties were not measured in this case. In their latest report, the authors studied the piezoelectric response of UV-treated MPB PZT films deposited on platinumized Si¹²⁵ and claimed that piezoelectricity is only present after an annealing step at a temperature of at least 400°C . Therefore, we can assume that the piezoelectric properties of MPB PZT fabricated on a polyimide substrate at 350°C in the first case were very weak. Further research on UV-annealed PZT thin films is therefore needed to evaluate their piezoelectric properties on polymer substrates at $T < 400^\circ\text{C}$.

Another promising approach is UV/ O_3 treatment. O_3 is a strong oxidant, which induces the cleavage of the organic compounds in gel films by ozonolysis.^{123,124} Shimura *et al.* processed 500 nm -thick PZT (40/60) thin films by using a commercial solution followed by UV irradiation at 200°C in O_3 with an annealing step at 450°C . As a result, the resulting PZT (40/60) film exhibited a preferential $\{111\}$ orientation with $P_r = 24 \mu\text{C cm}^{-2}$, $E_c = 110 \text{ kV cm}^{-1}$ measured at 100 Hz, and a leakage current of $10^{-6} \text{ A cm}^{-2}$.¹²³ A diaphragm-type actuator

TABLE II. Deposition parameters and electrical characteristics of low-temperature processed PZT based on various annealing technologies, high-pressure annealing, and solution combustion synthesis. The lines in yellow correspond to PZT films deposited on polymer substrates. The line with the sign * refers to a paper in which the reported polarization is too large to be trusted. Hydrothermal-based works are not collected on this table, because special substrates are needed and they are not suitable for direct CMOS-MEMS integration and flexible energy harvesters.

Material (Zr/Ti) thickness	Deposition technology	Processing temperature in °C	P_r in $\mu\text{C cm}^{-2}$	E_c in kV cm^{-1}	Leakage current in A cm^{-2}	Relative permittivity ϵ_r	Loss tangent $\tan \delta$	Piezoelectric coefficients	Reference
									$e_{31,f}$ in C m^{-2} $d_{33,f}$ in pm V^{-1}
Typical electrical characteristics of high temperature processed PZT films									
{100}-PZT (53/47)	CSD	700	20	50	...	1400	0.05	-17 150	68
UV-photo annealing									
{110}-PZT (40/60)	CSD	480	21	100	10^{-7} at 100 kV cm^{-1}	118
PZT (52/48) 190 nm	CSD	350	15 at 1300 kV cm^{-1}	500 at 1300 kV cm^{-1}	...	80	0.03	...	110
{111}-PZT (52/48) 70 nm	CSD	400	10	195	10^{-6} at 500 kV cm^{-1} 10^{-7} at 100 kV cm^{-1}	90	0.08	...	125
{111}-PZT (40/60) 500 nm	CSD	450	24 at 100 Hz	110 at 100 Hz	10^{-6} at 1000 kV cm^{-1}	123
{110}-PZT (53/47) 500 nm	CSD	500	20	38	124
Laser annealing									
{100}-PZT (50/50)	Excimer-laser-assisted multi-ion-beam sputtering technique	Room Temperature	5 at 500 kV cm^{-1}	100 at 500 kV cm^{-1}	...	250	0.04	...	134
{111}-PZT (52/47) 1.1 μm	PLD with in-situ laser annealing system	370	25 at 400 kV cm^{-1}	50 at 400 kV cm^{-1}	...	700	0.025	-6 after poling at 150 kV cm^{-1} at 150°C for 20 min	135
{100}-PZT (52/48) 350 nm	RF sputter	375	31 at 400 kV cm^{-1}	86 at 400 kV cm^{-1}	...	1000	0.06	-11	131
{111}-PZT (52/48) 350 nm	RF sputter	375	24 at 400 kV cm^{-1}	64 at 400 kV cm^{-1}	...	1000	0.06	-9	131

TABLE II. (Continued.)

Material (Zr/Ti) thickness	Deposition technology	Processing temperature in °C	P_r in $\mu\text{C cm}^{-2}$	E_c in kV cm^{-1}	Leakage current in A cm^{-2}	Relative permittivity ϵ_r	Loss tangent $\tan \delta$	Piezoelectric coefficients	Reference
{110}-PZT (52/48) 5 μm	Alternative deposition by sol-gel and powder-mixing processing	Room temperature	16 at 700 kV cm^{-1}	115	128
PZT (52/48) 200 nm	CSD	Room temperature	18 at 1000 kV cm^{-1}	140 at 1000 kV cm^{-1}	140
PZT (52/48) 200 nm	PECVD	200	16 at 1250 kV cm^{-1}	100–200 kV cm^{-1} at 1250 kV cm^{-1}	...	750	<0.1 at 10 kHz, 0.4 at 1 MHz	...	100 58
Microwave annealing									
{110}-PZT (53/47) 420 nm	CSD	450	47 at 600 kV cm^{-1}	86 at 600 kV cm^{-1}	...	1130	0.03	...	168
{110}-PZT (52/48) 1 μm	CSD	480	40 at 300 kV cm^{-1}	50 at 300 kV cm^{-1}	...	1100	0.04	...	169
PZT (52/48) 200 nm	CSD	450	20 at 250 kV cm^{-1}	100 at 250 kV cm^{-1}	151
{111}-PZT (52/48) 300 nm	CSD	525	30 at 500 kV cm^{-1}	100 at 500 kV cm^{-1}	162
Annealing in High-pressure oxygen									
*{100}-PZT (52/48) 300 nm	CSD	400	70 at 20 V	170 at 20 V	178
Solution combustion synthesis									
PZT (52/48) 220 nm	CSD	400	37 at 6 V	100 at 6 V	10^{-7} at 600 kV cm^{-1}	500	0.1	...	204

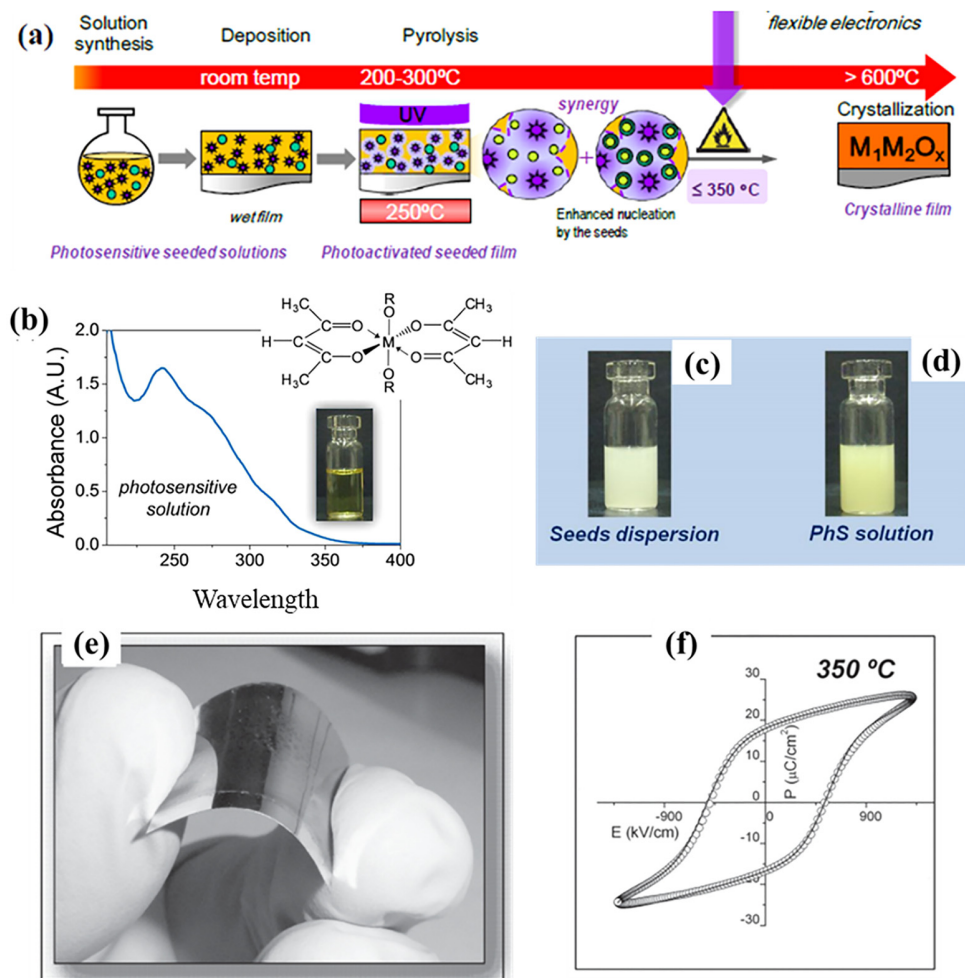


FIG. 12. (a) Mechanisms for low-temperature processing of inorganic ferroelectric thin films using activated solutions. Reproduced with permission from Bretos *et al.*, IEEE Trans. Ultrason. Ferroelectr. Freq. Control **67**, 1967 (2020). Copyright 2020 IEEE.⁹⁵ (b) Absorption in UV range of PZT precursor solutions containing titanium alkoxides modified with β -diketonate. Reproduced with permission from Bretos *et al.*, Adv. Mater. **26**, 1405 (2014). Copyright 2014 John Wiley and Sons.¹¹⁰ (c) Seed dispersion constituted by PZT nano-powders in ethanol. Reproduced with permission from Bretos *et al.*, Sci. Rep. **6**, 1 (2016). Copyright 2016 Authors, licensed under a Creative Commons Attribution (CC BY) license.¹²⁵ (d) PhS solution formed by the mixture of Ph sol and dispersion. (e) Photograph of a PZT film on flexible polyimide. Reproduced with permission from Bretos *et al.*, Adv. Mater. **26**, 1405 (2014). Copyright 2014 John Wiley and Sons.¹¹⁰ (f) Ferroelectric hysteresis loop of a PZT film on flexible polyimide (PI at 350 °C) with a thickness of 190 nm. Reproduced with permission from Bretos *et al.*, Adv. Mater. **26**, 1405 (2014). Copyright 2014 John Wiley and Sons.¹¹⁰

was fabricated based on these low-temperature processed films, which shows a maximum displacement of 130 nm at 10 V.

By contrast, PZT thin films using UV-based annealing technologies still lack good piezoelectric properties when annealed at temperature lower than 400 °C. It means that piezoelectric PZT deposited on polymer substrates (<400 °C) cannot be currently achieved through UV annealing and further research efforts are therefore required.

2. Laser annealing

The laser annealing (LA) technique is also an alternative approach to enable low temperature and fast crystallization.^{47,112,126–132} It makes use of a high energy laser beam to scan the

film of interest in continuous or pulsed modes. The energy provided by the laser and absorbed by the film has to exceed a certain threshold to break the bonds between organic components or anions in order to form M-O-M bonds. Note that it is not absolutely necessary to work with focused lasers. Two types of lasers are generally employed, namely, CO₂ laser¹²⁸ and UV laser.¹³³ The UV excimer laser is more suitable for annealing ferroelectric oxides, because they have an optical bandgap in the 2.5–4 eV range, which means that they are able to absorb UV light in the near-surface region. LA possesses three advantages compared with UV-photo annealing: (1) specific photosensitive solutions are no longer required; (2) LA can not only be used for CSD-based PZT, but also for sputtered PZT; (3) LA avoids thermal damages to the substrate (especially temperature-sensitive substrates) because

the annealing temperature of films is tunable by controlling laser energy and exposure time (milliseconds or sub-milliseconds), which means that flexible substrates can be used; and (4) it offers flexibility in manufacturing composites with different computer-assisted geometries. LA has been widely used in the display industry, strongly suggesting that low-temperature laser-annealed PZT films have the potential for future industrial production.

Significant research efforts on LA have been deployed during the past decades. Kanno *et al.* fabricated {100}-oriented PZT (50/50) thin films on Pt/MgO and platinized-Si at room temperature using an excimer-laser-assisted multi-ion-beam sputtering technique (wavelength = 308 nm, energy density of 60–500 mJ cm⁻², pulse width of 10 ns, and pulse rate of 10 Hz). These PZT films were exposed to the excimer UV laser during their deposition. On platinized Si, they exhibited a P_r of 5 $\mu\text{C cm}^{-2}$ and E_c of 100 kV cm⁻¹ at ± 500 kV cm⁻¹ and 1 kHz using a triangular signal. The corresponding permittivity and $\tan \delta$ were, respectively, 250 and 0.04. No piezoelectric data were reported in the paper.¹³⁴ Rajashekhar *et al.* fabricated 1.1 μm {111}-oriented MPB thick-PZT (52/48) films on a 70 nm-thick sol-gel crystallized PZT seed layer at 370 °C, utilizing PLD with an *in situ* laser annealing system (248 nm wavelength, 25 ns pulse length, and 400 mJ/pulse energy), which exhibited a P_r of 25 $\mu\text{C cm}^{-2}$, a coercive field of 50 kV cm⁻¹, loss tangent below 2.5%, and a permittivity of 700.¹³⁵ $e_{31,f}$ was measured to be -6 C m⁻² after poling at 150 kV cm⁻¹ at 150 °C for 20 min. The fabricated PZT thin film on a {100} SrTiO₃ single crystal exhibited {100} crystalline orientation and decent ferroelectric and piezoelectric properties. The results provided in this paper are plausible because on the one hand PLD can achieve relatively low-temperature deposition of PZT thin films and on the other hand an *in situ* laser annealing system has been built in the growth chamber. Bharadwaja *et al.* demonstrated that 248 nm-laser-annealed [KrF pulsed excimer laser (40–45 mJ cm⁻²)] sputtered PZT films showed a nearly uniform composition distribution across thickness, comparable with “gradient-free” sol-gel processed PZT films.^{131,136–138} These annealed 350 nm-thick MPB PZT (52/48) thin films at 375 °C had, respectively, P_r of 31 $\mu\text{C cm}^{-2}$ and E_c of 86 kV cm⁻¹ for {001}-oriented films and 24 $\mu\text{C cm}^{-2}$ and 64 kV cm⁻¹ for {111}-oriented films measured at ± 400 kV cm⁻¹.¹³¹ In the case of {001}-oriented PZT films, a 20 nm-thick {001}-oriented PbTiO₃ seed layer was used. $e_{31,f}$ on {001}-oriented films as large as -11 C m⁻² was measured after poling at 200 kV cm⁻¹ at room temperature for 5 min. In previous studies, crack issues were usually observed in the case of low-temperature thick PZT films irradiated with a CO₂ laser. In order to solve this, Tsai *et al.* used an alternative deposition of randomly oriented MPB PZT (52/48) thin and thick films derived from sol-gel and powder-mixing spin-coating processes, followed by continuous-wave CO₂ laser annealing with a laser energy density of 121 W cm⁻².¹²⁸ The resulting randomly oriented 5 μm -thick PZT films on Pt/Ti/SiO₂/Si showed a P_r of 16 $\mu\text{C cm}^{-2}$ and E_c of 115 kV cm⁻¹. Piezoelectric measurements were absent in this case. Suresh *et al.* found that this crack issue in the case of continuous-wave CO₂ laser annealed 200 nm-thick randomly oriented MPB PZT (52/48) films could be solved by using a sputtered (La_{0.7} Sr_{0.3}) MnO₃ (LSMO) buffered SUS430 substrate (LSMO/SUS430) instead of Pt/Ti/SiO₂/Si.¹³⁹ Hence, PZT ferroelectric properties could be enhanced.¹⁴⁰ The prepared PZT films showed a P_r of 18 $\mu\text{C cm}^{-2}$ and E_c of 140 kV cm⁻¹ measured at ± 1000 kV cm⁻¹. The annealing temperature in LA has always been

assumed using modeling, because the actual temperature cannot be measured at the moment. PZT films in all the cases detailed earlier have been deposited on high-temperature-compatible substrates. To evaluate their feasibility on temperature-sensitive substrates, successful depositions and crystallizations of PZT films on a glass or polymer substrate are required.

LA remains one of the most promising techniques to achieve direct crystallization of metal-oxide films on flexible polymer substrates.^{141–145} To avoid thermal damage to polymer substrates, a large laser energy combined with a short pulse width is needed to transfer the generated heat from the surface to the film but not to the substrate. However, a short pulse duration gives rise to dramatic temperature gradients across the film thickness. Recently, Kang *et al.* proposed a new growth mechanism to solve this issue, called laser-induced liquid phase crystallization (LLC),⁵⁸ which is depicted in Fig. 13(a). Amorphous LaNiO₃ (LNO) and MPB PZT (52/48) films were deposited by RF magnetron sputtering on polyimide. Figure 13(b) shows the inhomogeneous temperature profile in PZT films simulated by numerical modeling. A significant temperature variation between the surface and the bottom of the PZT film was observed, reaching 600 K. As a result, they found that a pulse energy density of 60 mJ cm⁻² applied for 24 ns can create an ultrafast surface melting of PZT films. Figure 13(c) is the surface morphology of a 50 nm-thick PZT film treated by various numbers of pulses (1–1000). The film exhibited a perovskite structure after 1000 pulses through its entire thickness. Figure 13(d) is a schematic of the LLC growth mechanism. PZT crystallites are initially grown near the interface region of the melted amorphous PZT/crystalline LNO film, and the grains grow from these crystallites. Figure 13(e) is an XRD pattern of an LA-PZT based flexible capacitor, which reveals a typical perovskite structure in PZT. The capacitor displays a P_r of 19.5 $\mu\text{C cm}^{-2}$ measured at high electric field ± 1250 kV cm⁻¹ and a relative dielectric permittivity of 700 [see P-E loops in Fig. 13(f)]. The effective longitudinal piezoelectric coefficient ($d_{33,f}$) calculated from mechanical displacement is about 100 pm V⁻¹ as revealed in Fig. 13(g). This new growth mechanism provides new ideas to process PZT with LA. The success of deposition of PZT on polymer substrates is ascribed to this annealing tool that can generate very short length pulses, in the ns range. In addition, LNO plays a key role in PZT film crystallization.

3. Flash lamp annealing

Flash lamp annealing (FLA, sometimes called photonic annealing or intense pulsed light sintering) is a short pulse-mode (in the range of μs to ms) annealing method. In this technique, photons with different wavelengths interact with an absorptive layer to deliver thermal energy to this layer. This technique works with PZT thin films on temperature sensitive substrates thanks to the mismatch of their thermal properties. FLA is significantly different from laser annealing because the light spectrum in use is broad and the beam is not focused. The typical spectrum spans from UV to IR wavelengths (200–1100 nm), with a maximum plateau in the visible range.

Yao *et al.* reported direct crystallization of solution-processed MPB PZT thin films on glass and polymer substrates with FLA.¹⁴⁶ Fig. 14(a) shows a schematic diagram of a typical waveform used during FLA. At the initial step, a low-density (220 V) and ten rather long pulses (1 ms each) were applied to induce pyrolysis in the PZT

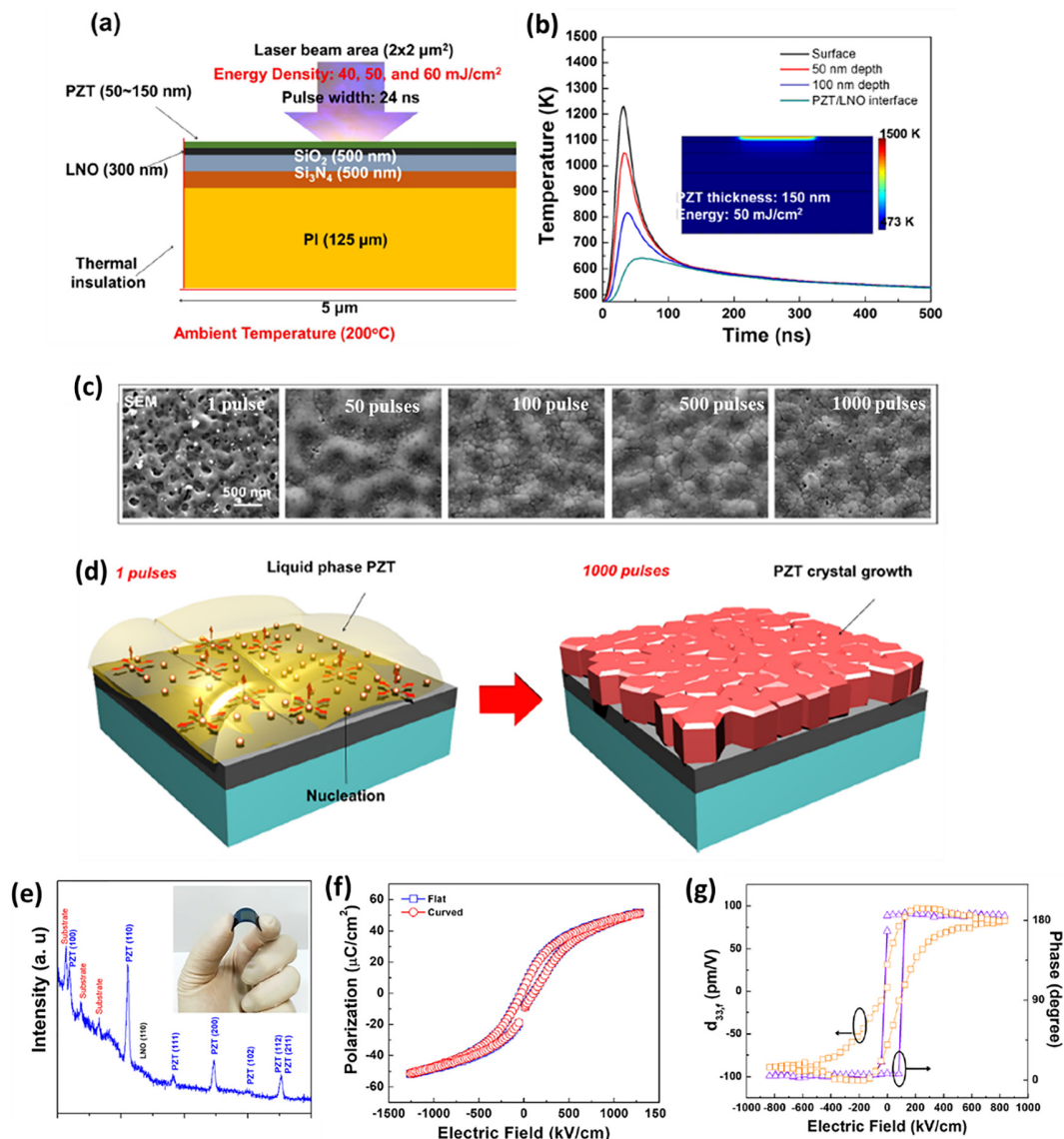


FIG. 13. (a) Modeling and boundary conditions of laser annealing. (b) Simulated temperature profile in a 50 nm-thick PZT film exposed to 50 mJ cm^{-2} laser energy. (c) Topography images of a PZT thin film after laser irradiation with various numbers of pulses (from 1 to 1000). (d) Schematic diagrams indicating the growth mechanism of laser-induced liquid-phase crystallization (LLC). (e) XRD pattern of a crystallized PZT thin film via laser annealing; the inset shows a photograph of the flexible PZT thin film crystallized on polymer. (f) Ferroelectric P-E loops of a flexible thin film capacitor in the original position and bent state. (g) Local piezo-response curves showing polarization switching (phase) and the effective longitudinal piezoelectric coefficient. Reproduced with permission from Kang *et al.*, *Chem. Mater.* **32**, 6483 (2020). Copyright 2020 American Chemical Society.⁵⁸

gel film. A dwell step was then performed to allow heat for transferring to the substrate up to a relatively high temperature before the actual crystallization step. The effects of pulse density and counts on the evolution of the crystallographic phase of 200 nm-thick PZT on glass were then studied to optimize the FLA parameters, as displayed in Fig. 14. When increasing the laser pulses at a fixed voltage (350 and 400 V), PZT thin films on a glass substrate are crystallized and predominately {111}-oriented [indicated in Figs. 14(b) and 14(c)]. An exception is

observed when pulses are 50. As voltage increases from 325 to 450 V, PZT perovskite phase orientation changes from {111} to {100} [cf. Figs. 14(d) and 14(e)]. When it comes to $1 \mu\text{m}$ -thick PZT films on polymer substrates (Kapton), 10–25 250 μs -long pulses at 200–250 V and a power density of 2.8 kW cm^{-2} are found to be optimal for the crystallization of {100}-oriented PZT films. Despite these encouraging XRD patterns and the evidence of local ferroelectric switching observed by piezoresponse force microscopy, neither ferroelectric nor

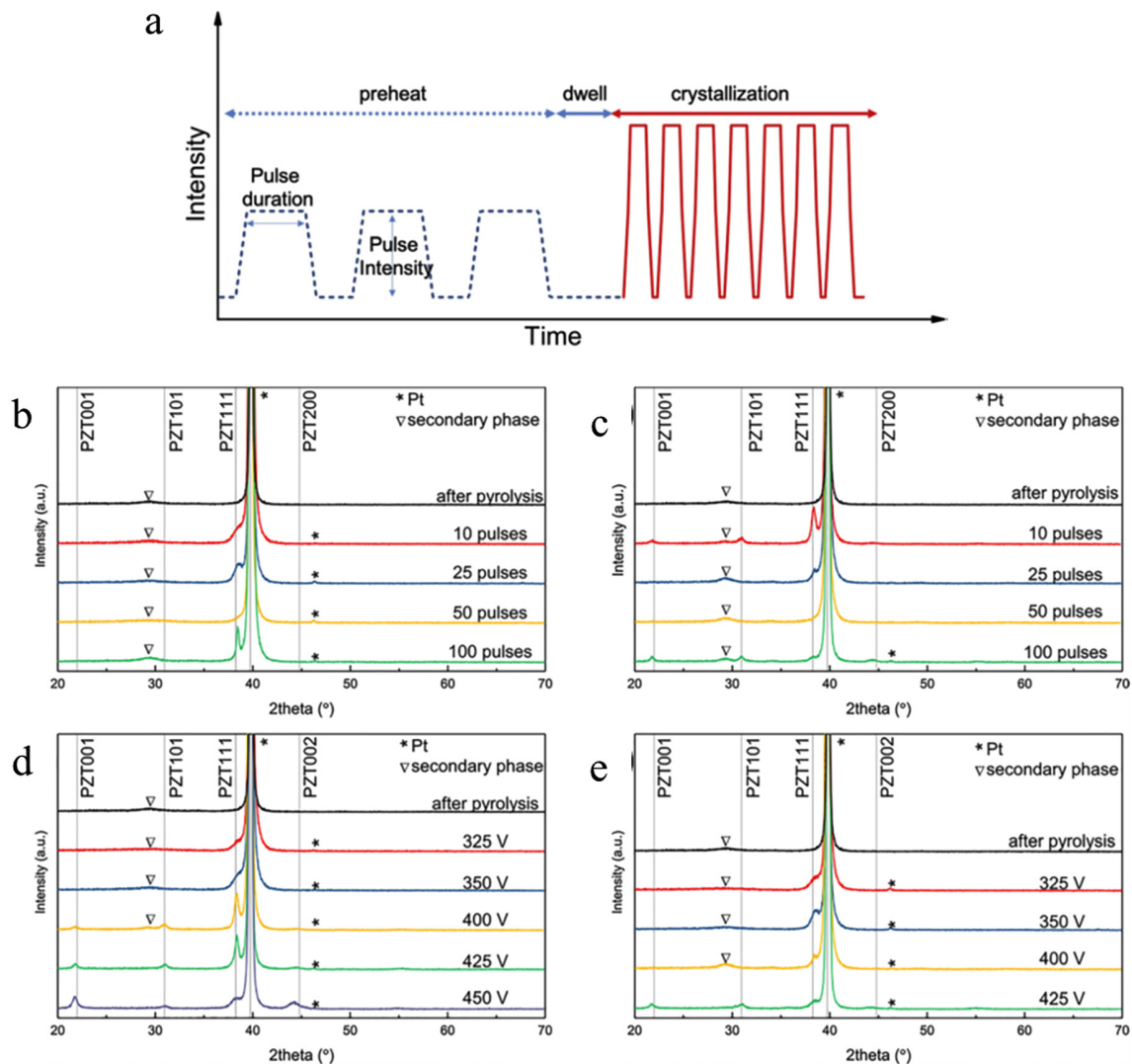


FIG. 14. (a) Scheme representing the applied waveform during pulsed thermal processing, where the dotted and solid lines stand, respectively, for the preheat and crystallization waveforms. X-ray diffraction patterns of PZT films after pyrolysis and crystallization with different pulse density and pulse counts: (b) at 350 V and (c) at 400 V with different pulse counts; (d) with 10 pulse counts and (e) with 25 pulse counts, as a function of applied voltage. A 500 μs pulse duration has been used in the preparation of all samples on glass substrate. Reproduced with permission from Yao *et al.*, *J. Eur. Ceram. Soc.* **40**, 5369 (2020). Copyright 2021 Elsevier.¹⁴⁶

piezoelectric macroscopic properties have been reported in this paper. In this regard, we assume that the piezoelectric properties of the prepared PZT films were not good. However, this work is the only example of FLA-processed PZT thin films on glass and polymer substrates. On the other hand, FLA is compatible with a roll-to-roll process in industry; therefore, this work can be considered as a good start to explore FLA-processed PZT on temperature-sensitive substrates.

Ouyang *et al.* fabricated aero sol-jet printed 6 μm -thick MPB PZT (52/48) thick films crystallized with flashlamp annealing ($87 \text{ J} \approx \text{cm}^{-2}$) with no extra heating and coupled with the simultaneous application of a poling electric field of 20 kV cm^{-1} for 5 min.¹⁴⁷ This specific set-up is displayed in Fig. 15(a). In this case, five groups of

PZT samples were prepared and their piezoelectric properties were compared. Top views and cross sections obtained from scanning electron microscope (SEM) are, respectively, displayed in Figs. 15(b)–15(j). These samples exhibited very large piezoelectric properties such as $g_{33} = 22 \cdot 10^{-3} \text{ Vm N}^{-1}$ and $d_{33} = 626 \text{ pm V}^{-1}$. Moreover, a dielectric constant ϵ_r as large as 3130 was measured. Note that g_{33} and ϵ_r were measured using a self-built cylinder system and an RC bridge circuit.

4. Microwave annealing

Microwave annealing (MA) is one of the most popular annealing technologies to lower the crystallization temperature of sol-gel derived

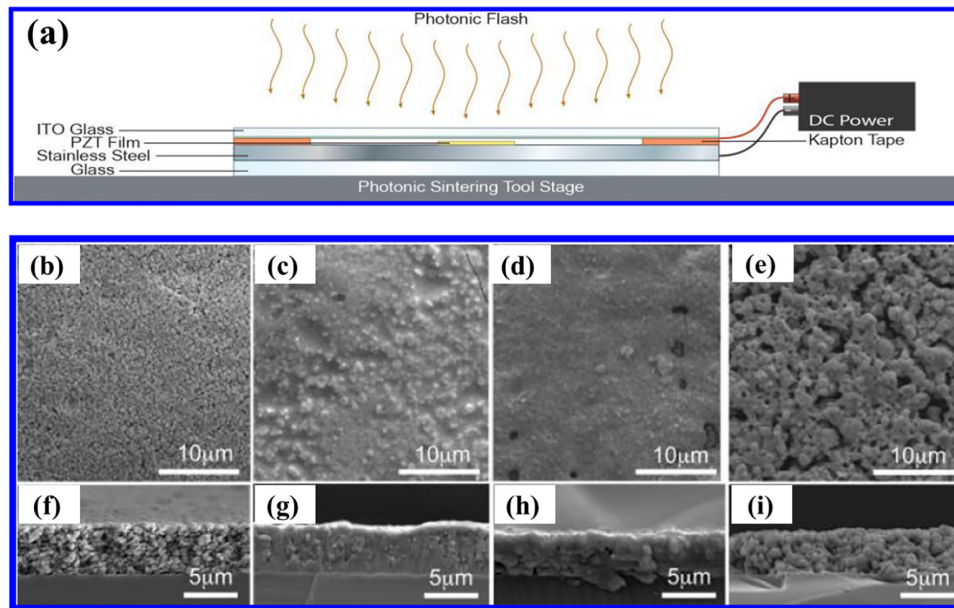


FIG. 15. (a) Schematic diagram of a specific photonic annealing technique using *in situ* poling of the annealed films. From (b) to (e), SEM images top views of PZT films processed with different annealing conditions: (b) without annealing; (c) conventional annealing (1000 °C for 1 h in an N₂ environment); (d) photonic annealing [202 J cm⁻² energy without the aid of indium tin oxides (ITO) glass]; (e) photonic annealing with simultaneous DC-field poling; images (f)–(i) are cross sections of the un-sintered, traditionally sintered, photonic annealing sintered, and photonic annealing with simultaneous DC-field poling sintered films, respectively. Reproduced with permission from J. Ouyang, D. Cormier, and D. A. Borkholder, ACS Appl. Energy Mater. **2**, 338 (2018). Copyright 2018 American Chemical Society.¹⁴⁷

PZT films.^{148–152} Microwaves are defined by electromagnetic waves with a wavelength in the range between 1 mm and 1 m, meaning frequencies from 1 to 300 GHz.^{153–155} MA includes two modes, namely, electrical field mode (E-mode) and magnetic field mode (H-mode). Microwave irradiation can be efficient, as it penetrates the material through molecular interactions with the incident electromagnetic field [see Figs. 16(a) and 16(b)].^{156–160} Therefore, the material becomes the heating source. The power P (W m⁻³) absorbed per unit of volume is expressed as follows:¹⁶¹

$$P = \sigma |E|^2 = 2\pi f \epsilon_0 \epsilon_r' \tan \delta |E|^2, \quad (7)$$

where E is the magnitude of the internal electric field, σ the total effective conductivity, f is the frequency, ϵ is the permittivity of free space ($\epsilon_0 = 8.86 \times 10^{-12}$ F m⁻¹), ϵ_r' is the relative dielectric constant, and $\tan \delta$ is the loss tangent. The penetration depth (D) at which the incident power is halved reads

$$D = 3\lambda_0 / 8.686\pi \tan \delta (\epsilon_r' / \epsilon_0)^{1/2}, \quad (8)$$

where λ_0 is the incident wavelength. Therefore, the dielectric properties of the material of interest, i.e., ϵ_r' and $\tan \delta$, are the factors influencing MA efficiency.

A tentative mechanism for the crystallization of PZT films treated by MA was proposed by Chen *et al.* as depicted in Fig. 16(c).¹⁶² In the case of conventional heating of PZT (52/48) films on Pt/Si, intermetallic Pt₃Pb generated by the interfacial interaction between film and bottom electrode plays the role of nuclei that induce the phase transition from pyrochlore (Py) to perovskite (Pv).^{163,164} However, at the initial

stage, they found that an intermediate phase (denoted Pv') crystallizes at the bottom of the film near PZT/Pt interface [Fig. 16(c)], which acts as nuclei for the perovskite phase growth (Pv). Thus, textured Pv grains grow gradually vertically, forming a flat interface between Pv and Py. Finally, columnar perovskite grains reach the surface of the film [Fig. 16(c)]. Figure 17 shows the schematic of the phase transition path with its associated Gibbs energy. The transformation process from amorphous to Py occurs in both conventional processing and microwave processing, indicating that the activation energy (E_0) is identical. However, the transition from Py to Pv is different. At the stage of nucleation, thanks to the formation of Pv', the activation energy of nucleating Pv was reduced from E_a to E_{a1} and E_{a2} . The formed Py/Pv flat interface also enhances the ion transport during the continuous growth of Pv grains, and thereby the Gibbs energy of activation is reduced from E_a to E_3 .

MA typical frequency is 2.45 GHz, although some attempts in the millimeter-wave range such as 28, 30, and 83 GHz were also performed.^{165–167} As reported by Bhaskar *et al.*, sol-gel processed 420 nm-thick {110}-prominent PZT (53/47) films were fabricated using single-mode 2.45 GHz E field MA (power 350 ± 50 W) at 450 °C for 30 min, showing a P_r of 47 $\mu\text{C cm}^{-2}$, a E_c of 86 kV cm⁻¹ measured at ± 600 kV cm⁻¹, a dielectric constant of 1140, and a dissipation factor of 0.03.¹⁶⁸ No piezoelectric data were reported in this paper. Because of its low dielectric properties, the initial amorphous gel film was not able to efficiently absorb microwave energy [see Eq. (10)]. Therefore, in the case of E-mode MA, SiC rods are normally needed as a sample holder to absorb microwave energy and transfer it as heat to the PZT thin film. Wang *et al.* reported that {110}-oriented

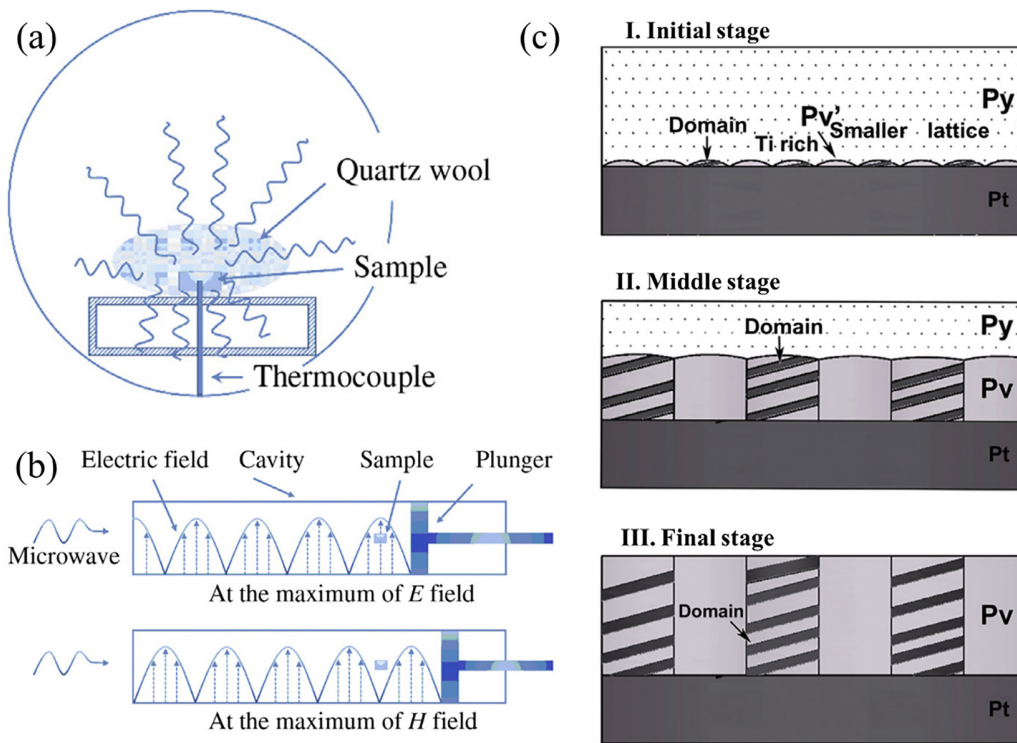


FIG. 16. Schematic illustrations of the distribution of microwave electromagnetic field: (a) in the cavity of a multimode microwave system and (b) the electric field and the magnetic field separated in space in the cavity of a single-mode microwave system. Reproduced with permission from Z. Wang and J. Ouyang, *Nanostructures in Ferroelectric Films for Energy Applications* (Elsevier, 2019), Vol. 203. Copyright 2019 Elsevier.¹⁴⁸ (c) Schematics of crystallization process of PZT films induced by MA. Reproduced with permission from Chen *et al.*, *Acta Mater.* 71, 1 (2014). Copyright 2014 Elsevier.¹⁶²

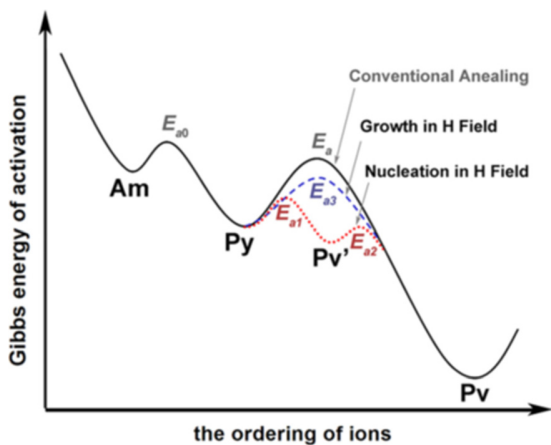


FIG. 17. Schematic of Gibbs energy of activation of PZT films during their crystallization vs the ordering of ions in the case of conventional and microwave annealings. Reproduced with permission from Chen *et al.*, *Acta Mater.* 71, 1 (2014). Copyright 2014 Elsevier.¹⁶²

perovskite PZT (52/48) thin films could be crystallized by the irradiation of a 28 GHz multimode millimeter-wave (power = 2.5 kW) at 480 °C for 1.5 min.¹⁶⁹ The dielectric constant, loss tangent, P_r , and E_c of 1 μm -thick PZT films were 1100, 0.04, 40 $\mu\text{C cm}^{-2}$, and 50 kV cm^{-1} , respectively. On the contrary, the undesired pyrochlore phase appears when using the conventional thermal process at 480 °C for 30 min.¹⁶⁹ P-E hysteresis loops indicate good ferroelectric properties of PZT thin films. However, it is worth noting that the polarization in this case is too large to be reliable, suggesting an over-estimated electrode area. Wang *et al.* also reported 2.45 GHz single-mode H field microwave processed 200 nm-thick MPB PZT (52/48) films.^{151,170} As shown in Fig. 18(a), the temperature reached by microwave irradiation was 450 °C. Figure 18(b) is the XRD patterns of PZT films using MA-processing (blue line), conventional annealing at 600 °C (red line), and 450 °C (black line). Interestingly, sharp {100} and {111} peaks were observed in MA-PZT films, while {111} was the dominating peak in conventional annealing at 600 °C. No peaks were observed in conventional annealing at 450 °C. The cross-section SEM image in Fig. 18(c) indicates that PZT films are well-crystallized, which correspond to the XRD results. The P-E hysteresis loop displayed in Fig. 18(d) reveals that MA-PZT films exhibit ferroelectric properties comparable to conventional annealing at 600 °C. They also reported that single-mode H-field MA is more effective than E-field MA and 28 GHz multimode

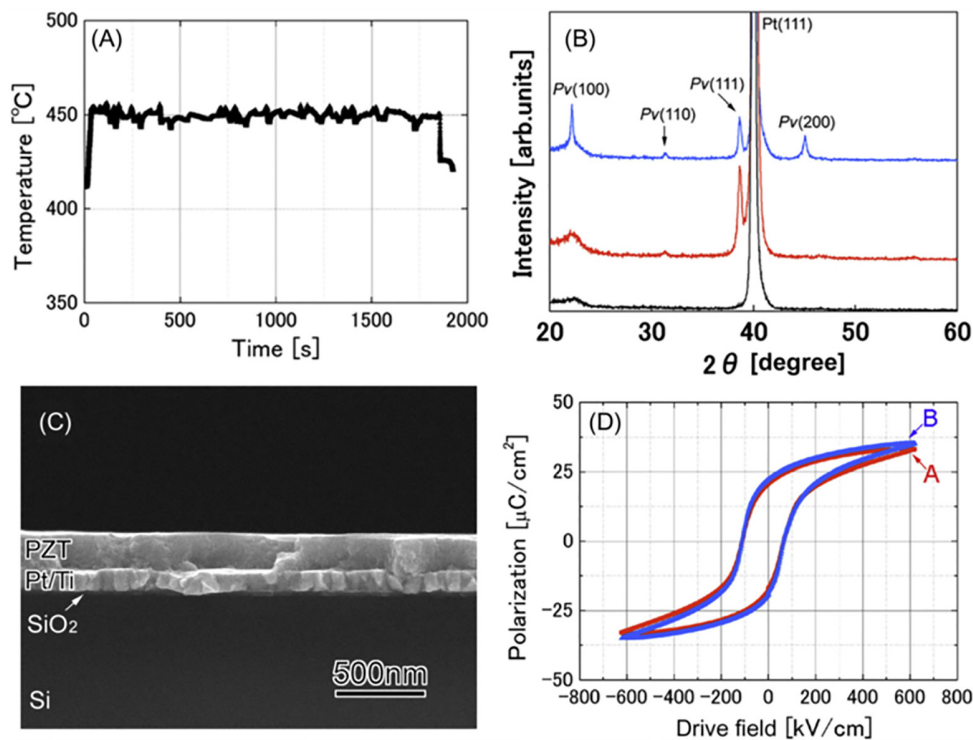


FIG. 18. (a) Temperature-time profile of a PZT thin film under MA. (b) XRD patterns of PZT thin films crystallized by microwave irradiation (blue line) and conventional thermal processing at 600 °C (red line) and 450 °C (black line) for 30 min, respectively. (c) Cross-section SEM image of MA processed PZT at 450 °C. (d) P-E hysteresis loops of PZT films crystallized by microwave irradiation (denoted by A) and conventional thermal processing at 600 °C (denoted by B), respectively. Pv stands for Perovskite phase. Reproduced from Wang *et al.*, *Appl. Phys. Lett.* **92**, 222905 (2008). Copyright 2008 AIP Publishing.¹⁵¹

millimeter-wave MA. The MA-processed (2.45 GHz) MPB thin films exhibit the lowest processing temperature at 450 °C, and it is reproducible.^{151,168,170} However, piezoelectric properties were not reported, meaning that the potential of MA-processed PZT thin films in piezo MEMS applications remains to be assessed.

An interesting question arises, though: why is *H*-field MA more efficient than *E*-field MA in the thermal processing of MPB PZT (52/48) films? In this regard, Cao *et al.* studied the heating origin and crystallization of PZT (52/48) films in a separated *E*-field and *H*-field MA.¹⁷¹ Cao confirmed that PZT was annealed and crystallized more efficiently in *H*-field than in *E*-field. Heating with *H*-field was obtained mainly from the contribution of the bottom electrode (Pt/Ti) and the substrate (Si). This result is consistent with what Wang *et al.* reported.^{151,170}

5. High-pressure annealing

High-pressure annealing (HPA) has been developed for the low-temperature processing of metal-oxide films.^{67,172–175} The mechanism on how HPA reduces the crystallization temperature is generally explained with Gibbs free energy, defined as¹⁷⁶

$$\Delta G(T, P) = \frac{1}{6} \pi d^3 (\Delta G^{gf \rightarrow of} + E_d) + \pi d^2 \sigma + P \Delta V, \quad (9)$$

where $\Delta G^{gf \rightarrow of}$ is the free energy change from amorphous to crystalline states, σ being the interface energy between amorphous and crystalline phases, V^C the oxide film molar volume, ΔV the volume change during crystallization, E_d the elastic energy induced by the volume change, and P the induced pressure. High pressure leads to $\Delta V < 0$, which in turn decreases the Gibbs free energy required for nucleation. This impacts the oxide formation kinetics.^{173,176} Apart from lowering crystallization temperature, HPA can also improve the density of oxides films.¹⁷⁷ In the case of PZT films, high oxygen pressure gives a retarding effect for lead and oxygen volatilization from PZT and enables incorporating more oxygen into PZT, which decreases oxygen vacancies.¹⁷⁸

Zhang *et al.* sputtered 300 nm-thick MPB PZT (52/48) films on LaNiO₃/Si substrate at 200 °C, followed by a crystallization process at 400 °C using high oxygen pressure annealing (HOPA, ~2–8 MPa).¹⁷⁸ As observed in the corresponding XRD patterns [Fig. 19(a)], {h00} signals occur after HPA processing (2–8 MPa), while there are no PZT-related signals in the XRD pattern of as-grown sputtered films. The corresponding *P*-*E* loops are shown in Fig. 19(b), revealing that P_r increased with pressure. Note also that the reported P_r beyond 100 $\mu\text{C cm}^{-2}$ sounds too high to be real, which could be induced by the overestimation of the actual electrode area or by large leakage current. Besides, piezoelectric properties were not reported. A potential issue is that high oxygen pressure might cause damage to semiconductor circuits.

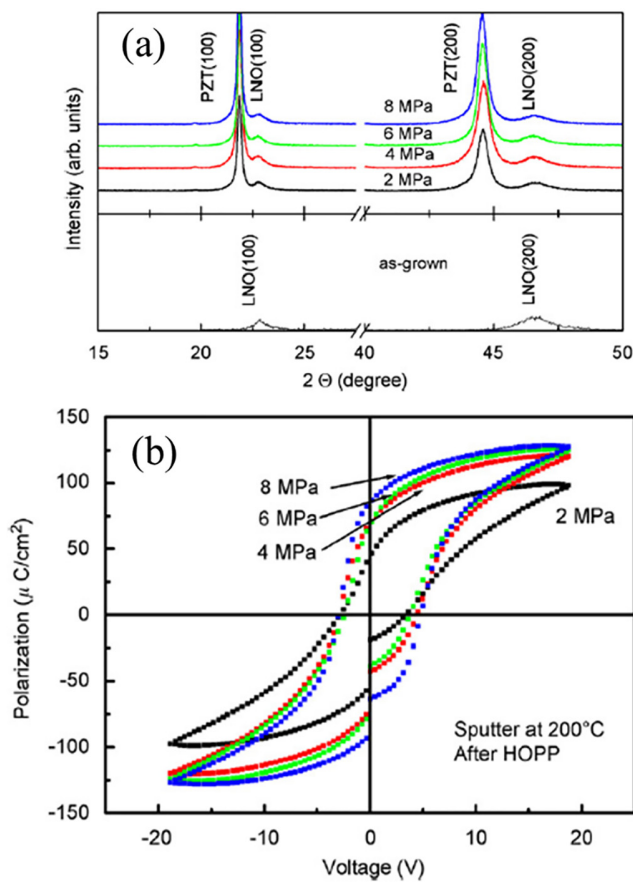


FIG. 19. XRD patterns (a) and P-E hysteresis loops (b) of as-grown and sputtered PZT thin films with an oxygen pressure of 2, 4, 6, and 8 MPa. Reproduced with permission Zhang *et al.*, *J. Cryst. Growth* **310**, 783 (2008). Copyright 2007 Elsevier.¹⁷⁸

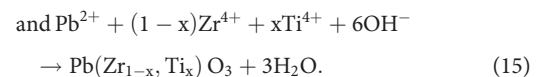
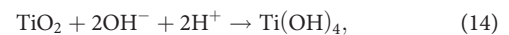
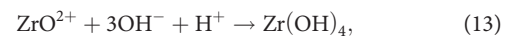
Zhang *et al.* also attempted to use high argon pressure annealing (HAPA) rather than oxygen.¹⁷⁹ They saw PZT {h00} peaks after HAPA. However, the ferroelectric properties were poorer than the ones obtained after by HOPA, which was probably induced by the occurrence of oxygen vacancies in HAPA.¹⁷⁹ The effectiveness of high-pressure annealing in lowering the crystallization temperature of oxides thin films has been demonstrated in previous reports,^{172–175} though studies on high-pressure annealed PZT thin films were all reported by Zhang's group.^{178,179} Therefore, this approach sounds valid. However, piezoelectric data were never provided, which means that the potential of high-pressure annealed PZT thin films in piezo MEMS applications remains to be assessed.

D. Hydrothermal method

The hydrothermal method^{180–183} is a simple chemical synthesis method to fabricate nanostructured metal-oxides or hydroxides.^{184–186} Hydrothermal reactions generally occur in a high-pressure reactor (Fig. 20), which is normally placed in an oven. The Ti substrate and SrRuO₃/single crystal SrTiO₃ has been used as substrates to deposit

polycrystalline and epitaxial PZT hydrothermal films, respectively (see Fig. 20). In a standard procedure, several metal ions sources are dissolved into a solvent, and PZT films are formed through a chemical reaction in an alkaline solution environment at low temperature (typically <200 °C). A stirring movement is usually applied to the solution to accelerate the chemical reaction rate. The common drawbacks of this approach are a rough surface caused by the relatively large nanoparticle size and the rather large thickness of these films (> 1 μm).

In the case of hydrothermally synthesized PZT films, the most common source materials are ZrOCl₂, Pb(NO₃)₂, TiO₂, or TiCl₄ and the mineralizer (KOH),^{187–190} although Kim *et al.* demonstrated that using Ti³⁺ (TiCl₃ for Ti source) reagent instead of Ti⁴⁺ allowed for an even lower reaction temperature.¹⁹¹ The chemical reactions in the alkaline solution environment can be expressed as follows:¹⁸³



Crystalline PZT films are hence deposited on substrates through the chemical reactions of Pb²⁺, Zr⁴⁺, Ti⁴⁺, and OH⁻. The process above is influenced by the following parameters: (1) temperature; (2) pressure; (3) stirring speed; (4) deposition time; and (5) solution concentration.

Significant research efforts have been devoted to hydrothermal synthesized PZT films. Wei *et al.* deposited well-crystallized MPB PZT (52/48) films on Pt/Ti/SiO₂/Si substrate using a hydrothermal method at 160 °C with various kinds of hydroxides [KOH, Pb(OH)₂, and Sr(OH)₂], followed by a post-annealing step at 400 °C to remove undesired residuals such as water and hydroxyl ions.¹⁸¹ PZT films fabricated in a mixture of KOH and Pb(OH)₂ solution exhibited a pure perovskite {111}-oriented structure. Note that the addition of Pb(OH)₂ can compensate for Pb loss in PZT during post-annealing. As-deposited PZT films post-annealed at 400 °C displayed a P_r of 26 μC cm⁻² and E_c of 40.1 kV cm⁻¹ measured at ± 200 kV cm⁻¹. The leakage current density of the films after annealing is about 5.78 × 10⁻⁸ A/cm² at ± 66 kV cm⁻¹. No piezoelectric data have been shown in this paper. In order to achieve high quality PZT films by hydrothermal reaction, one has to optimize the reaction parameters. Hence, Abe *et al.* studied how the deposition time and stirring affect the film thickness while the reaction temperature is 160 °C and pressure is 0.5 MPa.¹⁹² As observed in the SEM images displayed in Figs. 21(a)–21(d), the crystal size of nanoparticles remarkably grew larger as deposition time was extended from 2 to 6 h. The grains nearly stayed unchanged by further increasing deposition time [see SEM images in Figs. 21(e)–21(g), and also Fig. 21(i)]. Figure 21(j) underlines the correlation between stirring speed and film thickness. It was found that stirring speed in the range of 50–200 rpm does not influence thickness. However, an abrupt thickness increase occurred at a stirring speed of 245 rpm and deposition time of 6 h [Fig. 21(j)]. Except those results, there are no PZT electrical properties reported in this paper.

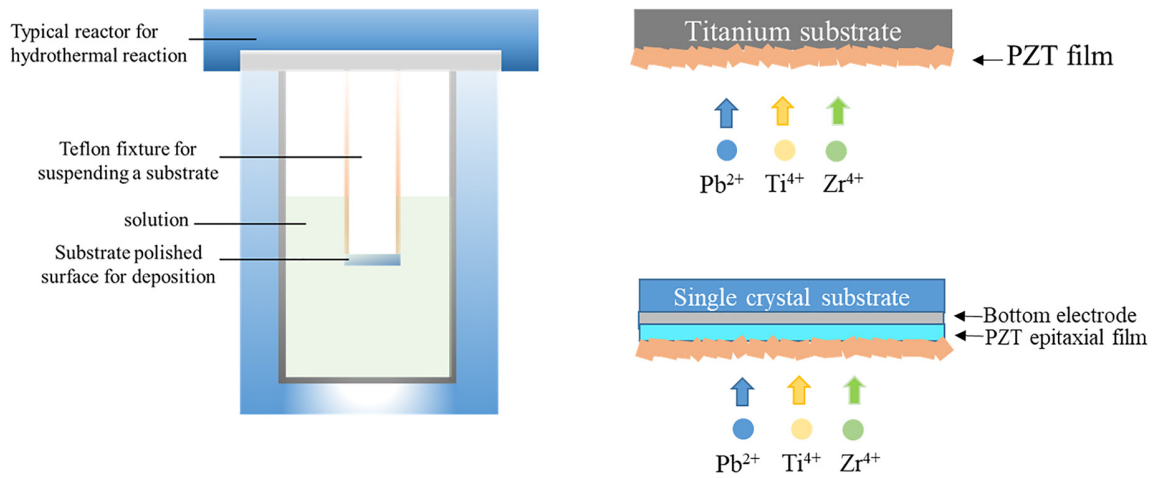


FIG. 20. Hydrothermal method to deposit polycrystalline (on Ti substrate) and epitaxial (on SrTiO₃ substrate) PZT films.

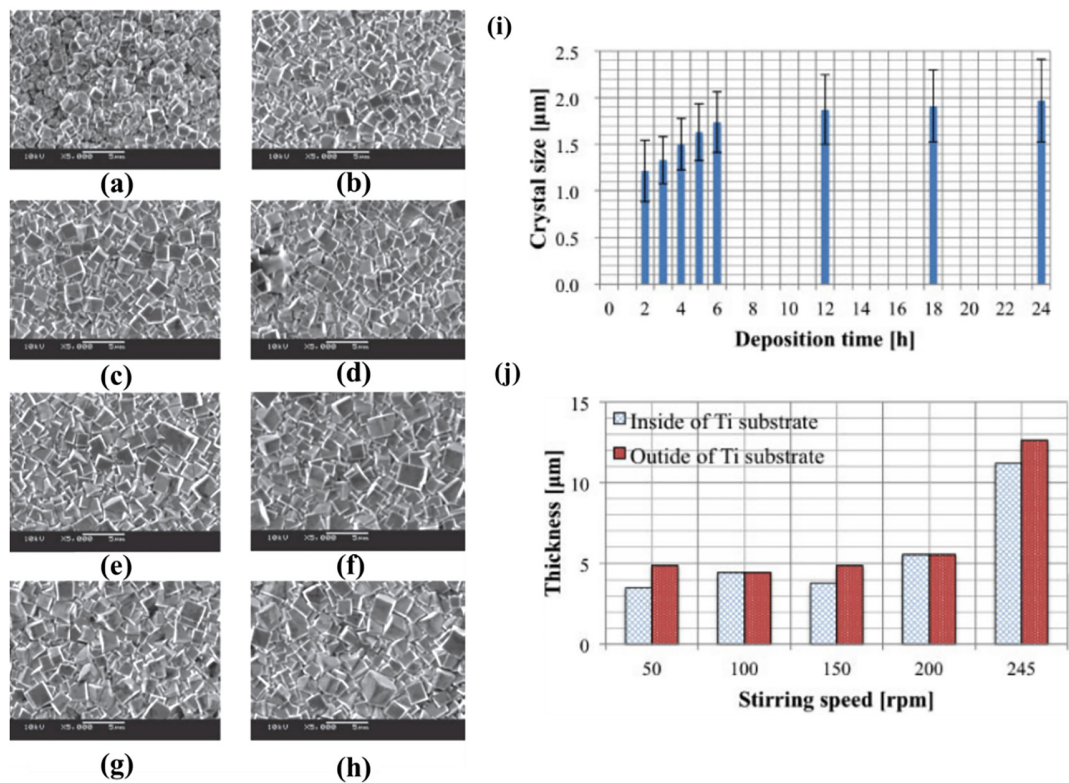


FIG. 21. SEM image of the surface of PZT polycrystalline films with different deposition time (stirring speed: 150 rpm). (a) 2 h. (b) 3 h. (c) 4 h. (d) 5 h. (e) 6 h. (f) 12 h. (g) 18 h. (h) 24 h. (i) Relationship between deposition time and the size of the PZT grains. (j) Relationship between the stirring speed and film thickness. Reproduced with permission from Abe *et al.*, Jpn. J. Appl. Phys. **54**, 07HB06 (2015). Copyright 2015 Japan Society of Applied Physics.¹⁹²

E. Solution chemistry design

Another promising strategy in the case of CSD-derived PZT films is the so-called solution chemistry design. It helps in removing organics and delivering the expected perovskite crystalline structure. During such a chemical reaction, MO_x is supposed to be the only product and the other chemical elements initially present are eliminated as gas products. Hence, chemical reaction design is an efficient and simple approach to suppress the need for high-temperature annealing. Controlling the compositions and homogeneity in PZT solutions and solution combustion chemistry are the most common chemical design approaches for low-temperature CSD PZT films. In this section, an overview about these two methods is presented.

1. Controlling the compositions and homogeneity in PZT solutions

In the case of CSD, rational solution chemistry design allows for modifying the phase composition, orientation, microstructure, and crystallization temperature. A low crystallization temperature can be achieved by forming the metal complexes or coordination compounds, which have the same arrangement of metal and oxygen ions as in the final crystalline state already in the solution, or by controlling the homogeneity of the solution.

Experiments have proved that the crystallization temperature of PZT reduces when the Zr/Ti ratio is decreased.¹⁹³ Hence, in a Zr-rich film, only a thin part of the film near the substrate could crystallize in perovskite phase at 400 °C, indicating the prevalence of heterogeneous nucleation. Most of the PZT films remained amorphous even after 5 h-annealing. On the contrary, a Ti-rich film crystallized in perovskite phase after only 1 h at 400 °C.¹⁹³ Kosec *et al.* reported the fabrication of Ti-rich PZT (30/70) thin films at 400 °C using a modified 2-methoxyethanol route. They found that the high reactivity of zirconium alkoxide n-propoxide results in chemical inhomogeneity of the PZT precursors.¹⁹³ To solve this problem, acetic acid was added to zirconium n-propoxide prior to PZT synthesis. PZT (30/70) films prepared at 400 °C displayed good ferroelectric properties with $P_r = 20 \mu\text{C cm}^{-2}$ and coercive field $E_c = 160 \text{ kV cm}^{-1}$.

2. Solution combustion synthesis (SCS)

Solution combustion synthesis (SCS) corresponds to an exothermic chemical reaction. It starts to be widely used for low-temperature metal-oxide thin films fabrication.^{194–201} It is simple and efficient because one only needs to add oxidizers (e.g., nitrates in the form of metal salts) and fuels (such as acetylacetone or urea for instance) to the standard components of a solution synthesis. The self-generated heat occurring in the exothermic reaction can fulfill the localized energy requirements for the formation of M-O-M bonds and crystallization and thereby lower the external annealing temperature needed. The difference of energy need between combustion and conventional processes is schematically represented in Fig. 22(a). In general, the driving force for such redox reaction is to reduce Gibbs free energy (G) by converting the chemical potential into heat. The initial state of precursor combustion can be regarded as a nonequilibrium quasi-stationary state because the Gibbs free energy is not minimal [see Fig. 22(a)]. When the “ignition temperature” is reached, the desired combustion occurs and Gibbs free energy decreases toward its

minimal value, reaching hence the equilibrium state. The released heat converted from the initial chemical potential enables the film reaching high temperature—so-called “combustion temperature,” T_c —for a short period of time. Therefore, the definition of the crystallization temperature T_c of combustion-derived MO_x films differs from conventional processes, in which it is simply the annealing temperature provided by an external apparatus. For a specific combustion reaction, T_c can be estimated using the following equation:²⁰²

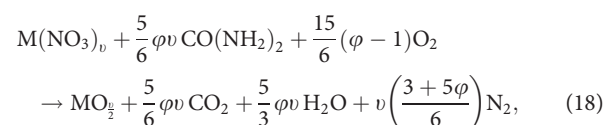
$$T_c = T_0 + \left(\Delta H_r^0 - \Delta H_p^0 \right) / C_p, \quad (16)$$

where T_0 is room temperature, ΔH_r^0 and ΔH_p^0 are the enthalpies of formation of the reactants and products, respectively, and C_p is the heat capacity of the products at constant pressure. For instance, Kim *et al.* reported an estimated generated temperature of 700 °C from the combustion reaction of $\text{Zn}(\text{NO}_3)_2/\text{urea}$ pairs under ideal adiabatic conditions.¹⁹⁶ Since the film is not an isolated system, the energy exchange with the environment can result in a much lower T_c .

Suitable fuel/oxidizer pairs are key to achieve high-efficiency combustion reaction.^{199,203} Table III shows the most commonly used oxidizers, fuels and solvents. In the case of combustion processing for PZT films, Tue *et al.* compared the thermal behaviors of combustion reactions with various fuels (citric acid, glycine, hydrazine, tricine, urea, and acetylacetone), and they found that tricine/ NH_4NO_3 and urea/ NH_4NO_3 pairs exhibit the highest efficiency to Pb- and Zr-solution combustion reactions over other fuel/ NH_4NO_3 pairs.²⁰⁴ Some reports also demonstrated that an addition of co-fuels or bi-fuels can be advantageous to improve the combustion reactivity.^{205,206} In addition, it is worth noting that fuel/oxidizer ratio is one of the most significant parameters impacting the quality of combustion. Parameter φ , proposed by Jain *et al.*,²⁰⁷ reads

$$\varphi = \frac{\text{Total valency of fuel}}{\text{Total valency of oxidizer}}. \quad (17)$$

Here, urea [$\text{CO}(\text{NH}_2)_2$] and $\text{M}(\text{NO}_3)_v$ were taken as an example to explore the effect of φ on combustion reaction. The stoichiometric equilibrium combustion reaction can be described such as



when $\varphi = 1$, the mixture is stoichiometric and atmospheric oxygen is not required; when $\varphi < 1$, there is too much fuel; conversely when $\varphi > 1$, there is fuel missing. The addition of large amount of fuel means that more oxygen is required [see Eq. (18)], which could lead to insufficient oxygen supply. In contrast, not enough fuel would cause incomplete combustion, resulting in a low combustion reaction. In the fuel/oxidizer ratio, the fuel should be always carefully chosen to have the best correlation with the nitrate precursor (i.e., $\varphi = 1$) in order to achieve the highest temperature of the reaction.²⁰⁸ When it comes to experiments, Tue *et al.* reported that the optimized molar ratio of fuel/ NO_3^- is 1:3 in the case of PZT (52/48) combustion.²⁰⁴

The occurrence of combustion is normally verified by thermal analysis tools, such as differential temperature analysis (DTA), thermogravimetry (TGA), or differential scanning calorimetry (DSC).

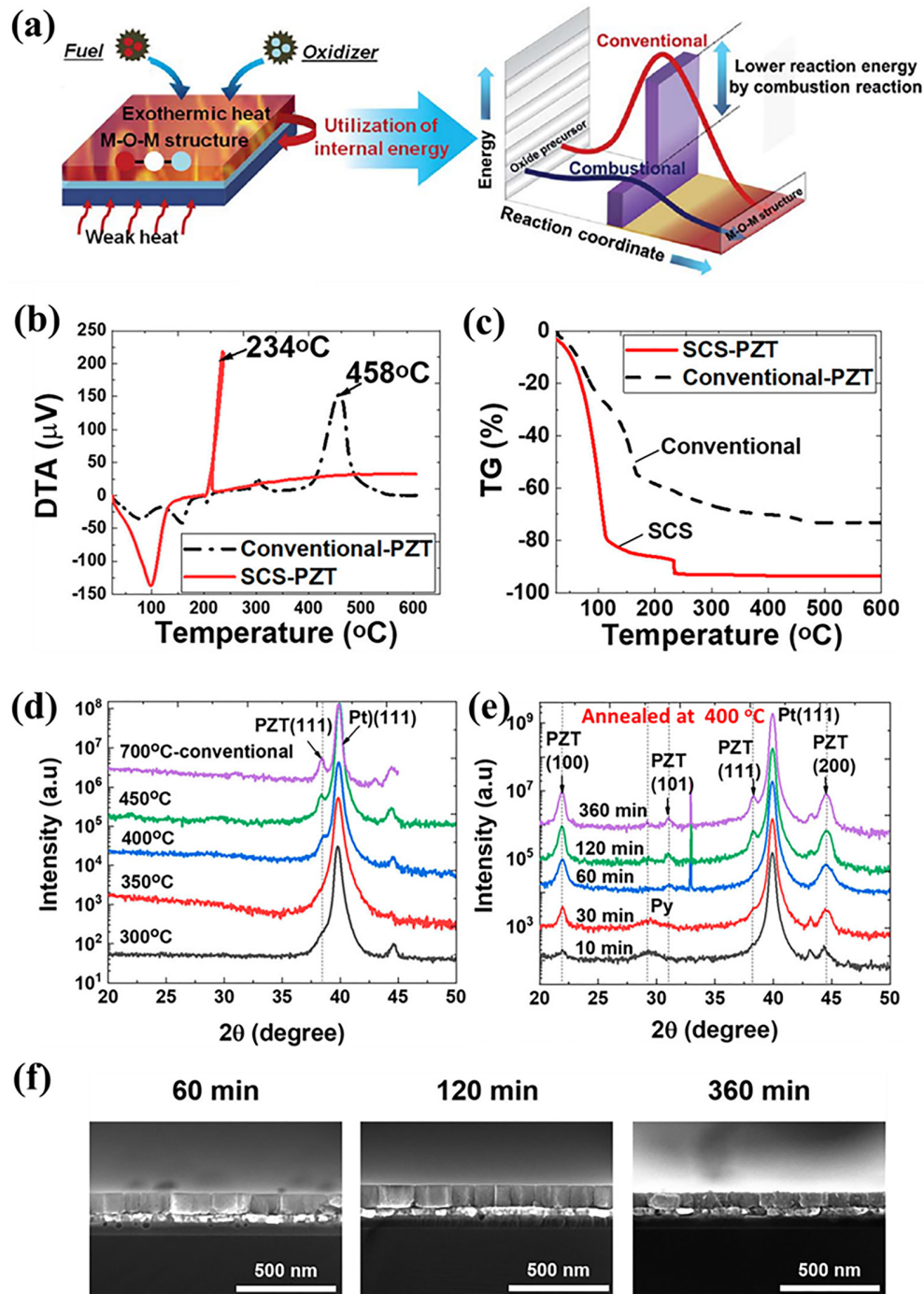


FIG. 22. (a) Scheme of the SCS process of metal-oxide films, underlying the difference in energy vs the conventional process. Reproduced with permission from Kang *et al.*, *J. Mater. Chem. C* **2**, 4247 (2014). Copyright 2013 Royal Society of Chemistry.²¹¹ (b) DTA and (c) TG analyses of the conventional PZT and SCS-PZT precursors. (d) XRD patterns of SCS-PZT and conventional PZT thin-films annealed at different temperatures. (e) XRD patterns of SCS-PZT thin-films annealed at 400 °C for different durations (10–360 min). (f) Cross-section SEM images of the SCS-PZT thin-films annealed at 400 °C for different durations: 60, 120, and 360 min. Reproduced from P. T. Tue, T. Shimoda, and Y. Takamura, *APL Mater.* **8**, 021112 (2020). Copyright 2020 AIP Publishing.²⁰⁴

TABLE III. Commonly used oxidizers, fuels, and solvents for solution combustion synthesis.^{198,203–205,209,210}

Oxidizers	Fuels	Solvents
Metal nitrates [M(NO ₃) _v]	Urea (CH ₄ N ₂ O) Acetylacetone (C ₅ H ₈ O ₂) Glycine (C ₂ H ₅ NO ₂)	Water Kerosene Benzene
Metal Nitrates Hydrotrate [M(NO ₃) _v].nH ₂ O	Sucrose (C ₁₂ H ₂₂ O ₆) Glucose (C ₆ H ₁₂ O ₆)	Ethanol Methanol
Ammonium nitrate (NH ₄ NO ₃)	Carbohydrazide (CH ₆ N ₄ O) Oxalyldihydrazide (C ₂ H ₆ N ₄ O ₂)	2-methoxyethanol formaldehyde
Nitric acid (HNO ₃)	Tricine (C ₆ H ₁₃ NO ₅) Hexamethylenetetramine (C ₆ H ₁₂ N ₄) <i>L</i> -ascorbic acid	

As performed by Tue *et al.*²⁰⁴ and shown in Figs. 22(b) and 22(c), the SCS-PZT (52/48) system exhibits an intensive exothermic signal at 234 °C observed by DTA, in agreement with the abrupt mass loss observed in TGA curves. It indicates that SCS-PZT enables a lower crystallization temperature than the conventional ones. Figure 22(d) shows the XRD patterns of 220 nm-thick SCS-PZT films pyrolyzed at 300 °C and annealed at 300–450 °C for 60 min. The PZT{111} peak is observed after 300 °C-annealing, though it overlaps with the Pt{111} peak. Its appearance indicates nucleation of the perovskite phase of PZT at a significantly lower temperature (300 °C) than with the conventional process. PZT{111} intensity increases with annealing temperature, such a way that the one corresponding to SCS at 450 °C is comparable with the conventional one at 700 °C. Figure 22(e) shows the XRD patterns of 220 nm-thick SCS-PZT (52/48) films pyrolyzed at 250 °C and annealed at 400 °C for different annealing times (10–360 min). The non-ferroelectric pyrochlore phase appears first in films annealed for short durations (10–30 min) and disappears in films annealed for 60 min or longer. Figure 22(f) shows SEM cross-sections of SCS-PZT films annealed at 400 °C for 60, 120, and 360 min. They all exhibit a highly dense columnar structure, which indicates that the energy generated from combustion enables crystallization at low temperature. Besides, an interesting observation is the appearance of PZT{100} peaks in SCS-PZT thin films pyrolyzed at 250 °C. This peak becomes stronger as annealing time is prolonged. The best SCS-PZT thin film exhibits a large P_r ($\sim 37 \mu\text{C cm}^{-2}$), $E_c = 100 \text{ kV cm}^{-1}$, leakage current = $0.1 \mu\text{A cm}^{-2}$ at 600 kV cm^{-1} , and a dielectric constant of 500, which was further used in a ferroelectric-gate memory transistor. The efficacy of the combustion synthesis approach has been demonstrated in other metal oxides.^{194–201} Further investigations are nonetheless needed to reveal the piezoelectric nature of combustion-processed PZT thin films.

V. TRANSFER PROCESSING

The transfer process enables the optimization of PZT film synthesis independently from the final host substrate. It plays an important role in current transparent and flexible PZT devices.^{49,54,60,212,213} In the transfer process, PZT is first deposited on a temperature-compliant substrate, enabling PZT full crystallization. Electrodes are often added to PZT at this step to make a functional stack. The latter is then glued/attached to a host substrate (often a polymer). The final step is the transfer of the PZT functional stack on the host substrate by

inducing a separation at the interface between PZT and the initial temperature-compliant substrate. In some cases, polymer substrates are also fabricated using a spin coating approach, which allows for the absence of glue.

Regarding the transfer itself, there are several possible approaches. A sacrificial layer lying between PZT and the initial substrate can be etched away, which in turn releases PZT from this initial substrate. In this case, PZT devices can be fabricated on silicon-on-insulator (SOI) wafers, which are well adapted to high-temperature crystallization steps. Then, the sacrificial layer such as, e.g., ZnO or MgO is removed by an etching process. The etching chemistries of PZT and the sacrificial layer must be different enough to avoid inducing damages to the final device. The flow chart in Fig. 23 describes the steps of a typical transfer process by etching, as reported by Liu *et al.*²¹⁴ After the deposition of ZnO, Pt was deposited, acting as the top electrode after transfer. A very thin Al₂O₃ layer (10–20 nm thick) was added on Pt to avoid the migration of hydrogen into PZT from polyimide during the imidization reaction. Indeed, hydrogen degrades the switchable polarization of PZT (52/48). Thereafter, a 0.8–1.1 μm -thick PZT thin film was deposited via a sol-gel process and crystallized at 700 °C, followed by the deposition of full sheet Pt (final bottom electrode). Then, polyimide (PI-2611) was spin-coated on the top of the sample and baked at 100 °C, making a 5 μm -thick polyimide substrate on the top of the functional stack. The release process occurred by immersing the sample stack in 33% acetic acid heated at 50–60 °C, which etched ZnO away. In this paper, a so-called “clamped device,” which meant a similar PZT device on a Si substrate, was used as a reference to compare with the transferred device’s performances. Hence, the authors could observe that P_r increased by 45% after transfer (from 18 to 26 $\mu\text{C cm}^{-2}$).

Another possible approach is to completely etch away the initial substrate.^{215,216} Morimoto *et al.* sputtered 2.8 μm MPB PZT (53/27) films on a Pt-coated MgO substrate. PZT was crystallized at 600 °C, followed by the deposition of a Cr electrode. This stack was then bonded to a cantilever-shaped stainless-steel sheet with epoxy resin (M610). The MgO substrate was etched away in phosphoric acid (20%) at 80 °C. The properties of transferred PZT remained nearly unchanged compared with the initial PZT films with $\epsilon_r = 166$ and $\tan \delta = 0.04$. PZT film $e_{31,f}$ values before and after transfer were -4.7 C m^{-2} and -4.5 C m^{-2} , respectively. This transfer process based

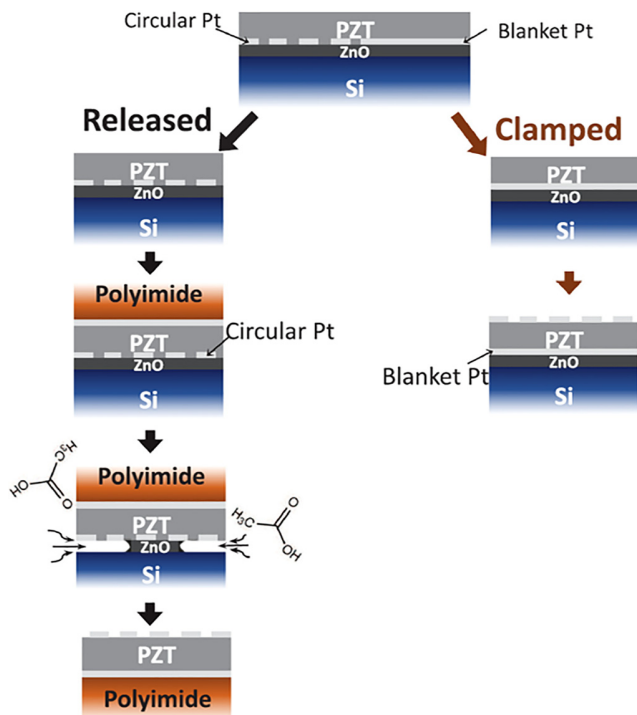


FIG. 23. Flow chart for preparing released (final device on polyimide) and clamped (final device on Si) PZT films from the same deposition procedure. Reproduced from Liu *et al.*, *J. Appl. Phys.* **122**, 164103 (2017). Copyright 2017 AIP Publishing.²¹⁴

on wet etching is safe for PZT because of the weak acid (such as phosphoric acid) used to etch MgO away.²¹⁶

Rhun *et al.* recently reported an etching-free transfer process.²¹⁷ Without using any sacrificial layer, solution processed PZT thin films crystallized at 700 °C were deposited on a SiO₂/Si substrate. Thus, a glass substrate was bonded on the top of PZT stack using a polymer glue. The PZT film stack was eventually transferred to the glass substrate by mechanically separating the SiO₂/Si substrate. Although no details were provided regarding the transfer process, the piezoelectric coefficient $d_{31,eff}$ of the transferred layer was as large as 125 pm V⁻¹.

Laser lift-off (LLO) is another option for etching-free transfer.^{60,66} Laser-lift-off separation of two layers mostly occurs by means of selective laser ablation and evaporation of a strongly absorbing interfacial area.²¹⁸ The first work of this kind was reported by Tsakalakos and Sands.²¹⁹ They transferred a 1.4 μm-thick La-doped PZT (50/50) film from the MgO substrate to stainless-steel substrate using a 248 nm excimer laser pulse. Typically, a PZT film stack can be deposited on a transparent substrate such as sapphire, MgO and fused silica, which allows for the laser to pass through the substrate, as illustrated in Fig. 24(a). This LLO process has been performed in order to obtain a flexible PZT pressure sensor, as reported by Zhu *et al.*⁵⁴ A thin sacrificial PZT layer is inserted between the PZT sensor and the sapphire substrate. After the deposition of patterned electrodes and functional 400 nm-thick PZT film, a polymer substrate with several micrometer of thickness was spin-coated. Next, a temperature sensor

made of a spiral Pt structure was also deposited on the top of the PI substrate and patterned by lithography. A laser with suitable wavelength and energy density was eventually used to scan the sample from the sapphire back side to separate the PZT film device and its PI substrate from the initial sapphire substrate. Figure 24(b) and c are microscopy images of these final flexible PZT devices. Figure 24(d) shows a bended device, indicating excellent flexibility of the transferred devices.

VI. APPLICATIONS OF LOW-TEMPERATURE PROCESSING

An interesting question that arises is the purpose behind the development of low temperature-processing of PZT. Currently, there are two critical reasons. The first one is that the current processing temperature of PZT films is much higher than the thermal budget of CMOS circuits (450 °C). In order to meet urgent demands on miniaturization and high performance of the new-generation of MEMS, it is necessary to explore low-temperature processing to enable the direct deposition of PZT films on CMOS chips, as illustrated in Sec. VI A. The second purpose is to enable using PZT films in emerging flexible and wearable devices, which requests the direct deposition or the transfer of PZT on temperature-sensitive polymer or glass substrates. The current progress in flexible PZT devices is introduced in Sec. VI B.

A. MEMS-CMOS integration

The majority of current PZT MEMS devices must be integrated and operated with silicon-based CMOS integrated circuits (IC). To do so, two approaches have been developed, namely, hybrid integration and system-on-chip (SoC).^{220–222} Hybrid integration uses a separate CMOS chip to operate MEMS, which is now the predominant approach in MEMS technologies [Fig. 25(a)]. As functional PZT thin films need high thermal budget that damages CMOS circuits, such an approach enables an independent optimization of the CMOS circuits and the MEMS devices. It results in higher packaging and test costs. Moreover, modular multi-chips occupy more space, which limits product miniaturization. Finally, when separate chips for MEMS and IC are used, performance-limiting parasitic signals are present due to the long interconnections between MEMS and logic. As illustrated in Fig. 25(b), the SoC approach integrates MEMS and CMOS circuits on the same wafer. SoC offers the possibility of one-step packaging for both MEMS and CMOS circuits at wafer level, which reduces the number of packaging and wire bonding steps performed at chip level. This way, the costs for packaging and testing can be largely reduced. On the other hand, SoC allows for high-density integration of multi-systems, thus reducing the size of MEMS devices. However, SoC imposes to obtain excellent yields for both CMOS and MEMS technologies.

Some attempts have been made to transfer PZT films on CMOS chips. For instance, Kousuke *et al.* fabricated PZT-actuated MEMS switches on a Si dummy wafer using sol-gel method and then transferred them to a CMOS wafer by polymer bonding (as shown in Fig. 26).²²³ After attaching PZT devices on polymer with glue (first step in Fig. 26), the dummy wafer with TiO₂ adhesion layer were removed by SF₆ and CHF₃ plasma, respectively (second step). Next, top electrodes were deposited on the top of PZT (third step). The polymer glue was finally etched away at 150 °C to release the switches

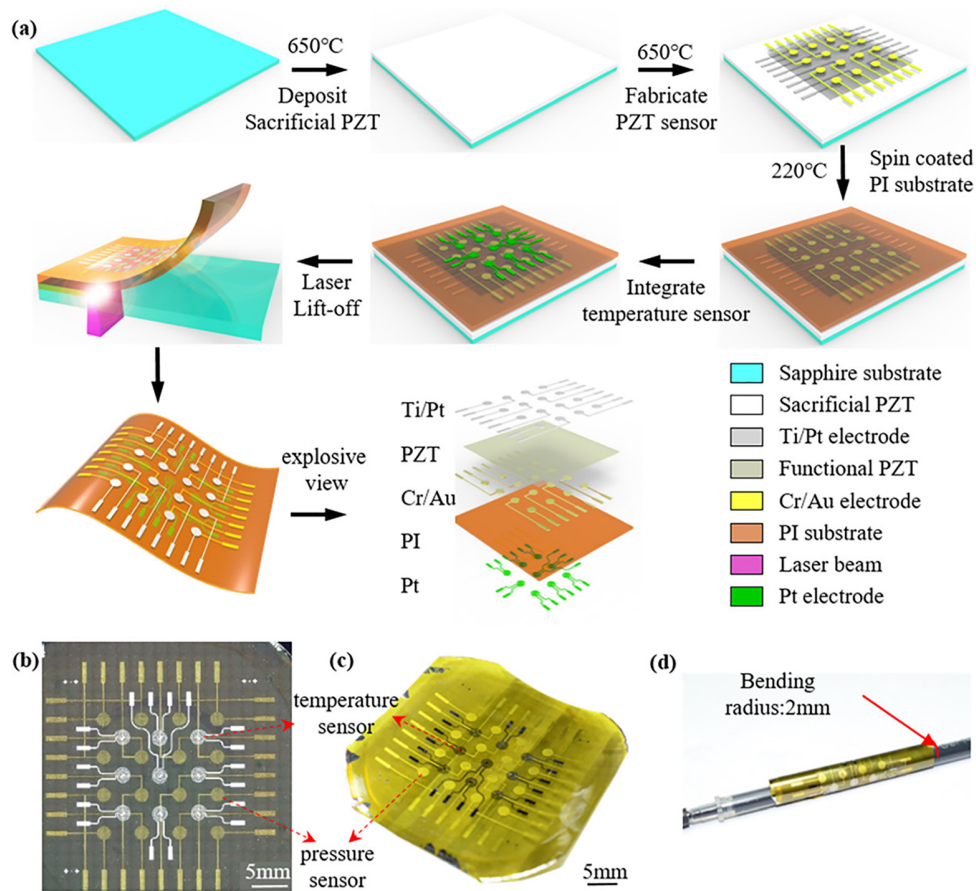


FIG. 24. Device fabrication via the laser lift-off (LLO) process. (a) Schematic of the fabrication steps for a PZT-integrated bilateral device. (b) Microscopy image of a typical flexible PZT-integrated bilateral device and (c) its corresponding photograph. (d) Device wrapped on a gel pen refill (bending radius: 2 mm). Reproduced with permission from Zhu *et al.*, *ACS Appl. Mater. Interfaces* **12**, 37354 (2020). Copyright 2020 American Chemical Society.⁵⁴

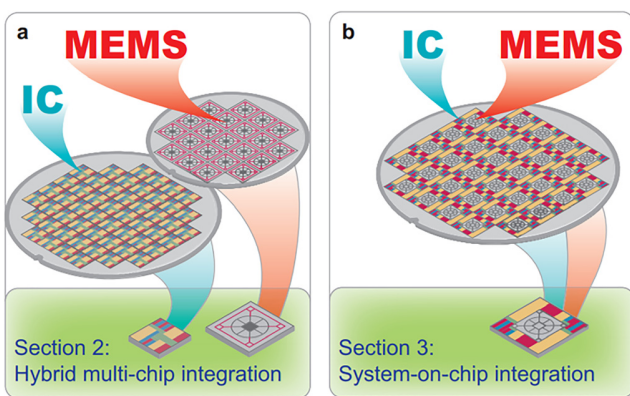


FIG. 25. MEMS and IC integration methods are based on either (a) hybrid multi-chip solutions or (b) system-on-chip solutions. A. C. Fischer *et al.*, *Microsyst. Nanoeng.* **1**, 1 (2015). Copyright 2015 Authors, licensed under a Creative Commons Attribution (CC BY) license.²²⁰

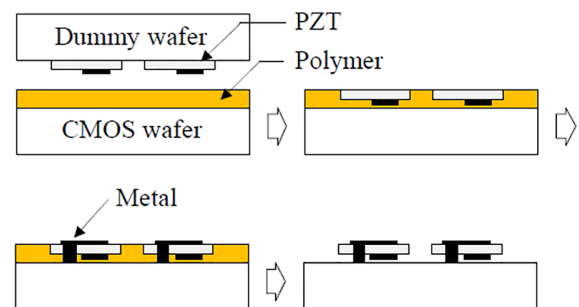


FIG. 26. Schematic diagram of wafer-level transfer technology to fabricate PZT-actuated MEMS switches on a CMOS wafer. Reproduced with permission from Kousuke *et al.*, 2012 IEEE 25th International Conference on Micro Electro Mechanical Systems (MEMS) (2012). Copyright 2012 IEEE.²²³

structures. However, the complicated process-control required in this technology makes it not well suited to large-scale industry production.

Hence, reducing the thermal budget appears to be the main hope to obtain PZT films through SoC technique. As discussed previously, various strategies for low-temperature processing have been explored to enable PZT direct deposition on CMOS chips, and progress has been made recently.^{123,224} Reijiro *et al.* directly deposited sol-gel processed PZT actuator arrays at 450 °C on a silicon substrate via a UV/O₃ assisted annealing process. The low-temperature processed PZT films exhibited a preferential {111} orientation. P_r, E_c, and leakage current of the PZT film obtained using this fabrication technique were 24 C cm⁻², 110 kV cm⁻¹ and 10⁻⁶ A cm⁻², respectively. The maximum amplitude of the actuators was around 130 nm at 10 V.¹²³

B. Flexible piezoelectric energy harvesters

PZT piezoelectric energy harvesters (PEH, sometimes called nanogenerators) take advantage of the direct piezoelectric effect to convert mechanical energy into electrical energy. It gives the opportunity to develop micro-size self-powered systems, which are able to generate power from people movements, wind or water flow. Flexible energy harvesters (FEH) on a polymer substrate have raised interest in the fields of electronic skin, implantable/wearable systems, and body sensor networks.

For instance, Park *et al.* reported an IDE-structured 2 μm-thick PZT (52/48) FEH (i.e., d₃₃ mode) achieved by laser lift off technology.⁴⁸ Figure 27(a) shows this FEH in unbended and bended states.

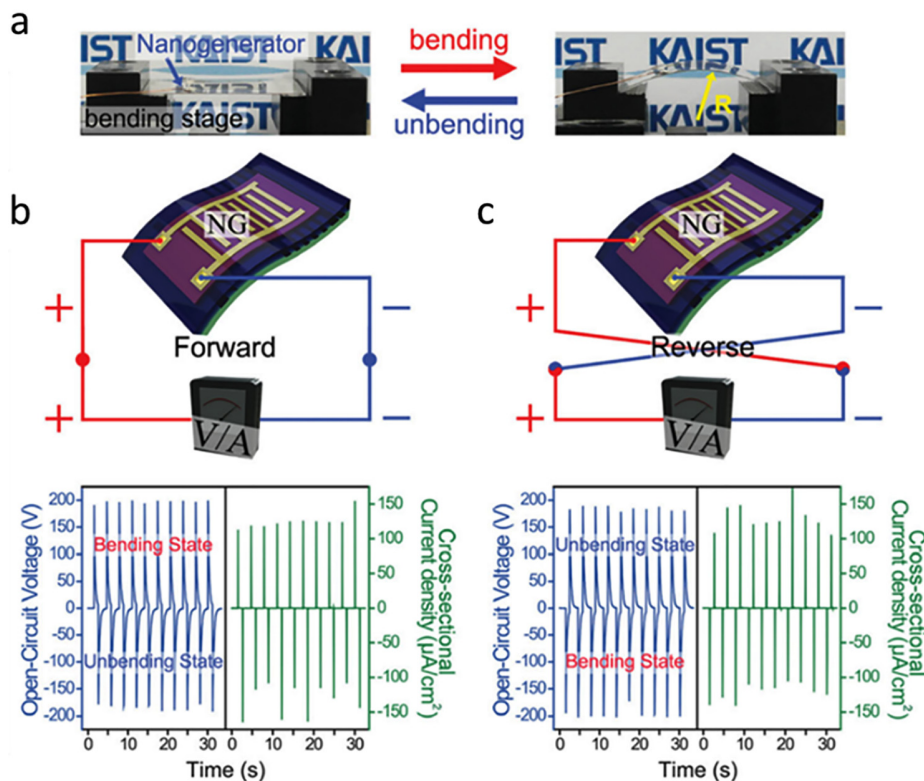


FIG. 27. (a) Photographs of a PZT flexible energy harvester captured not bent (left) and bent (right). (b) and (c) Open-circuit voltage and cross-sectional current density measured from PZT FEH in forward (b) and reverse (c) connections. Reproduced with permission from Park *et al.*, *Adv. Mater.* **26**, 2514 (2014). Copyright 2014 John Wiley and Sons.⁴⁸

While mechanically bending this device, charges are generated and accumulated between electrodes, which creates a signal. In released state, the piezo-potential between adjacent electrodes disappears and the charges recover their original position, generating a reverse signal. Figure 27(b) and c represent those signals issued from periodic bending and unbending motions. The presented 1.5 × 1.5 cm PZT FEH delivers an open-circuit voltage of 200 V and a short-circuit current of 1.5 μA.

Besides, PZT FEH is also a promising solution for wearable e-skin applications to monitor human health.^{225,226} Zhang *et al.* reported a PZT FEH fabricated via low-temperature PLD technology, and used it as wearable e-skin.⁵⁵ The as-fabricated PZT sensor delivers a high detection sensitivity of 5.82 kPa⁻¹, fast response of 0.38 s and release time of 0.79 s. They demonstrated that this enables to capture weak signals, such as human cough signal, fingertip pressing, and heart beats.

VII. CONCLUSION AND OUTLOOK

The motivation to grow PZT thin films at low temperature is twofold. First, direct deposition of PZT on CMOS devices (system-on-chip) and second, direct deposition of PZT on temperature-sensitive substrates such as polymer or glass. To enable this, processing temperature of PZT thin films must be reduced to at least 450 °C for CMOS and glass substrates and 350 °C for polymer substrates, goals for which substantial research efforts have already been deployed. Among the investigated approaches, the seeding method needs extremely long annealing time to crystallize PZT films, but this is an effective way to

assist other low-temperature processing to obtain the desired orientation and to decrease crystallization temperature. UV-based and microwave-based annealing can reduce thermal budget to 450 °C. Further developments strongly depend on equipment itself, such as high-power excimer UV light. Laser annealing offers an opportunity to reach much lower processing temperatures, though a careful control of processing time and laser density is extremely important. Although hydrothermal method enables the growth of PZT thick films at $T < 200$ °C, special substrates such as Ti must be used and the films exhibit weak properties. The investigation of combustion processing of PZT thin films started only in 2020, though this technique has been widely used in low-temperature semiconductor film fabrication. The reported results on PZT films are very promising.

When it comes to flexible devices on polymer substrates, the majority of the strategies mentioned earlier cannot reach PZT crystallization at such low temperature (350 °C). Today, high density laser annealing, especially UV-based lasers, is the most promising way to realize this, and impressive results have been demonstrated, showing that PZT thin films crystallize at 200 °C with good piezoelectric properties. Transfer technology, such as laser lift off, remains the key approach to obtain optimized PZT thin films independently from temperature-sensitive substrates. Combining seed effect and UV annealing enables the crystallization of solution processed PZT thin films at 350 °C. This suggests that associating two or even more annealing strategies could help in decreasing further PZT films crystallization temperature. Some attempts have proven successful in fabricating metal oxides thin films, such as highly conductive ITO thin films fabricated at 200 °C by the combination of UV annealing and combustion processing. However, only a few related works have been demonstrated in the case of PZT films. In this regard, we strongly suggest researchers to devote more efforts on this strategy and we believe that low-temperature processing of PZT thin films will be a key asset for system-on-chip MEMS-CMOS integration and for wearable electronics in the foreseeable future.

ACKNOWLEDGMENTS

The authors want to thank FNR (Luxembourg National Research Fund) for funding this work through the projects PACE (PRIDE17/12246511) and HARVESTORE (INTER/ANR/18/12618689).

AUTHOR DECLARATIONS

Conflict of Interest

The authors have no conflicts to disclose.

DATA AVAILABILITY

Data sharing is not applicable to this article as no new data were created or analyzed in this study.

REFERENCES

- ¹Y. Lee, J. Park, S. Cho, Y.-E. Shin, H. Lee, J. Kim, J. Myoung, S. Cho, S. Kang, and C. Baig, *ACS Nano* **12**, 4045 (2018).
- ²J. Park, M. Kim, Y. Lee, H. S. Lee, and H. Ko, *Sci. Adv.* **1**, 1500661 (2015).
- ³D. Damjanovic, P. Muralt, and N. Setter, *IEEE Sens. J.* **1**, 191 (2001).
- ⁴B. Morten, G. De Cicco, and M. Prudenziati, *Sens. Actuators A Phys.* **31**, 153 (1992).
- ⁵D. Polla and L. Francis, *MRS Bull.* **21**, 59 (1996).
- ⁶T. Sekine, R. Sugano, T. Tashiro, J. Sato, Y. Takeda, H. Matsui, D. Kumaki, F. D. Dos Santos, A. Miyabo, and S. Tokito, *Sci. Rep.* **8**, 4442 (2018).
- ⁷E. Defay, C. Millon, C. Malhaire, and D. Barbier, *Sens. Actuators A Phys.* **99**, 64 (2002).
- ⁸S. Aoyagi, S. Kumagai, D. Yoshikawa, and Y. Isono, *Sens. Actuators A Phys.* **139**(1–2), 88 (2007).
- ⁹G. J. Lee, B. H. Kim, S. A. Yang, J. J. Park, S. D. Bu, and M. K. Lee, *J. Am. Ceram. Soc.* **100**, 678 (2017).
- ¹⁰S. Goljahi, J. Gallagher, S. Zhang, J. Luo, R. Sahul, W. Hackenberger, and C. Lynch, *Smart Mater. Struct.* **21**, 055005 (2012).
- ¹¹K. Kunz, P. Enoksson, and G. Stemme, *Sens. Actuators A Phys.* **92**, 156 (2001).
- ¹²Z. Shen, C. Y. Tan, K. Yao, L. Zhang, and Y. F. Chen, *Sens. Actuators A Phys.* **241**, 113 (2016).
- ¹³I. Baginsky and E. Kostsov, *Optoelectron. Instrum. Data Process.* **53**, 294 (2017).
- ¹⁴C. C. Tsai, Y. C. Chien, C. S. Hong, S. Y. Chu, C. L. Wei, Y. H. Liu, and H. Y. Kao, *J. Am. Ceram. Soc.* **102**, 4056 (2019).
- ¹⁵B. Stadlober, M. Zirk, and M. Irimia-Vladu, *Chem. Soc. Rev.* **48**(6), 1787–1825 (2019).
- ¹⁶M. Rath, E. Varadarajan, S. Premkumar, S. Shinde, V. Natarajan, and M. Ramachandra Rao, *Ferroelectrics* **551**, 17 (2019).
- ¹⁷V. Petrov, *Proceedings* **4**, 40 (2019).
- ¹⁸G. Zhang, M. Li, H. Li, Q. Wang, and S. Jiang, *Energy Technol.* **6**(5), 791 (2018).
- ¹⁹M. T. Todaro, F. Guido, V. Mastronardi, D. Desmaele, G. Epifani, L. Algieri, and M. D. Vittorio, *Microelectron. Eng.* **183**, 23 (2017).
- ²⁰S. S. Won, H. Seo, M. Kawahara, S. Glinsek, J. Lee, Y. Kim, C. K. Jeong, A. I. Kingon, and S.-H. Kim, *Nano Energy* **55**, 182 (2019).
- ²¹H. G. Yeo and S. Trolrier-McKinstry, *Sens. Actuators A Phys.* **273**, 90 (2018).
- ²²M. D. Nguyen, E. Houwman, M. Dekkers, D. Schlom, and G. Rijnders, *APL Mater.* **5**, 074201 (2017).
- ²³C. K. Jeong, S. B. Cho, J. H. Han, D. Y. Park, S. Yang, K.-I. Park, J. Ryu, H. Sohn, Y.-C. Chung, and K. J. Lee, *Nano Res.* **10**(2), 437–455 (2017).
- ²⁴R. P. Dahl-Hansen, T. Tybell, and F. Tyholdt, paper presented at the 2018 IEEE ISAF-FMA-AMF-AMEC-PFM Joint Conference (IFAAP) (2018).
- ²⁵S. Rombach, M. Marx, S. Gu-Stoppel, and Y. Manoli, paper presented at the MOEMS and Miniaturized Systems XV (2016).
- ²⁶I. Kanno, paper presented at the 2019 20th International Conference on Solid-State Sensors, Actuators and Microsystems & Eurosensors XXXIII (TRANSDUCERS & EUROSensors XXXIII) (2019).
- ²⁷F. Ceysens, S. Sadeghpour, H. Fujita, and R. Puers, *Sens. Actuators A Phys.* **295**, 604 (2019).
- ²⁸M.-Y. Li, K.-C. Peng, Y.-F. Hsu, P.-J. Chen, C.-L. Tsui, W.-J. Wu, and W.-C. Wang, paper presented at the Integrated Optics: Devices, Materials, and Technologies XXIV (2020).
- ²⁹F. Filhol, E. Defay, C. Divoux, C. Zinck, and M.-T. Delaye, *Sens. Actuators A Phys.* **123**, 483 (2005).
- ³⁰I. Kanno, *Jpn. J. Appl. Phys.* **57**, 040101 (2018).
- ³¹D. J. Laser and J. G. Santiago, *J. Micromech. Microeng.* **14**, R35 (2004).
- ³²P.-H. Cazorla, O. Fuchs, M. Cochet, S. Maubert, G. Le Rhun, Y. Fouillet, and E. Defay, *Sens. Actuators A Phys.* **250**, 35 (2016).
- ³³M. Cuffe, E. Defay, P. Rey, G. L. Rhun, F. Perruchot, C. Ferrandon, D. Mercier, F. Domingue, A. Suhm, and M. Aid, paper presented at the 2010 IEEE 23rd International Conference on Micro Electro Mechanical Systems (MEMS) (2010).
- ³⁴F. Casset, J. Danel, C. Chappaz, Y. Civet, M. Amberg, M. Gorisse, C. Dieppedale, G. L. Rhun, S. Basrour, and P. Renaux, paper presented at the 2013 Transducers & Eurosensors XXVII: The 17th International Conference on Solid-State Sensors, Actuators and Microsystems (TRANSDUCERS & EUROSensors XXVII) (2013).
- ³⁵S. Glinsek, M. A. Mahjoub, M. Rupin, T. Schenk, N. Godard, S. Girod, J. B. Chemin, R. Leturcq, N. Valle, and S. Klein, *Adv. Funct. Mater.* **30**, 2003539 (2020).

- ³⁶K. Mawatari, A. Shimomura, T. Matsuo, D. Ishibashi, and H. Kobayashi, *NIP & Digital Fabrication Conference-Printing for Fabrication* **4**, 127 (2018).
- ³⁷J. Eloy and E. Mounier, Silicon Photonics Report (Yole Développement released in January 2018): http://www.yole.fr/iso_upload/News/2018/PR_SI_PHOTONICS_LatestTrendsYOle_Mar2018.pdf.
- ³⁸Yole Développement, Status of the MEMS Industry (Yole Développement, 2018), https://www.printedelectronicsnow.com/contents/view_breaking-news/2018-06-04/yole-development-issues-status-of-the-mems-industry-report/.
- ³⁹M. Tilli, M. Paulasto-Krockel, M. Petzold, H. Theuss, T. Motooka, and V. Lindroos, *Handbook of Silicon Based MEMS Materials and Technologies* (Elsevier, 2020).
- ⁴⁰F. Edalatfar, B. Yaghoobkar, A. Q. A. Qureshi, S. Azimi, and B. Bahreyni, paper presented at the 2016 IEEE sensors (2016).
- ⁴¹G. Shilpa, K. Sreelakshmi, and M. Ananthaprasad, paper presented at the IOP Conference Series: Materials Science Engineering (2016).
- ⁴²H.-C. Song, P. Kumar, D. Maurya, M.-G. Kang, W. T. Reynolds, D.-Y. Jeong, C.-Y. Kang, and S. Priya, *J. Microelectromech. Syst.* **26**, 1226 (2017).
- ⁴³A. P. Domanic, *J. Gujarat Res. Soc.* **21**, 481 (2019).
- ⁴⁴H. Takeuchi, A. Wung, X. Sun, R. T. Howe, and T.-J. King, *IEEE Trans. Electron. Devices* **52**, 2081 (2005).
- ⁴⁵C.-P. De Araujo, J. Cuchiaro, L. McMillan, M. Scott, and J. Scott, *Nature* **374**, 627 (1995).
- ⁴⁶B. Park, B. Kang, S. Bu, T. Noh, J. Lee, and W. Jo, *Nature* **401**, 682 (1999).
- ⁴⁷A. Rajashkhar, H. R. Zhang, B. Srowthi, I. M. Reaney, and S. Trolier-McKinstry, *J. Am. Ceram. Soc.* **99**, 43 (2016).
- ⁴⁸K. I. Park, J. H. Son, G. T. Hwang, C. K. Jeong, J. Ryu, M. Koo, I. Choi, S. H. Lee, M. Byun, and Z. L. Wang, *Adv. Mater.* **26**, 2514 (2014).
- ⁴⁹T. Dufay, B. Guiffard, R. Seveno, and J. C. Thomas, *Energy Technol.* **6**, 917 (2018).
- ⁵⁰Y. Ni, Y. Wang, and W. Xu, *Small* **17**, 1905332 (2020).
- ⁵¹M.-F. Tsai, J. Jiang, P.-W. Shao, Y.-H. Lai, J.-W. Chen, S.-Z. Ho, Y.-C. Chen, D.-P. Tsai, and Y.-H. Chu, *ACS Appl. Mater. Interfaces* **11**, 25882 (2019).
- ⁵²H.-J. Tseng, W.-C. Tian, and W.-J. Wu, *Sensors* **13**, 5478 (2013).
- ⁵³G. T. Hwang, V. Annapureddy, J. H. Han, D. J. Joe, C. Baek, D. Y. Park, D. H. Kim, J. H. Park, C. K. Jeong, and K. I. Park, *Adv. Energy Mater.* **6**, 1600237 (2016).
- ⁵⁴C. Zhu, D. Guo, D. Ye, S. Jiang, and Y. Huang, *ACS Appl. Mater. Interfaces* **12**, 37354 (2020).
- ⁵⁵S. Zhang, L. Zhang, L. Wang, F. Wang, and G. Pan, *J. Mater. Chem. C* **7**, 4760 (2019).
- ⁵⁶M. L. Hammock, A. Chortos, B. C. K. Tee, J. B. H. Tok, and Z. Bao, *Adv. Mater.* **25**, 5997 (2013).
- ⁵⁷R. Saleh, M. Barth, W. Eberhardt, and A. Zimmermann, *Micromachines* **12**, 78 (2021).
- ⁵⁸M.-G. Kang, M.-S. Noh, J. J. Pyeon, W.-S. Jung, H. G. Moon, S.-H. Baek, S. Nahm, S.-J. Yoon, and C.-Y. Kang, *Chem. Mater.* **32**, 6483 (2020).
- ⁵⁹G. Chen, Z. Liu, B. Liang, G. Yu, Z. Xie, H. Huang, B. Liu, X. Wang, D. Chen, and M. Q. Zhu, *Adv. Funct. Mater.* **23**, 2681 (2013).
- ⁶⁰Y. H. Do, W. S. Jung, M. G. Kang, C. Y. Kang, and S. J. Yoon, *Sens. Actuators A Phys.* **200**, 51 (2013).
- ⁶¹T. Yamashita, H. Okada, T. Kobayashi, K. Togashi, D. Zymelka, S. Takamatsu, and T. Itoh, paper presented at the 2016 IEEE Sensors (2016).
- ⁶²T. Kobayashi, T. Yamashita, N. Makimoto, S. Takamatsu, and T. Itoh, paper presented at the 2016 IEEE 29th International Conference on Micro Electro Mechanical Systems (MEMS) (2016).
- ⁶³I. Babu and G. de With, *Compos. Sci. Technol.* **104**, 74 (2014).
- ⁶⁴X. Ren, H. Fan, Y. Zhao, and Z. Liu, *ACS Appl. Mater. Interfaces* **8**, 26190 (2016).
- ⁶⁵Y. Zhang, W. Zhu, C. K. Jeong, H. Sun, G. Yang, W. Chen, and Q. Wang, *RSC Adv.* **7**, 32502 (2017).
- ⁶⁶M.-S. Noh, S. Kim, D.-K. Hwang, and C.-Y. Kang, *Sens. Actuators A Phys.* **261**, 288 (2017).
- ⁶⁷J. W. Park, B. H. Kang, and H. J. Kim, *Adv. Funct. Mater.* **30**, 1904632 (2020).
- ⁶⁸V. Kovacova, N. Vaxelaire, G. Le Rhun, P. Gergaud, T. Schmitz-Kempen, and E. Defay, *Phys. Rev. B* **90**, 140101 (2014).
- ⁶⁹J. Abergel, M. Allain, H. Michaud, M. Cuffeff, T. Ricart, C. Dieppedale, G. L. Rhun, D. Faralli, S. Fanget, and E. Defay, paper presented at the 2012 IEEE International Ultrasonics Symposium (2012).
- ⁷⁰K. Lefki and J. M. Dormans, *J. Appl. Phys.* **76**, 1764 (1994).
- ⁷¹S. Rossnagel, *J. Vac. Sci. Technol. A* **21**, 74 (2003).
- ⁷²K. H. Habig, *J. Vac. Sci. Technol. A* **4**, 2832 (1986).
- ⁷³R. Powell and A. Ulman, *Ionized Physical Vapor Deposition* (Academic Press, 1999).
- ⁷⁴U. Helmersson, M. Lattemann, J. Bohlmark, A. P. Ehasarian, and J. T. Gudmundsson, *Thin Solid Films* **513**, 1 (2006).
- ⁷⁵M. M. Moslehi, U.S. patent 6,136,165 (2000).
- ⁷⁶T. Haccart, E. Cattan, and D. Remiens, *Semicond. Phys. Quantum Electron. Optoelectron.* **5**, 78 (2002), <http://dspace.nbu.gov.ua/handle/123456789/121131>.
- ⁷⁷K. Tsuchiya, T. Kitagawa, and E. Nakamachi, *Precis. Eng.* **27**, 258 (2003).
- ⁷⁸Z. Bi, Z. Zhang, and P. Fan, paper presented at the Journal of Physics: Conference Series (2007).
- ⁷⁹D. J. Kester and R. Messier, *J. Vac. Sci. Technol.* **4**, 496 (1986).
- ⁸⁰A. Pignolet, R. A. Roy, J. P. Doyle, and J. J. Cuomo, *J. Vac. Sci. Technol.* **12**, 2840 (1994).
- ⁸¹R. H. Wilke, R. L. Johnson-Wilke, V. Cotroneo, W. N. Davis, P. B. Reid, D. A. Schwartz, and S. Trolier-McKinstry, *Appl. Opt.* **52**, 3412 (2013).
- ⁸²J. A. Thornton, *Model. Opt. Thin Films* **821**, 95 (1988).
- ⁸³J. A. Thornton, *J. Vac. Sci. Technol.* **11**, 666 (1974).
- ⁸⁴H. Kobayashi, K. Matsuoka, T. Tsuyuki, A. Suzuki, I. Kimura, T. Jimbo, and K. Suu, paper presented at the 2020 IEEE 33rd International Conference on Micro Electro Mechanical Systems (MEMS) (2020).
- ⁸⁵K. Tokita, M. Aratani, and H. Funakubo, *Appl. Phys. Lett.* **82**, 4122 (2003).
- ⁸⁶C. Rice, J. Cuchiaro, S. Sun, L. Provost, G. Tompa, H. Beratan, C. Hanson, and H. Tanner, *Integr. Ferroelectr.* **59**, 1465 (2003).
- ⁸⁷M. Shimizu, M. Okaniwa, H. Fujisawa, and H. Niu, *J. Eur. Ceram. Soc.* **24**, 1625 (2004).
- ⁸⁸J.-W. Moon, S. Tazawa, K. Shinozaki, N. Wakiya, and N. Mizutani, *Appl. Phys. Lett.* **89**, 202907 (2006).
- ⁸⁹M. Aratani, T. Oikawa, T. Ozeki, and H. Funakubo, *Appl. Phys. Lett.* **79**, 1000 (2001).
- ⁹⁰H. Funakubo, K. Tokita, T. Oikawa, M. Aratani, and K. Saito, *J. Appl. Phys.* **92**, 5448 (2002).
- ⁹¹M. Aratani, T. Ozeki, and H. Funakubo, *Jpn. J. Appl. Phys.* **40**, 343 (2001).
- ⁹²K. Suu, *Advances in Ferroelectrics* (IntechOpen, 2012), Vol. **369**.
- ⁹³N. Bassiri-Gharb, Y. Bastani, and A. Bernal, *Chem. Soc. Rev.* **43**, 2125 (2014).
- ⁹⁴I. Bretos, R. Jiménez, J. Ricote, and M. L. Calzada, *Chem. Soc. Rev.* **47**, 291 (2018).
- ⁹⁵I. Bretos, R. Jiménez, J. Ricote, and M. Calzada, *IEEE Trans. Ultrason. Ferroelectr. Freq. Control* **67**, 1967 (2020).
- ⁹⁶R. M. Pasquarelli, D. S. Ginley, and R. O'Hayre, *Chem. Soc. Rev.* **40**, 5406 (2011).
- ⁹⁷R. W. Schwartz, T. Schneller, and R. Waser, *C. R. Chim.* **7**, 433 (2004).
- ⁹⁸M. Avrami, *J. Chem. Phys.* **7**, 1103 (1939).
- ⁹⁹M. Avrami, *J. Chem. Phys.* **9**, 177 (1941).
- ¹⁰⁰C. Kwok and S. Desu, *Ceramic Transactions: Ferroelectric Films*, edited by A. Bhalla (American Ceramic Society, Westerville, OH, 1992), Vol. **7**, p. 433.
- ¹⁰¹N. Sama, R. Herdier, D. Jenkins, C. Soyer, D. Remiens, M. Detalle, and R. Bouregba, *J. Cryst. Grow.* **310**, 3299 (2008).
- ¹⁰²Y. Kokaze, I. Kimura, T. Jimbo, M. Endo, M. Ueda, and K. Suu, *ULVAC Tech. J.* **66E**, 13–20 (2007), see https://www.ulvac.co.jp/eng/r_d/new_technology/data/no66e-04.pdf.
- ¹⁰³F. Tyholdt, F. Calame, K. Prume, H. Reader, and P. Mural, *J. Electroceram.* **19**, 311 (2007).
- ¹⁰⁴K. Nittala, S. Mhin, K. M. Dunnigan, D. S. Robinson, J. F. Ihlefeld, P. G. Kotula, G. L. Brennecke, and J. L. Jones, *J. Appl. Phys.* **113**, 244101 (2013).
- ¹⁰⁵N. Inoue, T. Nakura, and Y. Hayashi, *IEEE Trans. Electron. Dev.* **50**, 2081 (2003).
- ¹⁰⁶A. Wu, P. M. Vilarinho, I. M. M. Salvado, J. L. Baptista, Z. Zhou, I. Reaney, A. R. Ramos, and M. F. da Silva, *J. Am. Ceram. Soc.* **85**, 641 (2002).
- ¹⁰⁷A. Wu, P. Vilarinho, I. Reaney, I. Miranda Salvado, and J. Baptista, *Integr. Ferroelectr.* **30**, 261 (2000).
- ¹⁰⁸A. Wu, I. M. Miranda Salvado, P. M. Vilarinho, and J. L. Baptista, *J. Eur. Ceram. Soc.* **17**, 1443 (1997).
- ¹⁰⁹A. Wu, P. Vilarinho, I. Reaney, and I. Miranda Salvado, *Chem. Mater.* **15**(5), 1147–1155 (2003).

- ¹¹⁰I. Bretos, R. Jiménez, A. Wu, A. I. Kingon, P. M. Vilarinho, and M. L. Calzada, *Adv. Mater.* **26**, 1405 (2014).
- ¹¹¹A. Schatz, D. Pantel, and T. Hanemann, paper presented at the 2016 Joint IEEE International Symposium on the Applications of Ferroelectrics, European Conference on Application of Polar Dielectrics, and Piezoelectric Force Microscopy Workshop (ISAF/ECAPD/PFM) (2016).
- ¹¹²A. Schatz, D. Pantel, and T. Hanemann, *Thin Solid Films* **636**, 680 (2017).
- ¹¹³Y.-H. Kim, J.-S. Heo, T.-H. Kim, S. Park, M.-H. Yoon, J. Kim, M. S. Oh, G.-R. Yi, Y.-Y. Noh, and S. K. Park, *Nature* **489**, 128 (2012).
- ¹¹⁴R. A. John, N. A. Chien, S. Shukla, N. Tiwari, C. Shi, N. G. Ing, and N. Mathews, *Chem. Mater.* **28**, 8305 (2016).
- ¹¹⁵B.-Y. Su, S.-Y. Chu, Y.-D. Juang, and H.-C. Chen, *Appl. Phys. Lett.* **102**, 192101 (2013).
- ¹¹⁶P. S. Wagenknecht and P. C. Ford, *Coord. Chem. Rev.* **255**, 591 (2011).
- ¹¹⁷M. Calzada, A. González, R. Poyato, and L. Pardo, *J. Mater. Chem.* **13**, 1451 (2003).
- ¹¹⁸J. Yue, Y. Chen, L. Li, K. Zhang, and Z. Li, *J. Sol-Gel Sci. Technol.* **83**, 647 (2017).
- ¹¹⁹I. Bretos, R. Jiménez, J. Ricote, and M. L. Calzada, *Chem.—A Eur. J.* **26**, 9157 (2020).
- ¹²⁰C. De Dobbelaere, A. Hardy, M. K. Van Bael, I. Bretos, R. Jiménez, and M. L. Calzada, *Nanoscale Ferroelectr. Multiferroics: Key Process. Charact. Issues Nanoscale Eff. I*, 1 (2016).
- ¹²¹M. L. Calzada, I. Bretos, R. Jiménez, H. Guillon, and L. Pardo, *Adv. Mater.* **16**, 1620 (2004).
- ¹²²I. Bretos, R. Jiménez, J. García-López, L. Pardo, and M. L. Calzada, *Chem. Mater.* **20**, 5731 (2008).
- ¹²³R. Shimura, P. T. Tue, Y. Tagashira, T. Shimoda, and Y. Takamura, *Sens. Actuators A Phys.* **267**, 287 (2017).
- ¹²⁴S. R. Shannigrahi, K. Yao, S. C. P. Ng, and F. E. H. Tay, *Integr. Ferroelectr.* **84**, 211 (2006).
- ¹²⁵I. Bretos, R. Jiménez, M. Tomczyk, E. Rodríguez-Castellón, P. M. Vilarinho, and M. L. Calzada, *Sci. Rep.* **6**, 1 (2016).
- ¹²⁶J. P. S. Bermundo, Y. Ishikawa, M. N. Fujii, H. Ikenoue, and Y. Uraoka, *Appl. Phys. Lett.* **110**, 133503 (2017).
- ¹²⁷K.-M. Yu, H.-M. Ji, M.-C. Nguyen, A. H.-T. Nguyen, S.-J. Choi, J.-G. Cheon, J.-H. Kim, S.-W. Kim, S.-Y. Cho, and R. Choi, *IEEE Electron Device Lett.* **40**, 167 (2019).
- ¹²⁸S.-D. Tsai, M. Suresh, and C.-C. Chou, *Phys. Scr.* **T129**, 175 (2007).
- ¹²⁹A. Queraltó, A. Pérez del Pino, M. de la Mata, J. Arbiol, M. Tristany, X. Obradors, and T. Puig, *Chem. Mater.* **28**, 6136 (2016).
- ¹³⁰J.-L. Wang, Y.-S. Lai, S.-C. Liou, B.-S. Chiou, C.-K. Jan, and H.-C. Cheng, *J. Vac. Sci. Technol. B* **26**, 41 (2008).
- ¹³¹S. Bharadwaja, F. Griggio, J. Kulik, and S. Trolier-McKinstry, *Appl. Phys. Lett.* **99**, 042903 (2011).
- ¹³²M.-G. Kang, K.-H. Cho, Y. Ho Do, Y.-J. Lee, S. Nahm, S.-J. Yoon, and C.-Y. Kang, *Appl. Phys. Lett.* **101**, 242910 (2012).
- ¹³³S. Bharadwaja, T. Dechakupt, and S. Trolier-McKinstry, *J. Am. Ceram. Soc.* **91**, 1580 (2008).
- ¹³⁴I. Kanno, S. Hayashi, R. Takayama, H. Sakakima, and T. Hirao, *Jpn. J. Appl. Phys.* **34**, 5211 (1995).
- ¹³⁵A. Rajashekar, A. Fox, S. Bharadwaja, and S. Trolier-McKinstry, *Appl. Phys. Lett.* **103**, 032908 (2013).
- ¹³⁶P. Schwaller, A. Fischer, R. Thapliyal, M. Aeberhard, J. Michler, and H. Hug, *Surf. Coat. Technol.* **200**, 1566 (2005).
- ¹³⁷F. Calame and P. Muralt, *Appl. Phys. Lett.* **90**, 062907 (2007).
- ¹³⁸K. Amanuma, T. Hase, and Y. Miyasaka, *Appl. Phys. Lett.* **65**, 3140 (1994).
- ¹³⁹M. Suresh, S.-D. Tsai, K.-H. Lai, and C.-C. Chou, *Ferroelectrics* **383**, 89 (2009).
- ¹⁴⁰B.-H. Liou, C.-C. Yu, and C.-C. Chou, *Ferroelectrics* **357**, 228 (2007).
- ¹⁴¹T. B. Daunis, K. A. Schroder, and J. W. Hsu, *npj Flexible Electron.* **4**, 1 (2020).
- ¹⁴²N. M. Twyman, K. Tetzner, T. D. Anthopoulos, D. J. Payne, and A. Regoutz, *Appl. Surf. Sci.* **479**, 974 (2019).
- ¹⁴³M. Benwadih, R. Coppard, K. Bonrad, A. Klyszcz, and D. Vuillaume, *ACS Appl. Mater. Interfaces* **8**, 34513 (2016).
- ¹⁴⁴S. Ding, J. Jiu, Y. Gao, Y. Tian, T. Araki, T. Sugahara, S. Nagao, M. Nogi, H. Koga, and K. Suganuma, *ACS Appl. Mater. Interfaces* **8**, 6190 (2016).
- ¹⁴⁵C. Glynn and C. O'Dwyer, *Adv. Mater. Interfaces* **4**, 1600610 (2017).
- ¹⁴⁶Y. Yao, A. B. Naden, F. Zhang, D. Edwards, P. Joshi, B. J. Rodriguez, A. Kumar, and N. Bassiri-Gharb, *J. Eur. Ceram. Soc.* **40**, 5369 (2020).
- ¹⁴⁷J. Ouyang, D. Cormier, and D. A. Borkholder, *ACS Appl. Energy Mater.* **2**, 338 (2018).
- ¹⁴⁸Z. Wang and J. Ouyang, *Nanostructures in Ferroelectric Films for Energy Applications* (Elsevier, 2019), Vol. 203.
- ¹⁴⁹A. Bhaskar, H. Chang, T. Chang, and S. Cheng, *Nanotechnology* **18**, 395704 (2007).
- ¹⁵⁰A. Bhaskar, T.-H. Chang, H.-Y. Chang, and S.-Y. Cheng, *Appl. Surf. Sci.* **255**, 3795 (2009).
- ¹⁵¹Z. Wang, Z. Cao, Y. Otsuka, N. Yoshikawa, H. Kokawa, and S. Taniguchi, *Appl. Phys. Lett.* **92**, 222905 (2008).
- ¹⁵²J. Ma, J. Diehl, E. Johnson, K. Martin, N. Miskovsky, C. Smith, G. Weisel, B. Weiss, and D. Zimmerman, *J. Appl. Phys.* **101**, 074906 (2007).
- ¹⁵³J. D. Katz, *Annu. Rev. Mater. Sci.* **22**, 153 (1992).
- ¹⁵⁴D. E. Clark, W. R. Tinga, and J. R. Laia, in *Microwaves: Theory and Application in Materials Processing II: Symposium: 95th Annual Meeting* (American Ceramic Society, 1993).
- ¹⁵⁵S. Singh, D. Gupta, V. Jain, and A. K. Sharma, *Mater. Manuf. Processes* **30**(1), 1–29 (2015).
- ¹⁵⁶V. G. Karayannis, paper presented at the 20th Innovative Manufacturing Engineering and Energy Conference (IManEE, 2016).
- ¹⁵⁷C. Saliel and A. K. Datta, *Advances in Heat Transfer* (Elsevier, 1999), Vol. 33.
- ¹⁵⁸D. E. Clark, D. C. Folz, and J. K. West, *Mater. Sci. Eng. A* **287**, 153 (2000).
- ¹⁵⁹S. Horikoshi, R. F. Schiffmann, J. Fukushima, and N. Serpone, *Microwave Chemical and Materials Processing* (Springer, 2018).
- ¹⁶⁰R. R. Mishra and A. K. Sharma, *Compos. Part A: Appl. Sci. Manuf.* **81**, 78 (2016).
- ¹⁶¹S. Das, A. K. Mukhopadhyay, S. Datta, and D. Basu, *Bull. Mater. Sci.* **32**, 1 (2009).
- ¹⁶²Y. Chen, Z. Wang, T. Yang, and Z. Zhang, *Acta Mater.* **71**, 1 (2014).
- ¹⁶³Z. Huang, Q. Zhang, and R. Whatmore, *J. Mater. Sci. Lett.* **17**, 1157 (1998).
- ¹⁶⁴Z. Huang, Q. Zhang, and R. Whatmore, *J. Appl. Phys.* **86**, 1662 (1999).
- ¹⁶⁵S. Rhee, T. R. Shrout, G. Link, and M. Thumm, *J. Ceram. Soc. Jpn.* **111**, 312 (2003).
- ¹⁶⁶K. H. Kim, K. M. Cho, D. W. Kim, S. J. Kim, J. Choi, S. J. Bae, S. Park, and H.-T. Jung, *ACS Appl. Mater. Interfaces* **8**, 5556 (2016).
- ¹⁶⁷D. E. Clark, F. D. Gac, and W. H. Sutton, *Microwaves: Theory and Application in Materials Processing* (American Ceramic Society, 1991).
- ¹⁶⁸A. Bhaskar, T. Chang, H. Chang, and S. Cheng, *Thin Solid Films* **515**, 2891 (2007).
- ¹⁶⁹Z. Wang, H. Kokawa, H. Takizawa, M. Ichiki, and R. Maeda, *Appl. Phys. Lett.* **86**, 212903 (2005).
- ¹⁷⁰Z. Wang, Y. Otsuka, Z. Cao, M. Zhu, N. Yoshikawa, and H. Kokawa, paper presented at the Smart Materials V (2008).
- ¹⁷¹Z. Cao, Z. Wang, N. Yoshikawa, and S. Taniguchi, *J. Phys. D Appl. Phys.* **41**, 092003 (2008).
- ¹⁷²M. Escote, F. Pontes, E. Leite, E. Longo, R. Jardim, and P. Pizani, *J. Appl. Phys.* **96**, 2186 (2004).
- ¹⁷³X. Zhang, X. Meng, J. Sun, T. Lin, and J. Chu, *Appl. Phys. Lett.* **86**, 252902 (2005).
- ¹⁷⁴W.-G. Kim, Y. J. Tak, B. Du Ahn, T. S. Jung, K.-B. Chung, and H. J. Kim, *Sci. Rep.* **6**, 23039 (2016).
- ¹⁷⁵Y. J. Kim, S. M. Kim, S. Heo, H. Lee, H. I. Lee, K. E. Chang, and B. H. Lee, *Nanotechnology* **29**, 055202 (2018).
- ¹⁷⁶F. Ye and K. Lu, *Phys. Rev. B* **60**, 7018 (1999).
- ¹⁷⁷Y. S. Rim, W. H. Jeong, D. L. Kim, H. S. Lim, K. M. Kim, and H. J. Kim, *J. Mater. Chem.* **22**, 12491 (2012).
- ¹⁷⁸X. Zhang, X. Meng, J. Sun, T. Lin, J. Ma, J. Chu, D. Kwon, and B. G. Kim, *J. Cryst. Growth* **310**, 783 (2008).
- ¹⁷⁹X. Zhang, X. Meng, J. Sun, T. Lin, J. Ma, J. Chu, N. Wang, and J. Dho, *J. Mater. Res.* **23**, 2846 (2008).
- ¹⁸⁰D. Wang, J. Ou-Yang, W. Guo, X. Yang, and B. Zhu, *Ceram. Int.* **43**, 9573 (2017).
- ¹⁸¹Z. Wei, K. Yamashita, and M. Okuyama, *Jpn J. Appl. Phys.* **40**, 5539 (2001).
- ¹⁸²T. Morita, *Materials* **3**, 5236 (2010).

- ¹⁸³G.-H. Feng and K.-Y. Lee, *R. Soc. Open Sci.* **4**, 171363 (2017).
- ¹⁸⁴B. Liu and H. C. Zeng, *J. Am. Chem. Soc.* **125**, 4430 (2003).
- ¹⁸⁵S. Feng and R. Xu, *Acc. Chem. Res.* **34**, 239 (2001).
- ¹⁸⁶A. Rabenau, *Angew. Chem. Int. Ed.* **24**, 1026 (1985).
- ¹⁸⁷T. Morita, T. Kanda, Y. Yamagata, M. Kurosawa, and T. Higuchi, *Jpn. J. Appl. Phys.* **36**, 2998 (1997).
- ¹⁸⁸K. Shimomura, T. Tsurumi, Y. Ohba, and M. Daimon, *Jpn. J. Appl. Phys.* **30**, 2174 (1991).
- ¹⁸⁹T. Morita, Y. Wagatsuma, Y. Cho, H. Morioka, H. Funakubo, and N. Setter, *Appl. Phys. Lett.* **84**, 5094 (2004).
- ¹⁹⁰Y. Seto, N. Kawashima, M. K. Kurosawa, and S. Takeuchi, *Jpn. J. Appl. Phys.* **47**, 3871 (2008).
- ¹⁹¹S. H. Kim and S. Komarneni, *Ceram. Int.* **37**, 1101 (2011).
- ¹⁹²T. Abe, S. Ozeki, M. K. Kurosawa, and S. Takeuchi, *Jpn. J. Appl. Phys.* **54**, 07HB06 (2015).
- ¹⁹³M. Kosec, B. Malic, and M. Mandeljc, *Mater. Sci. Sem. Proc.* **5**, 97 (2003).
- ¹⁹⁴S. L. Moffitt, K. L. Stallings, A. F. Falduto, W. Lee, D. B. Buchholz, B. Wang, Q. Ma, R. P. Chang, T. J. Marks, and M. J. Bedzyk, *ACS Appl. Electron. Mater.* **1**, 548 (2019).
- ¹⁹⁵L. Song, T. Schenk, E. Defay, and S. Glinsek, *Mater. Adv.* **2**, 700 (2021).
- ¹⁹⁶M.-G. Kim, M. G. Kanatzidis, A. Facchetti, and T. J. Marks, *Nat. Mater.* **10**, 382 (2011).
- ¹⁹⁷J. W. Hennek, J. Smith, A. Yan, M.-G. Kim, W. Zhao, V. P. Dravid, A. Facchetti, and T. J. Marks, *J. Am. Chem. Soc.* **135**, 10729 (2013).
- ¹⁹⁸X. Yu, J. Smith, N. Zhou, L. Zeng, P. Guo, Y. Xia, A. Alvarez, S. Aghion, H. Lin, and J. Yu, *Proc. Natl. Acad. Sci.* **112**, 3217 (2015).
- ¹⁹⁹F.-t. Li, J. Ran, M. Jaroniec, and S. Z. Qiao, *Nanoscale* **7**, 17590 (2015).
- ²⁰⁰J. W. Hennek, M.-G. Kim, M. G. Kanatzidis, A. Facchetti, and T. J. Marks, *J. Am. Chem. Soc.* **134**, 9593 (2012).
- ²⁰¹A. Liu, H. Zhu, Z. Guo, Y. Meng, G. Liu, E. Fortunato, R. Martins, and F. Shan, *Adv. Mater.* **29**, 1701599 (2017).
- ²⁰²J. C. Toniolo, A. Takimi, and C. P. Bergmann, *Mater. Res. Bull.* **45**, 672 (2010).
- ²⁰³A. Varma, A. S. Mukasyan, A. S. Rogachev, and K. V. Manukyan, *Chem. Rev.* **116**, 14493 (2016).
- ²⁰⁴P. T. Tue, T. Shimoda, and Y. Takamura, *APL Mater.* **8**, 021112 (2020).
- ²⁰⁵B. Wang, M. J. Leonardi, W. Huang, Y. Chen, L. Zeng, B. J. Eckstein, T. J. Marks, and A. Facchetti, *Adv. Electron. Mater.* **5**, 1900540 (2019).
- ²⁰⁶Y. Chen, B. Wang, W. Huang, X. Zhang, G. Wang, M. J. Leonardi, Y. Huang, Z. Lu, T. J. Marks, and A. Facchetti, *Chem. Mater.* **30**, 3323 (2018).
- ²⁰⁷S. Jain, K. Adiga, and V. P. Verneker, *Combust. Flame* **40**, 113 (1981).
- ²⁰⁸E. Carlos, R. Martins, E. M. C. Fortunato, and R. Branquinho, *Chem. A Eur. J.* **26**, 9099 (2020).
- ²⁰⁹S. T. Aruna and A. S. Mukasyan, *Curr. Opin. Solid State Mater. Sci.* **12**, 44 (2008).
- ²¹⁰K. C. Patil, S. T. Aruna, and T. Mimani, *Curr. Opin. Solid State Mater. Sci.* **6**(6), 507–512 (2002).
- ²¹¹Y. H. Kang, S. Jeong, J. M. Ko, J.-Y. Lee, Y. Choi, C. Lee, and S. Y. Cho, *J. Mater. Chem. C* **2**, 4247 (2014).
- ²¹²K.-Y. Li, N.-H. Tai, and I.-N. Lin, *Integr. Ferroelectr.* **69**, 135 (2005).
- ²¹³Y.-H. Chu, S.-J. Lin, K.-S. Liu, and I.-N. Lin, *Integr. Ferroelectr.* **57**, 1233 (2003).
- ²¹⁴T. Liu, M. Wallace, S. Trolier-McKinstry, and T. N. Jackson, *J. Appl. Phys.* **122**, 164103 (2017).
- ²¹⁵K. Morimoto, I. Kanno, K. Wasa, and H. Kotera, *Sens. Actuators A Phys.* **163**, 428 (2010).
- ²¹⁶Y. Qi, N. T. Jafferis, K. Lyons, Jr., C. M. Lee, H. Ahmad, and M. C. McAlpine, *Nano Lett.* **10**, 524 (2010).
- ²¹⁷G. L. Rhun, C. Dieppedale, B. Wagué, C. Querne, G. Enyedi, P. Perreau, P. Montméat, C. Licitra, and S. Fanget, paper presented at the 2019 20th International Conference on Solid-State Sensors, Actuators and Microsystems & Eurosensors XXXIII (TRANSDUCERS & EUROSENSORS XXXIII) (2019).
- ²¹⁸R. Delmdahl, R. Pätzelt, and J. Brune, *Phys. Procedia* **41**, 241 (2013).
- ²¹⁹L. Tsakalacos and T. Sands, *Appl. Phys. Lett.* **76**, 227 (2000).
- ²²⁰A. C. Fischer, F. Forsberg, M. Lapisa, S. J. Bleiker, G. Stemme, N. Roxhed, and F. Niklaus, *Microsyst. Nanoeng.* **1**, 15005 (2015).
- ²²¹J. W. Judy, *Smart Mater. Struct.* **10**, 1115 (2001).
- ²²²A. Witvrouw, paper presented at the 2006 IEEE/ACM International Conference on Computer Aided Design (2006).
- ²²³M. Kousuke, M. Moriyama, M. Esashi, and S. Tanaka, paper presented at the 2012 IEEE 25th International Conference on Micro Electro Mechanical Systems (MEMS) (2012).
- ²²⁴X. Y. Wang, C. Y. Lee, C. J. Peng, P. Y. Chen, and P. Z. Zhang, *Sens. Actuators A Phys.* **143**, 469 (2008).
- ²²⁵C. Dagdeviren, Y. Su, P. Joe, R. Yona, Y. Liu, Y.-S. Kim, Y. Huang, A. R. Damadoran, J. Xia, and L. W. Martin, *Nat. Commun.* **5**(1), 4496 (2014).
- ²²⁶Y. Liu, L. Zhao, L. Wang, H. Zheng, D. Li, R. Avila, K. W. Lai, Z. Wang, Z. Xie, and Y. Zi, *Adv. Mater. Technol.* **4**, 1900744 (2019).

Chapter 4

Low-temperature flash lamp process of PZT films

After thoroughly reviewing the existing solutions for low-temperature crystallization of PZT films in the previous chapter, it is evident that the current low-temperature processes for PZT thin films either require long processing times or involve complicated procedures. While a low crystallization temperature of PZT films has been often successfully achieved, the attainment of macroscopic piezoelectric properties has been barely reported.

In this chapter, we developed a flash-lamp process for the direct and low-temperature growth of PZT films on fused silica and SCHOTT AF32 glass in a few seconds. The resulting PZT films exhibited excellent piezoelectric properties, with an $e_{33,f}$ value of -5 C m^{-2} . These films were used to fabricate a haptic device, which met the required specifications for surface rendering applications. This work has been published as a preprint titled “Low-temperature growth of PZT piezoceramic films on glass” ,[\[121\]](#) which has been attached in this chapter.

Note that my colleague, Dr. Juliette Cardoletti, accomplished the growth of ferroelectric PZT films on soda lime glass, which was also included in the submitted paper[\[121\]](#) **but not in this thesis.**

Authors contributions: This research constitutes a collaborative effort, wherein my role encompassed the execution of experiments pertaining to the growth of PZT films on fused silica glass, as well as the development of a haptic device on AF32 glass, along with drafting this manuscript. Dr. Sebastjan Glinsek who also spearheaded the team, provided critical feedback on the experiments and revision on the manuscript. My supervisor, Dr. Emmanuel Defay, provided critical suggestions to the writing. My colleague, Dr. Juliette

Cardoletti, accomplished the growth of ferroelectric PZT films on soda lime glass, which was included in the submitted paper but not in this thesis, and she also performed data visualization and provided suggestions in writing. My colleague, Alfredo Blazquez Martinez, provided valuable suggestions on experiments and shared his knowledge on flash lamp annealing of ferroelectric films, and we worked together to investigate this process. Alfredo Blazquez Martinez and Dr. Stephanie Girod contributed to the fabrication of the interdigitated electrode (IDE) designs and aided in the lithography process. The transmission electron microscopy (TEM) analysis was conducted with the assistance of our colleagues in Slovenia (Prof. Andreja Bencan and Dr. Brigita Kmet).

4.1 Introduction, experimental results and discussions

Introduction of the research background, experimental methods and results as well as outlook have been provided in attached paper[\[121\]](#).

Crystallization of piezoceramic films on glass via flash lamp annealing

Longfei Song,^{a,b,1} Juliette Cardoletti,^{a,1} Alfredo Blázquez Martínez,^{a,b} Andreja Bencan,^c
Brigita Kmet,^c Stéphanie Girod,^a Emmanuel Defay,^a Sebastjan Glinsek^{a,*}

^a Materials Research and Technology Department, Luxembourg Institute of Science and
Technology, rue du Brill 41, L-4422 Belvaux, Luxembourg

^b University of Luxembourg, 41 rue du Brill, L-4422 Belvaux, Luxembourg

^c Electronic Ceramics Department, Jožef Stefan Institute, Jamova cesta 39, 1000 Ljubljana,
Slovenia

¹ These authors contributed equally: L. S. and J. C.

*Corresponding author: sebastjan.glinsek@list.lu

Abstract

Integration of thin-film oxide piezoelectrics on glass is imperative for the next generation of transparent electronics to attain sensing and actuating functions. However, their crystallization temperature (above 650 °C) is incompatible with most glasses. We developed a flash lamp process for growth of piezoelectric lead zirconate titanate films. The process enables crystallization on various types of glasses in a few seconds only. Functional properties of these films are comparable to the films processed with standard rapid thermal annealing at 700 °C. A surface haptic device was fabricated with a 1 μm-thick film (piezoelectric $e_{33,f}$ of -5 C m^{-2}). Its ultrasonic surface deflection reached 1.5 μm at 60 V, sufficient for its use in surface rendering applications. This flash lamp annealing process is compatible with large glass sheets and roll-to-roll processing and has the potential to significantly expand the applications of piezoelectric devices on glass.

1. Introduction

An important trend in next-generation large-scale electronics is the integration of functional films on glass wafers for smart windows and display screens. Among the available materials for sensors and actuators, piezoelectric oxide thin films are outstanding because of their superior electromechanical response compared to nitrides and polymers¹⁻⁵. The key for their successful integration in microelectromechanical systems (MEMS) has been efficient processing, which allows for the preparation of high-quality films in a controllable and reproducible manner. Chemical solution deposition (CSD) is among the most popular fabrication methods due to its low cost, flexibility in chemical composition and compatibility with large-scale microelectronics^{6,7}. The method is continuously evolving and emerging digital printing and roll-to-roll processing technologies will enable high-speed, high-throughput and large-scale additive manufacturing^{5,8}.

In CSD processing the as-deposited amorphous phase is transformed into a crystalline perovskite piezoelectric phase via high-temperature annealing. The crystallisation process traditionally relies on the use of isothermal heating in tube, box, or rapid thermal annealing (RTA) furnaces (see Fig. 1a)⁹. The typical processing temperatures are above 650 °C and the total annealing time (including heating and cooling) is in the order of tens of minutes. As the strain point - the maximum temperature at which glass can be used without experiencing creep - of most commercial glasses lies below 600 °C, the development of low-temperature processing is required^{10,11}.

Efforts have been dedicated to lowering processing temperature, including by photochemical processing^{12,13}, annealing under high-pressure of O₂/O₃¹⁴, combustion synthesis¹⁵, and laser annealing^{16,17}. While the global temperature has been lowered, the price to pay is either long annealing times (often several hours) or the use of reactive atmosphere, which limit the use of

these processes in large-scale and high-throughput production. Although laser annealing allows for the fast crystallization of films, the small laser spot size (typically in the μm^2 - mm^2 range) imposes the need for raster scanning of the laser beam, leading to inhomogeneities in the films ¹⁸. The indirect integration on glass via transfer process has been successful ¹⁹, however, it significantly complicates the process and adds processing steps.

Flash lamp annealing (FLA), i.e., annealing through the absorption of sub-millisecond light pulses with broad spectrum and strong intensity, enables selective annealing of the films on temperature-sensitive substrates ²⁰ and is schematically compared to box-furnace annealing in Fig. 1b. FLA can be performed in ambient atmosphere in a few seconds and the irradiated areas can reach several hundreds of cm^2 . These features are compatible with high-throughput, low-cost and large-scale roll-to-roll production ²¹. FLA has been successfully used for processing different functional thin films, such as conductors (e.g., indium tin oxide, metal nanoparticle films) ^{22,23}, semiconductors (e.g., indium zinc oxide) ^{24,25}, dielectrics (e.g., alumina, zirconia) ^{26,27}, hybrid perovskites for absorbers in solar cells ²⁸ and light-emitting diodes ²⁹. Yao et al. induced nano-crystallization of piezoelectric lead zirconate titanate on glass and polyimide substrates, however, macroscopic electromechanical properties, which are imperative for sensor and actuator applications, were not demonstrated ³⁰.

Inspired by the above results and guided by finite element modelling (FEM), we developed a process that enables macroscopic crystallization of solution processed $\text{PbZr}_{0.53}\text{Ti}_{0.47}\text{O}_3$ (PZT) films on a wide variety of glasses. First, we demonstrate a fast process (several seconds per crystallization) on 1 μm -thick PZT thin films on fused silica, resulting in remanent polarization P_r , dielectric permittivity ϵ_r , dielectric losses $\tan\delta$ and piezoelectric coefficient $e_{33, f}$ values of 12 $\mu\text{C cm}^{-2}$, 450, 5 %, and -5 C m^{-2} , respectively. A surface haptic device was realized on alumina-borosilicate glass (AF32, Schott), i.e., a standard substrate for semiconductor and MEMS industries. The device is based on a 1 μm -thick PZT film and its

ultrasonic-range surface deflection reaches 1.5 μm at 60 V, which fulfils requirement of a deflection of 1 μm for its commercialization in texture rendering operation ³¹. Finally, we demonstrate the universality of FLA process by direct growth of PZT films on soda-lime, i.e., the most widespread type of glass.

2. Results

2.1. Processes Design and Finite Element Modelling

Results of the finite element modelling are presented in Fig. 1c and 1d, where a 170 nm PZT/fused silica glass configuration was modelled. The absorbance of an amorphous PZT layer (~28.5 %) was estimated with a bolometer placed below the sample, considering that glass is mainly transparent in the ~300-1000 nm wavelength range of the Xe lamp utilised in this work (see Supplementary Section 1 for further information). The modelling of a 130 μs pulse with an energy density of 3 J cm^{-2} , indicates that the temperature at the top surface of PZT should reach 600 $^{\circ}\text{C}$, which is sufficiently high to crystallize PZT into the piezoelectric perovskite phase ⁶. Through the glass thickness, the temperature drops significantly as the process is non-adiabatic and performed in ambient environment. This maintains the interface between the film and the substrate at relatively low temperature, i.e., the temperature exceeds 400 $^{\circ}\text{C}$ for only 50 μs per pulse (see the purple line in Fig. 1c). 4 μm below this interface the temperature remains below 350 $^{\circ}\text{C}$. To provide enough energy and time for complete crystallization to occur, multi-pulse annealing is necessary. 30 pulses at 3.5 Hz enable the temperature of PZT to reach 800 $^{\circ}\text{C}$ while the bulk of the glass substrates remains below 400 $^{\circ}\text{C}$ (Fig. 1d).

2.2. Growth, Phase Composition and Microstructure of the Films

The films were deposited through a standard CSD process using 2-methoxyethanol as solvent, lead acetate and transition metals alkoxides precursors⁷. The solutions were spin coated, dried at 130 °C and pyrolyzed at 350 °C on hot plates. The deposition-drying-pyrolysis process was repeated four times to achieve a thickness of 170 nm. The crystallization was done with flash lamp annealing. Thick films were obtained by repeating the whole process several times.

Films on fused silica were investigated first and their phase composition was analysed as a function of the number of FLA light pulses. Pulsing was performed with the same conditions as described in the previous section and in Supplementary Section 2. After 10 pulses, {100} and {110} reflections of the perovskite phase appear in the grazing incidence X-ray diffraction pattern (Fig. 2a) of 170 nm-thick films. Reflection of the non-piezoelectric pyrochlore phase (a small peak at $2\theta = 29^\circ$), which is kinetically stabilized during annealing³², disappears when the number of pulses is increased to 30. When the number of pulses reaches 100, the intensity of perovskite reflections increases indicating enhanced crystallinity. The phase evolution agrees with the temperature evolution predicted with FEM during multi-pulse annealing (Fig. 1d), i.e., gradual increase of temperature stabilizes the perovskite phase. The standard θ - 2θ XRD pattern of 1 μm -thick PZT on fused silica is shown in Supplementary Fig. S2, and only perovskite peaks are present. In contrast, the perovskite phase does not form in the film annealed at 700 °C in RTA (Supplementary Fig. S4)³³. To the best of our knowledge, without the use of a nucleation layer (or bottom electrode), successful crystallization of solution-processed PZT films on amorphous substrates has not yet been reported, showing that the developed FLA process is even excelling a typical layer-by-layer deposition of solution-processed films in standard furnaces. It also enables the growth of films in a controllable and repeatable manner.

Transmittance of the 170 nm-thick films (50 pulses) at a wavelength of 550 nm is 64%, as shown in Fig. 2b, together with its visual appearance. Transparency is preserved in the 1 μm film on 2'' glass wafer (inset of Supplementary Fig. S5).

A cross-sectional scanning transmission electron microscope analysis was also performed. A dark field STEM image (Fig. 2c) reveals relatively porous granular microstructure, which agrees with the SEM micrograph of the 1 μm thick film shown in Supplementary Fig. S6. The high-resolution STEM image, with the corresponding Fast Fourier Transform (FFT) (inset in Fig. 2d), shows a (110) plane reflection with an interplanar spacing of 2.8 \AA , which is further demonstrated in the zoomed-in STEM image (inset in Fig. 2d). This interplanar spacing value is in good agreement with the perovskite phase of PZT and is additional confirmation of its presence in the film. While the film is chemically inhomogeneous (Supplementary Fig. S7) the energy dispersive X-ray spectroscopy 2D map (Fig. 2c) shows no diffusion of Pb into the substrate (as commonly observed in conventionally processed films)³⁴. It is also observed that there was partial diffusion of silicon into the PZT film, at a depth of approximately 100 nm (see Supplementary Fig. S8 for more details). However, this diffusion did not result in the formation of secondary phase that would compromise the ferroelectric and piezoelectric properties of the PZT film, as confirmed earlier in GIXRD patterns and later by electrical measurements.

2.3. Electromechanical Characterization

This section is focused on the films prepared with 50 pulses, as they show optimal ferroelectric response. Electrical properties were measured in interdigitated geometry employing surface Pt electrodes. Polarization versus electric field $P(E)$ loops are initially pinched (Supplementary Fig. S9). This is most likely caused by the presence of charged

defects (such as oxygen vacancies) in the films, which at low electric fields pin ferroelectric domain walls³⁵. Electric-field cycling (wake-up) enables their redistribution, which unpins the polarization. Indeed, the pinched hysteresis opens during cycling (Supplementary Fig. S9). Different number of wake-up cycles in different films could be due to different concentration of defects in the films and/or their different pinning energy.

Ferroelectric and piezoelectric properties are shown in Fig. 3 and were obtained on a 1 μm -thick film on fused silica glass after 10^4 wake-up cycles. The maximum polarization P_{max} and remanent polarization P_r are $25 \mu\text{C cm}^{-2}$ and $12 \mu\text{C cm}^{-2}$, respectively. Its coercive field E_c is 68 kV cm^{-1} . Two sharp peaks, which are linked to domain switching, are observed in the current loop (Fig. 3a). Similar results were obtained on 170 nm- and 500 nm-thick films (10 and $11 \mu\text{C cm}^{-2}$ in P_r , respectively, see Supplementary Fig. S9 and S10). The displacement of a cantilever structure shows a typical butterfly loop (Fig. 3b). At 100 V the vertical displacement at the free end of the cantilever is 700 nm, corresponding to a piezoelectric coefficient $e_{33,f}$ of -5 C m^{-2} ³⁶.

Butterfly loops were also observed in electric-field dependence of relative permittivity ϵ_r and dielectric losses $\tan\delta$ of the 1 μm -thick film (Fig. 3c). Their zero-field values are 450 and 5%, respectively. These quantities were also measured as functions of the small signal frequency (Fig. 3d). While permittivity slightly decreases with increasing frequency, losses remain practically constant, which are typical signatures of perovskite ferroelectric films³⁷. To have better overview of the results, a table with ferroelectric, piezoelectric and optical properties of the 170 nm, 500 nm and 1 μm -thick films on fused silica substrates is provided in Table S1 of the Supplementary Information.

2.4. Device Application

To demonstrate suitability of the flash lamp annealing process for piezoelectric applications, we fabricated and characterized a surface haptic device³⁸. AF32 glass, which is utilized in semiconductor and MEMS industry, was used³⁹. A 1 μm -thick film was employed to increase the force of the actuator during its operation (see Supplementary Section 3.2.1). Phase composition and electrical properties of the film are comparable to the films on fused silica, as shown in Supplementary Section 3.

As schematically shown in Fig. 4a, the dimensions of the fabricated haptic device are $15.4 \times 3 \text{ mm}^2$. The thickness of the glass and film are 0.3 mm and 1 μm , respectively. Two actuating areas were created by fabricating 100 nm-thick Pt IDE electrodes with a gap of 3 μm between the fingers. The distance between these two actuators is 8.4 mm. More details about the haptic device fabrication and measurements are described in the Methods and the Supplementary Section 3.2. The out-of-plane displacement at one of the resonance antinodes is shown as a function of frequency in Fig. 4b. At 40.2 kHz the device reveals a peak in deflection, which corresponds to its mechanical resonance at anti-symmetric (A_0) Lamb mode. For further info on Lamb mode analysis see Supplementary Fig. S14 and Ref.⁴⁰. Its position is at the same value as predicted by finite element modelling, whose details are described in Supplementary Section 3.2.2.

The out-of-plane surface displacement in the x -direction (along the length of the device) is shown in Fig. 4c. It was measured with an excitation voltage varying from 20 to 50 V_{pp} at the resonance frequency of 40.2 kHz. Four nodes equally spaced along its length are observed, which is in line with the wave-shape obtained from the modelling (Supplementary Fig. S13). Fig. 4d shows a 2D displacement map of the haptic plate excited at 60 V_{pp} (30 V_{AC} + 30 V_{DC}) at the resonance. The device exhibits a maximum peak-to-peak deflection of 1.5 μm , beyond the specification of 1 μm , which can be detected by a human finger³¹. It also confirms a neat

stationary Lamb wave. $e_{33,f}$ can be extracted by matching experimental deflection value with modelling ⁴¹ and the obtained value is -4.5 C m^{-2} , which is well in-line with the value obtained via cantilever measurements on fused silica (Fig. 3b).

Performance of the device is compared to the previously reported piezoelectric haptic devices on glass substrates based on spin-coated ³³ and inkjet-printed ⁵ PZT films with interdigitated geometry in Table S2 in Supplementary. Present device consumes 35 mW, which is comparable to the other two devices. Note also that 60 V can be applied to handheld devices by using either a cascade of several application-specific integrated circuits (ASICs) that can increase the output voltage from 3.3 to 100 V or by using an inductor L to make an LC resonator at the resonant frequency ³³.

2.5. Flash Lamp Annealing for Piezoelectric Films on Soda Lime Glass

To generalize the approach, we also used this flash lamp process to crystallize PZT films on soda-lime glass, which can only sustain temperatures below 400 °C. Because of the lower thermal conductivity of soda lime ($1.0 \text{ W m}^{-1} \text{ K}^{-1}$) compared to fused silica ($1.4 \text{ W m}^{-1} \text{ K}^{-1}$), the rate of heat transfer is slower, resulting in a higher temperature at the interface between the film and glass. A two-step process, resembling nucleation and growth in CSD process ⁶, was developed. This process is described in Supplementary Information Section 4, where also more details on phase composition and electrical properties are described (Fig. S16 and Fig. S17). The films on soda lime glass also crystallize in the perovskite phase and have P_r of $8 \mu\text{C cm}^{-2}$, ϵ_r of 400, and $\tan\delta$ of 2 %, respectively.

3. Discussion

Macroscopic ferroelectric and piezoelectric properties of the films crystallized during flash lamp annealing are demonstrated in this work. The previously unreported process of nucleation and grain growth of the perovskite phase has been enabled by the unique tool design, which enables creation of high-power pulses (above 20 kW cm^{-2}) with high repetition rates (3 Hz)^{30,42–44}. Detailed comparison with the literature can be found in Supplementary Section 5.

To better understand the effectiveness of flash lamp annealing process we, conducted a comparison of the electrical properties between $1 \mu\text{m}$ -thick flash lamp-processed films and RTA-processed films on fused silica glass³³. Table 1 displays the corresponding electrical parameters. It is worth noting that, in the RTA process, a hafnia buffer layer was applied to impede Pb diffusion, and that lead titanate oxide (PTO) nucleation was implemented to facilitate growth along $\{100\}$ and therefore enhance the piezoelectric response⁴⁵. Despite the doubling of the ϵ_r value enabled by PTO nucleation, the ferroelectric and piezoelectric properties of the material remain relatively comparable.

It is also interesting to compare flash lamp process with other low-temperature processes of chemical solution-deposited PZT films. While reduced processing temperature has often been achieved, macroscopic piezoelectric properties of such films are seldomly reported, as demonstrated in a recent review paper⁹. The highest value reported so far in low-temperature films is $d_{33,f} = 49 \text{ pm V}^{-1}$ in laser-annealed (LA) PZT films on platinised silicon¹⁷. For comparison, this $d_{33,f}$ value was translated into $e_{33,f}$ (-3.9 C m^{-2}) by taking the typical value of Young's modulus (80 GPa) of PZT^{46,47}, which is slightly lower than those of flash lamp annealed films.

Given that the electrical properties are comparable, it is crucial to assess the processes. RTA necessitates a buffer and a processing time of tens of minutes and is incompatible with low-temperature glass. Laser annealing, on the other hand, requires non-transparent bottom electrodes (such as Pt or LaNiO_3) for nucleation, without which films cannot crystallize^{16,17}. The small laser spot size also requires raster scanning of the laser beam, leading to inhomogeneities in the films. These limitations hinder process efficiency, resulting in reduced productivity. In contrast, the flash lamp process offers direct and rapid growth in an ambient environment without relying on any buffer or nucleation, while also being highly compatible with roll-to-roll production thanks to its large irradiation area. These unique advantages make it a high-output process.

The previous comparison and the results presented above provide evidence that the flash lamp process facilitates direct growth of piezoelectric films on a variety of glass substrates, which exhibit electromechanical properties meeting the requirements for piezoelectric applications, as demonstrated by the successful realisation of haptic rendering device. A distinctive advantage of the flash lamp process is its high compatibility with digital inkjet printing and large-scale roll-to-roll manufacturing, which puts it ahead of other low-temperature processes. Through the interaction of light with material, the process allows for growth of perovskite films without nucleation layers. Compared to aerosol-based deposition technique⁴⁸⁻⁵¹, the FLA-based process enables in-situ crystallization of perovskite phase and eliminates the need for post-annealing step to improve the properties. All these points are strong assets in favour of perovskite piezoelectric films for future transparent and flexible electronics.

4. Methods

4.1. Processing and deposition of PZT solution

$\text{Pb}(\text{Zr}_{0.53}\text{Ti}_{0.47})\text{O}_3$ solution was prepared via the standard 2-methoxyethanol (99.8 %, Sigma-Aldrich) route using freeze-dried lead(II) acetate trihydrate (99.99 %, Sigma-Aldrich), titanium(IV) isopropoxide (97 %, Sigma-Aldrich) and zirconium(IV) propoxide (70 % in propanol, Sigma-Aldrich) as starting compounds⁵². Concentration ($C_{\text{Zr}} + C_{\text{Ti}}$) was 0.3 M with a stoichiometry of metal cations $\text{Zr}:\text{Ti} = 0.53:0.47$, which corresponds to the morphotropic phase boundary composition with 10 mol.% Pb excess. For more details see Ref.⁵². The solutions were spin coated on glass substrates for 30 s at 3000 rpm with an acceleration of 500 rpm/s. Three types of glasses were used: fused silica (2'' and 0.5 mm-thick, SIEGERT Wafer, fused silica)⁵³, AF32 (2'' and 0.3 mm-thick, SCHOTT, AF32)³⁹ and soda lime (38x26x1 mm³, Marienfield, ref 1100020 (microscope slides) and 38x25x1 mm³, EpreDia, ref AB00000102E01MNZ10 (microscope slides))⁵⁴. Drying and pyrolysis were performed on hot plates for 2 min each at 130 °C and 350 °C, respectively. The deposition-drying-pyrolysis cycle was repeated four times to obtain 170 nm thick amorphous PZT films.

4.2. Flash lamp annealing

Crystallization of the amorphous films was performed with a flash lamp annealer (Pulseforge Invent, Novacentrix). The parameters to control the annealing process include energy density, pulse duration, and repetition rate. The respective values for a standard one-step process (fused silica and AF32 glasses) were 3 J cm⁻², 130 μs and 3.5 Hz. Note that the energy density was experimentally measured using a bolometer, and variation within 5 % in lamp energy density is observed in fast multipulse process due to the lamp stability. In a two-step process (soda lime glass), films were annealed for a few pulses at high energy density

followed by numerous pulses at lower energy density. This two-step process is described in more details in Supplementary Information Section 4.1.

4.3. Microstructural and optical characterization

Phase composition and orientation of the films were investigated with grazing incidence X-ray diffraction (GIXRD) and standard θ - 2θ XRD, which were performed on a D8 Discover diffractometer (Bruker) using Cu-K α radiation. The incidence angle of GIXRD was 0.5°. Both GIXRD and standard θ - 2θ XRD patterns were recorded in the 2θ -range from 20° to 60° with a step-size of 0.02°.

Samples for scanning transmission electron microscopy (STEM) analyses were prepared by grinding, dimpling and final Ar milling (Gatan PIPS Model 691, New York, NY, USA). STEM studies were carried out using a probe Cs-corrected Jeol ARM200 CF (Jeol, Tokyo, Japan) equipped with Centurio energy-dispersive X-ray spectroscopy system (EDS, Jeol, Tokyo, Japan), operated at 200kV.

Optical spectra were obtained using a UV/Vis spectrophotometer (Spectro L1050, PerkinElmer).

4.4. Electromechanical characterization

Interdigitated (IDE) Pt electrodes were deposited and patterned on top of the films with lift-off photolithography using direct laser writing (MLA, Heidelberg Instruments), as described in our previous work³³. Pt was chosen as it is the most mature electrode material for piezoelectric thin films. Two sizes of IDE electrodes were used. Finger width, length of digits facing each other, interdigital gap, and pairs of digits were 5 μ m (5 μ m), 1730 μ m (370 μ m),

3 μm (3 μm), and 615 (50), respectively for large (small) IDEs. 100 nm-thick Pt electrodes were sputtered with a MED 020 metallizer (BalTec).

Electrical characterization was performed using a TF Analyzer 2000 (aixACCT). The polarization was measured as a function of electric field $P(E)$ with a triangular waveform at 100 or 10 Hz. Bipolar fatigue cycling was performed at 1 kHz, with a triangular fatigue voltage of 100 V.

The converse piezoelectric response of 500 nm PZT film on fused silica glass (Fig. 3b) was measured with a thin-film sample holder unit (aixACCT) and an interferometer (SP120/2000, SIOS)⁵⁵. Cantilevers with dimensions of $25 \times 3.4 \text{ mm}^2$ were cut from the wafers using a wire saw. Geometry of the IDE capacitor was the same as for large IDE. The converse piezoelectric coefficient $e_{33,f}$ was extracted as described in Ref.³⁶. A Young's modulus of 73 GPa has been used for the fused silica substrate.

Relative permittivity ϵ_r and dielectric losses $\tan\delta$ of 1 μm -thick film were measured as functions of DC voltage with a probing AC signal of 0.5-1 V at 1 kHz. The IDE used for this measurement (Fig. 3c) has finger width of 10 μm , length of digits facing each other of 872 μm , interdigital gap of 10 μm , and 502 pairs of digits, respectively, corresponding to an effective area of 0.86 mm^2 . Capacitance C and $\tan\delta$ were measured as functions of frequency f with an Agilent E4990A impedance analyzer with an AC voltage of 1 V. Corresponding ϵ_r was calculated from capacitance. The IDE used for this measurement (Fig. 3d) has the respective parameters of 10 μm , 2340 μm , 10 μm and 51, respectively, corresponding to an effective area of 0.209 mm^2 .

4.5. Haptic device

The 1- μm -thick PZT film was prepared on AF32 glass, as described above. Based upon FEM, the IDE Pt electrodes had the overall dimension of $2050 \times 2340 \mu\text{m}^2$ and were distributed on the $15.4 \times 3 \text{ mm}^2$ device as schematically shown in Fig. 4a. Copper wires bonded using silver epoxy were used to connect voltage and ground electrode pads. The haptic device was placed on suspended flexible foam tape and was connected to a waveform generator (33210A Keysight) via an amplifier (WMA-300, Falco Systems). The out-of-plane displacement was recorded using an OFV-5000 Polytec laser doppler vibrometer. A computer-controlled x - y stage was used to move the haptic device for line scans and 2D mapping. The whole set-up was controlled with the vibrometer via a LabVIEW program, which have been also demonstrated in a previous paper³³. Note that the two actuators were connected in parallel, therefore, the voltage applied to each actuator is the same. Note also that all the measurements in Fig. 4 were done with a unipolar voltage.

Data Availability

The data that support the findings of this study are available from the corresponding author upon reasonable request.

References

1. Muralt, P. Recent progress in materials issues for piezoelectric MEMS. *J. Am. Ceram. Soc.* **91**, 1385–1396 (2008).
2. Defay, E. *Integration of ferroelectric and piezoelectric thin films.* (2011). doi:10.1002/9781118616635.
3. Gao, X. *et al.* Giant piezoelectric coefficients in relaxor piezoelectric ceramic PNN-PZT for vibration energy harvesting. *Adv. Funct. Mater.* **28**, 1706895 (2018).
4. Yeo, H. G. *et al.* Strongly (001) oriented bimorph PZT film on metal foils grown by rf-sputtering for wrist-worn piezoelectric energy harvesters. *Adv. Funct. Mater.* **28**, 1–9 (2018).
5. Glinsek, S. *et al.* Inkjet-printed piezoelectric thin films for transparent haptics. *Adv. Mater. Technol.* **7**, 2200147 (2022).
6. Bassiri-Gharb, N., Bastani, Y. & Bernal, A. Chemical solution growth of ferroelectric oxide thin films and nanostructures. *Chem. Soc. Rev.* **43**, 2125–2140 (2014).
7. Brennecka, G. L., Ihlefeld, J. F., Maria, J. P., Tuttle, B. A. & Clem, P. G. Processing technologies for high-permittivity thin films in capacitor applications. *J. Am. Ceram. Soc.* **93**, 3935–3954 (2010).
8. Yu, M. J. *et al.* Amorphous InGaZnO thin-film transistors compatible with roll-to-roll fabrication at room temperature. *IEEE Electron Device Lett.* **33**, 47–49 (2012).
9. Song, L., Glinsek, S. & Defay, E. Toward low-temperature processing of lead zirconate titanate thin films: Advances, strategies, and applications. *Appl. Phys. Rev.* **8**, 041315 (2021).

10. Park, J. W., Kang, B. H. & Kim, H. J. A review of low-temperature solution-processed metal oxide thin-film transistors for flexible electronics. *Adv. Funct. Mater.* **30**, 1904632 (2020).
11. Joe, D. J. *et al.* Laser-material interactions for flexible applications. *Adv. Mater.* **29**, 1606586 (2017).
12. Bretos, I. *et al.* Activated solutions enabling low-temperature processing of functional ferroelectric oxides for flexible electronics. *Adv. Mater.* **26**, 1405–1409 (2014).
13. Bretos, I., Jiménez, R., Ricote, J. & Calzada, M. L. Low-temperature crystallization of solution-derived metal oxide thin films assisted by chemical processes. *Chem. Soc. Rev.* **47**, 291–308 (2018).
14. Zhang, X. D. *et al.* Low-temperature preparation of sputter-deposited $\text{Pb}(\text{Zr}_{0.52}\text{Ti}_{0.48})\text{O}_3$ thin films through high oxygen-pressure annealing. *J. Cryst. Growth* **310**, 783–787 (2008).
15. Tue, P. T., Shimoda, T. & Takamura, Y. A facile solution-combustion-synthetic approach enabling low-temperature PZT thin-films. *APL Mater.* **8**, 21112 (2020).
16. Kang, M. G. *et al.* Direct growth of ferroelectric oxide thin films on polymers through laser-induced low-temperature liquid-phase crystallization. *Chem. Mater.* **32**, 6483–6493 (2020).
17. Fink, S., Lübber, J., Schneller, T., Vedder, C. & Böttger, U. Impact of the processing temperature on the laser-based crystallization of chemical solution deposited lead zirconate titanate thin films on short timescales. *J. Appl. Phys.* **131**, 125302 (2022).
18. Prucnal, S., Rebohle, L. & Skorupa, W. Doping by flash lamp annealing. *Mater. Sci. Semicond. Process.* **62**, 115–127 (2017).

19. Pavageau, F. *et al.* Highly transparent piezoelectric PZT membranes for transducer applications. *Sensors Actuators A Phys.* **346**, 113866 (2022).
20. Angmo, D., Larsen-Olsen, T. T., Jørgensen, M., Søndergaard, R. R. & Krebs, F. C. Roll-to roll inkjet printing and photonic sintering of electrodes for ITO free polymer solar cell modules and facile product integration. *Adv. Energy Mater.* **3**, 172–175 (2013).
21. Rebohle, L., Prucnal, S. & Reichel, D. *Flash Lamp Annealing: From Basics to Applications*. (Springer International Publishing, 2019). doi:10.1007/978-3-030-23299-3.
22. Gilshtein, E. *et al.* Inkjet-printed conductive ITO patterns for transparent security systems. *Adv. Mater. Technol.* **5**, 2000369 (2020).
23. Shin, J. H. *et al.* A flash-induced robust Cu electrode on glass substrates and its application for thin-film μ LEDs. *Adv. Mater.* **33**, 2007186 (2021).
24. Loganathan, K. *et al.* Rapid and up-scalable manufacturing of gigahertz nanogap diodes. *Nat. Commun.* **2022 131** **13**, 1–8 (2022).
25. Weidling, A. M., Turkani, V. S., Luo, B., Schroder, K. A. & Swisher, S. L. Photonic curing of solution-processed oxide semiconductors with efficient gate absorbers and minimal substrate heating for high-performance thin-film transistors. *ACS Omega* **6**, 17323–17334 (2021).
26. Yarali, E. *et al.* Low-voltage heterojunction metal oxide transistors via rapid photonic processing. *Adv. Electron. Mater.* **6**, 2000028 (2020).
27. Daunis, T. B., Schroder, K. A. & Hsu, J. W. P. Photonic curing of solution-deposited ZrO_2 dielectric on PEN: a path towards high-throughput processing of oxide electronics. *npj Flex. Electron.* **4**, 7 (2020).

28. Sánchez, S., Jerónimo-Rendon, J., Saliba, M. & Hagfeldt, A. Highly efficient and rapid manufactured perovskite solar cells via Flash InfraRed Annealing. *Mater. Today* **35**, 9–15 (2020).
29. Jung, D. H. *et al.* Flash-induced ultrafast recrystallization of perovskite for flexible light-emitting diodes. *Nano Energy* **61**, 236–244 (2019).
30. Yao, Y. *et al.* Direct processing of $\text{PbZr}_{0.53}\text{Ti}_{0.47}\text{O}_3$ films on glass and polymeric substrates. *J. Eur. Ceram. Soc.* **40**, 5369–5375 (2020).
31. Kim, J., Son, K. J. & Kim, K. An empirical study of rendering sinusoidal textures on a ultrasonic variable-friction haptic surface. *2015 12th Int. Conf. Ubiquitous Robot. Ambient Intell. URAI 2015* 593–596 (2015) doi:10.1109/URAI.2015.7358839.
32. Kwok, C. K. & Desu, S. B. Pyrochlore to perovskite phase transformation in sol-gel derived lead-zirconate-titanate thin films. *Appl. Phys. Lett.* **60**, 1430–1432 (1992).
33. Glinsek, S. *et al.* Fully transparent friction-modulation haptic device based on piezoelectric thin film. *Adv. Funct. Mater.* **30**, 2003539 (2020).
34. Gueye, I. *et al.* Chemistry of surface nanostructures in lead precursor-rich $\text{PbZr}_{0.52}\text{Ti}_{0.48}\text{O}_3$ sol-gel films. *Appl. Surf. Sci.* **363**, 21–28 (2016).
35. Fengler, F. P. G. *et al.* Domain pinning: Comparison of hafnia and PZT based ferroelectrics. *Adv. Electron. Mater.* **3**, 1600505 (2017).
36. Nguyen, C. H. *et al.* Probing-models for interdigitated electrode systems with ferroelectric thin films. *J. Phys. D. Appl. Phys.* **51**, 175303 (2018).
37. Damjanovic, D. Ferroelectric, dielectric and piezoelectric properties of ferroelectric thin films and ceramics. *Reports Prog. Phys.* **61**, 1267–1324 (1998).

38. Casset, F. *et al.* Low Voltage Haptic Slider Built Using Sol-Gel Thin-Film PZT Actuators Reported on Glass. in *2019 IEEE 32nd International Conference on Micro Electro Mechanical Systems (MEMS)* 990–993 (IEEE, 2019).
39. AF32 Glass Datasheet. <https://www.pgo-online.com/intl/af32.html> (2022).
40. Bernard, F. Conception, fabrication et caractérisation d'une dalle haptique à base de microactionneurs piézoélectriques. (Université Grenoble Alpes, 2016).
41. Song, L. *et al.* Piezoelectric thick film for power-efficient haptic actuator. *Appl. Phys. Lett.* **121**, 212901 (2022).
42. Yamakawa, K. *et al.* Novel Pb(Ti,Zr)O₃ (PZT) crystallization technique using flash lamp for ferroelectric RAM (FeRAM) embedded LSIs and one transistor type FeRAM devices. *Jpn. J. Appl. Phys.* **41**, 2630–2634 (2002).
43. Palneedi, H. *et al.* Intense pulsed light thermal treatment of Pb(Zr,Ti)O₃/metglas heterostructured films resulting in extreme magnetoelectric coupling of over 20 V cm⁻¹ O⁻¹. *Adv. Mater.* 2303553 (2023).
44. Ouyang, J., Cormier, D., Williams, S. A. & Borkholder, D. A. Photonic sintering of aerosol jet printed lead zirconate titanate (PZT) thick films. *J. Am. Ceram. Soc.* **99**, 2569–2577 (2016).
45. Ledermann, N. *et al.* {100}-textured, piezoelectric Pb(Zr_xTi_{1-x})O₃ thin films for MEMS: integration, deposition and properties. *Sensors Actuators A Phys.* **105**, 162–170 (2003).
46. Casset, F. *et al.* Young modulus and Poisson ratio of PZT thin film by picosecond ultrasonics. in *IEEE International Ultrasonics Symposium, IUS* 2180–2183 (2012).
47. Cohen, R. E., Heifets, E., Fu, H. & Phys Lett, A. First-principles computation of elasticity of Pb(Zr, Ti)O₃: The importance of elasticity in piezoelectrics. *AIP Conf. Proc.*

- 582**, 11–22 (2001).
48. Sadl, M. *et al.* Energy-storage-efficient $0.9\text{Pb}(\text{Mg}_{1/3}\text{Nb}_{2/3})\text{O}_3\text{--}0.1\text{PbTiO}_3$ thick films integrated directly onto stainless steel. *Acta Mater.* **221**, 117403 (2021).
 49. Patil, D. R. *et al.* Piezoelectric thick film deposition via powder/granule spray in vacuum: A review. *Actuators* **9**, 59 (2020).
 50. Hwang, G. T. *et al.* Self-powered wireless sensor node enabled by an aerosol-deposited PZT flexible energy harvester. *Adv. Energy Mater.* **6**, 1–9 (2016).
 51. Sadl, M. *et al.* Multifunctional energy storage and piezoelectric properties of $0.65\text{Pb}(\text{Mg}_{1/3}\text{Nb}_{2/3})\text{O}_3\text{--}0.35\text{PbTiO}_3$ thick films on stainless-steel substrates. *J. Phys. Energy* **4**, 0–9 (2022).
 52. Godard, N., Glinsek, S. & Defay, E. Inkjet-printed silver as alternative top electrode for lead zirconate titanate thin films. *J. Alloys Compd.* **783**, 801–805 (2019).
 53. Corning. Corning® HPFS® 7979, 7980, 8655 Fused Silica, Optical Materials Product Information.
https://www.corning.com/media/worldwide/csm/documents/HPFS_Product_Brochure_All_Grades_2015_07_21.pdf (2015).
 54. See more information about soda lime glass used for common microscope slides:
<https://www.marienfeld-superior.com/microscopes-slides-special-size-76-x-52-mm.html> (2022).
 55. Mazzalai, A., Balma, D., Chidambaram, N., Matloub, R. & Murali, P. Characterization and fatigue of the converse piezoelectric effect in PZT films for MEMS applications. *J. Microelectromechanical Syst.* **24**, 831–838 (2015).
 56. ICDD database PDF4+ v.19. (2019).

Acknowledgements

Luxembourg National Research Fund (FNR) is acknowledged for the financial support through projects FLASHPOX (C21/MS/16215707). L.S. and A.B.M. acknowledge financial support from the FNR under the project PACE (PRIDE/17/12246511/PACE). A.B. and B.K. acknowledge funding by the Slovenian Research Agency (projects J2-3041, J2-2497). Barnik Mandal and Poorani Gnanasambandan are acknowledged for performing SEM.

Author Contributions

L.S. and J.C. contributed equally to the acquisition, analysis, interpretation of data and writing of the work. A.B. contributed to the acquisition and analysis of data. A.B.M., B.K. and S.G. contributed to the acquisition of data. E.D. contributed to the conception of the work. S.G. contributed to the conception of the work and substantively revised it.

Competing Interests

The authors declare no conflict of interest.

Figures

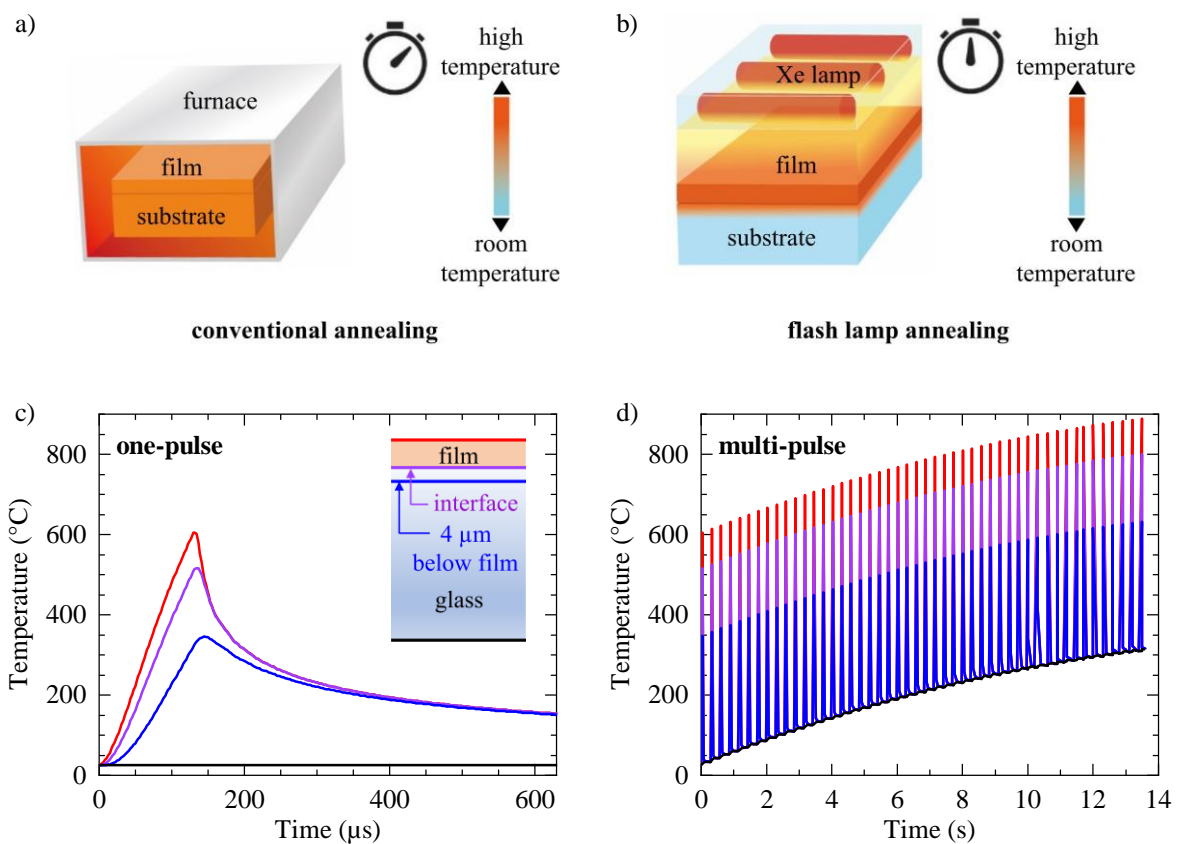


Figure 1. **Schematic representation of annealing processes.** Heat distribution in a film, its substrate, and processing time in the case of a) conventional box furnace annealing and b) flash lamp annealing. **Finite element modelling.** Temperature profiles during c) single-pulse and d) 50-pulse flash lamp annealing of a 170 nm-PZT/fused silica glass stack. The red, purple, blue, and black lines correspond to the temperature profiles of the top PZT surface, the interface between the film and glass, 4 μm below this interface, and the bottom of the substrate (500 μm), respectively. The schematic structure of the sample is shown in the inset of c). The pulse duration, energy density and repetition rate are 130 μs , 3 J cm^{-2} , and 3.5 Hz, respectively.

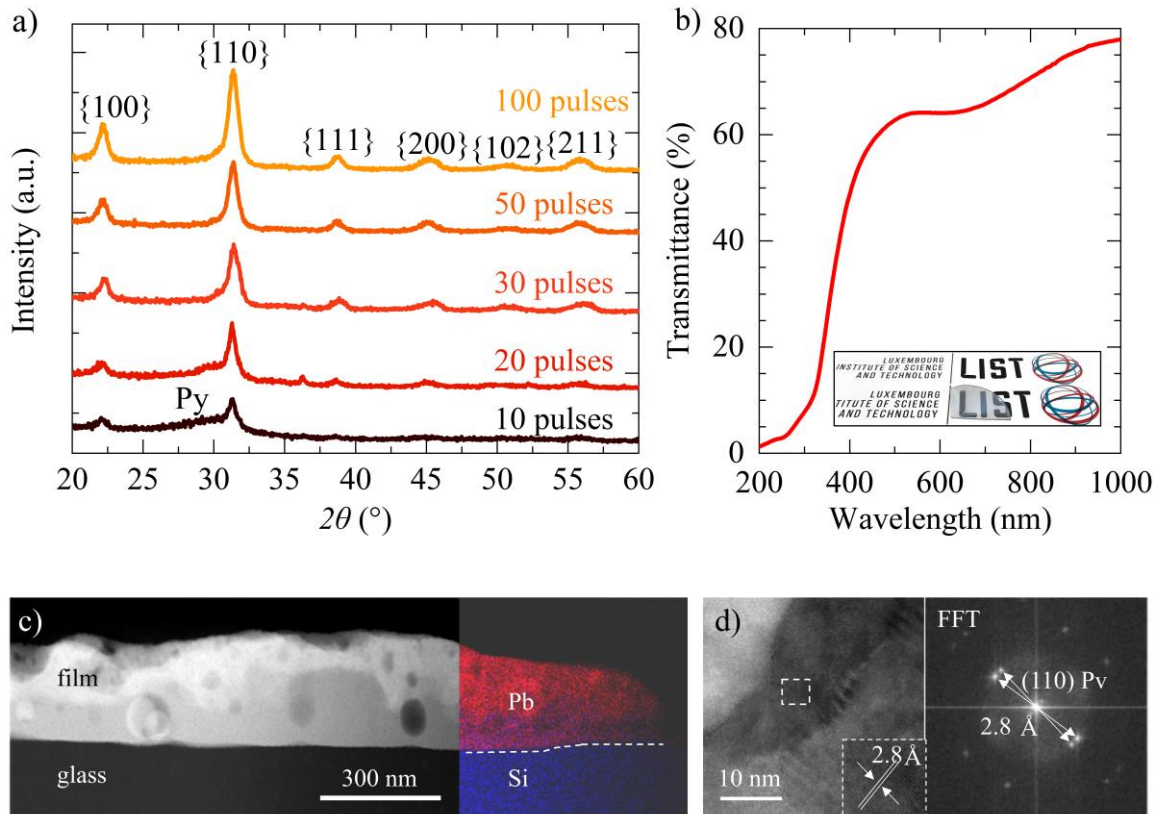


Figure 2. **Microstructural and optical characterization of 170 nm-thick PZT films on fused silica glass.** a) GIXRD patterns of films annealed with different number of light pulses. In a) perovskite reflections are denoted according to a powder diffraction file (PDF) No 01-070-4264⁵⁶. Py indicates the pyrochlore reflection according to PDF No 04-014-5162⁵⁶. b) Transmittance of the 50-pulse film. Inset shows its optical appearance. STEM results of the 100-pulse film: c) cross sectional dark-field STEM image and EDS analysis across substrate/film interface (marked by dashed line) using Pb M and Si K line, d) high-resolution bright-field STEM image of two perovskite grains with corresponding FFT image showing (110) planes. Flash lamp annealing was performed with energy density, pulse duration and repetition rate of 3 J cm⁻², 130 μs, and 3.5 Hz, respectively.

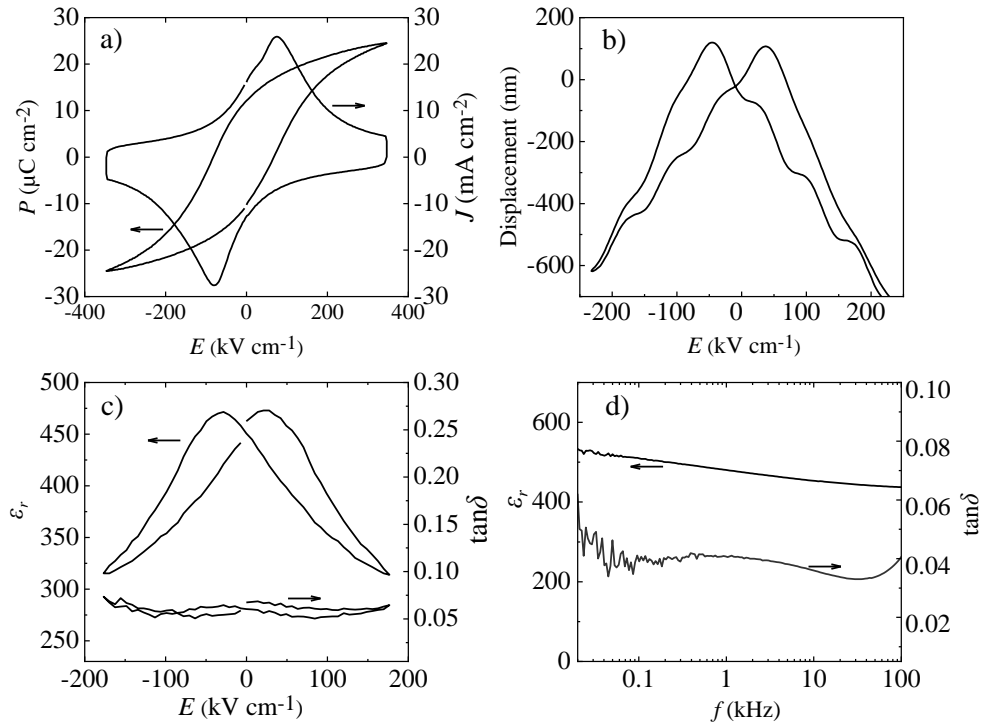


Figure 3. **Electromechanical characterization of a 1 μm-thick PZT film on fused silica glass.**

a) Ferroelectric and b) displacement characterizations of the PZT film at 100 Hz and 11 Hz, respectively.

Dielectric measurements of the PZT film: relative permittivity ϵ_r and dielectric losses $\tan\delta$ as function of c) DC bias at 1 kHz and d) frequency f . The samples were processed with 50 pulses per layer with energy density, pulse duration and repetition rate of 3 J cm², 130 μs, and 3.5 Hz, respectively.

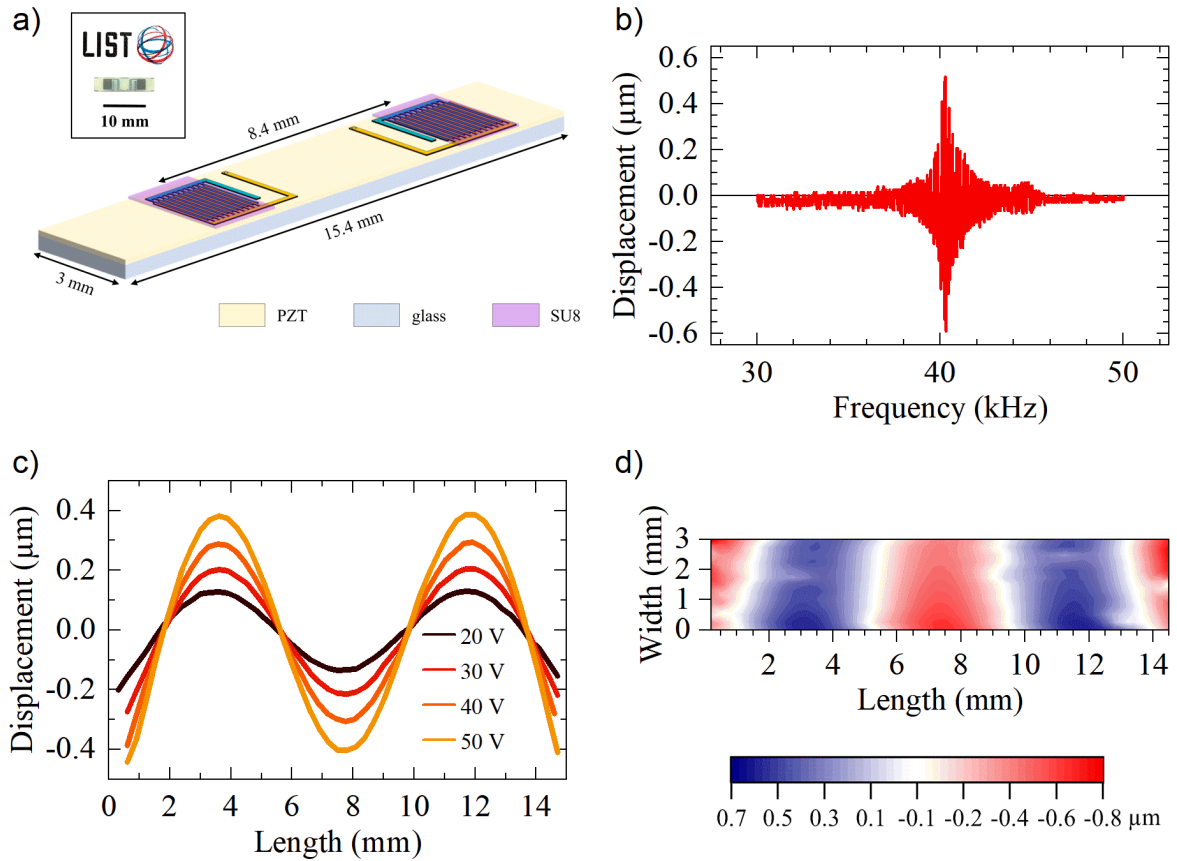


Figure 4. **Electromechanical characterization of the haptic device.** a) Schematic of the device made of the flash lamp annealed $1\ \mu\text{m}$ -thick PZT on AF32 glass. Two sets of interdigitated Pt electrodes are placed on top to create the actuators. Inset shows its visual appearance. b) Out-of-plane displacement of the surface measured as a function of frequency at one of the antinodes. $60\ \text{V}_{\text{pp}}$ ($30\ \text{V}_{\text{AC}}+30\ \text{V}_{\text{DC}}$) were applied. c) The displacement along x -axis (length of the device) excited at various driving voltages. d) 2D map of the displacement at $60\ \text{V}_{\text{pp}}$. c) and d) are measured at the resonance frequency of $40.2\ \text{kHz}$.

Tables

Table 1. **Comparison of ferroelectric, dielectric and piezoelectric properties of chemical solution deposited PZT films processed by flash lamp annealing (FLA), rapid thermal annealing (RTA) and laser annealing (LA).** In Ref. ³³ a lead titanate oxide nucleation layer was used to promote growth along (100) orientation, which enhances piezoelectric response ⁴⁵. MIM stands for metal-insulator-metal structure.

Process	Substrate	Structure	P_r ($\mu\text{C cm}^{-2}$)	ϵ_r	$\tan\delta$	$e_{33,f}$ (C m^{-2})	Ref.
RTA	Fused silica	IDE	16	900	0.05	-8	Glinsek et al. ³³
FLA	Fused silica	IDE	11	450	0.05	-5	This work
FLA	AF32	IDE	5	350	0.07	-5	This work
LA	Platinised silicon	MIM	28	-	-	-4	Fink et al. ¹⁷

Supplementary Information for

Crystallization of piezoceramic films on glass via flash lamp annealing

Longfei Song,^{a,b,1} Juliette Cardoletti,^{a,1} Alfredo Blázquez Martínez,^{a,b} Andreja Bencan,^c Brigita Kmet,^c Stéphanie Girod,^a Emmanuel Defay,^a Sebastjan Glinsek^{a,*}

^aMaterials Research and Technology Department, Luxembourg Institute of Science and Technology, rue du Brill 41, L-4422 Belvaux, Luxembourg

^bUniversity of Luxembourg, 41 rue du Brill, L-4422 Belvaux, Luxembourg

^cElectronic Ceramics Department, Jožef Stefan Institute, Jamova cesta 39, 1000 Ljubljana, Slovenia

¹These authors contributed equally: L. S. and J. C.

*Corresponding author: sebastjan.glinsek@list.lu

Contents

1. Finite element modelling (FEM)	3
2. Films grown on fused silica glass	4
2.1. Phase composition and microstructural characterizations	4
2.2. Electrical measurements	9
2.2.1. <i>170 nm-thick film grown on fused silica glass</i>	<i>9</i>
2.2.2. <i>500 nm-thick film grown on fused silica glass</i>	<i>10</i>
2.3. Comparison of properties at different thicknesses	11
3. Thick PZT film on AF32 glass for surface haptic device	12
3.1. Phase composition and microstructural characterization	12
3.2. Haptic devices	14
3.2.1. <i>Thickness of piezoelectric film</i>	<i>14</i>
3.2.2. <i>Finite element modelling (FEM)</i>	<i>14</i>
3.2.3. <i>Device performance</i>	<i>15</i>
3.3. Electrical measurements	17
4. Flash lamp process for growing films on soda lime glass	18
4.1. Two-step flash lamp annealing process	18
4.2. Phase composition characterization	19
4.3. Electrical measurements	20
5. Comparison with previous works	21

1. Finite element modelling (FEM)

In order to investigate the feasibility of crystallization of PZT thin films via flash lamp annealing, finite element modelling was performed using surface mode of SimPulse software to study the temperature evolution across the thickness of the samples¹.

To estimate the absorbance inside the amorphous PZT films two approaches were tested. First, the energy density on the surface of the stage of the flash-lamp annealer was measured with a bolometer after the light passed through air (2.8 J cm^{-2}), bare fused silica glass (2.6 J cm^{-2}), and a fused silica glass with amorphous PZT on top (1.8 J cm^{-2}), see Figure S1. This indicates that the absorbed energy density is 0.8 J cm^{-2} , corresponding to an absorbance value of 28.5 %. A second approach was also tried by measuring the transmittance and reflectance of an amorphous PZT film on fused silica glass with an UV-vis spectrophotometer (see Figure S1b). In this method, the average absorbance in the wavelength range of 200-900 nm is 34 %, calculated by $100 \% - T \% - R \%$. The difference between the two values can be explained by the non-uniform absorbance of the sample through the relevant spectrum range and the fluctuating energy density of the emitted Xe light. Therefore, in FEM, the value obtained from the bolometer measurement was utilized.

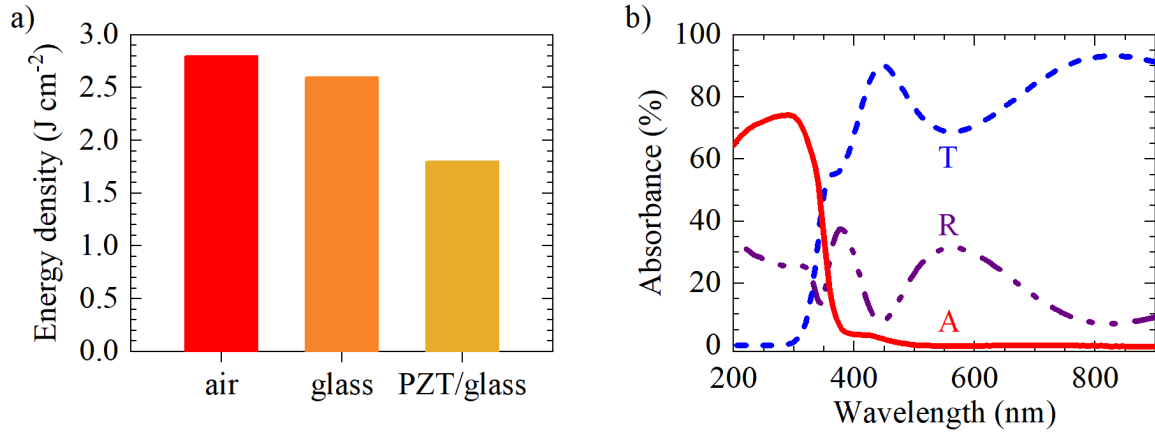


Figure S1. **Absorbance estimation:** a) Energy density measured with a bolometer after the light passing through: air (empty chamber), 500 μm -thick fused silica glass, and pyrolyzed PZT/fused silica stack. The energy density and the length of the applied light pulse were 2.8 J cm⁻² and 130 ms. b) Measured transmittance T %, reflectance R %, and calculated absorption A of pyrolyzed PZT film on fused silica glass.

2. Films grown on fused silica glass

2.1. Phase composition and microstructural characterizations

A standard θ - 2θ XRD pattern of a flash lamp annealed 1 μm -thick PZT film on fused silica is shown in Figure S2. Presence of piezoelectrically active perovskite phase is revealed, and all the reflections can be identified with the PZT powder diffraction file (PDF) No 01-070-4264². Reflections of secondary phases are not observed.

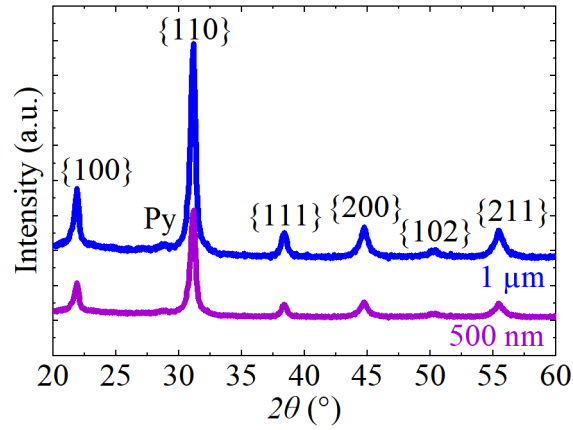


Figure S2. **XRD study.** θ - 2θ XRD patterns of flash lamp annealed 500 nm and 1 μm PZT films on fused silica glass. The films were processed with 50 pulses per layer (3 and 6 crystallizations in total, respectively). Parameters of each pulse are reported in caption of Fig. 2 in the main manuscript. The powder diffraction files (PDF) No 01-070-4264 and 04-014-5162² have been used to identify the perovskite and pyrochlore phases, respectively.

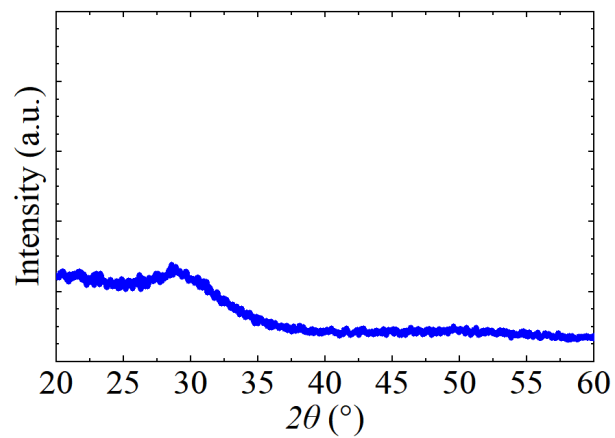


Figure S3: **XRD study.** GIXRD pattern of an as-deposited (before FLA treatment) PZT film on fused silica glass. Peaks of the perovskite phase are completely absent.

GIXRD pattern of the film annealed in a conventional RTA furnace at 700 °C is shown in Figure S4. Only pyrochlore phase is detected and cracks appeared on the surface, as previously reported in Ref.³.

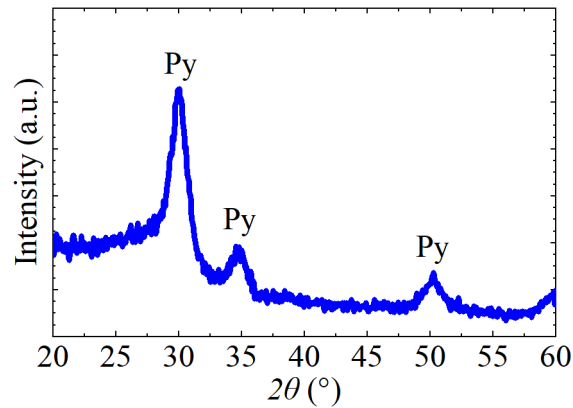


Figure S4. **XRD study.** GIXRD pattern of a conventionally RTA-processed film on fused silica at 700 °C. Py indicates the pyrochlore reflection according to PDF No 04-014-5162².

The transmittance spectra of PZT thin films of various thicknesses on fused silica glass are shown in Figure S5. The inset shows that 1 μm-thick PZT films are transparent.

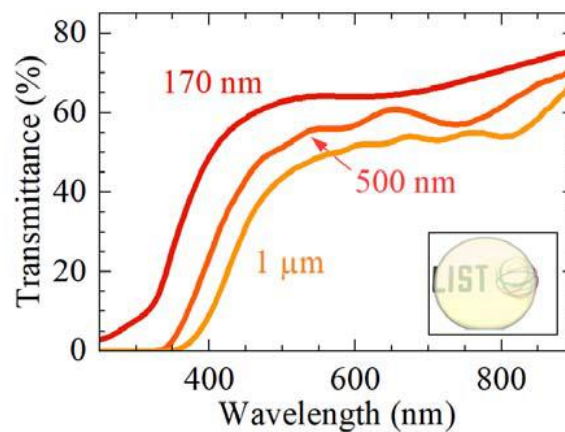


Figure S5. **Transmittance of 170 nm, 500 nm and 1 μm-thick PZT thin films on fused silica glass.** Inset shows the optical appearance of the 1 μm-thick film. The films were processed with 50 pulses per layer (3 and

6 crystallizations in total, respectively). Parameters of each pulse are reported in caption of Fig. 2 in the main manuscript.

Figure S6 displays cross-sectional scanning electron microscopy (SEM) image of a flash lamp annealed 1 μm -thick PZT, showing a clean interface between PZT film and glass. The microstructure is granular with present porosity.

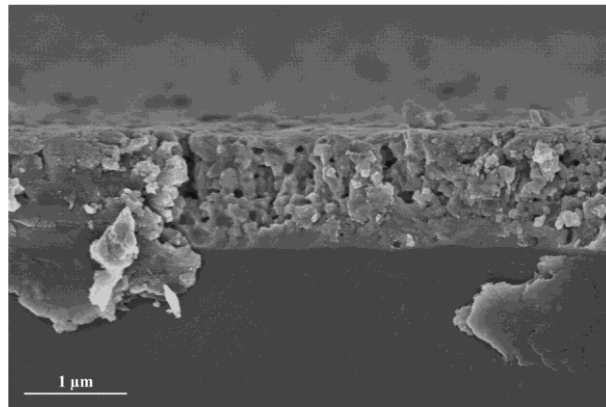


Figure S6. **Microstructure characterization.** Cross-sectional SEM image of flash lamp annealed 1 μm PZT film on fused silica glass. Note that the large flake-like structures observed in the glass are due to glass cleaving.

A detailed TEM analysis of the 170 nm-thick PZT thin film on fused silica glass is shown in Figure S7.

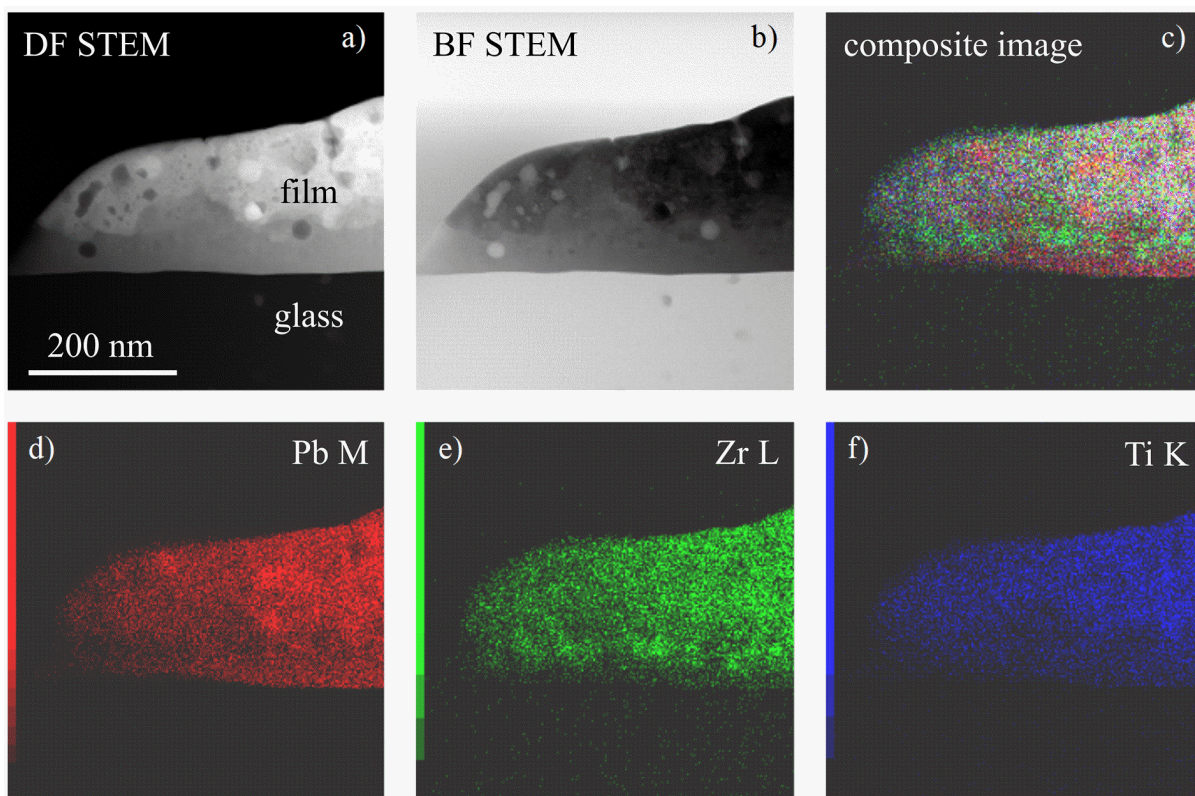


Figure S7. TEM analysis of 170 nm PZT thin film on fused silica glass. a) Cross sectional dark-field (DF) and b) bright-field (BF) STEM image with c-f) corresponding EDS mapping showing porous, chemically non-homogenous film. Pores are darker/brighter spots on DF/BF STEM images, correspondingly.

A 2D map of EDS analysis of the film cross-section (already shown in Fig. 2c in the main article) is shown in Figure S8. In the marked area an EDS analysis was performed showing that the Si signal extends into the PZT layer.

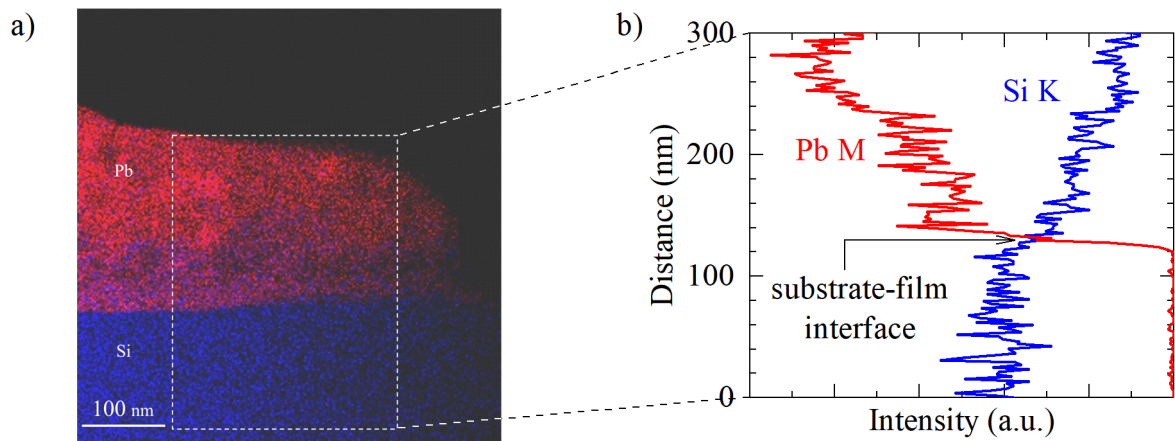


Figure S8. **TEM and EDS analysis of 170 nm PZT thin film on fused silica glass.** EDS analysis across substrate-film interface using the Pb M and Si K lines showing partial diffusion of Si into the PZT film. The dashed area in a) marks the region where the b) EDS line analysis was performed.

2.2. Electrical measurements

2.2.1. 170 nm-thick film grown on fused silica glass

We found that the films annealed with 50 pulses exhibit the optimal electrical properties. Polarization as a function of electric field $P(E)$ and corresponding current density $J(E)$ loops of the 170 nm-thick films treated with 50 pulses at 100 and 10 Hz are shown in Figure S9. The polarization loops of the films are initially pinched, before opening up during (wake-up effect) upon electric-field cycling (1.1×10^6 bipolar cycles). At 10 Hz, the P_r is $10 \mu\text{C cm}^{-2}$, and two sharp peaks in $J(E)$, linked to ferroelectric switching, are observed.

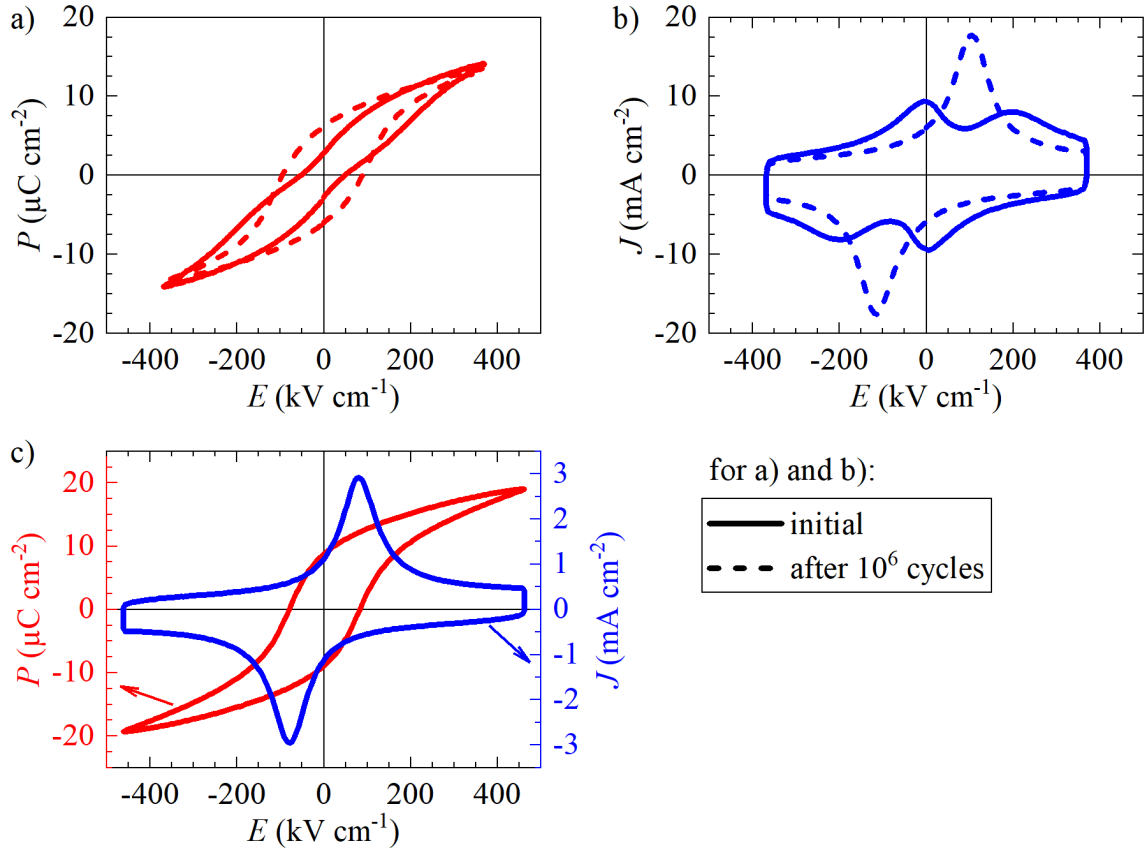


Figure S9. **Ferroelectric characterization.** a) Polarization $P(E)$ hysteresis loops of the 50 pulses annealed 170-nm-thick PZT film on fused silica before and after 1.1×10^6 wake-up cycles, measured at 100 Hz. b) corresponding current density loops $J(E)$. c) $P(E)$ and $J(E)$ measured at 10 Hz, by taking the average after 500 cycles. Large IDEs were used in these measurements, corresponding to an effective area of 0.36 mm^2 .

2.2.2. 500 nm-thick film grown on fused silica glass

The $P(E)$ and $J(E)$ loops of the 500 nm-thick PZT film on fused silica glass are shown in Figure S10a with a maximum polarization P_{max} of $21 \mu\text{C cm}^{-2}$ and a remanent polarization P_r of $11 \mu\text{C cm}^{-2}$. Its coercive field E_c is 95 kV cm^{-1} . Note that these values were obtained after 10^3 wake-up cycles. The displacement of a cantilever structure shows a typical butterfly loop

(Figure S10b). At 150 V the vertical displacement at the free end of the cantilever is 625 nm, corresponding to a piezoelectric coefficient $e_{33,f}$ of -5 C m^{-2} .

All the results confirm good ferroelectric properties of 50 pulses flash lamp annealed films.

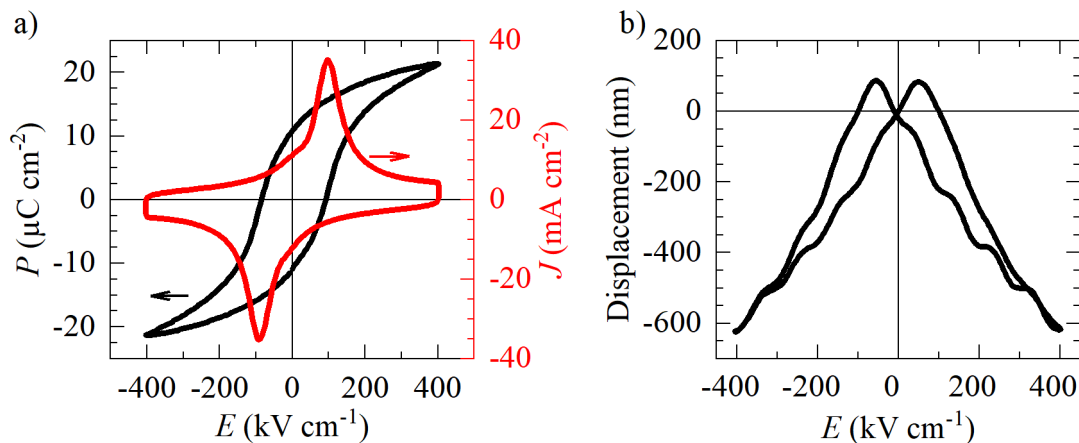


Figure S10. Electromechanical characterization of a 500 nm-thick PZT film on fused silica glass.

a) Ferroelectric and b) displacement characterizations of the PZT film at 100 Hz and 11 Hz, respectively. The samples were processed with 50 pulses per layer with energy density, pulse duration and repetition rate of 3 J cm^{-2} , $130 \mu\text{s}$, and 3.5 Hz , respectively.

2.3. Comparison of properties at different thicknesses

To have better overview of the results, a table with ferroelectric, piezoelectric and optical properties of the 170 nm, 500 nm and $1 \mu\text{m}$ -thick films on fused silica substrates is provided in Table S1.

Table S1. **Properties of 170 nm, 500 nm and 1 μm -thick PZT films on fused silica glass.** Remanent and maximum polarization (P_r and P_{max}) at an applied voltage of 150 V, relative permittivity and dielectric losses (ϵ_r and $\tan\delta$), piezoelectric coefficient $e_{33,f}$, and transmittance (T) at a wavelength of 550 nm. The films were processed with 50 pulses per layer with energy density, pulse duration and repetition rate of 3 J cm^{-2} , 130 μs , and 3.5 Hz, respectively. Large IDEs were used in these measurements, corresponding to an effective area of 0.36 mm^2 .

Film thickness	P_r ($\mu\text{C cm}^{-2}$)	P_{max} ($\mu\text{C cm}^{-2}$)	ϵ_r	$\tan\delta$	$e_{33,f}$ (C m^{-2})	T (%)
170 nm	10	19	200	0.05	-2	64
500 nm	11	21	270	0.05	-5	56
1 μm	12	24	450	0.05	-5	49

3. **Thick PZT film on AF32 glass for surface haptic device**

3.1. Phase composition and microstructural characterization

A 1 μm -thick PZT film was grown on AF32 glass. Process parameters were the same as for the films on fused silica, namely 3 J cm^{-2} in energy density, 130 μs pulse duration and 50 pulses with a repetition rate of 3.5 Hz. Figure S11 shows θ - 2θ XRD pattern of the film. Reflections of the perovskite phase are revealed and all of them can be identified with the PZT PDF No 01-070-4264², as for the film grown on fused silica. Note that the reflection at around 39° comes from the Pt electrodes.

Figure S12 shows cross-sectional SEM image of a 1 μm -thick PZT film on AF32 glass, used for haptic device. It reveals a dense and granular microstructure, and also a clear interface between the film and glass.

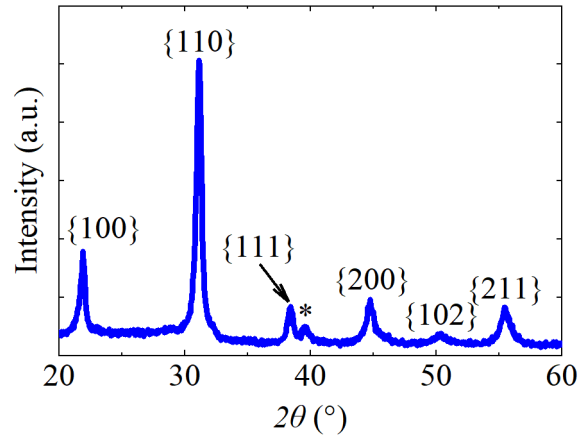


Figure S11. **XRD study.** θ - 2θ XRD pattern of flash lamp annealed 1 μm thick PZT film on AF32 glass used for the haptic device. * denotes the signal of Pt IDE electrode on top of the PZT film. The powder diffraction file (PDF) No 01-070-4264² has been used to identify the perovskite phase.

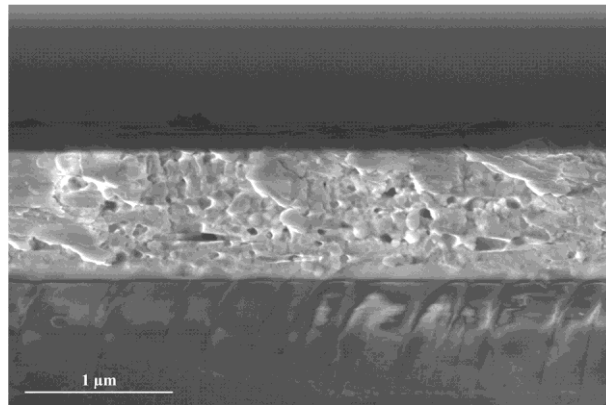


Figure S12. **Microstructure characterization.** Cross-sectional SEM image of 1 μm -thick PZT on AF32 glass, used for haptic device. The processing conditions have been described in the Methods.

3.2. Haptic devices

3.2.1. Thickness of piezoelectric film

In general, piezoelectric films show increased electromechanical response with increasing thickness due to larger contributions of domains⁵. In the case of piezoelectric actuators with interdigitated (IDE) geometry, additional benefit of using thicker film is an increased in-plane force F_3 exerted by the piezoelectric layer upon applied electric field E_3 . The force is expressed as:

$$F_3 = -e_{33,f}E_3A, \quad (1)$$

where E_3 is an in-plane electric field, $e_{33,f}$ is an effective piezoelectric coefficient and A is a cross-section. In IDE geometry E_3 roughly equals to an applied voltage U divided by a gap a between the fingers, while A equals to a film thickness t_f multiplied by a finger length l . The above equation can be therefore re-written as:

$$F_3 = -e_{33,f}\frac{U}{a}lt_f, \quad (2)$$

from which it follows that the force exerted by IDE piezoelectric actuator (at constant voltage) can be increased by increasing film's thickness (and decreasing the gap between the fingers). Considering these points and ease of processing, we defined 1 μm -thick PZT film as a good compromise.

3.2.2. Finite element modelling (FEM)

Two-dimension (2D) FEM was carried out using COMSOL software to design a haptic device. 1 μm PZT/AF32 glass structure was used in the modelling with the total length of 15.4 mm. Two symmetric actuating areas were created with IDEs with 129 pairs of digits and a spacing of 8.4 mm. The width of the fingers and the interdigital gap are 5 μm and 3 μm , respectively.

Young's modulus and Poisson ratio for AF32 glass are 74.8 GPa and 0.238, respectively⁶. Influence of the electrodes on the deflection were ignored due to their lower thicknesses. The effective transverse piezoelectric coefficient $e_{33,\text{eff}}$ and relative permittivity ϵ_r were set to

-4.5 C m⁻² and 400, respectively. Note that $e_{33,\text{eff}}$ was extracted from the modelling by matching the experimental displacement value of the haptic device, after having measured the damping loss factor η^7 , which was obtained by sweeping the frequency of the actuator and collecting the displacement, as shown in Fig. 4b. η corresponds to the breadth of the resonance peak ($\Delta f/f$), where Δf is the full-width-at-half-maximum and f is the resonance frequency. The obtained value of η is 0.0163.

At a simulated resonant frequency of 40.2 kHz, the device exhibits a maximum displacement (1.7 μm peak-to-peak) when driven with 60 V. Figure S13 illustrates the device's mode shape at resonance, specifically a Lamb wave mode featuring four equally spaced nodes along its length.

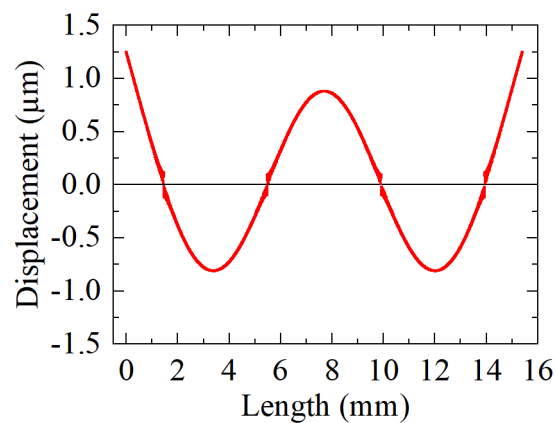


Figure S13. **Finite element modelling of haptic device.** Wave shape along the length of the device at resonant frequency.

3.2.3. *Device performance*

The device is operating in a resonance mode and the standing wave correspond to the anti-symmetric (A_0) Lamb wave, which has been considered as optimal for piezoelectric haptics in

previous works⁸. Lamb waves in glass plates for haptics were extensively studied by Bernard⁹. Below we show a Figure from his work showing wavevectors of Lamb waves as functions of a frequency-thickness product. In our work the glass is 300 μm -thick and is operated at a frequency of 40.2 kHz, leading to the frequency-thickness product of 0.012 MHz mm. This is below the appearance of any other modes than A_0 . The fact that Bernard used EAGLE XG and we are using AF32 glass does not change the outcome of this analysis as both glasses have comparable mechanical properties and density.

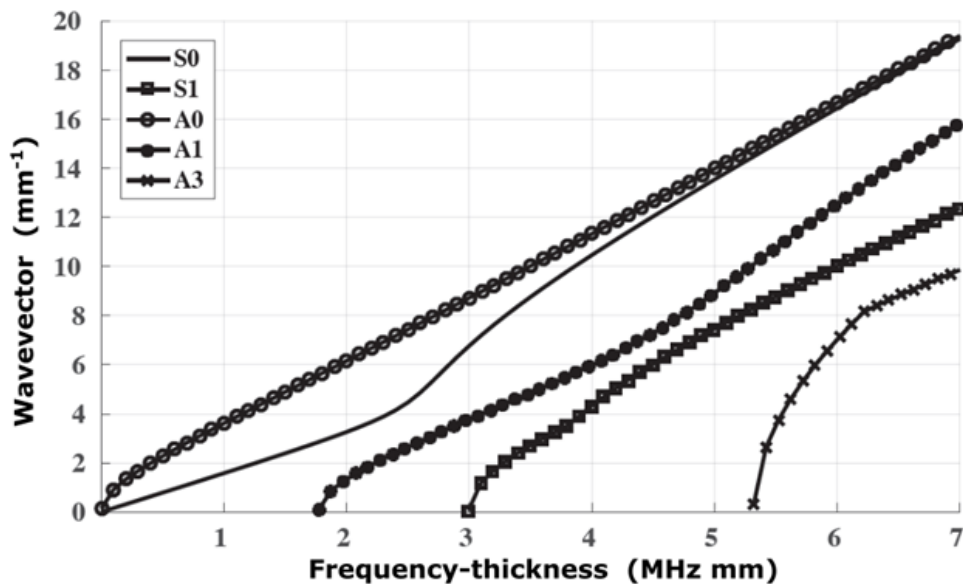


Figure S14: Wavevectors of different Lamb wave modes as function of frequency-thickness product. Adapted from Bernard⁹.

Performance of the device is compared to other piezoelectric haptic devices on glass with interdigitated geometry in Table S2. The three devices are similar in geometry (~3 mm x 15 mm) and have interdigitated electrode structure, which makes the comparison of device performance straightforward. Several points stem from the Table: 1) The device demonstrated

in this work operates at lower frequency. This is mainly due to thinner substrate (300 μm vs. 500 μm). 2) Device in this work needs lower U_{rms} to achieve 1 μm displacement. This is mainly due to decreased gap between the fingers (3 μm vs. 10 μm , see Equation (2)) and lower substrate thickness. 3) Higher total capacitance in the current device is mainly due to a combination of smaller gap and finger width (5 μm vs. 10 μm). Most importantly, this device shows similar power consumption (35 mW) compared to the other two devices, which confirms its high quality.

Table S2: Comparison of piezoelectric thin-film haptic devices on glass with interdigitated geometry. f – resonant (operating) frequency; U_{rms} – root mean square (rms) voltage at 1 μm deflection; C_{device} – capacitance of the device; P_{cons} – power consumption estimated as $P_{\text{cons}} = Cf(U_{\text{rms}})^2$. In all three cases thickness of PZT was 1 μm and devices had similar geometries.

Device	Glass	f (kHz)	U_{rms} (V)	C_{device} (pF)	P_{cons} (mW)
Spin-coated ³	Fused silica	73.0	43	240	32
Inkjet-printed ¹⁰	Fused silica	63.3	46	230	31
This work	AF32	40.2	34	760	35

3.3. Electrical measurements

Figure S15 shows initial $P(E)$ and $J(E)$ loops for a single haptic actuator. Similarly pinched loops are observed as on fused silica (see Figure S9). Note that this initially pinched behaviour does not influence haptic performance, as was demonstrated in inkjet-printed (RTA-processed) PZT films with similar behaviour¹¹. Permittivity and losses values at zero field are 350 and 0.07, respectively.

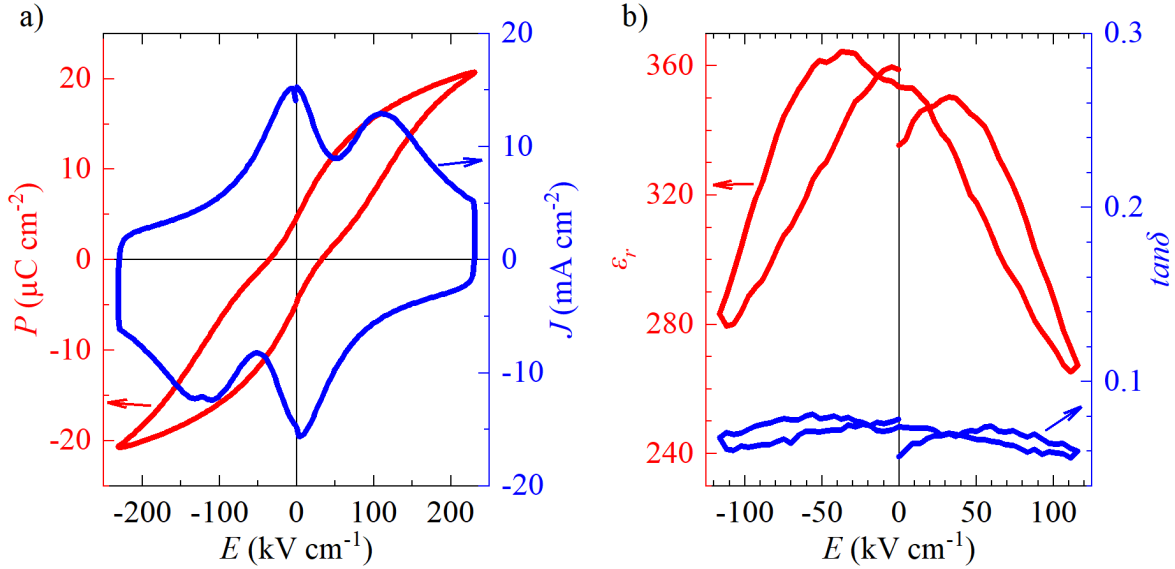


Figure S15. **Ferroelectric and dielectric characterizations** of 1 μm thick PZT actuator on Schott AF32 glass. a) $P(E)$ and $J(E)$ loops of per actuator, measured at 100 Hz. b) corresponding $\epsilon_r(E)$ and $\tan\delta(E)$ loops of the actuator, measured as functions of DC voltage with a probing AC signal of 0.5 V at 1 kHz.

4. Flash lamp process for growing films on soda lime glass

4.1. Two-step flash lamp annealing process

The one-step process used for fused silica and AF32 glass is not suitable for growing PZT film on soda lime glass due to appearance of cracks. This can be attributed to the low thermal conductivity ($1.0 \text{ W m}^{-1} \text{ K}^{-1}$) of the substrate, which leads to a slower rate of heat transfer and consequently a higher temperature at the interface between the film and glass.

To address this issue, we have developed a two-step process consisting of "nucleation" and "growth" stages. In the first step, 6 pulses with higher power density (2.5 J cm^{-2} and $170 \mu\text{s}$) are applied to induce the formation of nuclei within the film. This formation of nuclei reduces

the activation energy required for the phase transition from an amorphous to a crystalline phase. In the second step, the "growth" step, 240 pulses with a lower power density (2.5 J cm^{-2} and $250 \text{ }\mu\text{s}$) are applied to grow the film at a lower temperature, thereby preventing the occurrence of cracks. For both steps, the repetition rate is set to 0.5 Hz to increase the heat diffusion through the sample.

4.2. Phase composition characterization

Figure S16 displays GIXRD patterns of PZT films with thicknesses of 170 and 500 nm deposited on soda lime glass. The dominant reflections in both patterns correspond to the piezoelectrically active perovskite phase, suggesting that the FLA process is suitable for layer-by-layer preparation in solution processing. This is particularly significant for various applications. Although a weak reflection at approximately 29° indicates the presence of the secondary pyrochlore phase, its relative intensity is considerably lower than that of the perovskite reflections.

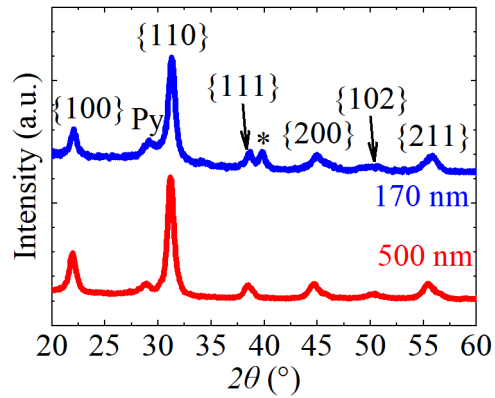


Figure S16. **XRD study.** GIXRD patterns of 170 nm- and 500 nm-thick PZT films on soda lime glass. * denotes the signal of Pt IDE electrode on top of the PZT film. The powder diffraction files (PDF) No 01-070-4264 and 04-014-5162² have been used to identify the perovskite and pyrochlore phases, respectively.

4.3. Electrical measurements

The $P(E)$ and $J(E)$ loops of a 170 nm-thick PZT thin film on soda lime are shown in Figure S17 along with its dielectric characterization.

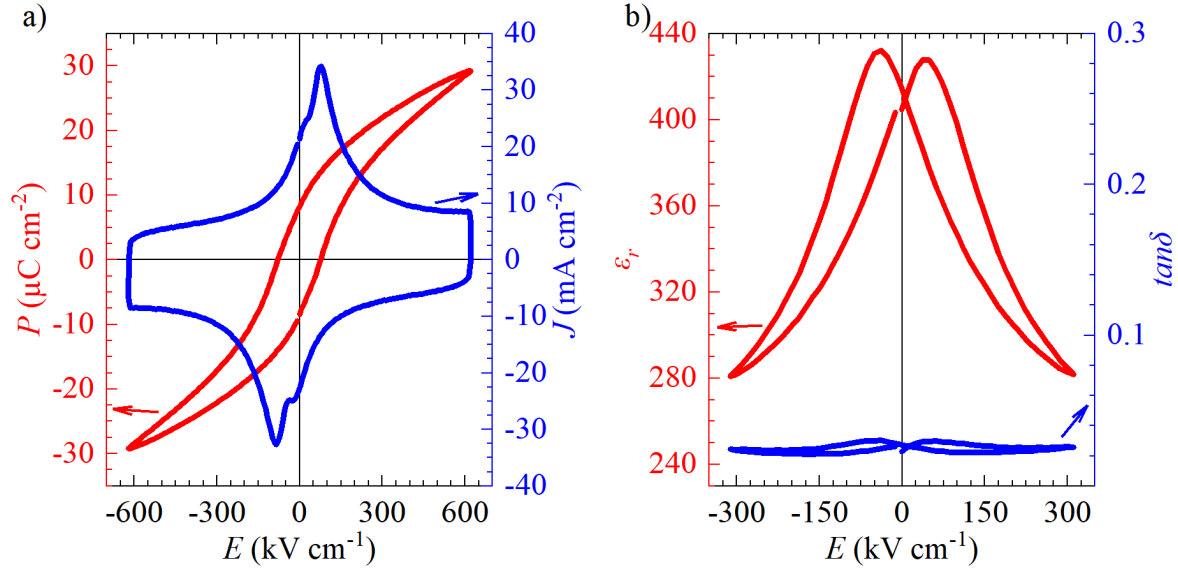


Figure S17. **Ferroelectric and dielectric characterizations.** Ferroelectric and dielectric measurements of 170 nm-thin PZT on soda lime glass. a) $P(E)$ and $J(E)$ loops, measured at 100 Hz. b) $\epsilon_r(E)$ and $\tan\delta(E)$ loops, measured at 1kHz. Small IDEs was used, whose parameters are 5 μm in digit width, 3 μm in interdigital gap, 50 pairs of digits and 370 μm in length of digits facing each other.

5. Comparison with previous works

Table S3: **Summary** of relevant points in the references previously reporting FLA treatment of PZT films and major advancement shown in this work.

Reference	Relevant points in the reference	Major advancement in our work compared to reference
Yamakawa et al., Jpn. J. Appl. Phys., 41 2630 (2002) ¹² .	<ul style="list-style-type: none"> • FLA treatment of PZT thin films. • Ambient temperature between 300 and 500 °C. • Crystalline perovskite phase present prior FLA treatment. • No piezoelectric properties. 	<ul style="list-style-type: none"> • Ambient environment at room temperature. • Crystallization of completely amorphous initial films. • Demonstration of piezoelectric properties and a device.
Yao et al., J. Eur. Ceram. Soc., 40, 5396 (2020) ¹³ .	<ul style="list-style-type: none"> • FLA treatment of PZT thin films. • No macroscopic electromechanical characterization (films too leaky). 	<ul style="list-style-type: none"> • Demonstration of macroscopic electromechanical properties and a device.

Palneedi et al., Adv. Mater., 2303553 (2023) ¹⁴ .	<ul style="list-style-type: none"> • FLA sintering of crystalline PZT powders deposited on metglas (amorphous metal). 	<ul style="list-style-type: none"> • <i>In-situ</i> FLA crystallization of amorphous PZT thin films.
Ouyang et al., J. Am. Ceram. Soc., 99, 2569 (2016) ¹⁵ .	<ul style="list-style-type: none"> • FLA sintering of crystalline PZT powders on stainless steel. • Non-saturated P-E loops. 	<ul style="list-style-type: none"> • <i>In-situ</i> FLA crystallization of amorphous PZT thin films. • Good ferroelectric properties.
Ouyang, PhD Thesis, Rochester Institute of Technology (2017) ¹⁶ .	<ul style="list-style-type: none"> • FLA sintering crystalline PZT powders on stainless steel and PET substrates. • Non-saturated P-E loops. 	<ul style="list-style-type: none"> • <i>In-situ</i> FLA crystallization of amorphous PZT thin films. • Good ferroelectric properties.
Marotta, MSc Thesis, Rochester Institute of Technology (2019) ¹⁷ .	<ul style="list-style-type: none"> • FLA treatment of printed PZT thin films. • No crystallization (XRD) reported. • No macroscopic electromechanical characterization. 	<ul style="list-style-type: none"> • <i>In-situ</i> FLA crystallization of amorphous PZT thin films. • Demonstration of macroscopic electromechanical properties.

Two major points are stemming from the Table:

- 1) In all the previous reports with demonstrated macroscopic functional properties, FLA sintering was performed on already crystalline PZT powders. In this work, FLA crystallization, i.e., nucleation of perovskite grains and their growth, was performed from amorphous films (see Figure S3). Perovskite formation is nucleation-controlled, with activations energies for nucleation and grain growth of 441 kJ mol⁻¹ and 112 kJ mol⁻¹, respectively¹⁸. In other words, the most energetically demanding process for perovskite formation is nucleation from the amorphous phase, which this study is the only one to demonstrate with FLA.
- 2) In the remaining reports, where they worked on FLA treatment of amorphous PZT films, macroscopic ferroelectric results could not be obtained. The only exception is the work of Yamakawa et al.¹² on sputtered PZT films. In that case, the FLA treatment was performed at elevated ambient temperatures and XRD reveals the presence of the perovskite phase already before FLA treatment (Figure 8 in the article). Therefore, this work is the only one that shows macroscopic ferroelectric results starting from fully amorphous films.

Table S4: **FLA processing parameters taken from the literature and compared to the parameters used in this work.** Note that Ouyang's PhD thesis¹⁶ is omitted as its results are summarized in the article in Journal of the American Ceramics Society¹⁵. Marotta's MSc thesis¹⁷ is omitted from this analysis also, as little information on FLA process is given. *Energy per pulse in Yamakawa's work¹² is estimated from the current delivered to the Xe lamp when the voltage is applied. Real energy delivered to the sample is probably much lower. +Power per pulse (unless given) is estimated from the energy divided by pulse width. #In this work energy delivered to the sample was measured using bolometer.

Reference	Energy per pulse J cm ⁻²	Pulse width μs	Power per pulse ⁺ kW cm ⁻²	Number of pulses	Pulse frequency Hz
Yamakawa et al., Jpn. J. Appl. Phys., 41 2630 (2002) ¹² .	27*	1000-1500	18-27	up to 5	not given
Yao et al., J. Eur. Ceram. Soc., 40, 5396 (2020) ¹³ .	not given	250-500	Up to 6.4	up to 100	not given
Palneedi et al., Adv. Mater., 2303553 (2023) ¹⁴ .	1.7 – 7.4	250-1000	7	up to 3	1
Ouyang et al., J. Am. Ceram. Soc., 99, 2569 (2016) ¹⁵ .	2.8	1300	2.2	Up to 15	2
This work	3 [#]	130	up to 23	Up to 100	3

References

1. Guillot, M. J., McCool, S. C. & Schroder, K. A. Simulating the thermal response of thin films during photonic curing. *ASME Int. Mech. Eng. Congr. Expo. Proc.* **7**, 19–27 (2013).
2. ICDD database PDF4+ v.19. (2019).
3. Glinsek, S. *et al.* Fully transparent friction-modulation haptic device based on piezoelectric thin film. *Adv. Funct. Mater.* **30**, 2003539 (2020).
4. Nguyen, C. H. *et al.* Probing-models for interdigitated electrode systems with ferroelectric thin films. *J. Phys. D. Appl. Phys.* **51**, 175303 (2018).
5. Muralt, P. Recent progress in materials issues for piezoelectric MEMS. *J. Am. Ceram. Soc.* **91**, 1385–1396 (2008).
6. AF32 Glass Datasheet. <https://www.pgo-online.com/intl/af32.html> (2022).
7. Song, L. *et al.* Piezoelectric thick film for power-efficient haptic actuator. *Appl. Phys. Lett.* **121**, 212901 (2022).
8. Bernard, F., Casset, F., Danel, J. S., Chappaz, C. & Basrour, S. Characterization of a smartphone size haptic rendering system based on thin-film AlN actuators on glass substrates. *J. Micromechanics Microengineering* **26**, 84007 (2016).
9. Bernard, F. Conception, fabrication et caractérisation d'une dalle haptique à base de microactionneurs piézoélectriques. (Université Grenoble Alpes, 2016).
10. Hua, H., Chen, Y., Tao, Y., Qi, D. & Li, Y. A highly transparent haptic device with an extremely low driving voltage based on piezoelectric PZT films on glass. *Sensors Actuators A Phys.* **335**, 113396 (2022).

11. Glinsek, S. *et al.* Inkjet-printed piezoelectric thin films for transparent haptics. *Adv. Mater. Technol.* **7**, 2200147 (2022).
12. Yamakawa, K. *et al.* Novel Pb(Ti,Zr)O₃ (PZT) crystallization technique using flash lamp for ferroelectric RAM (FeRAM) embedded LSIs and one transistor type FeRAM devices. *Jpn. J. Appl. Phys.* **41**, 2630–2634 (2002).
13. Yao, Y. *et al.* Direct processing of PbZr_{0.53}Ti_{0.47}O₃ films on glass and polymeric substrates. *J. Eur. Ceram. Soc.* **40**, 5369–5375 (2020).
14. Palneedi, H. *et al.* Intense pulsed light thermal treatment of Pb(Zr,Ti)O₃/metglas heterostructured films resulting in extreme magnetoelectric coupling of over 20 V cm⁻¹ O⁻¹. *Adv. Mater.* 2303553 (2023).
15. Ouyang, J., Cormier, D., Williams, S. A. & Borkholder, D. A. Photonic sintering of aerosol jet printed lead zirconate titanate (PZT) thick films. *J. Am. Ceram. Soc.* **99**, 2569–2577 (2016).
16. Ouyang, J. Enhanced piezoelectric performance of printed PZT films on low temperature substrates. (Rochester Institute of Technology, 2017).
17. Marotta, A. R. Printable thin-film sol-gel lead zirconate titanate (PZT) deposition using nanojet and inkjet printing methods. (Rochester Institute of Technology, 2019).
18. Chen, K. C. & Mackenzie, J. D. Crystallization kinetics of metallo-organics derived PZT thin film. *MRS Online Proc. Libr.* **180**, 663–668 (1990).

4.2 Chapter conclusion

In conclusion, a one-step fast low-temperature flash lamp annealing process was developed to facilitate the direct growth of a PZT film on glass, specifically fused silica and AF32 glass. The resulting films demonstrate a piezoelectric coefficient ($e_{33,f}$) of -5 C m^{-2} . Subsequently, a piezoelectric surface haptic device was fabricated using a $1 \text{ }\mu\text{m}$ PZT film on AF32 glass. By inducing a standing Lamb wave at 40.2 kHz , an out-of-place peak-to-peak displacement of $1.5 \text{ }\mu\text{m}$ was achieved, surpassing the threshold required to create the sensation of a squeezed-air film effect on a finger.

4.3 Challenges

Our current research in this thesis marks a significant step towards the exploration of this novel process for growing PZT films. However, transforming it into a mutually beneficial process remains a challenging endeavor.

1. The effectiveness of flash lamp annealing relies on the absorption of the initially deposited PZT films. When annealing a film deposited on glass, it has been observed that a thicker film (exceeding 100 nm) is advantageous in absorbing sufficient energy to reach the crystallization temperature threshold. Consequently, it becomes challenging to perform flash lamp annealing on a thin nucleation layer (such as PTO developed by our group[95]) to facilitate crystallization along a specific orientation.

2. The films obtained exhibit a porous structure and a relatively uniform surface, leading to reduced transmittance compared to conventionally processed PZT films. This, in turn, adversely affects the piezoelectric properties. Additionally, the film displays an uneven distribution of elements, indicating inhomogeneity. Finding solutions to address these issues requires explore the underlying mechanisms.

For example, 1) consider the mechanism behind the light-material reaction for film crystallization. Are the nuclei forming inside the film body or at the bottom of the film, given that glass is amorphous? The latter possibility could potentially trigger a reaction between the film and the glass, similar to the formation of PtPb alloy during the growth of PZT on platinised silicon. 2) Lead loss: In the conventional annealing of PZT films, it is typically necessary to add 10% excess Pb into the solution to compensate for lead loss. However, it is unclear whether this amount is still sufficient in the context of this new process. Further investigation and efforts are required to determine the adequacy of this approach.

3. Experimental findings indicate that the developed one-step fast flash lamp process

is incompatible with glass materials that possess low thermal conductivity, such as soda lime glass. The inadequate heat dissipation in these glasses leads to high temperatures, causing cracks to form on the glass surface.

4. In contrast to laser annealing, which primarily affects the surface of the film, flash lamp annealing involves the absorption of light energy by both the film and the substrate. This poses a challenge when growing PZT films on polymer substrates since polymers tend to absorb light in the same UV region as PZT films, resulting in high temperatures of the polymer substrate as well.

In the end, more efforts are required to improved the quality of flash lamp annealed PZT films.

Chapter 5

Inkjet printing of indium tin oxides top electrodes

This chapter focuses on the improvement of an ITO ink through a combustion reaction to enable the printing of ITO films at low processing temperatures. The resulting printed ITO films processed at 400 °C were used as top electrodes in PZT capacitors and showed comparable results to those obtained with sputtered ITO top electrodes. The ITO/PZT/Pt stack shows a remanent polarization of 14 $\mu\text{C cm}^{-2}$, coercive field of 80 kV cm^{-1} , relative permittivity of 750 and dielectric loss of 0.1.

Authors contributions: In this work, I was responsible for developing ITO ink, conducting printing, and measuring the devices. Dr. Sebastjan Glinsek and my former colleague, Dr. Nicolas Godard, developed the PZT solution utilized in this work. Dr. Sebastjan Glinsek also helped and trained me to perform printing and electrical measurements. SIMS analysis was conducted by our colleagues, Dr. Brahime EI Adib and Dr. Nathalie Valle.

5.1 Motivation

In recent decades, oxides-based transparent and flexible electronic devices that are conformable and have a large area have become promising candidates for various applications such as sensing, imaging, energy-harvesting, healthcare, and robotics.[104] Among the various transparent conductors, oxide conductors are considered good electrodes for oxides-based electronics because of their favorable work function, ease of fabrication, superior optical properties, and excellent conductivity. Indium tin oxide (ITO) is regarded as one of the best oxide conductors and has been widely used in electronics. Currently, ITO electrodes are typically fabricated using sputtering technology. However, sputtered

ITO has relatively low transmittance (only 80% for commercial ITO/PET), which is a significant obstacle to its use in future transparent electronics.[104] The sputtered ITO electrodes require expensive ITO target, complicated process control and post-patterning through lithography, which induces extra cost and process complexity.

Recent reports have emphasized the advancement of solution-processed ITO electrodes that provide exceptional transparency and conductivity. For instance, Fellahi et al. employed spray pyrolysis to produce solution-processed ITO, which displayed a conductivity exceeding 3000 S cm^{-1} and a transmittance of up to 94%.[122] Nonetheless, the high-temperature annealing process required for solution-processed ITO, typically exceeding $500 \text{ }^\circ\text{C}$, poses a significant challenge. As previously mentioned, our objective is to utilize ITO films as a transparent top electrode in a piezoelectric actuator. Nevertheless, utilizing such a high processing temperature would result in indium diffusion into the PZT film, which would compromise the piezoelectric performance of the PZT film.

In this work, low-temperature solution-processed transparent ITO electrodes were developed using a combination of combustion synthesis and inkjet printing technology. Combustion synthesis is based on the exothermicity of redox reaction and can significantly reduce the crystallization temperature of solution-based oxide films.[83] It is quite simple and just needs to add indium nitrate as oxidizer and acetylacetone as fuel into the solution, as has been introduced in Chapter 2 (E.2. Solution combustion synthesis).

On the other hand, inkjet printing is more suitable for industrial manufacturing platforms because of its low cost, ease of process control, and high production throughput, unlike traditional solution-based methods such as spin-coating, dip coating, and spraying. Ultimately, we aim to utilize the printed ITO electrode to produce fully printed and transparent piezoelectric actuators.

In this chapter, we introduce the developed inkjet printed low-temperature processed ITO films as top electrodes of PZT film. The processing temperature is as low as $400 \text{ }^\circ\text{C}$, which enables to prevent any diffusion between ITO and PZT films. The PZT capacitors using inkjet printed exhibited and comparable ferroelectric properties with ones using the state-of-the-art sputtered ITO electrodes. The P_r and E_c are $14 \text{ } \mu\text{C cm}^{-2}$ and 80 kV cm^{-1} , respectively.

5.2 Materials and methods

5.2.1 Processing of PZT thin films

In this study, PZT films with a morphotropic-phase-boundary composition were utilized, which was deposited onto a platinised silicon substrate (SINTEF wafer, 100 nm Pt/20 nm TiO₂/500 nm SiO₂/Si) using standard chemical solution deposition via spin coating.

Prior to deposit PZT film, a solution-processed 10 nm-thick lead titanate oxide (PTO) nucleation layer was employed to promote the growth of the film along the (100) orientation, which was also deposited via a chemical solution process, as demonstrated in Godard et al. [95]. The PTO seed layer was deposited via spin coating at 3000 rpm for 30 s, followed by drying at 130 °C for 3 min, pyrolysis at 350 °C for 3 min and final crystallization in RTA furnace (AS-Master, Annealsys, France) at 700 °C for 1 min.

The PZT solution was synthesized based on a standard 2-MOE route, as previously demonstrated in [123]. Freeze-dried lead(II) acetate trihydrate (99.99%, Sigma-Aldrich, USA), titanium(IV) isopropoxide (97%, Sigma-Aldrich, USA) and zirconium(IV) propoxide (70% in propanol, Sigma-Aldrich, USA) were added and dissolved into 2-methoxyethanol (2-MOE) solvent (99.8%, Sigma-Aldrich, USA). The precursor was refluxed at 130 °C for around 2 h, distilled and diluted to obtain a final concentration of 0.3 M with a Zr:Ti=0.53:0.47 and 10% Pb excess. PZT film was spun onto the PTO nucleation layer at a spin speed of 3000 rpm for 30 s. Subsequently, the film was dried at 130 °C for 3 minutes and pyrolyzed at 350 °C for 3 minutes, both done on a hot plate. This deposition-drying-pyrolysis process was repeated four times, and then the film was crystallized for 5 minutes at 700 °C in air using a rapid thermal annealing furnace (AS-Master, Annealsys, France). The entire process was repeated three times to obtain a 500 nm-thick film.

5.2.2 Inkjet printing of ITO top electrodes

ITO ink synthesis

ITO solutions (10 ml) were created using *In(NO₃)₃* (99.99%, Sigma-Aldrich) and *SnCl₂* (99.99%, Sigma-Aldrich) salts, dissolved in 2-methoxyethanol solvent (99.8%, Sigma-Aldrich), with an In:Sn ratio of 9:1 and a concentration of 0.4 M. To produce combustion solutions, 800 μ l acetylacetone (99%, Sigma-Aldrich) and 360 μ l aqueous *NH₃*

(99%, Sigma-Aldrich, 25wt.%) were added. A mixture of 2-methoxyethanol and ethylene glycol in a volumetric ratio of 1:1 was used as solvent, resulting in inkjet-printable ink. The ITO ink that was prepared did not exhibit any signs of aging, even after being stored for near two years.

Jetting behavior of ITO

For printing, a Ceradrop X-series inkjet printer was utilized and the inks were added into DMC-11610 (Fujifilm) cartridges. Jetting was executed at 26 V and 1 kHz, with printing nozzles kept at 30°C and the substrate maintained at room temperature. The ITO ink has shown a stable jetting (Figure 5.1).

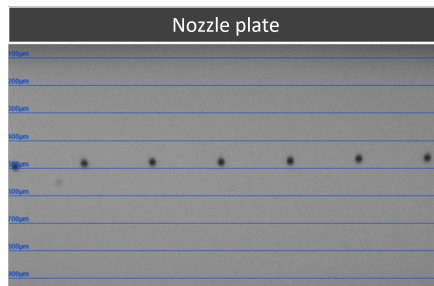


Figure 5.1: Jetting of ITO ink with a nozzle voltage of 26 V and a nozzle temperature of 30 °C.

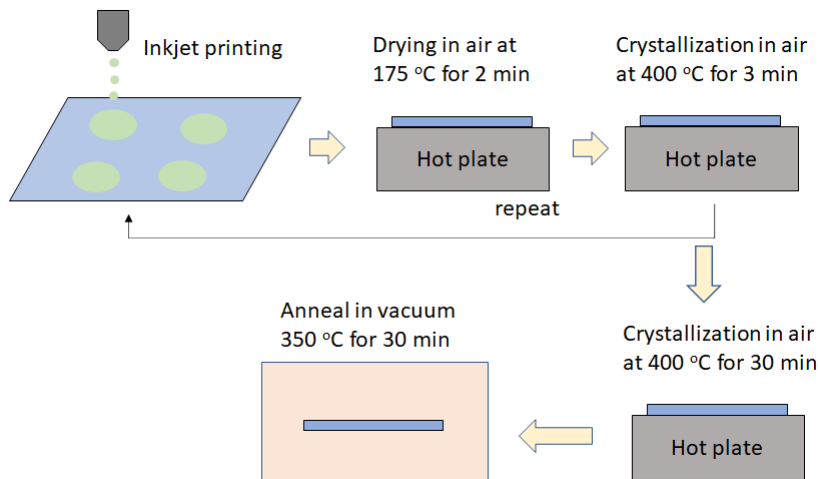


Figure 5.2: **Schematic diagram** of annealing processes of inkjet printed ITO.

Following the printing of each layer, the deposited material underwent two annealing steps. The first annealing step was performed on a hot plate at 175°C for 2 minutes, followed by a second annealing step at 400°C for 3 minutes. Upon completion of all the layers, the material underwent a final annealing step on a hot plate at 400°C for 20-30 minutes, followed by annealing in a rapid thermal annealing furnace (RTA, AS-Master,

Annealsys) under low pressure (3.72×10^{-2} mbar) at 350°C for 20-30 minutes, (see Figure 5.2).

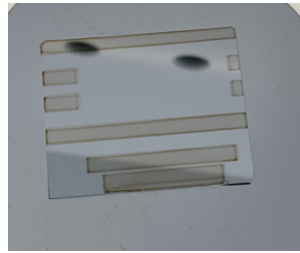


Figure 5.3: **Optical appearance** of inkjet-printed ITO rectangular patterns on silicon substrate.

Figure 5.3 displays an inkjet-printed ITO film on a silicon substrate. While a coffee ring effect is noticeable along the edge, the ITO film in the central region of the printed patterns appears to be quite smooth.

5.3 Experimental results

5.3.1 XRD and SEM of PZT thin film

X-ray diffraction (XRD) patterns were obtained on a Bruker D8 Discover diffractometer (Bruker), using $\text{Cu-K}\alpha$ radiation, in the 2θ range from 20 to 60° with a step size of 0.02° . More descriptions on XRD measurement have been provided in Appendix 4.1 on Page 189. The XRD pattern of the as-prepared PZT film is shown in Figure 5.4a, which indicates a desirable $\{100\}$ orientation. Additionally, a dense microstructure of the PZT

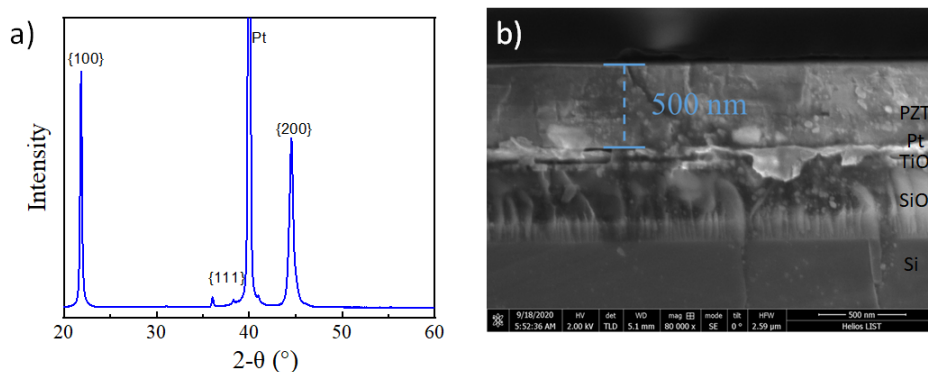


Figure 5.4: **Characterizations of PZT film.** a) X-ray diffraction (XRD) of PZT film deposited on platinised silicon substrate (SINTEF wafer, 100 nm Pt/20 nm TiO_2 /500 nm SiO_2 /Si). b) Cross-sectional scanning electron microscope (SEM) image of PZT film deposited on platinised silicon substrate. Note that in order to promote PZT film to grow along $\{100\}$ orientation, a 10 nm-thick PTO nucleation was used.

film is revealed by the cross-sectional scanning electron microscope (SEM, FEI Helios NanoLab 650 microscope) image in Figure 5.4b. More descriptions on SEM measurement have been provided in Appendix A3 on Page 191. The various characterizations performed indicate that the PZT film is of good quality and suitable for use in estimating inkjet printed ITO electrodes.

5.3.2 Optical transparency of ITO film

Transmittance was measured via Perkin Elmer Lambda 1050 spectrophotometer, as shown in Figure 5.5. At the wavelength of 550 nm the transmittance reaches up to 89%. Although in this study the whole device is not transparent, its good transmittance provides potential for the applications in transparent electronics.

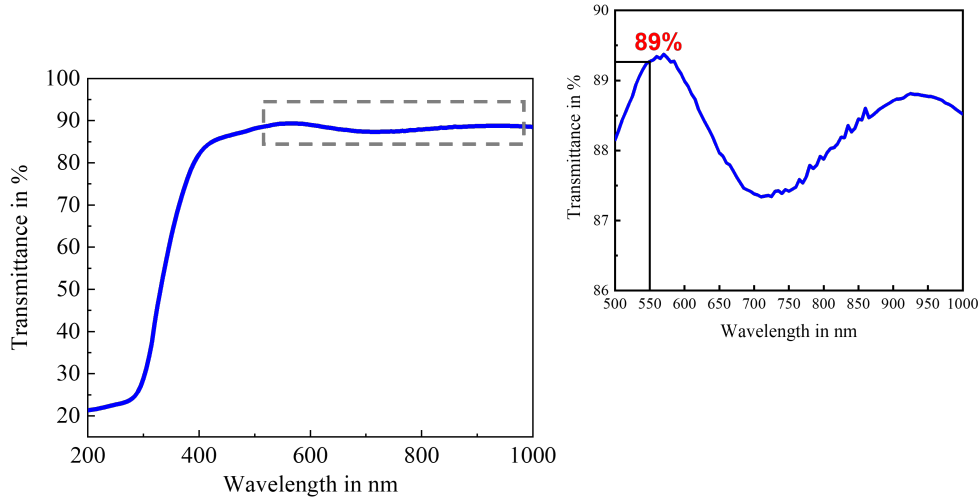


Figure 5.5: **Optical transparency.** Transmittance of $1 \times 1 \text{ cm}^{-2}$ -large and 120 nm-thick inkjet printed $400 \text{ }^\circ\text{C}$ -processed ITO film on fused silica glass.

5.3.3 Electrical conductivity of ITO film

A $1 \times 1 \text{ cm}^{-2}$ -large ITO film was printed on a fused silica substrate, and its thickness was measured using a profilometer. Two scans were performed along different directions (as shown in Figure 5.6), and the estimated thickness of the film was found to be around 120 nm in the center of pattern. We can also observe that the thickness at the edge is much thicker, due to the coffee ring effect.

The sheet resistance, denoted by R_s , of an indium tin oxide (ITO) film was determined using a four-probe in linear configuration with a Keithley 2614B source meter, as depicted

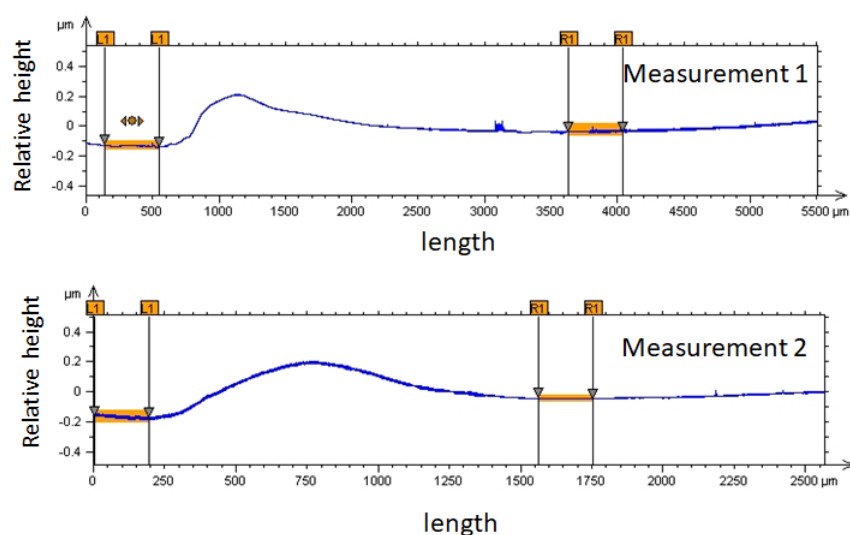


Figure 5.6: **Thickness profile** of printed ITO film on fused silica substrate.

in Figure 5.7 and also in Appendix A4.1 on Page 192. The sheet resistance of the ITO film was measured to be approximately $70 \Omega/\square$, with measurements taken at the central point of the ITO pattern, marked by a red box in Figure 5.8.

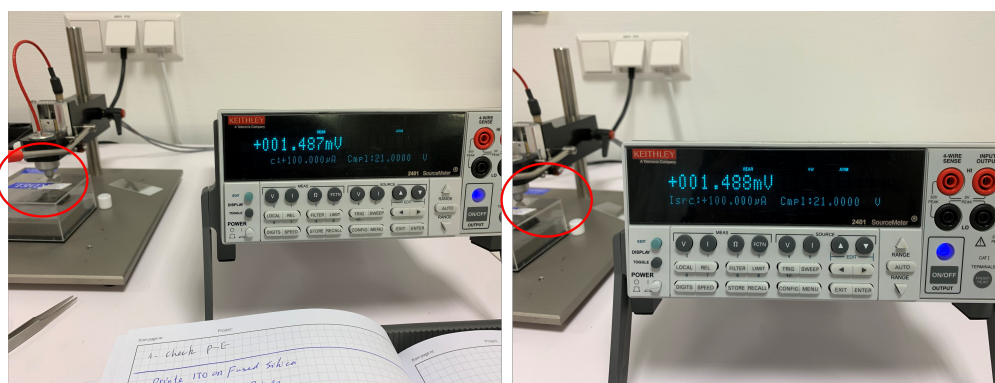


Figure 5.7: **Sheet resistance measurements** of inkjet printed ITO film on fused silica glass. In the measurements, current was set as $100 \mu\text{A}$. ITO film contacted with probe is marked by red box.

The corresponding conductivity of inkjet printed ITO film can be calculated through the equation:

$$\sigma = \frac{1}{R_s t} \quad (5.1)$$

where t is the thickness of ITO film (120 nm thick). This way, the average conductivity is obtained to be 1250 S cm^{-1} . It is worth noting that these measurements were performed after annealing the ITO film in a vacuum.

As previously stated in Chapter 2, ITO's parent material is indium oxide, a semiconductor substance. It is well-known that metal-oxide semiconductors are susceptible to changes in temperature and humidity within their ambient surroundings. It was ob-

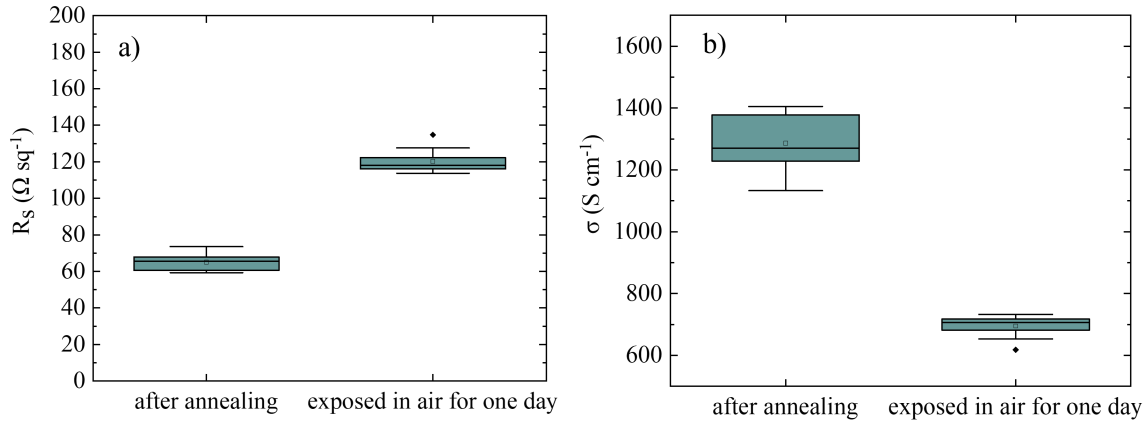


Figure 5.8: **Electrical conductivity.** a) Sheet resistance of inkjet printed ITO film after annealing and after exposed in air for one day, obtained by measuring 10 points in the center of printed ITO pattern. b) corresponding calculated conductivity.

served that the conductivity of ITO films deteriorates when exposed to air. Figure 5.8 illustrates the sheet resistance and corresponding conductivity of an ITO film after being exposed to air for one day. The conductivity value decreased from 1250 to 700 S cm^{-1} . Nonetheless, the conductivity can be restored by re-annealing the films at 350 °C under vacuum conditions. Another possible solution to this issue is to apply a passivation layer to the ITO film in order to prevent its exposure to air.

5.3.4 SIMS of ITO/PZT stacks

To investigate the interface between inkjet-printed 400 °C ITO film (2x2 mm²-large and 200 nm thick) and the PZT film, secondary ion mass spectrometry (SIMS) was performed prior to using ITO as the top electrode of the PZT capacitor (Figure 5.9). More details on SIMS have been described in Appendix A2 on Page 190. In addition, SIMS analysis was conducted on a sputtered ITO electrode (2x2 mm²-large and 100 nm thick) on the same PZT film as a reference. While a sharper interface between sputtered ITO and PZT was observed due to the smooth interface, the spectra of sputtered ITO/PZT and inkjet-printed ITO/PZT are essentially identical. Small amounts of other elements, such as Pb, Zr, Ti, and Pt, were detected at the beginning of the sputtering process. These elements are attributed to the mass effect of the SIMS tool used in this work and are not considered as diffusion. In our previous work, we employed sputtered ITO electrodes in the production of piezoelectric devices using PZT, and the results demonstrated excellent performance as reported in the study by Glinsek et al. (2020).[17] It is crucial to ensure

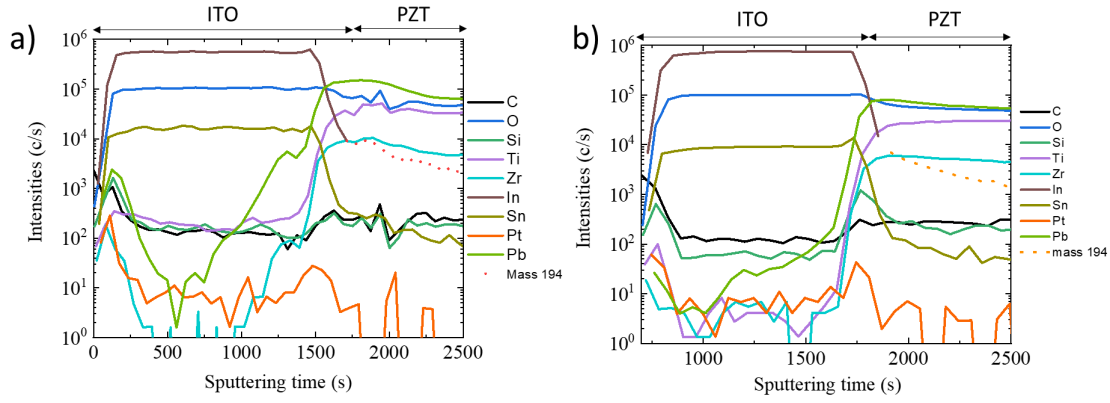


Figure 5.9: **SIMS analysis** of a) inkjet printed ITO electrode on PZT film. b) Sputtered ITO electrode on PZT film. Note that sputtered ITO was annealed at 300 °C for 20 min in air.

that no diffusion of other elements occurs into the ITO electrode, as any such diffusion could lead to the malfunctioning of the device.

5.3.5 Ferroelectric properties of ITO/PZT/Pt stacks

Small ITO top electrodes

The top electrodes of the PZT film were ITO dots, which were printed using a layer-by-layer process onto the film's surface. Figure 4.9a provides an optical appearance of the printed ITO dots, which covered an area of 0.226 mm². The initial ITO layer was directly printed onto the PZT film, and subsequent layers were deposited on the previously crystallized layers, resulting in differences in droplet size due to the distinct surface energies of the two films. Figure 5.10 indicates that the initial layer was larger than the later layers due to the difference between the surface energies of PZT film and ITO film.

Using a profilometer shown in Figure 5.10b, the thickness of the ITO electrodes was estimated to be approximately 200 nm. The coffee ring effect was not observed in the printed ITO electrodes, as shown in Figure 5.10b.

Figure 5.11 shows the $P(E)$ loop of an ITO/PZT/Pt capacitor measured at 100 Hz, exhibiting a remanent polarization P_r^+ and P_r^- of 13 and 16 $\mu\text{C cm}^{-2}$ and the coercive field E_c^+ and E_c^- of 80 kV cm^{-1} and 43 kV cm^{-1} , respectively. The current versus electric field $I(E)$ loop has two distinct peaks, indicating domain switching, a common ferroelectric film characteristic. The $P(E)$ and $I(E)$ loops obtained at 10 Hz (Figure 5.12b) have similar characteristics, while those obtained at 1000 Hz (Figure 5.12a) are broader due

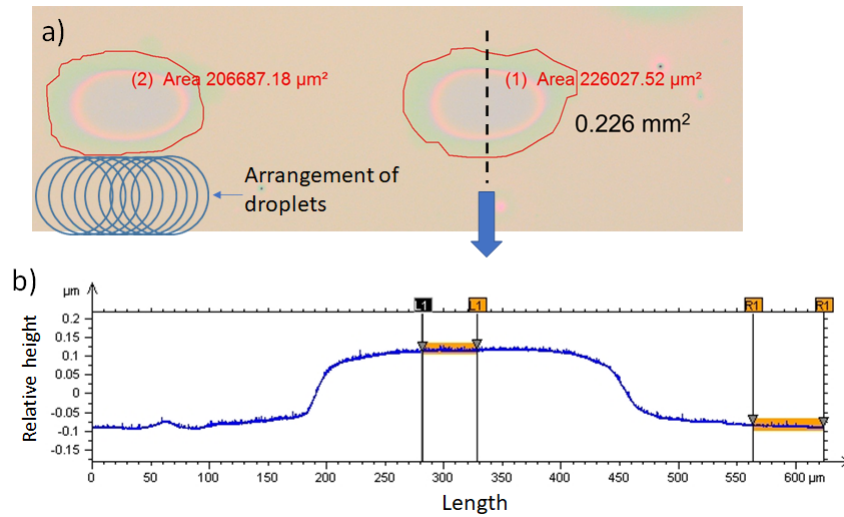


Figure 5.10: **Thickness of electrode.** a) Optical appearance of inkjet printed ITO dots as top electrodes on PZT film. b) Thickness profile of one of inkjet printed ITO electrode, which was scanned along the black dash line in a). 15 layers were printed in total.

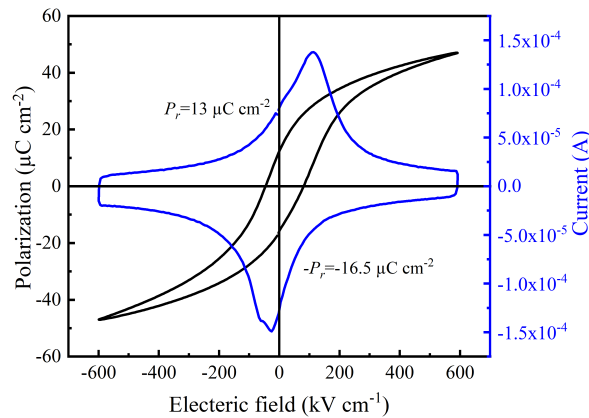


Figure 5.11: **Ferroelectric property.** Polarization P and current I versus electric field E loops measured at 100 Hz.

to the increased dielectric losses observed with increasing frequency, resulting from the relatively lower conductivity of the inkjet-printed ITO electrode.[17]

To evaluate the performance of PZT capacitors employing inkjet printed ITO as top electrodes, it is worthwhile to compare them with those utilizing sputtered ITO and Pt electrodes, as shown in Figure 5.13. Figure 5.13a shows their $P(E)$ loops measured at 100 Hz. Although E_c of inkjet printed ITO/PZT/Pt is slightly higher than the ones using sputtered ITO and Pt, their maximum polarization value P_{max} and P_r stay rather comparable. The corresponding current density versus electric field $J(E)$ loops are shown in Figure 5.13. The peak current density (J) of Pt/PZT/Pt capacitor is double of ones using ITO as electrodes (both sputtered and inkjet printed ITO), thanks to its extremely

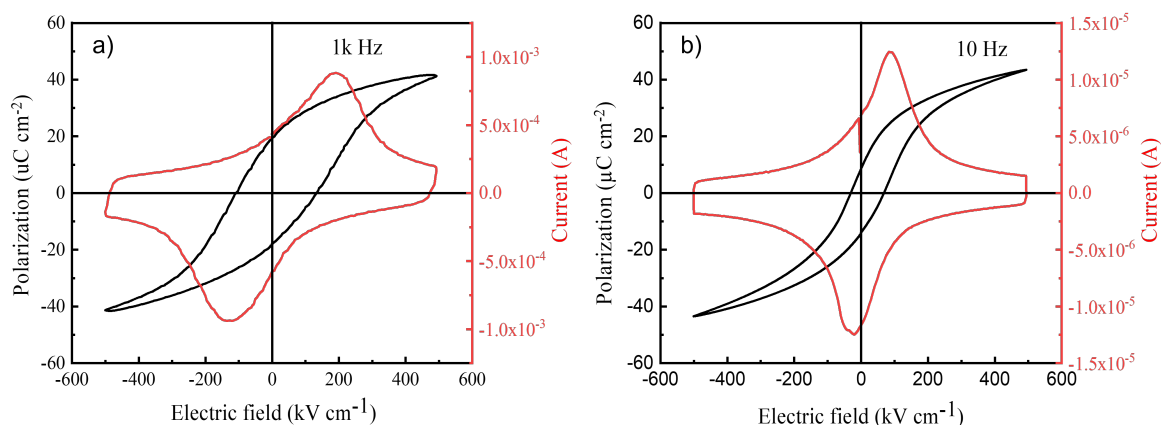


Figure 5.12: **Ferroelectric property.** $P(E)$ and $I(E)$ loops measured at a) 1 kHz and b) 10 Hz.

high conductivity (see $J(E)$ in Figure 5.13b). Importantly, it is observed that the $J(E)$ loops of capacitors using inkjet printed ITO and sputtered ITO electrodes are comparable. This comparison confirms that inkjet printed ITO electrode is an alternative of sputtered ITO, which enables direct pattern and lithography free.

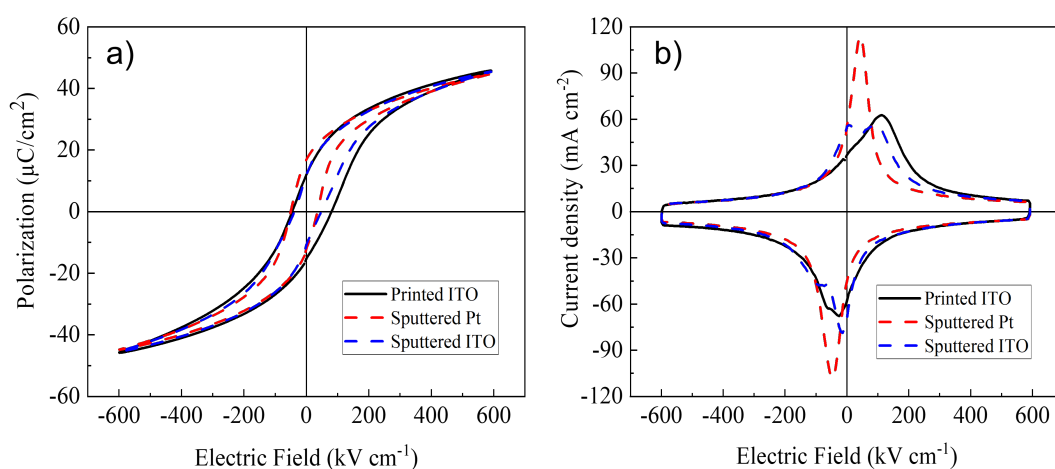


Figure 5.13: **Ferroelectric property comparison.** a) $P(E)$ and b) $J(E)$ loops of PZT capacitors with inkjet printed 200 nm-thick ITO, sputtered 100 nm-thick ITO, and sputtered 100 nm-thick Pt as top electrodes, respectively, were measured at 100 Hz. The sputtered ITO and Pt electrodes were deposited in-house. The conductivity of sputtered ITO was enhanced by post-annealing at 300 °C for 20 minutes in air, resulting in a conductivity of 3000 S cm^{-1} . The dimension of sputtered ITO and Pt circular electrodes are 200 μm and 100 μm , respectively. It is important to note that PZT films were deposited on platinised silicon substrate (SINTEF Wafer) in all cases, whose information has been introduced earlier.

Figure 5.14 depicts the variation of relative permittivity (ϵ_r) and dielectric loss ($\tan\delta$) with respect to electric field. The measurements were conducted by applying an AC signal with a frequency of 1 kHz and amplitude of 100 mV on top of a staircase-like DC bias with a maximum amplitude of 200 kV/cm. The values of relative permittivity (ϵ_r) and dielectric loss ($\tan\delta$) at zero field are 750 and 0.15, respectively. The loops exhibit an asymmetrical shape, which can be attributed to the asymmetry of the top and bottom electrodes (i.e., ITO and Pt electrodes, respectively).

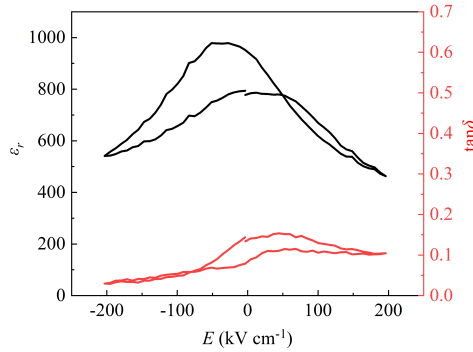


Figure 5.14: **Dielectric property.** Relative permittivity ϵ_r and dielectric loss $\tan\delta$ versus electric field measured via applying an ac signal at 1 kHz frequency and 100 mV amplitude.

Large ITO top electrodes

In the aforementioned measurements, small ITO electrodes were utilized. It is well-known that device properties can deteriorate when large electrodes are employed, owing to the increased density of defects with increasing electrode area. In light of this, we also investigated a capacitor with large inkjet-printed ITO electrodes, with an area of 4 mm² (2 mm × 2 mm square). The $P(E)$ and $I(E)$ loops obtained at 100 Hz are illustrated in Figure 5.15. Notably, the P_r ($11 \mu\text{C cm}^{-2}$ in P_r^- and $7 \mu\text{C cm}^{-2}$ in P_r^+) decreased in comparison to those obtained using small ITO electrodes at the same electric field (Figure 5.11). Additionally, the corresponding $I(E)$ loop exhibited less sharp peaks.

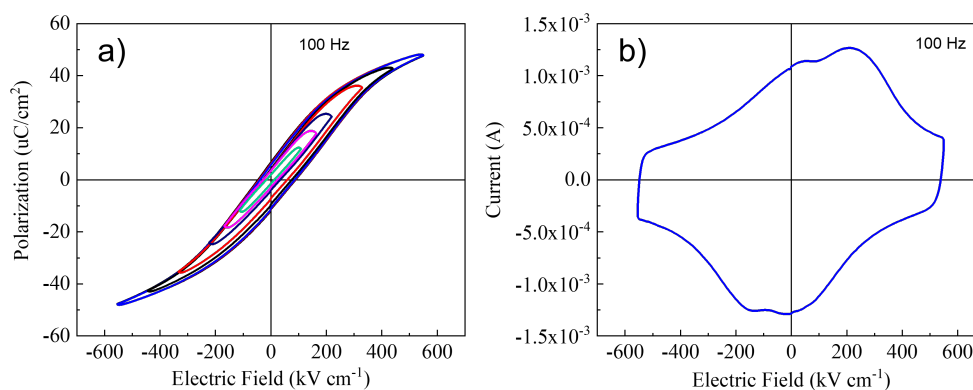


Figure 5.15: **Ferroelectric property of devices with big ITO electrode.** a) $P(E)$ b) $I(E)$ loops of PZT capacitors using 4 mm^2 and 90 nm -thick electrodes. PZT film used in this measurement is 900 nm -thick and deposited on platinised silicon substrate using a standard CSD process.

The $\epsilon_r(E)$ and $\tan\delta(E)$ hysteresis curves of PZT capacitors, employing larger ITO electrodes (4 mm^2), were measured at a frequency of 1 kHz (Figure 5.16). The outcomes show that the $\epsilon_r(E)$ values remain relatively constant, while the $\tan\delta(E)$ values at the zero field exhibit a significant increase, up to 0.3 . This finding suggests that using large ITO electrodes can result in elevated losses, due to the relatively low conductivity of inkjet-printed ITO.

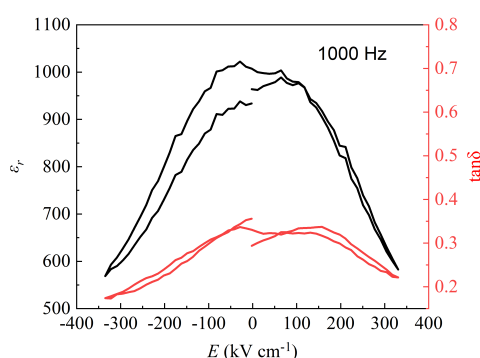


Figure 5.16: **Dielectric property of devices with big ITO electrode.** $\epsilon_r(E)$ and $\tan\delta(E)$ loops of PZT capacitors using large ITO electrodes. The sample is same with ones used for the measurements in Figure 5-15.

5.4 Chapter conclusion

To prevent indium diffusion into PZT film, a low-temperature processed inkjet printed ITO was developed based on a combustion synthesis. The processing temperature of inkjet printed ITO electrode is as low as $400 \text{ }^\circ\text{C}$. PZT capacitors using the inkjet printed

small ITO electrodes displayed ferroelectric properties comparable to those using highly conductive sputtered ITO electrodes. An increase of dielectric loss was observed when using large ITO electrode.

5.5 Challenges

Despite ongoing efforts, utilizing ITO electrodes in ferroelectric capacitors remains a challenge. The relatively low conductivity of ITO electrodes, leads to significant dielectric losses when devices operate at high frequencies, especially when using large ITO electrodes. This can be clearly observed in the next chapter when using ITO electrode in an ultrasonic haptic devices working at beyond 20 kHz.

A large stress between ITO and PZT films was also observed when using a large ITO electrode. When applying voltage to inkjet printed large ITO electrodes, ITO films cracks (see Figure 5.17).

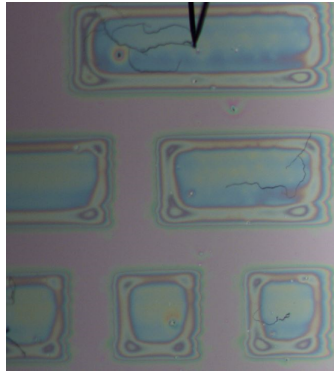


Figure 5.17: Image that shows inkjet-printed large ITO electrodes ($2 \times 2 \text{ mm}^2$, $2 \times 4 \text{ mm}^2$, and $2 \times 6 \text{ mm}^2$) on a 500 nm-thick PZT film. Upon applying voltage to these electrodes, the ITO films exhibit cracking. The inset depicts a cross-sectional SEM image of a PZT thin film.

Remarkably, by annealing the sample at 100-150 °C followed by immediate immersion in acetone, both the ITO and PZT films were lifted off from the Pt substrate, as shown in Figure 5.18. This is corroborated by performing a scan of the thickness profile across the width of the pattern (Figure 5.19). For applications requiring device isolation, this technique could be a convenient means for roughly patterning PZT films.

5.6 Outlook

The focus of this study is on utilizing inkjet-printed ITO as the top electrode of PZT capacitors to propose the possibility of achieving a transparent capacitor in the future. However, our low-temperature inkjet printing process for ITO films, which we have developed, can also be applied to various other applications. As an example, a fully

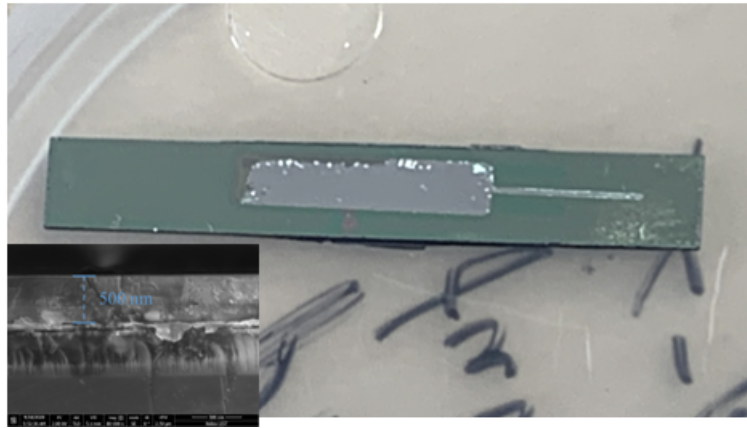


Figure 5.18: Photograph shows the sample with large ITO electrodes after immersion in acetone, resulting in the lifting off of both the ITO and PZT films.

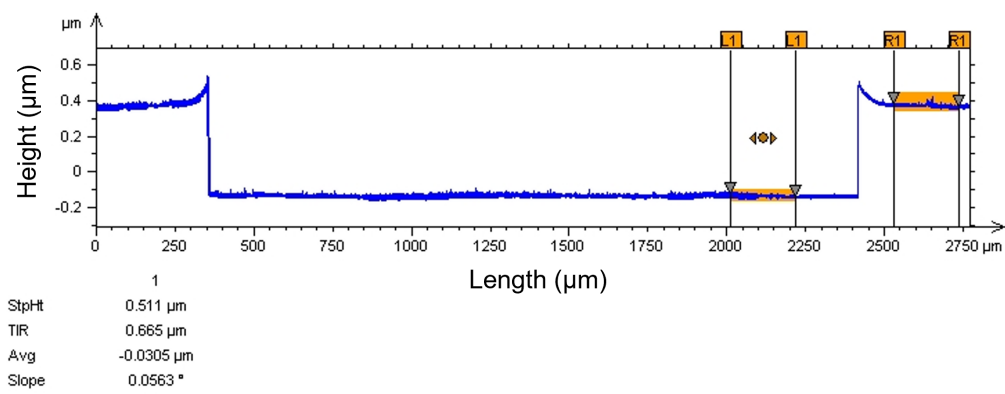


Figure 5.19: The thickness profile of the lifted-off area depicted in Figure 5.18.

transparent antenna has already been printed using this technique, whose performance is comparable with those made of sputtered ITO films.

Chapter 6

All inkjet-printed haptic actuators on platinised Si substrate

This chapter demonstrates the development of all-inkjet printed haptic actuators on platinised silicon substrates using inkjet-printed ITO and PZT films. The device was able to produce an out-of-plane deflection beyond the specification for human finger sensitivity ($1\ \mu\text{m}$) at 22 V and 21.23 kHz. Lithography and etching were not utilized in the direct patterning of the actuators.

Authors contributions: In this work, I developed ITO ink, conducted printing of all layers, designed and measured the devices. I prepared PZT ink utilized in this work, while Dr. Sebastjan Glinsek and my former colleague, Dr. Nicolas Godard, developed the recipe of PZT ink. I received assistance from my colleague Dr. Veronika Kovacova in measuring the all-printed haptic devices. Alfredo Blazquez Martinez helped to perform the SEM analysis.

6.1 Motivation

Recently, Glinsek et al. developed a transparent haptic device on fused silica glass by employing sol-gel PZT thin film.[17] The device achieved transparency through the utilization of interdigitated ITO electrodes (IDE), which took advantage of the longitudinal piezoelectric coefficient (d_{33} or e_{33}). This innovative design facilitated the generation of a Lamb wave at a frequency of 73 kHz, resulting in an out-of-plane displacement of $2.9\ \mu\text{m}$ at a unipolar voltage of 150 V. However, the limitation of IDE structures is their requirement for high operating voltages compared with the typical metal-insulator-metal (MIM) structure. In their study, the PZT film was deposited onto a full wafer using spin coating, while the ITO electrode underwent patterning through lithography, leading to

additional costs and process steps.

The precise patterning of PZT thin films is crucial for fabricating functional haptic devices suitable for practical applications. One promising approach for achieving direct patterning is through inkjet printing (IJP) technique, which allows for the direct structuring of these films using computer-aided design (CAD). Notably, inkjet printing offers an advantage over spin coating as it is a wasteless process, unlike spin coating, which often leads to over 90% solution wastage. These advantages make inkjet printing compatible with large-scale fabrication in the field of microelectronics.

However, all-inkjet printing of a multi-layer stack poses challenges due to differences in wetting properties among materials, leading to poor reproducibility and performance. Although the concept of all-inkjet printing has been demonstrated for organic thin-film transistors,[\[124\]](#) its application in inorganic piezoelectric devices is yet to be proven. Several challenges need to be addressed, including the rational design of crystallization temperatures for each layer, achieving desired piezoelectric properties while avoiding undesired orientation and rough surfaces in inkjet-printed piezoelectric thin films, and the necessity for a printable nucleation layer for {100}-oriented MPB PZT. Additionally, a printable conductive material that is compatible with PZT thin films is required as electrodes. Previous study has shown the use of inkjet-printed silver dots as top electrodes on spin-coated PZT thin films; however, the electrode size was limited to a few hundred micrometers.[\[123\]](#)

This chapter presents an all inkjet printing approach employed to create MIM-structured piezoelectric haptic actuator on a 0.3 mm-thick platinised Si substrates. The haptic actuator was constructed by utilizing an inkjet printed ITO film as the top electrode and an inkjet printed PZT film as the functional piezoelectric layer. The all-printed haptic device demonstrates an out-of-plane peak-to-peak displacement of 1.2 μm , meeting the threshold required to generate a haptic effect.

6.2 Chosen films deposition technologies and thickness

Table 6.1 summarizes the deposition methods employed for the films. A 10 nm layer of TiO_2 and a 100 nm-thick layer of Pt were deposited on a 500 nm-thick SiO_2 layer coated on a 0.3 mm-thick Si substrate using evaporation techniques. Note that Ti was deposited by evaporation and then annealed at 700 $^\circ\text{C}$ in air for 5 min via RTA to form TiO_2 .

Nucleation PTO, piezoelectric PZT, and top electrode ITO films were created using inkjet printing, with their respective thicknesses listed in Table 6.1.

Table 6.1: Layer thickness and deposition methods

Functions	Materials	Techniques	Thickness
Substrate	SiO ₂ /Si	-	0.3 mm
Adhesion layer	TiO ₂	Evaporation	10 nm
Bottom electrode	Pt	Evaporation	100 nm
Nucleation layer	PTO	Inkjet printing	10 nm
Piezoelectric layer	PZT	Inkjet printing	1 μm
Top electrode	ITO	inkjet printing	100 nm

6.3 Ink synthesis and jetting parameters

Synthesis of printable inks is the first step in the development of printing process. In our previous reports, in-house processed solutions suitable for spin coating have been developed to deposit PTO,^[95] PZT^[108] and ITO^[125] films. The inks in this work were synthesized by modifying those former solutions. The details of inks formula were collected in Table 5-1.

Table 6.2: PTO, PZT and ITO inks formula, developed in this work.

Functional materials	Ink concentration	Added organics	Solvent	Lifetime
PTO	0.1 M	-	1-methoxy-2-propanol	1 month
PZT	0.4 M	1,3-propandiol	2-MOE	6 months
ITO	0.4 M	ethylene glycol	2-MOE	1.5 year

The PTO ink used a 0.1 M 1-methoxy-2-propanol-based solution with a 30% lead excess. Either concentrating or adding co-solvent can not realize a {100}-oriented PTO thin film. The trick to print such a low-viscosity ink is to use a cartridge with small droplet volume, 1 pl in our case (DMC-11601 type), because it requires less viscous inks. The final PTO ink provided stable jetting at 1 kHz, a nozzle voltage of 20 V and with nozzle temperature of 30 °C.

The PZT ink was formulated using a spin-coating solution with a Zr:Ti ratio of 53 : 47, 10% excess lead, and a concentration of 0.3 M in 2-methoxyethanol (2-MOE). To increase

ink density and viscosity, the solution was concentrated to 0.4 M and 1,3-propanediol (1-3-P) was used as a co-solvent at a ratio of 3 : 2 (1-3-P:2-MOE). The resulting modified ink was stable and suitable for printing with DMC-11610 cartridges, which have a nominal droplet volume of 10 pl. The ink exhibited stable jetting at a frequency of 2 kHz, a nozzle voltage of 26 V, and a nozzle temperature of 30 °C, with no nozzle clogging or droplet deviations observed.

Table 6.3: Conditions set in inkjet printer to print these films, and their crystallization temperature.

ink	cartridge nozzle size	substrate tempera- ture	nozzle tempera- ture	voltage	frequency	crystallization tempera- ture
PTO	1 pl	25 °C	30 °C	20 V	1000 Hz	700 °C
PZT	10 pl	25 °C	30 °C	26-29 V	2000 Hz	700 °C
ITO	10 pl	25 °C	30 °C	26-29 V	1000 Hz	400 °C

Chapter 5 has provided a description of the ITO ink formula and printing parameters, which have also been compiled in Tables 6.2 and 6.3. Figure 6.1 shows the stable jetting properties of PZT and ITO inks.

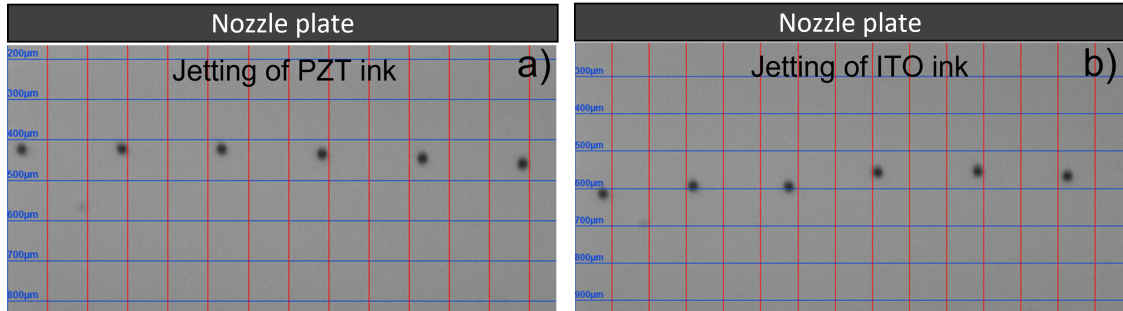


Figure 6.1: **Depiction of the jetting process** for a) PZT ink and b) ITO ink, utilizing the conditions outlined in Table 6.3.

6.4 Inkjet printing and thermal annealing process

Inks were injected into cartridges using a 0.2 µm PTFE filter. Then, the cartridges were mounted onto the printhead of a Ceradrop X-Serie (MGI Group, France) inkjet printer. The distance between printhead and substrate surface was always set as 0.7 cm.

To enhance the surface energy, the platinised Si substrate (SINTEF wafer) was heated at 400 °C for 5-10 minutes before printing. The first step involved printing a single layer of PTO nucleation onto the Pt surface. This was followed by drying at 130 °C for 3

minutes and pyrolyzing at 350 °C for 3 minutes, both performed on a hot plate. The final step was to crystallize the PTO film via RTA (AS-Master, Annealsys) at 700 °C for 1 minute in air.

After the PTO nucleation was crystallized, the PZT film was printed onto it. The printed layers were dried at 175 °C for 1 minutes and pyrolyzed at 350 °C for 3 minutes, both on a hot plate. This printing-drying-pyrolysis process was repeated six times before crystallizing the film in air at 700 °C for 5 minutes via RTA. This entire printing-drying-pyrolysis-crystallization process was repeated six times (36 layers in total) to achieve a PZT film thickness of approximately 0.9 μm .

In this case, 400 °C-process was used to crystallize ITO. Following the deposition of each layer, the deposited ITO layer underwent two annealing steps. The first annealing step was performed on a hot plate at 175°C for 2 minutes, followed by a second annealing step at 400°C for 3 minutes. Upon completion of all the layers (8 layers to achieve around 100 nm), the material underwent a final annealing step on a hot plate at 400°C for 20-30 minutes, followed by annealing in a rapid thermal annealing furnace (RTA, AS-Master, Annealsys) under low pressure (3.72×10^{-2} mbar) at 350°C for 20-30 minutes.

6.5 Device design and finite element modelling

For this study, we employed inkjet printing to create patterns on 0.3 mm-thick platinised silicon substrate with uniform dimensions of 40 mm in length and 10 mm in width for the haptic device. Two identical actuators were built and arranged in a symmetrical manner on the Si plate, with a spacing of 26.7 mm between them. The dimensions of the haptic actuator are 1 mm in length and 10 mm in width.

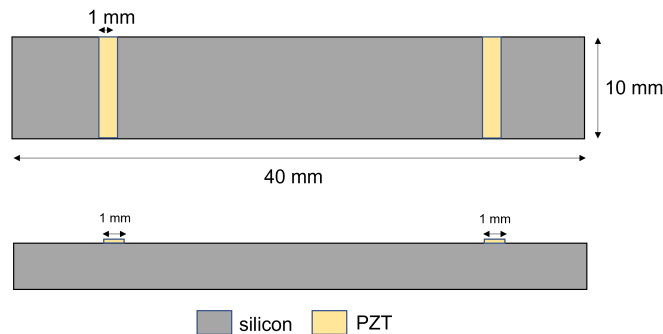


Figure 6.2: **Finite element modelling.** Schematic diagram of haptic design based on 0.3 mm Si plate, used in the modelling.

Piezoelectricity module in COMSOL software was utilized to carry out finite element modeling and determine the resonance frequency at which the A0 Lamb mode was stim-

ulated. The size of the haptic device utilized in the modeling can be observed in Figure 6.3. Analysis of the eigenfrequency indicated that a Lamb wave was stimulated at a resonant frequency of 21.9 kHz.

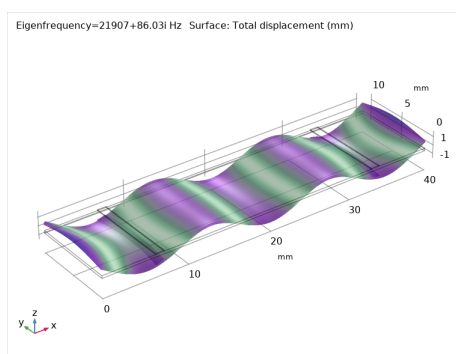


Figure 6.3: **Mode shape** obtained from the modelling, at its resonance.

6.6 Printing design

Based on the modeling, a pattern was designed for printing haptic devices, as shown schematically in Figure 6.4. The design involves two actuators positioned on a platinised silicon substrate with 0.3 mm in thickness and 40 mm x 10 mm in size. The actuators are spaced apart by 26.7 mm. The lengths of the PTO, PZT, and ITO films are 4 mm, 4 mm, and 1 mm, respectively, while their corresponding widths are 10 mm, 10 mm, and 8 mm. Note that to prevent contact issues between the ITO and Pt electrodes, the ITO electrode does not span the entire width.

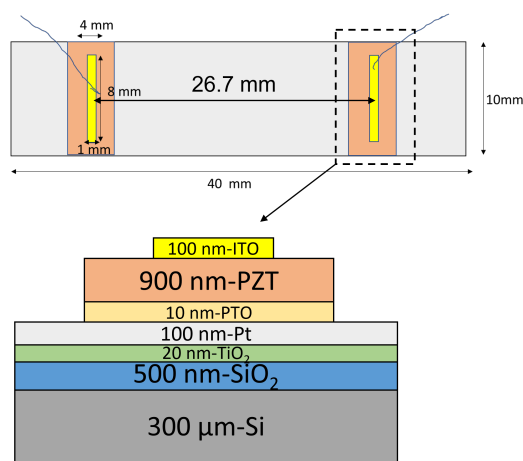


Figure 6.4: **Schematic diagram of the design** of all inkjet printed haptic device.

To verify the precise dimensions and thickness of the inkjet-printed films, profile maps were generated as shown in Figure 6.5. The lengths of the PTO, PZT, and ITO films were found to be 4 mm, 3.6 mm, and 1 mm, respectively. The PZT and ITO films were accurately positioned at the center of the PTO film. While the coffee ring effect was

observed at the edges of the PZT film, it was not present in the center. The thicknesses of the PZT and ITO films were measured to be 900 nm and 100 nm, respectively, which aligned with our initial design and SEM results which will be shown later. These findings confirm the accuracy of our printing process.

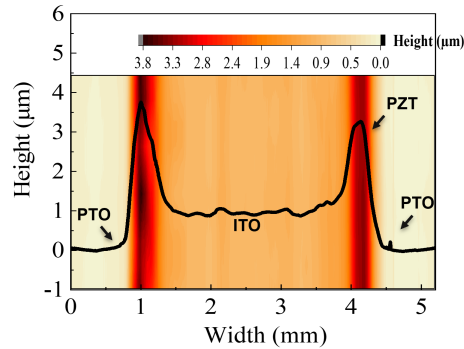


Figure 6.5: 1D and 2D profilometry of the printed device.

6.7 Characterizations of inkjet printed actuators

6.7.1 Phase composition

θ - 2θ XRD patterns were obtained on a Bruker D8 diffractometer. More descriptions on XRD measurement have been provided in Appendix A1 on Page 189. The XRD pattern presented in the figure depicts the ITO/PZT film that was inkjet-printed with the assistance of PTO nucleation. The pattern shows a prominent $\{100\}$ orientation in the 0.9 μm -thick PZT film (Fig. 3b). It should be noted that the strongest signal from the ITO film comes from the (222) reflection. This plane coincides with the (110) reflection of the PZT film. Additionally, three Pt peaks were observed because our X-ray diffraction tool operates with various wavelengths ($\text{Cu } \alpha_1$, $\text{Cu } \alpha_2$, $\text{Cu } \beta$ radiations, as marked in Figure 6.6), which leads to the shift of the platinum peak. The variation between these three wavelengths appears when measuring highly dense and oriented samples, such as $\{111\}$ -oriented platinum.

6.7.2 Microstructure characterization

Scanning electron microscopy (SEM, FEI Helios NanoLab 650 microscope) was performed to study the microstructure of printed films. More descriptions on SEM have been provided in Appendix A3 on Page 191. The cross-sectional SEM image of the all-inkjet-printed device is shown in Figure 6.7. The PZT film exhibits a dense columnar structure, with grains extending across the entire thickness of the film. The thickness of the PZT

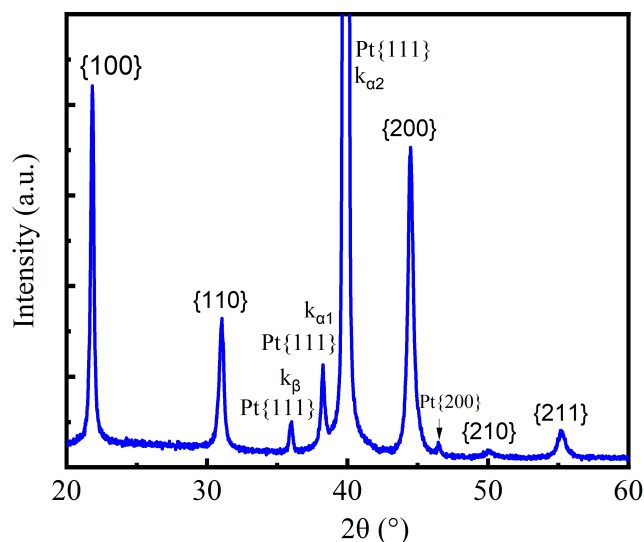


Figure 6.6: **XRD pattern** of inkjet printed actuator, identified via PZT and In_2O_3 powder diffraction file (PDF) No 01-070-4264 and No. 71-2194, respectively.

film was measured to be 900 nm. The printed ITO film displays a textured structure, with a thickness of 100 nm, verifying that the combustion process can crystallize ITO film at 400 °C. Clear interfaces between different crystallized layers, particularly between ITO and PZT, are observed. These results demonstrate that inkjet printing can effectively fabricate layered structures with well-defined interfaces.

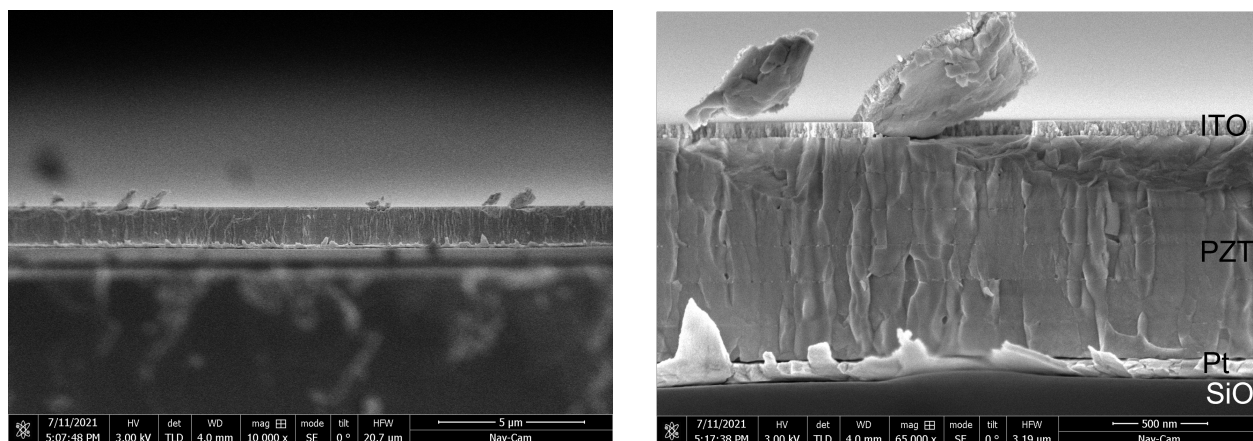


Figure 6.7: **SEM**. Cross-sectional SEM images of all inkjet-printed haptic actuator (low-resolution image (left) and zoomed-in image (right)).

6.7.3 Electrical measurement

Ferroelectric and dielectric measurements were performed using a TF Analyzer 2000 (aixACCT, Germany). Polarization-electric field $P(E)$ hysteresis loops were measured

using a triangular waveform, while relative permittivity versus electric field $\epsilon_r(E)$ loops were measured at a DC bias with a small ac signal at 1 kHz. More details have been provided in Appendix A4.2 on Page 192.

The P-E loop of per printed haptic actuator is shown in Figure 6.8a, which reveals a non-switching behavior. To prevent damage to the haptic actuator, a voltage limit of 10 V was applied during the measurement. However, this voltage level is likely insufficient to induce a switching behavior. This has been shown in Figure 5.15 in Chapter 4 (Page 131). Additionally, the relatively low conductivity of the ITO electrode results in a reduction of the voltage applied to the PZT film, which may be another reason. This also results in a rather high dielectric loss of 0.9. Although it is a significant problem that needs to be addressed in the future, I continued to measure the device in this case.

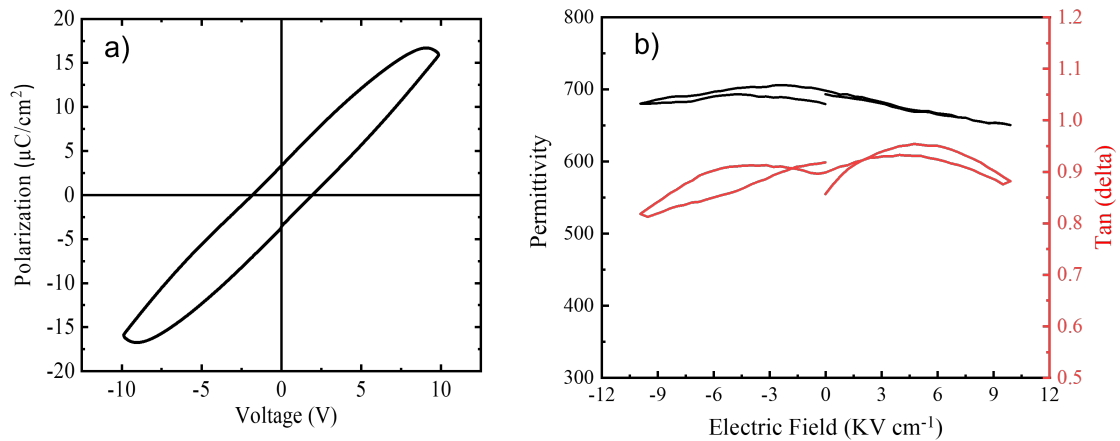


Figure 6.8: **Electrical measurement of inkjet printed haptic actuator:** a) polarization versus voltage loop measured at 100 Hz, b) capacitance and dielectric loss versus electric field, measured at 1 kHz.

6.8 Acoustic measurements

The actuators, all of which were printed using inkjet technology, were connected in series using copper wires attached with silver epoxy. The haptic device was affixed to flexible bars that were suspended, and then it was positioned on a computer-controlled stage that was constructed in-house. An electrical signal was generated using a wavefunction generator (Agilent 33210A) and then amplified 50 times using a Falco amplifier (WMA-300). This amplified voltage signal was then used to operate the haptic device. The out-of-plane displacement of the haptic device was monitored using a vibrometer (Polytec OFV-5000), which recorded data from the back of the device. The entire setup was controlled by a LabVIEW program (National Instruments) that also controlled the

vibrometer. More details have been provided in Appendix A5 on Page 195.

In the haptic measurement, a reduction in current was achieved by connecting two actuators in series, halving the total capacitance. Experimental results indicate a resonant frequency of 21.23 kHz. Line scans of out-of-plane displacement at different frequencies (Figure 6.9a) reveal a Lamb wave pattern with six nodes. At 21.23 kHz and a unipolar total voltage of $44 V_{pp}$ ($22 V$ AC + $22 V$ DC, $22 V_{pp}$ to each actuator), the device exhibits maximum peak-to-peak out-of-plane displacement of $1 \mu\text{m}$, sufficient for the squeezed-air film effect to be perceived by a human finger. Figure 6.9b shows the voltage-dependent displacement at resonance frequency of 21.23 kHz. The displacement increases with the increasing of voltage.

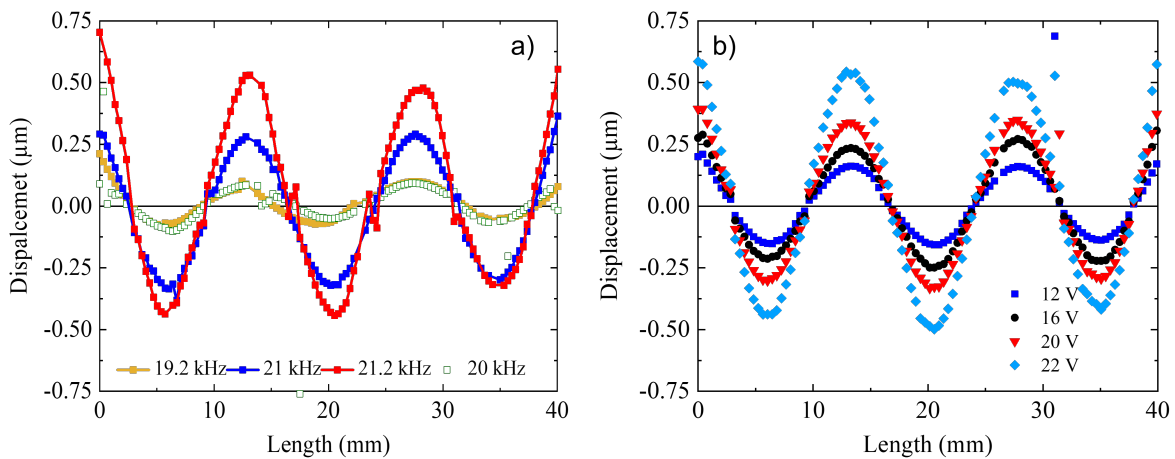


Figure 6.9: **Line scans:** a) Frequency-dependent displacement line scan with a unipolar $22 V_{pp}$ applied voltage to each actuator. b) Displacement line scan at 21.23 kHz excitation frequency, showing voltage dependence. Note: the presence of noisy data points resulting from noise interference caused by soiled points on the back surface of the device.

The Lamb wave shape and peak-to-peak displacement of $1.2 \mu\text{m}$ at 21.23 kHz and $22 V$ applied voltage to each actuator are confirmed by the 2D map of out-of-plane displacement presented in Figure 6.10.

6.9 Chapter conclusion

This study aimed to develop haptic devices using inkjet-printed haptic actuators composed of ITO/PZT/PTO/Pt layers. All layers, except the bottom electrode, were deposited via inkjet printing. An in-house manufactured 0.3 mm-thick platinized Si sub-

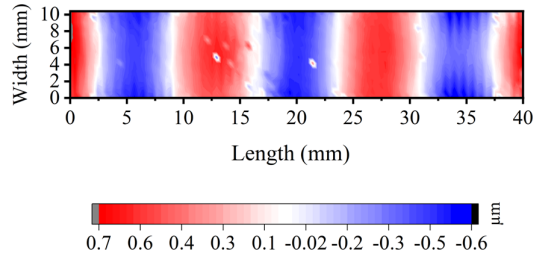


Figure 6.10: 2D map of out-of-plane displacement of the fabricated haptic device, at 44 V unipolar and total voltage (22 V for each actuator) and at its resonant frequency of 21.23 kHz. Note that all the values of voltage are read from oscilloscope.

strate was utilized as haptic plates. A standing A0 Lamb waves were induced at 21.23 kHz, and two actuators printed on the 0.3 mm-Si plate generated over 1 μm of deflection, making them suitable for surface rendering applications.

6.10 Challenges

1) The functional performance of inkjet-printed PZT has not been fully demonstrated due to the relatively low conductivity of the ITO electrodes. As have mentioned earlier, this results in a rather high dielectric loss. Typically, the threshold of dielectric loss that allows an actuator to be used in practical applications is less than 0.2. To resolve this issue, either the electrical conductivity of the ITO film needs to be further improved or a thicker ITO film is required. The former is challenging to achieve in a low-temperature process, while the latter could lead to significant stress between the ITO and PZT films, potentially causing film cracks as demonstrated in Chapter 5.

2) A significant challenge in haptic actuator design is the requirement for a thick PZT film (at least 1 μm), which results in large stress between the PZT film and Pt bottom electrode. During the annealing process, the volume shrinkage of initially inkjet-printed films generates substantial stress between the films and substrate, particularly when a coffee ring effect is present. This stress can cause cracks in both the films and bottom electrode. Such cracking was observed at the edges of printed PZT patterns on in-house produced Si substrates, but not on commercial SINTEF wafers, likely due to the lower quality of the in-house evaporated Pt film.

6.11 Outlook

In spite of the aforementioned difficulties, the utilization of inkjet-printed haptic actuators offers a viable approach to achieve haptic actuators with direct patterning on haptic plates. The compatibility between inkjet printing and the fabrication of large-

scale microelectronics, makes it a promising solution for those seeking to pattern haptic actuators on haptic plates.

Chapter 7

Power efficient haptic devices based on piezoelectric thick films

7.1 Piezoelectric thick film for power efficient haptic actuator

In this chapter, our focus was on exploring the potential of low-power haptic devices utilizing thick PZT films, exceeding 10 μm in thickness. In section 7.1, we proposed the use of piezoelectric thick film actuators as a means to achieve comparable deflection and low power consumption. Finite element modelling confirmed that deflection is primarily dependent on voltage, rather than film thickness, as long as the stiffness of the device does not change. As thickness increases, capacitance decreases linearly, leading to a reduction in power consumption. This was experimentally validated by comparing the consumption of a sol-infiltrated 10 μm PZT actuator with that of a sol-gel processed 0.5 μm PZT actuator. The former exhibited a consumption that was 15 times less than the latter. My first-author publication “Power efficient haptic devices based on piezoelectric thick films” [126] has been attached in Section 7.1.

Authors contributions: I developed the sol-filtration process, conducting the necessary characterizations and electrical measurements on the fabricated devices, as well as drafting the manuscript. While, Dr. Emmanuel Defay and Dr. Sebastjan Glinsek provided critical assistance in the writing the manuscript. Additionally, I received help from my colleague Dr. Veronika Kovacova in depositing the Pt electrodes. The PZT powders used in this work were provided by our Slovenian colleagues, Silvo Drnovsek and Prof. Barbara Malic.

Piezoelectric thick film for power-efficient haptic actuator

Cite as: Appl. Phys. Lett. **121**, 212901 (2022); <https://doi.org/10.1063/5.0106174>

Submitted: 27 June 2022 • Accepted: 04 November 2022 • Published Online: 21 November 2022

 Longfei Song,  Sebastjan Glinsek, Silvo Drnovsek, et al.

COLLECTIONS

Paper published as part of the special topic on [Piezoelectric Thin Films for MEMS](#)



View Online



Export Citation



CrossMark

ARTICLES YOU MAY BE INTERESTED IN

[Investigation of film bulk acoustic resonators for sensing applications in liquid environment](#)
Applied Physics Letters **121**, 213501 (2022); <https://doi.org/10.1063/5.0124829>

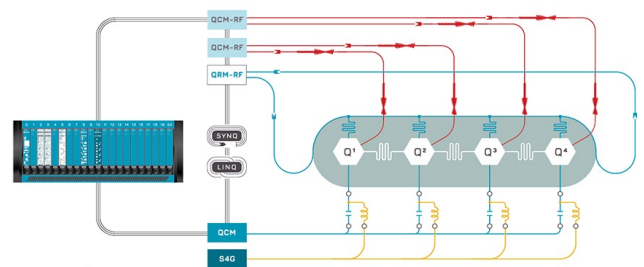
[Polarization analysis of terahertz emission from Bi-2212 cross-whisker intrinsic Josephson junction devices and their refractive index](#)
Applied Physics Letters **121**, 212601 (2022); <https://doi.org/10.1063/5.0123290>

[Lorentz-force gyrator based on AlScN piezoelectric thin film](#)
Applied Physics Letters **121**, 213505 (2022); <https://doi.org/10.1063/5.0122325>

 QBLOX

Integrates all
Instrumentation + Software
for Control and Readout of

Superconducting Qubits
NV-Centers
Spin Qubits



Superconducting Qubit Setup

[find out more >](#)

Appl. Phys. Lett. **121**, 212901 (2022); <https://doi.org/10.1063/5.0106174>

121, 212901

© 2022 Author(s).

Piezoelectric thick film for power-efficient haptic actuator

Cite as: Appl. Phys. Lett. **121**, 212901 (2022); doi: [10.1063/5.0106174](https://doi.org/10.1063/5.0106174)

Submitted: 27 June 2022 · Accepted: 4 November 2022 ·

Published Online: 21 November 2022



View Online



Export Citation



CrossMark

Longfei Song,^{1,2,a)}  Sebastjan Glinsek,^{1,a)}  Silvo Drnovsek,³ Veronika Kovacova,¹  Barbara Malic,³ 
and Emmanuel Defay¹ 

AFFILIATIONS

¹Materials Research and Technology Department, Luxembourg Institute of Science and Technology, rue du Brill 41, L-4422 Belvaux, Luxembourg

²University of Luxembourg, 41 rue du Brill, L-4422 Belvaux, Luxembourg

³Electronic Ceramics Department, Jožef Stefan Institute, Jamova cesta 39, 1000 Ljubljana, Slovenia

Note: This paper is part of the APL Special Collection on Piezoelectric Thin Films for MEMS.

^{a)}Authors to whom correspondence should be addressed: sebastjan.glinsek@list.lu and longfei.song@list.lu

ABSTRACT

Emerging haptic technology based on piezoelectric actuators enables to realize innovative tactile human-machine interface. The standard solution is based on stand-alone bulk ceramics glued directly on the haptic device. Thin-film actuators with metal-insulator-metal structure have been developed to directly integrate actuators on haptic plates. The thickness of thin films is limited to $2\ \mu\text{m}$, leading to large capacitance and, thus, too high-power consumption. To solve this issue, we developed haptic devices based on a $10\ \mu\text{m}$ -thick PZT film deposited on a $0.65\ \text{mm}$ -thick platinized silicon substrate. These thick films are made of a PZT composite slurry associated with sol-gel sol infiltration. They are dense and exhibit a permittivity of 1000 and dielectric loss lower than 0.05. Our fabricated haptic device containing three actuators connected in series exhibits an antisymmetric Lamb wave resonant mode at $62.0\ \text{kHz}$, in line with finite element modeling. At the limit of touch detection ($1\ \mu\text{m}$ out of plane deflection), the power consumption of the haptic device is $150\ \text{mW}$ at $40\ \text{V}$. This represents a 15-fold consumption reduction with respect to the same haptic device made with $0.5\ \mu\text{m}$ -thick PZT thin films.

© 2022 Author(s). All article content, except where otherwise noted, is licensed under a Creative Commons Attribution (CC BY) license (<http://creativecommons.org/licenses/by/4.0/>). <https://doi.org/10.1063/5.0106174>

Although human-machine interface (HMI) strongly depends on vision and hearing, it calls for adding the sense of touch.^{1,2} Hence, surface haptic based on piezoelectric actuators is developed to generate tactile effect on surfaces.^{3–5} Piezoelectric actuators can induce an ultrasonic wave at certain frequencies.^{6–8} A squeezed-air film appears between the vibrating surface and a sliding finger, which in turn decreases the coefficient of friction.^{9–11} This enables real-time control of the friction coefficient of someone's finger, thus emulating artificial textures.

Bulk piezo-ceramic haptic actuators stand for the nominal technological solution. They enable large deflections and are typically made of PZT ceramics with thickness in the mm-range,^{12,13} which require large voltage, typically beyond $100\ \text{V}$, and which prevents using collective fabrication means, inducing fabrication costs difficult to overcome.

One alternative enabling acceptable deflection and technology compatible with mass production is based on piezoelectric thin

films.^{14,15} However, the main drawback of piezoelectric thin film actuators for haptic is large power consumption induced by their large capacitance. For example, Hua *et al.* recently demonstrated a transparent haptic device based on $0.5\ \mu\text{m}$ -ITO/ $2\ \mu\text{m}$ -PZT/ $0.5\ \mu\text{m}$ -ITO metal-insulator-metal (MIM) stack on Corning LotusTM NXT Glass ($71 \times 60 \times 0.5\ \text{mm}^3$).¹⁵ The haptic device showed an out-of-plane deflection of $1\ \mu\text{m}$ at $10\ \text{V}_{\text{pp}}$ at $22.5\ \text{kHz}$. The power consumption of the whole haptic device reached $3.6\ \text{W}$.

Efforts have nonetheless been devoted to developing power-efficient devices. Glinsek *et al.* demonstrated a transparent haptic device based on a PZT thin film and ITO interdigitated (IDE) electrodes on fused silica glass.¹⁶ The device exhibited a Lamb mode at $73\ \text{kHz}$ and an out-of-plane peak-to-peak displacement of $3\ \mu\text{m}$ at $150\ \text{V}$ unipolar. The benefit of the IDE structure is a smaller capacitance than MIM ($120\ \text{pF}$ for each capacitor in this case), which therefore leads to much lower power consumption, namely, $75\ \text{mW}$ per actuator (at $150\ \text{V}$ unipolar = $92\ \text{V}_{\text{rms}}$). Note though that the footprint

of this device is very much reduced ($15 \times 3 \times 0.5 \text{ mm}^3$). A simple linear increase in the width of the actuators, in order to make a fair comparison with the previous work, would multiply by 20 the value of the capacitance, reaching then 1.5 W per actuator. These examples not only show that consumption is substantial in various haptic devices from the literature but also that it is not straightforward to come up with a fair comparison between designs.

To obtain low-power haptic devices, our idea is to develop piezoelectric thick films actuated with a MIM structure. This enables decreasing the capacitance value (C) while keeping a similar out of plane deflection at a given voltage, as explained hereafter. The 1D-lateral force F induced by voltage U applied to a piezoelectric layer on a plate is¹⁷

$$F = e_{31,f} \frac{U}{t_{film}} A_{film}, \tag{1}$$

where $e_{31,f}$ is the effective piezoelectric coefficient, t_{film} is the film thickness, A_{film} is the cross-sectional area of the film, which equals film thickness times film width (i.e., $A_{film} = t_{film} \times w_{film}$). Equation (1), therefore, simply reads $F = e_{31,f} \times U \times w_{film}$. This indicates that the induced force does not depend on PZT thickness. As will be shown in the finite element modeling (FEM) section, the increase in the structure's stiffness remains negligible if the film's thickness remains within 10% of the substrate's thickness. In addition, increasing the film's

thickness proportionally decreases C , the capacitance of the actuator. As the power consumption is proportional to the capacitance value, this in turn linearly decreases the overall consumption of the haptic device. Indeed, power consumption P equals $C \times f \times U_{rms}^2$, with U_{rms} the applied voltage at frequency f .

In this work, we first investigated the impact of PZT film thickness on the performance of a simple haptic device using FEM. It reveals that the device deflection is hardly ever impacted by PZT thickness. A thicker film enables decreasing power consumption as discussed before. Based on this analysis, we fabricated two haptic transducers with identical dimensions but actuated, respectively, with thin ($0.5 \mu\text{m}$) and thick ($10 \mu\text{m}$) $\text{Pb}(\text{Zr}_{0.53}\text{Ti}_{0.47})\text{O}_3$ (PZT) films. The thin and thick films were based, on the one hand, on a standard sol-gel approach and, on the other hand, on a composite slurry coupled with an infiltration sol-gel process. The fabricated haptic devices moved by three actuators each exhibited standing Lamb waves at 62.0 kHz (thick films) and 71.5 kHz (thin films). The capacitance of one thin film actuator is 160 nF whereas that of one thick film actuator is only 12 nF, both measured at 1 kHz. When 13 V_{pp} (peak to peak) were applied to each actuator, the thin and thick film haptic devices exhibited, respectively, a peak-to-peak deflection of 0.4 and 1 μm (limit of detection with a finger) and a consumption of 2.3 W (thin film) and 150 mW (thick film). This experiment, therefore, proves that increasing the thickness of PZT films in haptic devices decreases drastically

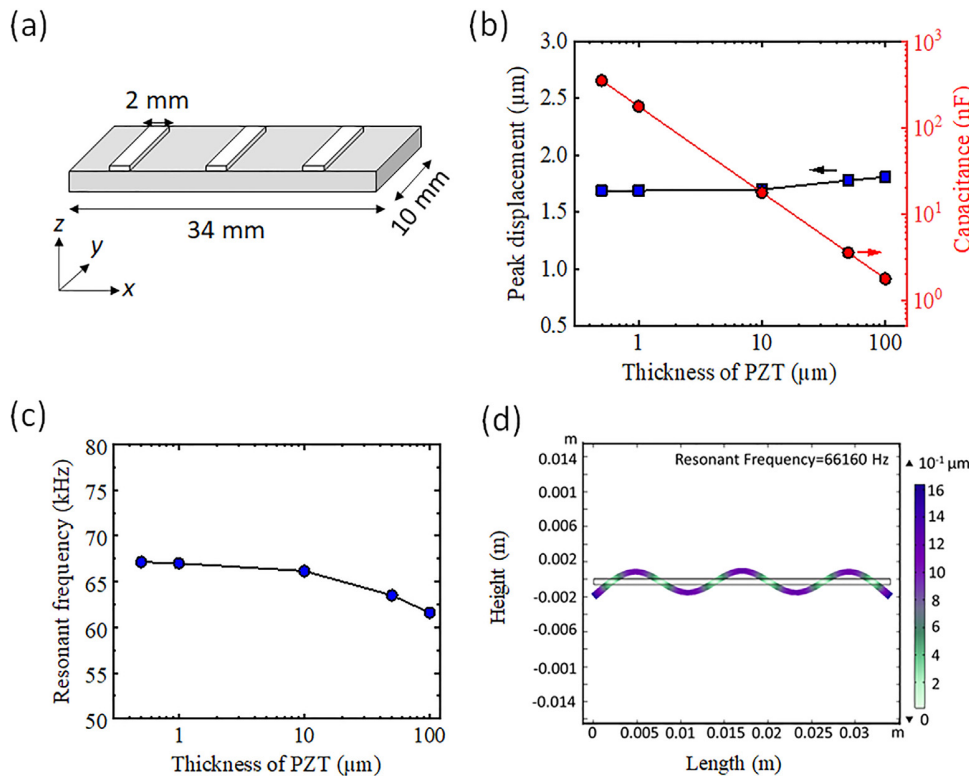


FIG. 1. Finite element modeling. (a) Geometry of the model built with three PZT capacitors on a 0.65 mm-thick silicon substrate. (b) The displacement of the haptic device (black symbol) and the capacitance of each actuator (red symbol) as a function of PZT thickness. (c) Resonant frequency plotted as a function of PZT thickness. (d) Modeled shape of haptic device based on a 10 μm -thick PZT film.

the power consumption and not at the expense of reducing the haptic effect.

A 2D FEM was performed using COMSOL 5.5 to study the relationship between PZT thickness and deflection of a simple haptic plate. A scheme of the haptic device ($34 \times 10 \times 0.65 \text{ mm}^3$) is shown in Fig. 1(a). Three PZT capacitors ($2 \times 10 \text{ mm}^2$) are placed symmetrically on the silicon substrate with spacing of 11.3 mm between each other. Electrodes, passivation, and barrier layers were not modeled because they are too thin to influence the device performance. A voltage of 40 V was applied to each PZT actuator. The piezoelectric coefficient e_{31} and relative permittivity ϵ_r were set to -7 C m^{-2} and 1000, respectively. The damping loss factor calculated as $\Delta f/f_r$, where f_r and Δf are resonant frequency and resonance width at full width at half maximum, respectively, is 0.0063 for 0.65 mm-thick platinized silicon. Figure 1(b) shows the modeled maximum deflection of the haptic device from Fig. 1(a) and each actuator's capacitance as a function of PZT thickness. A linear decrease in the capacitance is observed with PZT thickness, meaning that 1, 10, and 100 μm -thick films, respectively, exhibit capacitances of 180, 18, and 1.8 nF. As expected, the corresponding peak displacements vs PZT thickness of the haptic device spread in a much smaller range, varying from 1.6 to 1.8 μm only. The displacement is slightly improved when PZT increases because adding PZT has a softening effect, visible on the acoustic resonance. Indeed, the frequency of the latter decreases when PZT thickness increases, as

displayed in Fig. 1(c). It makes sense because PZT is softer and heavier than Si. Figure 1(d) represents the mode shape of a 10 μm -PZT haptic device at its A_0 -Lamb wave mode resonance (66.1 kHz) where the maximum deflection appears.

In this part, only the thick films fabrication process is detailed. The thin film process is very well established, for instance, in Ref. 16 and the details are given in the [supplementary material](#). The comparison between thick and thin film haptic devices will though be performed in the main paper.

PZT thick films were fabricated by the deposition of a composite slurry (1 g/mL), which was synthesized by dispersing crystalline Nb-PZT [$\text{Pb}(\text{Zr}_{0.53}\text{Ti}_{0.47})_{0.98}\text{Nb}_{0.02}\text{O}_3$] powder into PZT [$\text{Pb}(\text{Zr}_{0.53}\text{Ti}_{0.47})\text{O}_3$] chemical solution deposition (CSD) solution. More details on processing and characterization are provided in the [supplementary material](#). The slurry was deposited on platinized silicon via spin coating and was annealed at 700 $^\circ\text{C}$ to sinter the powders and crystallize the amorphous deposit. The deposition-heating-crystallization process was repeated up to seven times to obtain the desired thickness. The cross section scanning electron microscopy (SEM) micrograph of a four-layer-thick film reveals a porous microstructure [Fig. 2(a)] in which individual deposited layers can be observed. Its thickness is 6 μm .

To improve the density of the films, a so-called “x(1C + 4S)” procedure¹⁸ was deployed, in which one composite slurry deposition (1C) is followed by four CSD solution depositions (4S) to enable infiltration

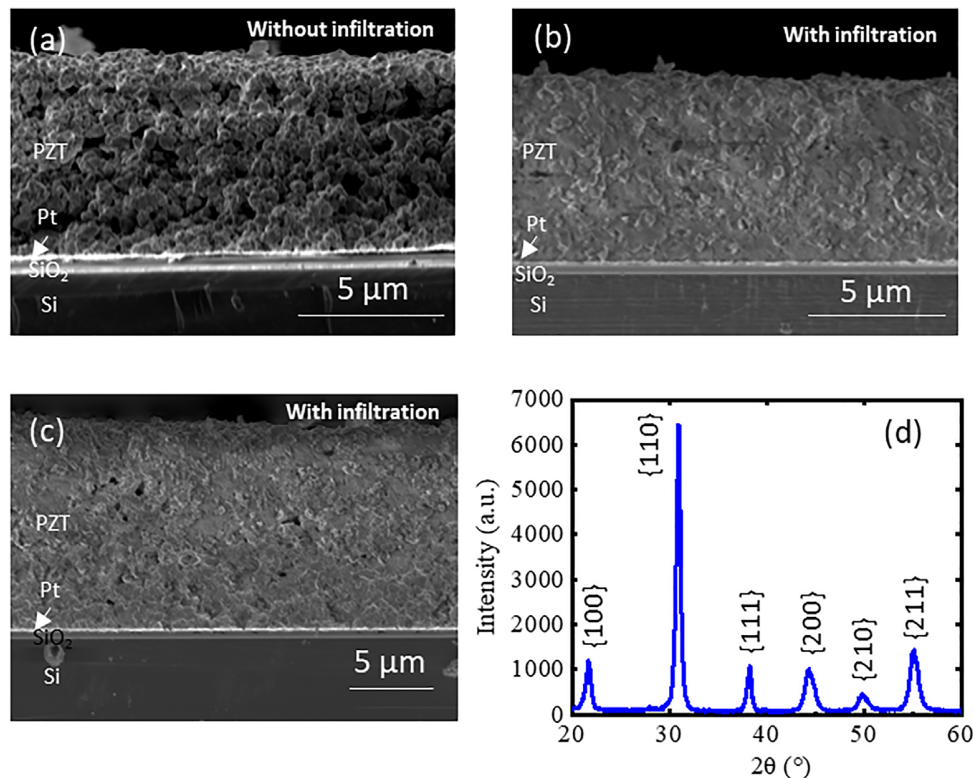


FIG. 2. Cross-sectional SEM micrographs of (a) a PZT composite thick film after four depositions without infiltration. Sol infiltrated PZT composite thick films with four (b) and seven (c) depositions. (d) The XRD pattern of the 10 μm -thick PZT film shown in (c). Peaks are denoted with pseudo-cubic Miller indices corresponding to the PZT perovskite phase.¹⁹

of the sol into the composite. x denotes the number of deposition-infiltration cycles. Details about this process can be found in the [supplementary material](#) (Fig. S2). The cross section of 4(1C + 4S) films displays a much denser microstructure [Fig. 2(b)] than the sample without infiltration [Fig. 2(a)]. 10 μm -thick films were achieved with a 7(1C + 4S) procedure [Fig. 2(c)].

The x-ray diffraction (XRD) pattern of the 10 μm -thick film with sol-infiltration [7(1C + 4S)] is shown in Fig. 2(d). A pure perovskite phase is identified using the powder diffraction file (PDF) No. 01-070-4264.¹⁹ The presence and intensity of {100}, {110}, and {200} peaks indicate random orientation, which is a typical feature of nanoparticles-based thick films.²⁰

Figure 3(a) shows the polarization-electric field [$P(E)$] loops of 6 μm -thick PZT film deposited without infiltration. The remanent polarization (P_r) is $25 \mu\text{C cm}^{-1}$, and the coercive field (E_c) is 125 kV cm^{-1} . E_c is rather large and linearly shifts as voltage increases. It suggests substantial leakage current as observed in the current density $j(E)$ loops [Fig. 3(b)]. ϵ_r and $\tan\delta$ are, respectively, 400 and 0.2, as shown in Fig. 3(c).

Figure 3(d) shows the $P(E)$ loops of 10 μm -thick PZT films deposited by the 7(1C + 4S) sol-infiltration process. P_r is $27 \mu\text{C cm}^{-1}$ and E_c is 42 kV cm^{-1} , values that are standard for PZT films. E_c is divided by three after sol-infiltration. It suggests lower leakage current, which is confirmed in the $j(E)$ loops of Fig. 3(e). At high field, current is indeed much smaller. The $j(E)$ loops also show two sharp peaks in current that are linked with the switching of PZT ferroelectric domains, as expected. ϵ_r is 1000 and $\tan\delta$ is 0.05 [Fig. 3(f)], values comparable to the values of our sol-gel deposited PZT thin films ($\epsilon_r = 900$ and $\tan\delta = 0.08$, as shown in Fig. S5).

Two slider haptic devices with three actuating areas each were fabricated according to the modeling [cf. Fig. 1(a)], one based on 0.5 μm -thick sol gel films (for comparison) and one with 10 μm -thick sol-infiltrated PZT films. Both devices have the same dimensions, namely, $34 \times 10 \times 0.65 \text{ mm}^3$.

The three PZT actuators were obtained by depositing and patterning, respectively, 100 nm-thick and 500 nm-thick Pt top electrodes of $2 \times 8 \text{ mm}^2$ on PZT thin and thick films. In Fig. 4(b), the $P(E)$ loop of the marked actuator confirms its ferroelectric nature with $P_r = 15 \mu\text{C cm}^{-2}$. The corresponding current curve does not display excessive leakage at high field [Fig. 4(c)]. In addition, the $C(E)$ loop exhibits an expected value of capacitance around 12 nF per actuator [cf. Fig. 4(d)]. The losses are around 5% at maximum, which is a rather low value. The respective curves for the thin film actuators are displayed in Fig. 4(d) [$P(E)$ loop] and Fig. 4(e) [$C(E)$ loop]. The polarization is very similar to the one obtained for thick films. However, the capacitance is much larger, as expected, reaching 160 nF at maximum, with associated dielectric losses around 8%.

The observed resonant frequencies of the thin and thick film actuators are, respectively, 71.5 and 62.0 kHz, corresponding to the frequency at which the deflection is the largest. Note that these values are not exactly the same as the ones predicted by modeling (67 kHz for the thin films and 66 kHz for the thick films) because the actual final dimensions, and especially the lengths, was slightly different from initial design due to imperfect cut.

The out-of-plane displacement of the thick film haptic device was recorded by scanning across the area of the device, as plotted in Fig. 5(a). 120 V peak-to-peak and unipolar (which means 60 V DC + 60 V AC)

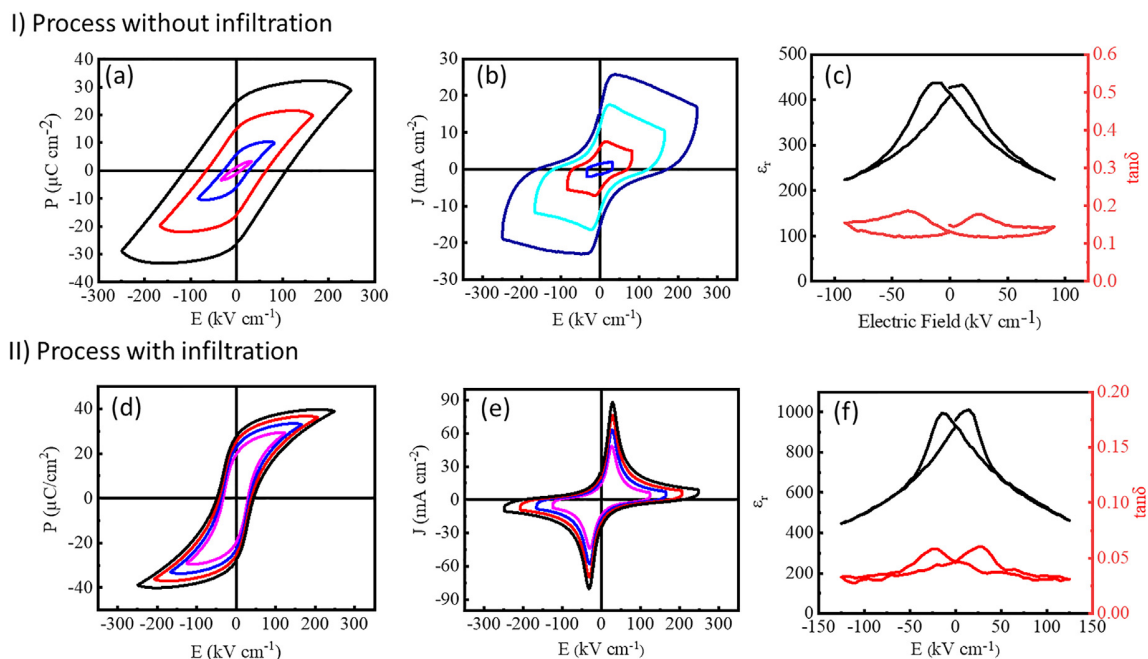


FIG. 3. Electrical characterizations of PZT thick films (I) deposition of PZT slurry without infiltration (6 μm -thick) and (II) with infiltration (10 μm -thick). (a) and (d) polarization-electric field $P(E)$ hysteresis loops, (b) and (e) current density-electric field $j(E)$ curves, and (c) and (f) permittivity ϵ_r (black curve) and loss tangent $\tan\delta$ (red curves) measurements. Electrode area is 3.14 mm^2 .

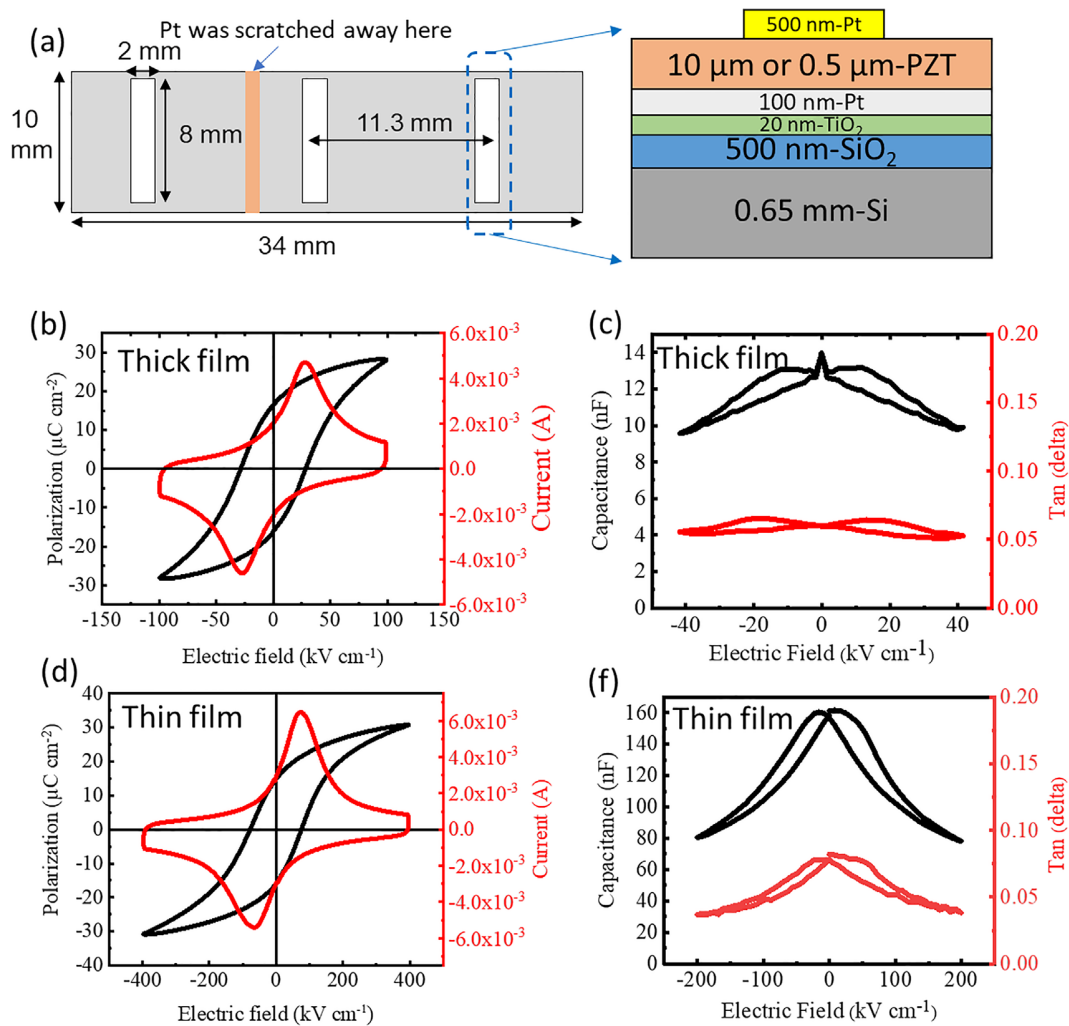


FIG. 4. (a) Top-view and (b) cross-section schematic diagram of fabricated haptic devices based on a 10 μm -thick or 0.5 μm -thick PZT film. (b) and (d) $P(E)$ hysteresis loop and (c) and (e) $C(E)$ and $\tan\delta$ of one of the fabricated actuators based on thick and thin films, respectively.

were applied to the three actuators in series, which corresponds to 40 V applied to each actuator. A typical anti-symmetric Lamb wave A_0 was observed, which agrees well with the mode shape predicted by FEM. The maximum displacement reaches 3.0 μm peak-to-peak. We also observed that only 13.3 V is needed to achieve the minimum deflection that can be detected by a finger, namely 1 μm . A 2D-scan over the entire device surface [Fig. 5(b)] of the deflection at resonance has also been performed. The same Lamb stationary wave with four nodes equally spaced along the length was observed. Note also that the deflection along the y -axis stays unchanged as expected. The thin film haptic device could only withstand 20 V peak-to-peak and unipolar (which means 10 V DC + 10 V AC) for the three capacitors in series, which means 6.7 V per each actuator. The maximum deflection at the Lamb wave resonance at 71.5 kHz only reached 0.2 μm peak-to-peak, as shown in Fig. S7. The deflection is proportional to the applied voltage, so peak-to-peak

deflection at 13.3 V should be 0.4 μm , which is 2.5 times less than the thick film device.

Note that increasing the film thickness could induce a change in piezoelectric properties due to stress relaxation or clamping effect, as described in Ref. 21. In our specific case, $e_{31,f}$ values obtained by fitting the model to experimental deflection were -7 and -5 C m^{-2} for thick and thin films, respectively. Therefore, there is a significant increase in piezoelectric properties in our thick films (+40%). The converse $e_{31,f}$ coefficient of the PZT thick film was also experimentally measured through a cantilever structure.²² Its value is -7.6 C m^{-2} , which is in line with the value extracted from the haptic experiment. All the details are described in the [supplementary material](#).

As exposed earlier, the purpose of developing PZT thick film-based haptic devices is to reduce the power consumption. The power consumption P to drive one capacitor can be estimated as $P = CfU_{rms}^2$, where C , U_{rms} , and f are capacitance, rms voltage, and

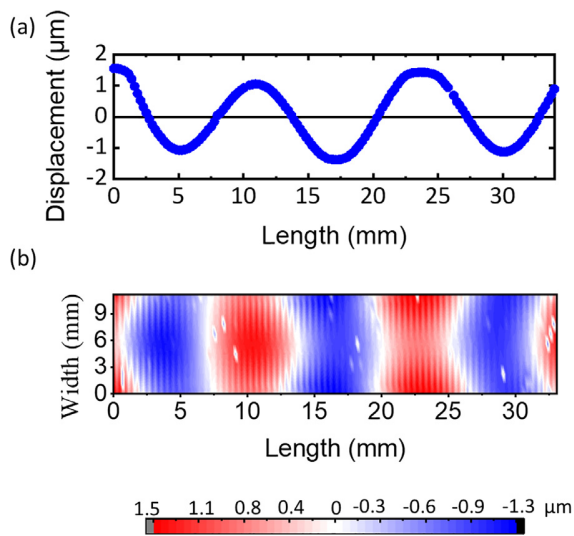


FIG. 5. (a) Line scan along the haptic device length and (b) 2D-map measured atop the PZT thick films haptic device when 120 V unipolar were applied to the three actuators in series, at its A_0 Lamb wave mode resonance frequency (62.0 kHz).

resonant frequency, respectively. In order to perform a fair comparison, we applied the same voltage to the thin and the thick film haptic devices, namely, 40 V unipolar (20 V DC + 20 V AC, at 24 V_{rms}). The results are displayed in Table I and show that one thin film actuator consumes 750 mW, whereas one thick film actuator consumes 50 mW. Therefore, the haptic device with thick films consumes 15 times less than the one with thin films. As shown before, the thick film haptic device can withstand 120 V with the actuators in series. In this case, the consumption of all actuators is 450 mW. When 40 V (unipolar, peak-to-peak) are applied to the actuator at the resonance, the directly measured power consumption ($U_{rms} \times I_{rms}$) is 500 mW, which is in line with the value (450 mW) obtained through $Cf(U_{rms})^2$. More measurement details are described in the supplementary material.

TABLE I. Comparison of 10 μm -PZT thick film-based haptic device fabricated in this work with 0.5 μm -PZT thin film-based haptic device. For a fair comparison, the haptic devices have the same dimensions. The same voltage has been applied to both (40 V unipolar, at 24 V_{rms}) at their respective resonant frequency.

Characteristics	Thick film haptic device	Thin film haptic device
Permittivity of PZT measured at 1 kHz	1000	900
Dielectric loss of PZT	0.05	0.08
Remanent polarization of PZT	27 $\mu\text{C cm}^{-2}$	15 $\mu\text{C cm}^{-2}$
Haptic device frequency	62.0 kHz	71.5 kHz
Capacitance of one actuator	12 nF	160 nF
Peak-to-peak deflection	1 μm	0.4 μm
Power consumption of one actuator (of the three actuators)	50 mW (150 mW)	750 mW (2.3 W)

Finally, we can also compare approximately these values with the ones reported in the literature in the introduction by normalizing the consumption with the actuators' width. Hence, if all actuators were 10 mm in width and if they were driven in order to reach 3–4 μm in deflection, Hua's¹⁵ and Glinsek's¹⁶ would, respectively, consume 3.5 W and 250 mW. In these conditions, our thick film haptic device consumes 450 mW, which is much less than Hua's because our capacitance is smaller. It is though twice as much as Glinsek's but our device enables working at lower voltage (40 V_{pp} per actuator vs 150 V_{pp}). Note also that we used a 0.65 mm-thick Si substrate as haptic plate, which is more difficult to deflect than the glass substrate used in Ref. 16 (0.5 mm thick). At constant voltage, modeling shows that the deflection of a haptic device with 0.5 mm-glass is four times larger than the same one with 0.65 mm-Si. Therefore, this indicates that our thick film actuators should only need 10 V_{pp} to actuate the same glass haptic plate with the same dimension to reach a deflection of 3 μm . Our solution clearly calls for even thicker films, as suggested by our modeling in Fig. 1(b).

As suggested by simple equations, finite element modeling demonstrated that using thick piezoelectric films for haptic devices enables decreasing power consumption. Dense 10 μm -thick PZT films were fabricated. They were based on a PZT composite slurry complemented with a sol-infiltration process. Thanks to their dense microstructure, these PZT thick films exhibit ferroelectric properties comparable with state-of-art sol-gel PZT thin films. Two haptic devices were fabricated, respectively, based on PZT thin and thick films. Both are functional and exhibit an A_0 Lamb wave resonant mode at 71.5 and 62.0 kHz, respectively. The power consumption per thick-film actuator is 50 mW for generating a 1 μm out-of-plane displacement, which represents a 15-fold reduction compared with our 500 nm-PZT thin film haptic device. Our PZT deposition technique enables reaching 10 μm in thickness. Modeling clearly shows that reaching 100 μm in PZT thickness would allow the same deflection with the same voltage, but this would also reduce consumption by one order of magnitude, down to a few mW per actuator.

See the supplementary material for further details about processing of solutions, powders, slurries, and films. Microstructural and electrical characterization of the films and haptic devices is also further described.

The authors acknowledge the Fonds National de la Recherche (FNR) of Luxembourg for supporting this work through the Project No. PRIDE17/12246511/PACE. S.D. and B.M. acknowledge the support of Slovenian Research Agency (core funding P2-0105).

AUTHOR DECLARATIONS

Conflict of Interest

The authors have no conflicts to disclose.

Author Contributions

Longfei Song: Data curation (equal); Investigation (equal); Writing – original draft (equal); Writing – review & editing (equal). **Sebastjan Glinsek:** Conceptualization (equal); Methodology (equal); Supervision (supporting); Validation (equal); Writing – review & editing (equal).

Silvo Drnovsek: Data curation (supporting); Investigation (supporting).
Veronika Kovacova: Investigation (supporting). **Barbara Malic:** Investigation (supporting); Writing – review & editing (supporting).
Emmanuel Defay: Conceptualization (equal); Supervision (equal); Validation (equal); Writing – review & editing (lead).

DATA AVAILABILITY

The data that support the findings of this study are available from the corresponding authors upon reasonable request.

REFERENCES

- ¹S. Standing, *Gray's Anatomy E-Book: The Anatomical Basis of Clinical Practice* (Elsevier Health Sciences, Philadelphia, PA, 2015).
- ²I. Poupyrev, S. Maruyama, and J. Rekimoto, in Proceedings of the 15th Annual ACM Symposium on User Interface Software and Technology, 2002.
- ³T. H. Yang, J. R. Kim, H. Jin, H. Gil, H. Koo, and H. J. Kim, *Adv. Funct. Mater.* **31**, 2008831 (2021).
- ⁴C. Basdogan, F. Giraud, V. Levesque, and S. Choi, *IEEE Trans. Haptics* **13**, 450 (2020).
- ⁵Y. Huang, K. Yao, J. Li, D. Li, H. Jia, Y. Liu, C. K. Yiu, W. Park, and X. Yu, *Mater. Today Phys.* **22**, 100602 (2022).
- ⁶F. Bernard, F. Casset, J. Danel, C. Chappaz, and S. Basrour, *J. Micromech. Microeng.* **26**, 084007 (2016).
- ⁷M. Wiertelwski and Colgate, J. E., *IEEE Trans. Haptics* **8**, 43 (2015).
- ⁸F. Casset, J.-S. Danel, P. Renaux, C. Chappaz, F. Bernard, T. Sednaoui, S. Basrour, B. Desloges, and S. Fanget, *Mechatronics* **40**, 264 (2016).
- ⁹M. Biet, F. Giraud, and B. Lemaire-Semail, *IEEE Trans. Ultrason, Ferroelect, Freq. Contr.* **54**, 2678 (2007).
- ¹⁰M. Wiertelwski, R. F. Friesen, and J. E. Colgate, *Proc. Natl. Acad. Sci.* **113**, 6907 (2016).
- ¹¹T. Watanabe and S. Fukui, in *IEEE International Conference on Robotics and Automation* (IEEE, Piscataway, NJ, 1995), pp. 1134–1139.
- ¹²See <https://www.hap2u.net/haptic-technology/> for further information on piezoelectric haptics.
- ¹³See https://product.tdk.com/en/products/sw_piezo/haptic/piezo/hapt/index.html for further information on piezoelectric haptics.
- ¹⁴S. Glinsek, L. Song, V. Kovacova, M. A. Mahjoub, N. Godard, S. Girod, J.-L. Biagi, R. Quintana, T. Schlee, M. Guedra, M. Rupin, and E. Defay, *Adv. Mater. Technol.* **7**, 2200147 (2022).
- ¹⁵H. Hua, Y. Chen, Y. Tao, D. Qi, and Y. Li, *Sens. Actuator, B* **335**, 113396 (2022).
- ¹⁶S. Glinsek, M. A. Mahjoub, M. Rupin, T. Schenk, N. Godard, S. Girod, J. B. Chemin, R. Leturcq, N. Valle, S. Klein, C. Chappaz, and E. Defay, *Adv. Funct. Mater.* **30**, 2003539 (2020).
- ¹⁷K. R. Oldham, J. S. Pulskamp, R. G. Polcawich, and M. Dubey, *J. Microelectromech. Syst.* **17**, 890 (2008).
- ¹⁸R. A. Dorey, S. B. Stringfellow, and R. W. Whatmore, *J. Eur. Ceram. Soc.* **22**, 2921 (2002).
- ¹⁹S. Gates-Rector and T. Blanton, *Powder Diffr.* **34**(4), 352–360 (2019).
- ²⁰T. Bakarič, B. Malič, and D. Kuscer, *J. Eur. Ceram. Soc.* **36**, 4031 (2016).
- ²¹G. Han, J. Ryu, W. H. Yoon, J. J. Choi, B. D. Hahn, and D.-S. Park, *J. Am. Ceram. Soc.* **94**, 1509–1513 (2011).
- ²²A. Mazzalai, D. Balma, N. Chidambaram, R. Matloub, and P. Murali, *J. Microelectromech. Syst.* **24**, 831–838 (2015).

Supplementary Information

Piezoelectric thick film for power-efficient haptic actuator

Longfei Song,^{1,2} Sebastjan Glinsek,¹ Silvo Drnovsek,³ Veronika Kovacova,¹ Barbara Malic,³
Emmanuel Defay¹

S1. Experimental Methods

1) Synthesis of Precursors

Solution Synthesis. $\text{Pb}(\text{Zr}_{0.53}\text{Ti}_{0.47})\text{O}_3$ (PZT) solution was prepared based on the standard 2-methoxyethanol route. The stoichiometry of metal cations was $\text{Pb}:\text{Zr}:\text{Ti}=1.10:0.53:0.47$, namely morphotropic phase boundary composition with 10% Pb excess. The solution concentration was 0.3 mol l^{-1} . Further details of the synthesis were described in Godard et. al. [1].

Powder Synthesis. $\text{Pb}(\text{Zr}_{0.53}\text{Ti}_{0.47})_{0.98}\text{Nb}_{0.02}\text{O}_3$ (Nb-PZT) powder was synthesized by solid-state synthesis from PbO (99.9%, Aldrich), ZrO_2 (99.1%, Tosoh), TiO_2 (99.8%, Alfa Aesar) and Nb_2O_5 (99.9%, Sigma Aldrich) at $1100 \text{ }^\circ\text{C}$, as described in Ref. [2]. The powder had average particle size of $0.4 \text{ }\mu\text{m}$.

Slurry Synthesis. Synthesis of the composite slurry is schematically presented in Fig. S1a. 30 mg of Nb-PZT powder was added into a 30 ml of PZT solution. 3 wt% of Triton X-100 relative to Nb-PZT powder was added. Next, the mixture was mixed with a digital disperser (IKA Ultra-Turrax T25) with a speed of 10,000 rpm for 10 min.

2) Deposition of the Films

Deposition of Thick Films via standard route. The deposition and heating steps are shown in Fig. S1b. The PZT composite slurry was spin coated on platinised silicon ($\text{Pt}/\text{TiO}_x/\text{SiO}_2/\text{Si}$, SINTEF) with a spin-speed of 3000 rpm for 30 s, followed by drying at $130 \text{ }^\circ\text{C}$ for 3 min and pyrolysis at $350 \text{ }^\circ\text{C}$ for 3 min (both performed on a hot plate). The crystallization and sintering were done at $700 \text{ }^\circ\text{C}$ for 30 min in a rapid thermal annealing (RTA) furnace (AS-Master,

Annealsys). The whole deposition-drying-pyrolysis-sintering process was repeated four times to achieve 6 μm -thick film.

Deposition of Thick Films via sol-infiltration route. The sol-infiltration route is schematically presented in Fig. S2. In the first step, a single PZT sol-gel layer was spin-coated on the substrate (spin speed 3000 rpm for 30s), followed by drying and pyrolysis at 130 °C and 350 °C, respectively, for 3 min. Afterwards, PZT slurry was spin coated (3000 rpm for 30 s), followed by four coatings of PZT solution (500 rpm for 60 s), which is the so-called “sol infiltration” process. Drying at 130 °C and pyrolysis at 350 °C steps were done after every slurry and solution deposition. Afterwards, the crystallization and sintering step was performed at 700 °C for 30 min in an air atmosphere in RTA furnace. This process was denoted as (1C+4S), where 1C stands for one layer of PZT slurry and 4S stands for four layers of the solution. The (1C+4S) process was repeated x times to achieve the final thickness, denoted as x(1C+4S). To reach 10 μm -thick film, it was repeated seven times.

Deposition of Thin Films: The PZT solution was spin-coated on a platinised silicon with a spin speed of 3000 rpm for 30 s. Drying and pyrolysis were again performed on hot plates at 130 °C for 3 minutes and 350 °C for 3 minutes. The deposition-drying-pyrolysis steps were repeated four times before the crystallization, which was then done in an air atmosphere at 700 °C in an RTA furnace (AS-Master, Annealsys). The whole deposition-heating-crystallization process was repeated three times to achieve the final 0.5 μm . Detailed processing was described in Ref.[1].

3) Microstructural Characterization

Phase composition of the films was investigated with an X-ray diffractometer (XRD, D8 Discover, Bruker, USA) using Cu-K α radiation. The patterns were recorded in θ -2 θ geometry in a 2 θ -range of 20-60°, with step size and integration time of 0.04° and 4 s, respectively. Scanning electron microscope (SEM, Helios NanoLab 650, FEI) was used to analyze the cross-sectional microstructures of the films.

4) Electrical Characterization

Platinum top electrodes with diameter of 2 mm were sputtered (BALTEC MED 020 Metallizer) through a shadow mask on the surface of the films. The electrode thickness for thin and thick

film are respectively 200 nm and 500 nm. All electrical measurements were performed using TF Analyzer 2000 E (aixACCT). Polarization-electric field $P(E)$ hysteresis loops were measured using a triangular waveform at 100 Hz. The relative permittivity-electric field $\epsilon_r(E)$ and loss tangent-electric field loops $\tan\delta(E)$ of thick films were measured at 1 kHz, with a small AC signal of 250 mV and 50 mV for thick and thin films, respectively.

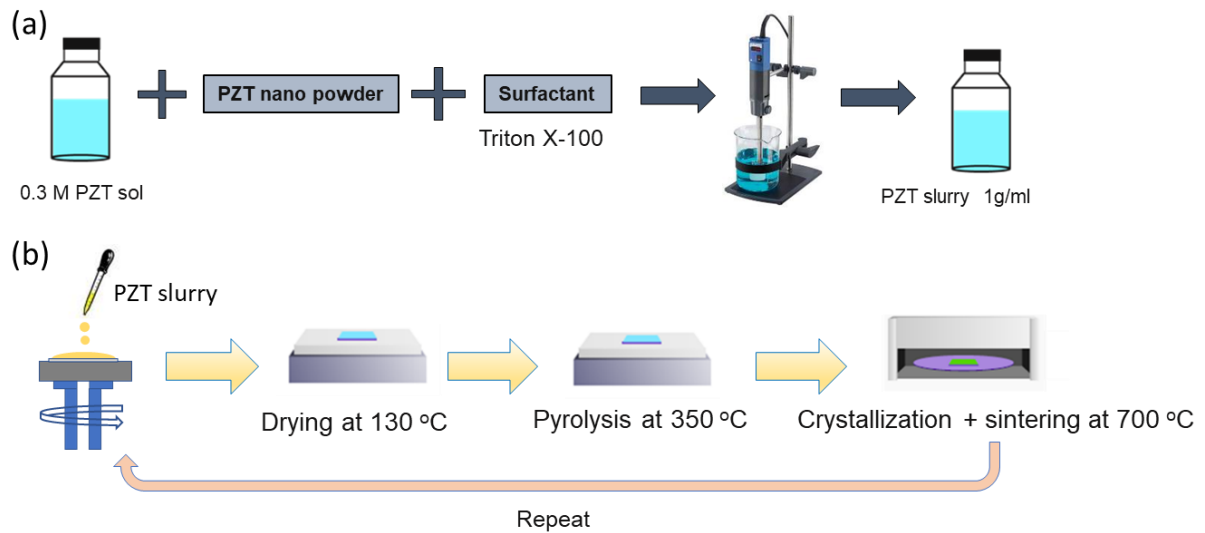


Fig. S1 (a) Scheme of PZT composite slurry preparation process. (b) Scheme of the standard thick-film deposition process.

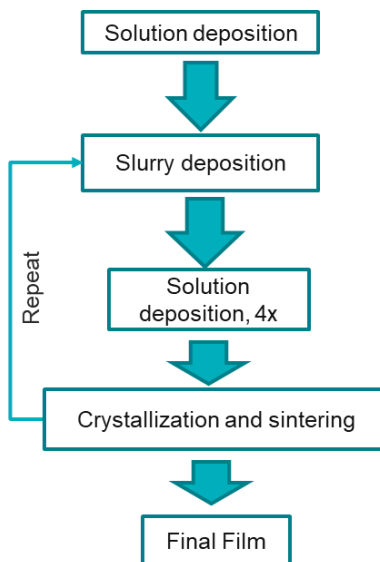


Fig. S2 Scheme of the sol-infiltration process route for fabrication of thick films.

S2. Characterizations and electrical measurements of sol-gel deposited thin film

Characterizations were performed and analysed in this section to confirm the quality of as-deposited PZT thin film. Fig. S3 is the cross-section scanning electron microscope image (SEM) that reveals a dense microstructure. θ - 2θ X-ray diffraction pattern in Fig. S4 confirms a typical perovskite phase with no sign of a secondary phase. P(E) loop in Fig. S5a ensures PZT thin film's ferroelectric nature, showing a P_r of $15 \mu\text{C cm}^{-2}$. ϵ_r and $\tan\delta$ are 900 and 0.08, respectively, as observed in $\epsilon_r(E)$ and $\tan\delta(E)$ butterfly loops in Fig. S5b.

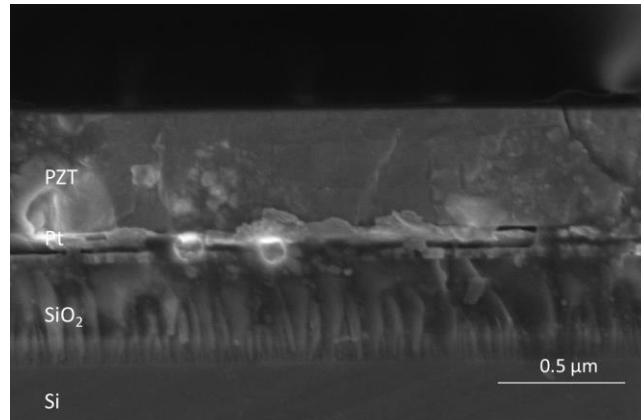


Fig. S3 Cross-section SEM image of sol-gel deposited PZT thin film on platinum-silicon substrate.

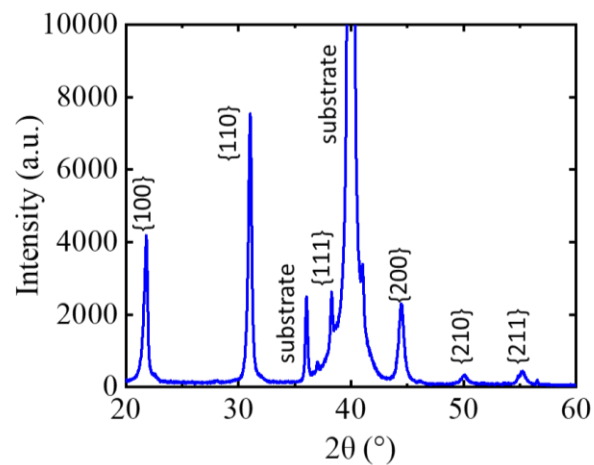


Fig. S4 XRD pattern of sol-gel deposited PZT thin film.

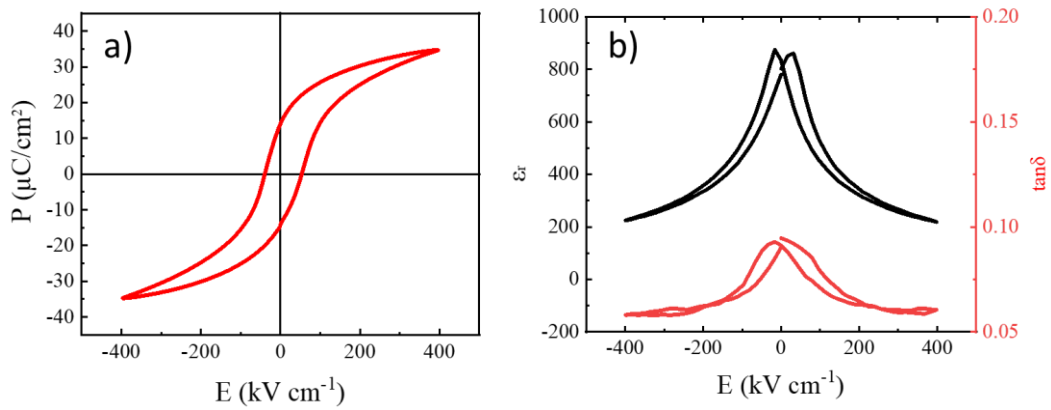


Fig. S5 Ferroelectric characterizations of PZT thin film: a) Polarization-voltage $P(E)$ hysteresis loop, b) Permittivity-voltage $\epsilon_r(E)$ and $\tan\delta(E)$ loops. Electrode area is 0.785 mm^2 .

S3. Fabrication of Haptic Devices and their Characterizations

Thick- and thin-film samples were cut into $34 \times 10 \text{ mm}^2$ (obtained via FEM modelling) using a diamond cutter. Three actuators were created by sputtering of Pt electrodes with the size of $2 \times 8 \text{ mm}^2$ and spacing of 11.3 mm (shown in Fig. 4a). The respective electrode thickness for thin and thick film are 200 nm and 500 nm. The electrodes were patterned using Kapton tapes. The three capacitors were connected in series to reduce the current needed to drive them. To do so, Pt between two capacitors was scratched away using a diamond cutter.

The haptic device was placed on suspended flexible bars and was connected to a waveform generator (33210A Keysight) via an amplifier (WMA-300, Falco Systems). A photo of the measurement system has been shown in our previous work.[3] The out-of-plane displacement was monitored using a vibrometer (OFV-5000, Polytec). A computer-controlled X-Y stage was used to move the haptic device for two-dimension mapping. The whole set-up was controlled together with the vibrometer via a LabVIEW program. Three actuators were connected in series for haptic measurement. To do so, a cut has been performed on the bottom electrode, as schematically shown in Fig. 5a. This cut has been made by simply scratching Pt with a diamond cutter. This series connection happened to be necessary to decrease the current needed to drive the large capacitance of the thin film actuators (160 nF each).

Note that Falco WMA-300 high voltage amplifier enabling $50\times$ voltage amplification was employed to apply high voltage to the haptic device. However, due to the limitation of its

output current (300 mA), the actual amplification factor depends on the capacitance and frequency (shown in Fig. S6). In this regard, the voltage values mentioned in our paper are the actual voltage values measured by Tektronix TDS2024C oscilloscope (shown in Table S1).

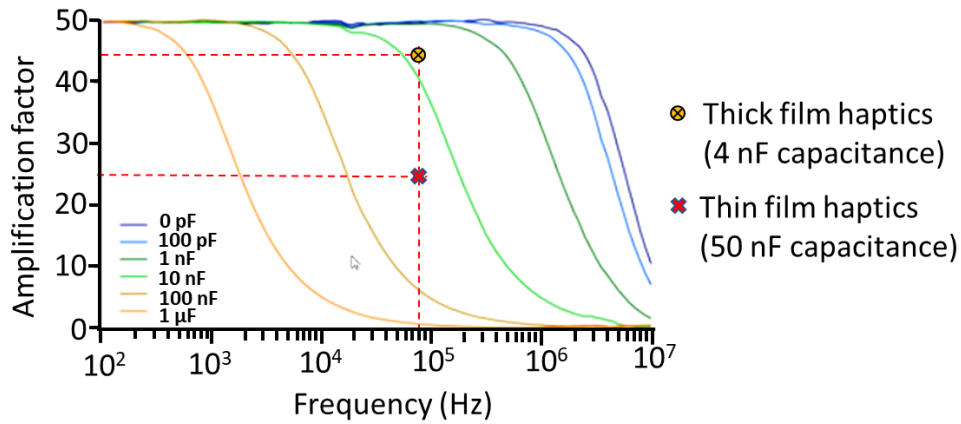


Fig. S6 Full output swing 300V_{pp} frequency response of Falco WMA-300 high voltage amplifier. This figure was re-drawn based on the information provided on the website of Falco System: http://www.falco-systems.com/High_voltage_amplifier_WMA-300.html.

Table S1. Comparison between the voltage provided by the source generator, 50-folds amplified voltage and actual amplified voltage observed from the oscilloscope. Based on those values, amplification factors specific to thick and thin films haptics were calculated and shown in the table.

	Thick film haptics	Thin film haptics
Capacitance	4 nF	50 nF
Voltage provided by source generator (U_g)	2.8 V _{pp}	0.8 V _{pp}
$U_g \times 50$	140 V	40 V
Actual amplified voltage (U_a)	120 V	20
Amplification factor (U_g/U_a)	43	25

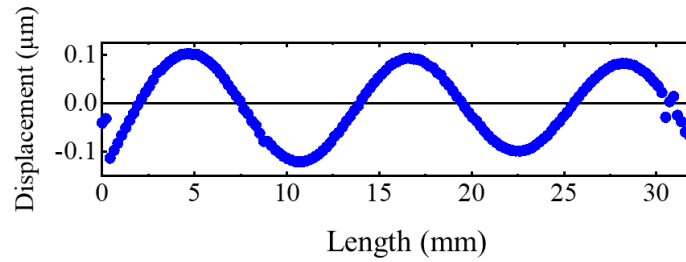


Fig. S7 Out-of-plane displacement scanned along the x axis at 20 V unipolar voltage and 71.5 kHz

S4. Impedance analysis

In principle, a mechanical resonance in an electromechanical device induces extra current need at this resonance because impedance generally decreases. Consequently, we measured the impedance of an equivalent haptic actuator to measure specifically the drop of impedance at resonance. This haptic actuator was made of 10 μm sol-infiltrated PZT thick film on a haptic plate ($34 \times 10 \text{ mm}^2$), and the applied AC voltage was 5 V_{pp} . Note that the measurement was performed with only one haptic actuator ($2 \times 6 \text{ mm}^2$). The capacitance versus frequency $C_p(f)$, impedance vs. frequency $Z(f)$, and phase vs. frequency $\theta(f)$ as shown in Fig. S8, obtained experimentally by using a HIOKI IM3570 impedance analyser.

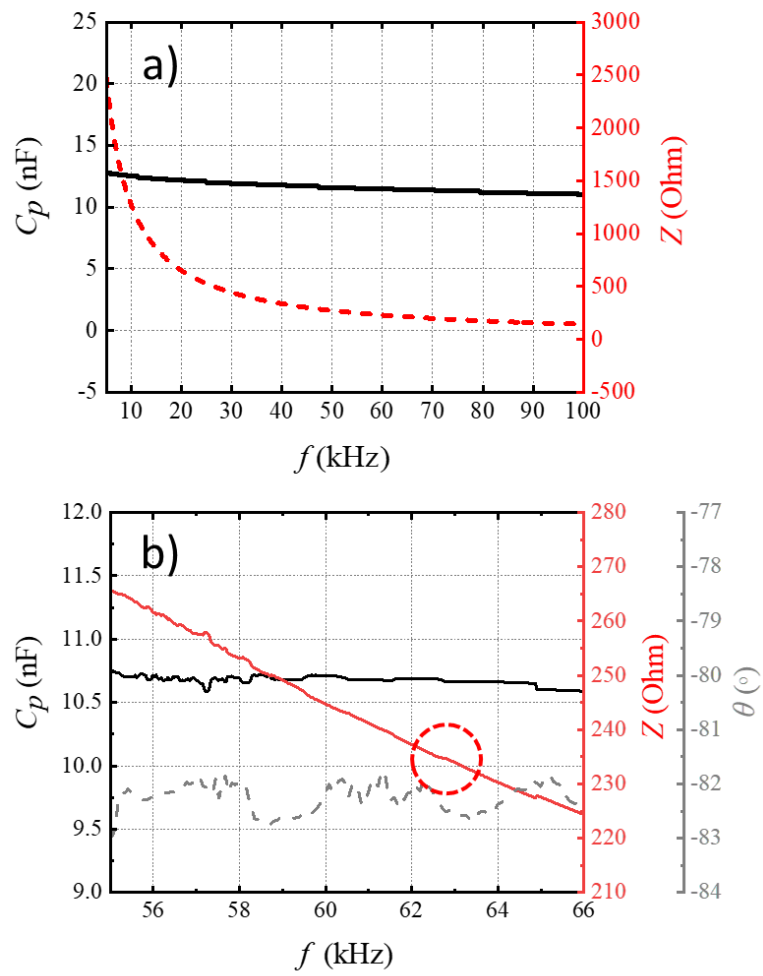


Fig. S8 a) Capacitance C_p and impedance Z of the actuator between 5kHz and 100kHz. (b) Impedance Z and phase θ , and c) capacitance of the actuator between 55kHz and 66kHz. Note that the measurement was performed with only one haptic actuator made of 10 μm sol-infiltrated PZT thick film, and the applied AC voltage is 5 V_{pp} .

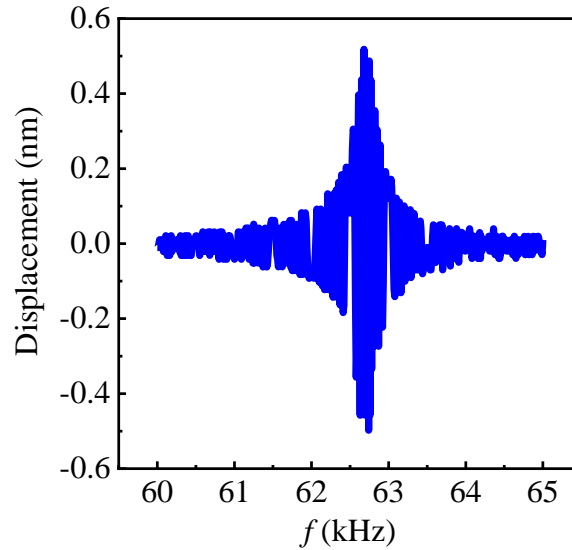


Fig. S9 Out-of-plane displacement versus frequency. The measurement was performed with an actuator ($2 \times 6 \text{ mm}^2$) to drive a $34 \times 10 \text{ mm}^2$ platinised silicon haptic plate. The applied voltage is 40 V_{pp} ($20 \text{ V AC} + 20 \text{ V DC}$), which is read from oscilloscope. The peak-to-peak out-of-plane displacement generated with one actuator at resonance frequency reaches $1.2 \text{ }\mu\text{m}$.

Fig. S8a shows the impedance and the capacitance of the actuator versus frequency. The resonance is not visible. When we zoom in the frequency range of the resonance (which has been identified at 62.6 kHz from the out of plane amplitude versus frequency displayed in Figure S9), we can see a slight change in phase (grey dash line in Fig S8b) and in capacitance (black line in Fig S8b). However, the change of capacitance is limited to 0.3% at 62.6 kHz .

This means that our approach of extracting the reactive power via $Cf(U_{rms})^2$ is valid.

Besides, we checked that other teams observed similar very small variations of impedance at resonance on haptic devices.[4]

We also directly measured the power consumption per actuator from consumed current. A small resistor ($12 \text{ }\Omega$) was connected in series with one haptic actuator made of sol-infiltrated PZT thick film, as shown in Fig. S10. Because the resistance of this resistor is less than 5% of the actuator's impedance ($250 \text{ }\Omega$), its contribution to the total resistance is negligible. As the actuator and the resistor are connected in series, the voltage drop across the resistor can be measured to calculate the current through the actuator.

Applying 40 V (unipolar, peak to peak) at the resonance (62 kHz), the voltage on the small resistor was 1.2 V (peak to peak) and the calculated current was 100 mA (peak to peak). Therefore, the power consumption of the actuator was 500 mW, which is very close to the value calculated using $Cf(U_{rms})^2$ (450 mW).

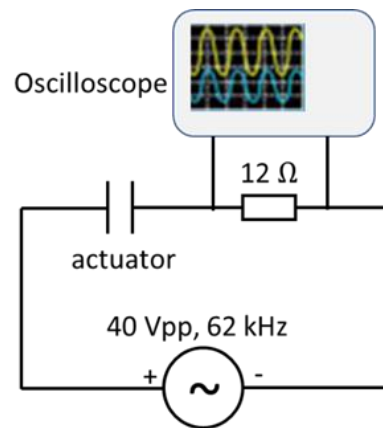


Fig. S10 Schematic diagram of the circuit for measuring the current.

S5. Measurement of piezoelectric coefficient

We employed a method using cantilever structure, as proposed by Mazzalai et. al.,⁵ to experimentally evaluate the transverse piezoelectric coefficient $e_{31,f}$. We used sol-infiltrated 10 μm -thick PZT film-based haptic device ($34 \times 10 \text{ mm}^2$) as the cantilever, on which one of the top electrodes ($2 \times 8 \text{ mm}^2$) was used to deflect the cantilever, as schematically shown Fig. S11. The cantilever was firmly clamped as also shown in the Figure.

In the sector between the clamp at $x = 0$ and the top electrode end at $x_1 = 2 \text{ mm}$ (see Fig. S11), the cantilever shows a constant curvature when the voltage is applied. Using a Polytech's laser vibrometer in velocity mode, we measured the displacement (denoted as $w(x_2)$) of the cantilever at $x_2 = 27 \text{ mm}$.

Fig. S12 shows the screenshot of the oscilloscope window, which respectively reveals signals of the source generator, voltage amplifier output and vibrometer output, when applying 40 V (unipolar, peak to peak) at 100 Hz. As velocity is measured with the vibrometer, the displacement can be calculated following the equation: $w = Vm/(2\pi f)$, where V is the

vibrometer voltage output, m is the velocity range of the vibrometer ($5 \text{ mm s}^{-1} \text{ V}^{-1}$), and f is the frequency, respectively. At 40 V_{pp} and 100 Hz , the peak-to-peak vibrometer output is 70 mV , corresponding to the peak-to-peak $w(x_2)$ displacement of 560 nm .

Following ref.[5], the $e_{31,f}$ can be calculated following the equation:

$$e_{31,f} = -\frac{1}{3} \frac{Y_{sub}}{(1 - \nu_{sub})c_f} [c_f + (1 - c_f)(1 - \nu_{sub})] \frac{w(x_2)}{x_1(2x_2 - x_1)} \frac{t_{sub}^2}{U}$$

where Y_{sub} , ν_{sub} and t_{sub} , are Young's modulus (170 GPa), Poisson ratio (0.28), and thickness of the substrate (0.65 mm), respectively. $c_f(0.8)$ is the top electrode coverage factor, defined as b_{elec}/b_{cant} , where b_{elec} and b_{cant} are the top electrode width (8 mm) and the cantilever width (10 mm), respectively. U is the applied voltage, which is 40 V (unipolar, peak-to-peak).

The experimentally obtained $e_{31,f}$ of the sol-infiltrated PZT thick film is -7.6 C m^{-2} , which is in line with the value extracted from the haptic experiment (-7 C m^{-2}).

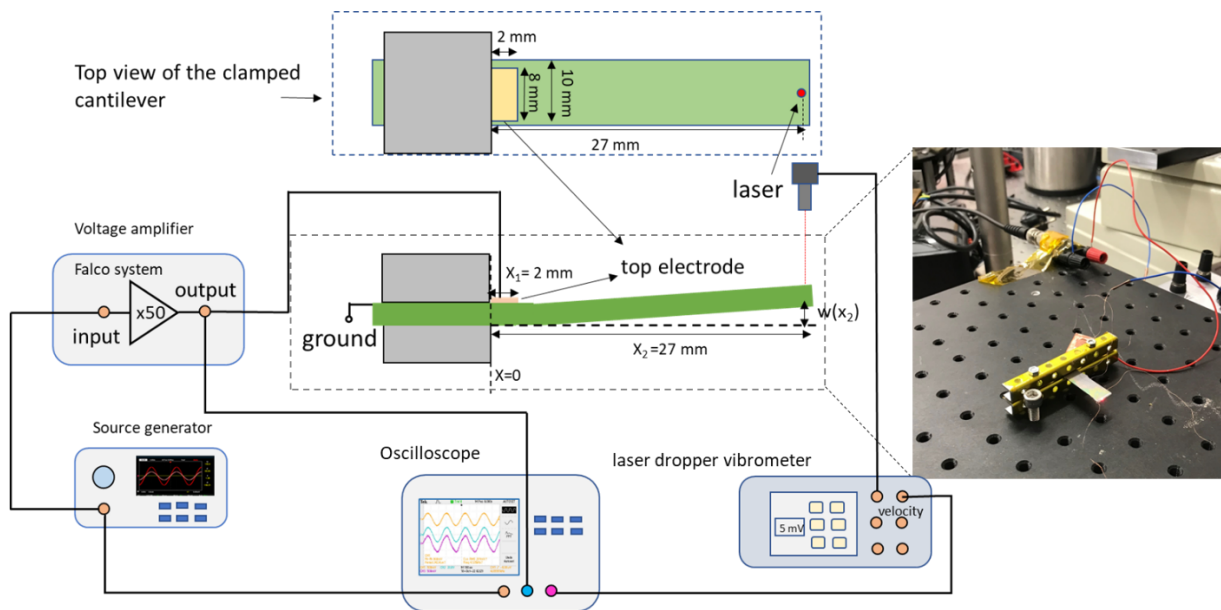


Fig. S11 Scheme of the cantilever-tip displacement measurement setup developed for the measurement of the transverse piezoelectric coefficient $e_{31,f}$.

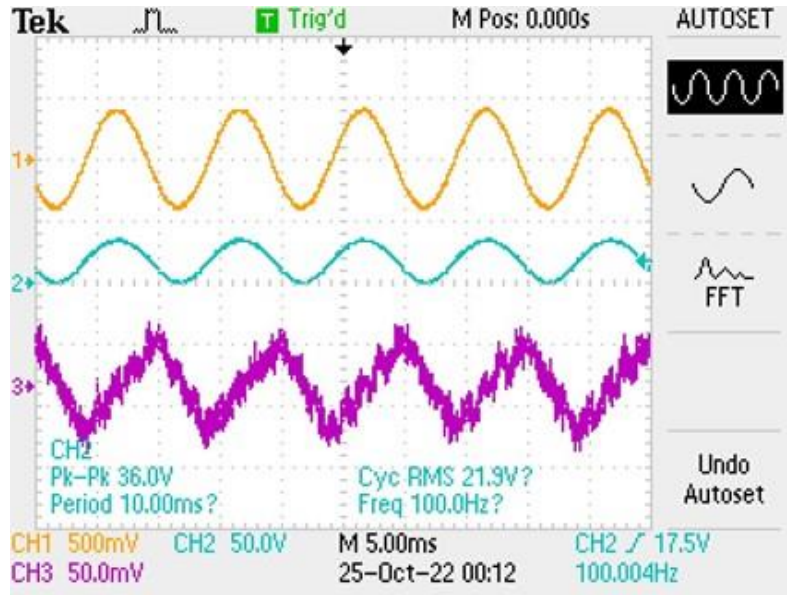


Fig. S12 Signals of the source generator (channel 1 in orange), voltage amplifier output (channel 2 in cyan) and vibrometer output (channel 3 in purple).

To make sure that $e_{31,f}$ was not measured at mechanical resonance, we also performed frequency sweep from 10 Hz to 20 kHz, as shown in Fig. S13. The first resonance is observed at 500 Hz, significantly above the piezoelectric measurement (100 Hz).

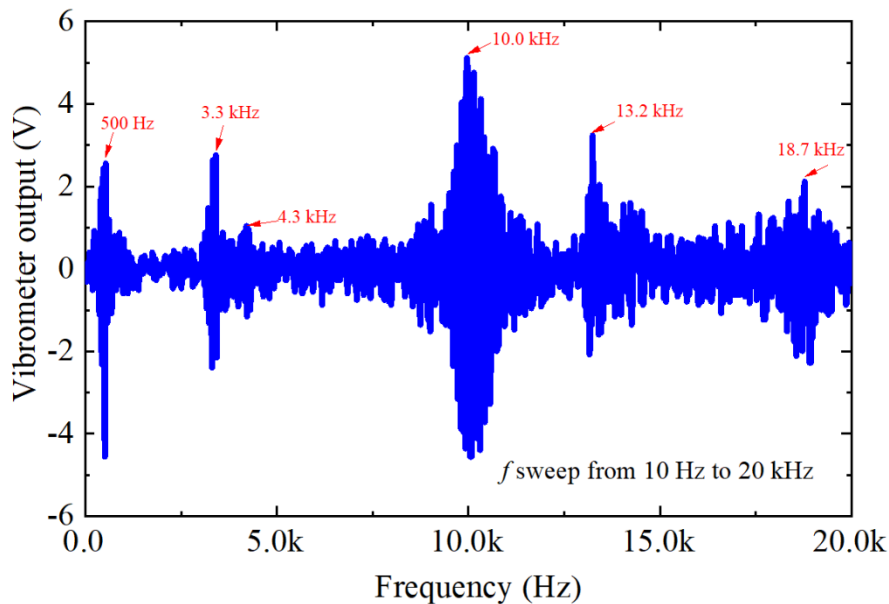


Fig. S13 Vibrometer output as a function of frequency in the range from 10 Hz to 20 kHz. Note that the velocity range of vibrometer for this measurement is $10 \text{ mm s}^{-1} \text{ V}^{-1}$. The applied voltage is 40 V (unipolar, peak-to-peak).

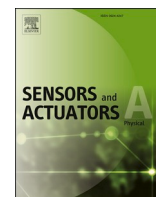
References:

- [1] N. Godard, S. Glinsek, and E. Defay, *J. Alloys Compd.* 2019, 783,801.
- [2] M.S. Bernardo, B. Malič, D. Kuscer, *J. Electrochem. Soc.*, 2015, 162 (11), 3040-3048.
- [3] S. Glinsek, M. A. Mahjoub, M. Rupin, T. Schenk, N. Godard, S. Girod, J. B. Chemin, R. Leturcq, N. Valle, S. Klein, C. Chappaz, E. Defay. *Adv. Funct. Mater.* 2020, 30, 2003539.
- [4] F. Bernard. Conception, fabrication et caractérisation d'une dale haptique à base de microactionneurs piézoélectriques, 2016: <https://www.theses.fr/2016GREAT039>).
- [5] A. Mazzalai, D. Balma, N. Chidambaram, R. Matloub and P. Murali, *Journal of Microelectromechanical Systems*, 4, 831-838, 2015.

7.2 Screen-printed power-efficient haptic device with large deflection

In section 7.2, we extended our investigation to constructing an 80 μm PZT actuator via screen printing to significantly lower power consumption to a few mW. We found that only 5 mW were required for a printed thick PZT haptic device to produce 1 μm of deflection at 20 V and 17.8 kHz. At 150 V, the same device was capable of producing a deflection of 9 μm . My first-author publication “Piezoelectric thick film for power efficient haptic actuator” has been attached in Section 7.2.[127]

Authors contributions: I was able to observe the deposition process of thick film thanks to the opportunity provided by my supervisor Dr. Emmanuel Defay and Prof. Barbara Malic for my secondment, during which this work was carried out. The PZT thick film used in this work was prepared by our Slovenian colleagues, Prof. Hana Ursic, Silvo Drnovsek, and Prof. Barbara Malic. I was responsible for designing and measuring the fabricated haptic devices and drafting the manuscript, which was subsequently revised by my supervisor Dr. Emmanuel Defay and Dr. Sebastjan Glinsek. Additionally, I received assistance from my colleague Dr. Matej Sadl from the Jozef Stefan Institute in conducting some films characterizations.



Power-efficient piezoelectric haptic actuators with large deflection

Longfei Song^{a,b,*}, Sebastjan Glinsek^a, Hana Ursic^{c,d}, Silvo Drnovsek^c, Matej Sadl^{c,d}, Barbara Malic^{c,d}, Emmanuel Defay^a

^a Materials Research and Technology Department, Luxembourg Institute of Science and Technology, rue du Brill 41, L-4422 Belvaux, Luxembourg

^b University of Luxembourg, 41 rue du Brill, L-4422 Belvaux, Luxembourg

^c Electronic Ceramics Department, Jožef Stefan Institute, Jamova cesta 39, 1000 Ljubljana, Slovenia

^d Jožef Stefan International Postgraduate School, Jamova cesta 39, 1000 Ljubljana, Slovenia

ARTICLE INFO

Keywords:

Screen printing
Piezoelectric film
Haptic device
Low power consumption
Large deflection

ABSTRACT

Surface haptic devices based on piezoelectric actuators are one of the most promising solutions to achieve subtle touch feedback on various surfaces. In comparison to stand-alone actuators, piezoelectric thick film actuators not only have a low power consumption and a large deflection range, but also allow for direct integration on various substrates. Herein, we fabricated power-efficient haptic actuators by screen-printing 10 μm -thick platinum bottom electrode and 80 μm -thick niobium-doped lead zirconate titanate (PZT) on alumina substrate (25.5 \times 12.5 mm^2). Our fabricated haptic device containing two actuators (10 \times 1 mm^2 per actuator) connected in parallel exhibits an antisymmetric Lamb wave resonant mode at 17.8 kHz, in line with finite element modelling. At the limit of touch detection (1 μm out of plane deflection), the device consumes only 5 mW at a unipolar voltage of 20 V_{pp} . At a unipolar voltage of 150 V_{pp} , the peak-to-peak out-of-plane displacement reaches nearly 10 μm .

1. Introduction

Haptic technology enables to add the sense of touch in human-machine interactions, [1,2] which can be used in the next generations of smart electronics, such as smart phones, smart cars and home appliances. Piezoelectric actuators are one of the most attractive solutions, which can generate ultrasonic vibrations at resonance. [3–5] When a finger slides across a haptic vibrating plate, a squeezed-air thin film is formed in the contact region between the plate and the finger by the high-speed compression-decompression cycle of air. [6,7] This enables real-time control of the friction coefficient of a sliding finger, which gives the opportunity to emulate artificial textures. Experience shows that creating a squeezed-air film effect that anyone can feel requires the haptic device to produce at least 1 μm in out-of-plane surface deflection.⁶

Piezoelectric actuators can be made of bulk ceramics, thin films, or thick films. Bulk piezoelectric ceramic actuators are the current technological solution for commercialization. They are made of PZT ceramics with a thickness in the several 100 μm -range, which can hardly be thinner. The bulk ceramic actuators are known to enable larger

deflection than thin and thick film ones, thanks to their higher piezoelectric coefficient. [8,9] However, they are stand-alone and need to be glued to the haptic plate, preventing them from using collective fabrication means, which induces extra fabrication costs.

Piezoelectric thin films enable reaching detectable deflection. And they are fabricated with technologies compatible with mass production. [10] However, the main drawback of piezoelectric thin film actuators with metal-insulator-metal (MIM) geometry is large power consumption caused by their large capacitance. For example, Hua et al. recently demonstrated a transparent haptic device based on 0.5 μm -ITO/2 μm -PZT/0.5 μm -ITO stack on Corning Lotus™ NXT Glass (71 \times 60 \times 0.5 mm^3). [11] The haptic device generated an out-of-plane deflection of 1 μm at 10 V_{pp} at 22.5 kHz. The power consumption of the whole haptic device reached up to 3.6 W.

With an attempt to reduce the power consumption and fabricate a fully transparent device, Glinsek et al. developed a haptic device (15 \times 3.7 \times 0.5 mm^3) on fused silica glass based on 1 μm PZT thin film and ITO interdigitated electrodes (IDE) [12], without bottom electrode. At a unipolar voltage of 150 V at 73 kHz, the out-of-plane peak-to-peak displacement reached 3 μm . The benefit of the IDE structure is the small

* Corresponding author at: Materials Research and Technology Department, Luxembourg Institute of Science and Technology, rue du Brill 41, L-4422 Belvaux, Luxembourg.

E-mail address: longfei.song@list.lu (L. Song).

<https://doi.org/10.1016/j.sna.2023.114346>

Received 14 December 2022; Received in revised form 25 March 2023; Accepted 3 April 2023

Available online 11 April 2023

0924-4247/© 2023 The Author(s). Published by Elsevier B.V. This is an open access article under the CC BY-NC-ND license (<http://creativecommons.org/licenses/by-nc-nd/4.0/>).

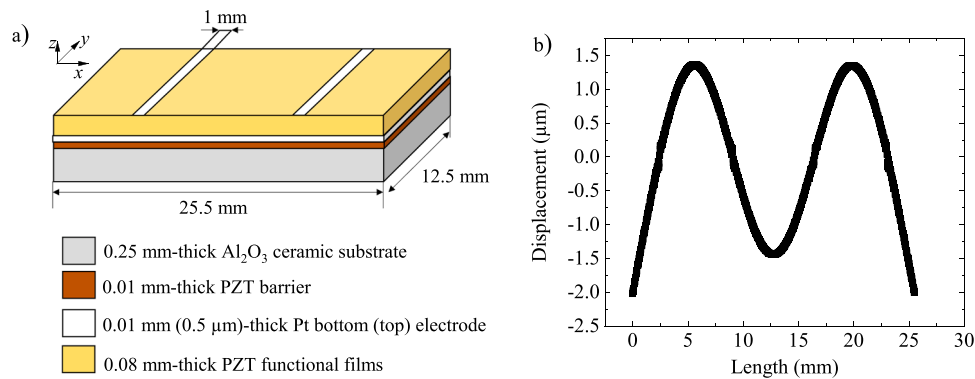


Fig. 1. a) Schematic diagram of the device's structure used for the modelling. x , y and z axis represent the directions of the length, width and height, respectively. b) Mode shape at resonance, obtained from the modelling.

capacitance of the actuator, i.e., 120 nF per actuator, and thereby the low power consumption (32 mW to obtain 1 μm displacement). If the actuator had the same width (60 mm) as Hua's actuator, the device would consume 640 mW to generate a 1 μm -deflection. Therefore, consumption decreases, but the voltage remains high.

In our previous work, we showed that 10 μm -thick PZT films consume 50 mW to generate a 1 μm -out-of-plane amplitude Lamb wave, whereas the same actuator with 0.5 μm -thick film requires 750 mW, i.e. 15 times more. [13] Our model confirmed what we observed experimentally, namely that 1) deflection depends on voltage, not on film thickness, as long as the latter does not affect stiffness of the device and 2) increasing film thickness reduces power consumption by linearly decreasing actuator capacitance.

The screen-printing technology that uses ceramic powder-based dispersions as inks allows not only for the efficient production of thick films but also for their patterning. [14–16] It is the preferred deposition technology for films with a thickness in the range of 10–100 μm . Screen-printed thick PZT films have already been used in piezoelectric micro-electro-mechanical systems (MEMS). [17,18].

In this work, haptic devices consisting of 80 μm PZT thick films were screen printed on platinized 0.25 mm thick Al_2O_3 substrates. The haptic device has a dimension of $25.5 \times 12.5 \text{ mm}^2$ composed of two actuating areas of $10 \times 1 \text{ mm}^2$ connected in parallel. When actuated, the fabricated device exhibits a standing Lamb wave at 17.8 kHz, in line with finite element modelling. At 20 V_{pp} (10 V_{AC} + 10 V_{DC} , $U_{rms} = 12.2 \text{ V}$), the haptic device generated a peak-to-peak out-of-plane deflection of 1 μm , reaching the touch limit. The power consumption of each actuator is 2.6 mW (5.2 mW for the entire device), which is 300 times less than the power consumption of a 0.5 μm thin film actuator with the same width at the same voltage (750 mW per actuator, as reported in ref. 13). At a unipolar voltage of 150 V_{pp} (75 V_{AC} + 75 V_{DC}) the peak-to-peak displacement reaches 10 μm .

2. Finite element modelling

Two-dimension finite element modelling (FEM) was performed using COMSOL software. A scheme of the haptic device ($25.5 \times 12.5 \times 0.25 \text{ mm}^3$) composed of 80 μm -PZT and 0.25-mm Al_2O_3 substrate is shown in Fig. 1a. Two actuating areas ($10 \times 1 \text{ mm}^2$) were created symmetrically on the substrate with a spacing of 12.5 mm between each other. A voltage of 50 V was applied to each PZT actuator. The effective transverse piezoelectric coefficient $e_{31,f}$ and relative permittivity ϵ_r were set to -5 C m^{-2} and 900, respectively. Note that $e_{31,f}$ was extracted from the modelling by matching the experimental displacement value of the haptic device, after having measured the damping loss factor η .¹³ The latter was obtained by sweeping the frequency of the actuator and collecting the displacement, as will be explained in Fig. 4a. η corresponds to the width of the resonance peak ($\Delta f/f$), which is 0.0168 in our specific

case. Young's modulus and Poisson's ratio for Al_2O_3 substrate used in the modelling are 420 GPa and 0.2, respectively. [19] The influence of the electrodes and barrier on the deflection was ignored due to their lower thicknesses.

The simulated resonant frequency was 19.7 kHz, where the device shows its maximum displacement (4 μm peak-to-peak) at 50 V. Fig. 1b represents the mode shape of the device at its resonance, which shows a Lamb wave mode with four nodes equally spaced along its length. Peak-to-peak displacement plotted as a function of voltage is shown in Fig. S1.

3. Methods

1) Powder Synthesis

The powder was synthesized by solid-state synthesis from PbO (99.9%, Alfa 12220), ZrO_2 (99.1%, Tosoh Tz-0), TiO_2 (99.8%, Alfa Aesar 42681) and Nb_2O_5 (99.9%, Sigma Aldrich 208515) in the molar ratio corresponds to the stoichiometry of $\text{Pb}(\text{Zr}_{0.53}\text{Ti}_{0.47})_{0.98}\text{Nb}_{0.02}\text{O}_3$ (PZT) with 2 mol% excess of PbO. The powder mixture was milled and heated at 900 $^\circ\text{C}$ for 2 h. After an additional milling step, the powder had an average particle size of 0.4 μm .

2) Thick-film samples

Al_2O_3 substrates (99.9%, CoorsTEK) were prepared by slip-casting Alcoa A-16 powder and sintered at 1600 $^\circ\text{C}$ for 4 h. Their size, thickness and surface roughness are $5 \times 5 \text{ mm}^2$, 0.25 mm and $< 0.2 \mu\text{m}$, respectively. Standard as-fired thickness tolerance is $\pm 10\%$. They were laser-cut into $25.5 \times 12.5 \text{ mm}^2$ used for printing haptic devices. The PZT screen-printing paste was prepared from the PZT powder and an organic vehicle consisting of alpha-terpineol 2-2-butoxy-ethoxy-ethyl acetate and ethyl cellulose in a mass ratio of 60/25/15. First, the PZT barrier layer was deposited by screen-printing the paste on the Al_2O_3 substrate, then it was dried at 150 $^\circ\text{C}$, heated at 600 $^\circ\text{C}$ for 1 h to remove the organic vehicle and sintered at 1100 $^\circ\text{C}$ for 2 h. In the next step, the platinum paste (Ferro E1192) was screen-printed, dried, and heated at 1100 $^\circ\text{C}$ for 1 h to form the bottom electrode. All the thermal processes were performed in air.

To create the functional haptic layer, the PZT paste was printed on top of the platinized substrate, dried at 150 $^\circ\text{C}$, heated at 600 $^\circ\text{C}$ for 1 h and sintered at 950 $^\circ\text{C}$ for 2 h. The packing powder with the composition PbZrO_3 with an excess of 2 mol% PbO was introduced to sustain the vapour pressure of lead oxide in the local atmosphere within the covered crucible and prevent expected lead-oxide losses from the film. [20]

3) Microstructural Characterization

The phase composition of the film was studied with an X-ray diffractometer (XRD, D8 Discover, Bruker, USA) using $\text{Cu-K}\alpha$ radiation. The patterns were recorded in θ - 2θ geometry in a 2θ -range of

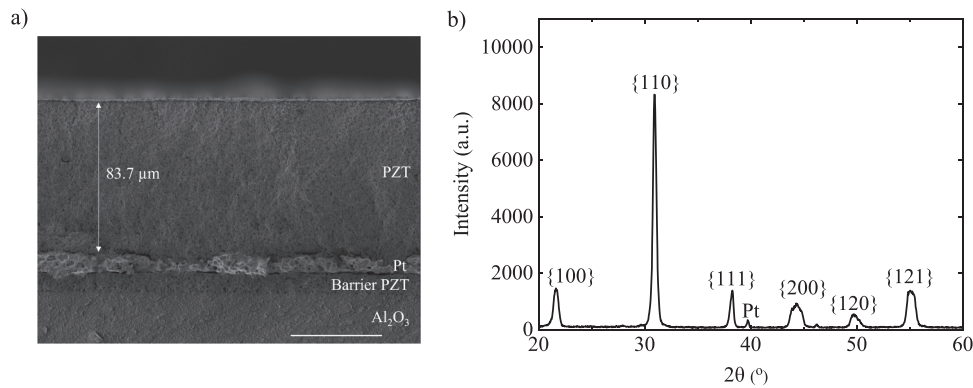


Fig. 2. a) Cross-sectional scanning electron microscope (SEM) of the printed thick film structure on Al_2O_3 substrate. Scale bar is $50\ \mu\text{m}$. b) X-ray diffraction pattern of the printed PZT thick film.

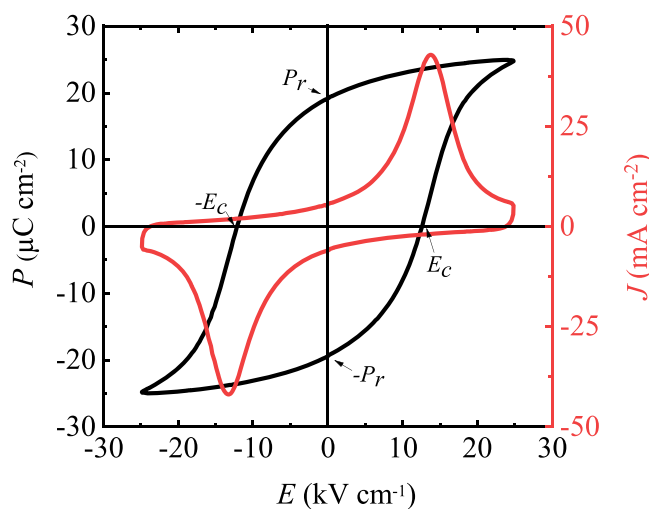


Fig. 3. Polarization and corresponding current density versus electric field ($P(E)$, $j(E)$) of the printed capacitor ($10 \times 1\ \text{mm}^2$).

20° – 60° , with step size and integration time of 0.04° and 4 s, respectively. Scanning electron microscope (SEM, Helios NanoLab 650, FEI) was used to analyze the cross-sectional microstructures of the films.

4) Electrical Characterization

500 nm-thick platinum top electrodes with $10 \times 1\ \text{mm}^2$ were sputtered (BALTEC MED 020 Metallizer) and simply patterned with Kapton tape. Polarization-electric field $P(E)$ hysteresis loops were measured using a TF Analyzer 2000 E (aixACCT) with a triangular waveform at 100 Hz. The relative capacitance and loss were measured using an Impedance Analyzer HIOKI at 17.8 kHz and 500 Hz, respectively, while applying a voltage of $5\ \text{V}_{\text{AC}}$.

5) Acoustic characterization

The haptic device was placed on suspended flexible bars and was connected to a waveform generator (33210 A Keysight) via an amplifier (WMA-300, Falco Systems). The out-of-plane displacement was recorded using an OFV-5000 Polytec vibrometer. We used a computer-controlled X-Y stage to move the haptic device for line scans and 2D mapping. The whole set-up was controlled with the vibrometer via a LabVIEW program. Note that the two actuators were connected in parallel, meaning the voltage applied to each actuator is the same. Note also that all the measurements in Fig. 4 were all done at a unipolar voltage.

There was no specific poling process performed prior to the measurements. The actual poling of actuators occurred during the measurements as soon as the unipolar voltage reached a value beyond the

film's coercive voltage at 100 V.

4. Results

4.1. Material characterizations

Fig. 2a shows a cross-sectional scanning electron microscope (SEM) image. PZT film is $80\ \mu\text{m}$ -thick, dense, and exhibits a smooth surface. The Pt bottom electrode and the barrier PZT film are both approximately $10\ \mu\text{m}$ -thick. The barrier PZT film was used to prevent Pt diffusion into the Al_2O_3 ceramic substrate, which has been previously demonstrated in ref [21,22].

Fig. 2b is the X-ray diffraction (XRD) pattern of the screen-printed $80\ \mu\text{m}$ -thick PZT film. A pure perovskite phase is identified by comparing with the powder diffraction file (PDF) No 01-070-4264. [23] The relative intensity of {100}, {110}, {111}, {200}, {120} and {121} peaks indicate a random orientation, which is a typical feature of polycrystalline thick films. [24].

4.2. Electrical measurements

Fig. 3 shows one actuator's polarization versus electric field $P(E)$ hysteresis loop. Its remanent polarization (P_r) is $20\ \mu\text{C cm}^{-2}$ and the coercive field (E_c) is $13\ \text{kV cm}^{-1}$. The corresponding current density versus electric field $J(E)$ is shown in Fig. 3. At E_c it reveals two sharp peaks that link with the domain switching in the PZT film. All the results confirm the good ferroelectric properties of the printed PZT film.

The capacitance per actuator is 1 nF at the resonant frequency of the haptic device. Consequently, the relative permittivity ϵ_r is calculated as 950. The dielectric loss $\tan\delta$ is 0.03 at 500 Hz, which is a rather low value. The cantilever structure was utilized to measure the piezoelectric coefficient $e_{31,f}$, which is obtained to be $-7\ \text{C m}^{-2}$, consistent with the modelling value of $-5\ \text{C m}^{-2}$. Additional information is provided in the Supplementary material.

4.3. Acoustic characterizations

Fig. 4a shows the out-of-plane displacement versus frequency at $150\ \text{V}_{\text{pp}}$ (unipolar, peak-to-peak, $75\ \text{V}_{\text{AC}} + 75\ \text{V}_{\text{DC}}$). At 17.8 kHz the device exhibits a peak-to-peak displacement of $9.5\ \mu\text{m}$, corresponding to its resonance. It is slightly different from the modelling, which is due to uncertainties on the parameters of the ceramic substrate.

The out of plane surface displacement versus the position along the length of the device (y-axis) is shown in Fig. 4b. It is given at different excitation voltages (25, 50 and 150 V). A clear stationary Lamb wave with four nodes equally spaced along its length is observed, in line with the wave shape extracted from the modelling. The displacement is proportional to the applied voltage, as indicated in Fig. 4c. At $150\ \text{V}_{\text{pp}}$

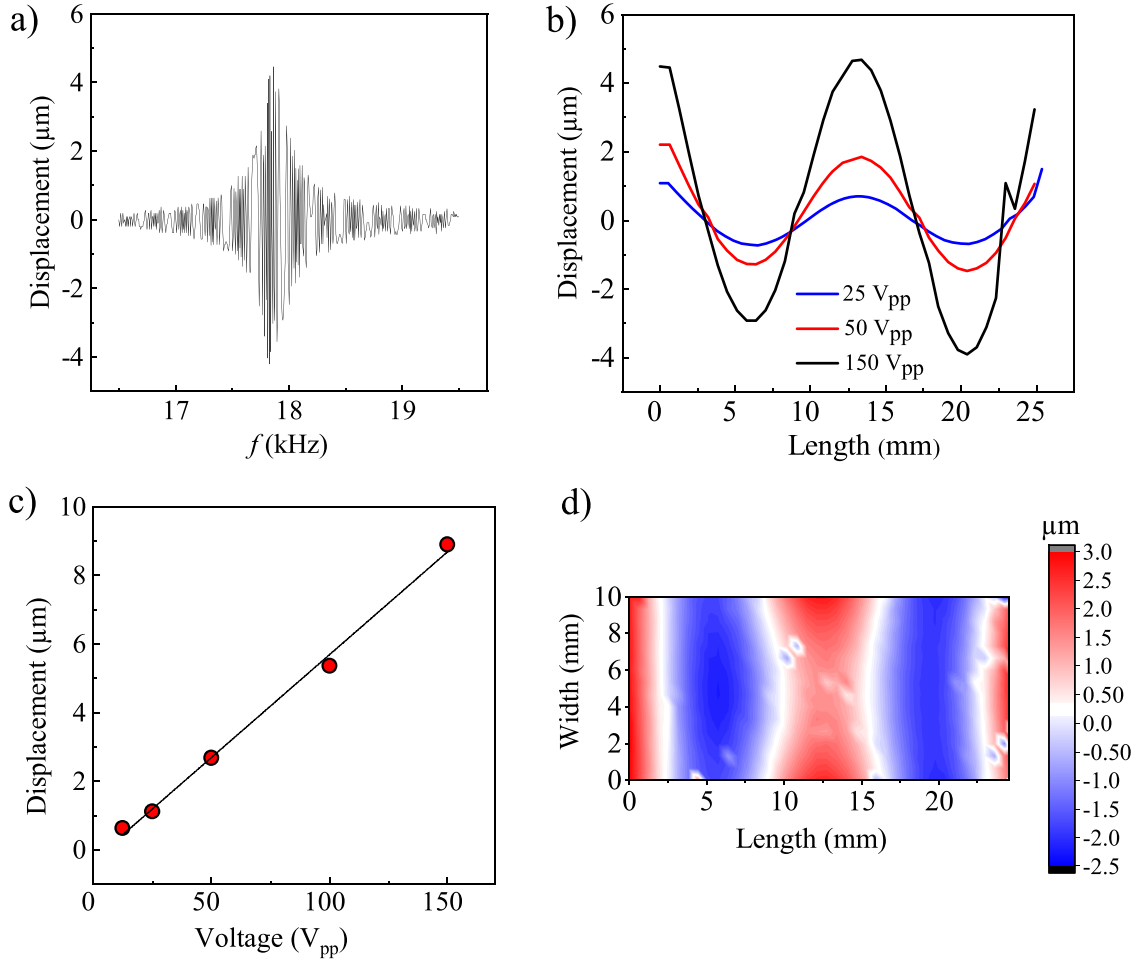


Fig. 4. a) Out-of-plane displacement of the surface versus frequency, showing the resonance frequency at 17.8 kHz. b) Out-of-plane surface displacement along y axis (length) at various voltage. c) Peak-to-peak maximum displacement versus voltage. d) 2D map of displacement of the whole haptic plate at 100 V (50 V_{AC}+50 V_{DC}).

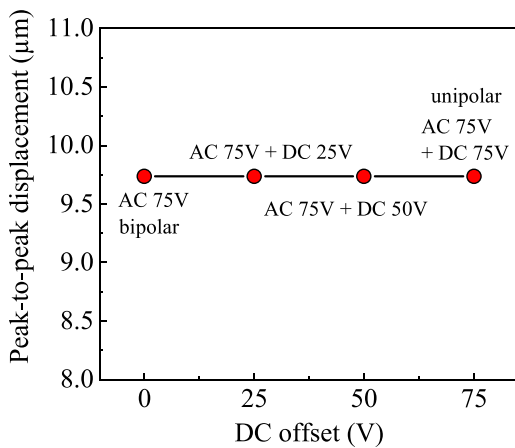


Fig. 5. Out-of-plane peak-to-peak displacement measured with an AC voltage with an amplitude of 75 V, plus various DC offset from 0 V to 75 V.

(75 V_{AC} + 75 V_{DC}) the peak-to-peak out-of-plane displacement reaches nearly 10 μm , which is essentially one order of magnitude more than the lowest finger detectable vibration amplitude. For haptic applications, only 20 V_{pp} (10 V_{AC} + 10 V_{DC}) are required to meet this specification (1 μm). Fig. 4d shows a 2D displacement map of the haptic plate excited at 100 V_{pp} (50 V_{AC} + 50 V_{DC}) and 17.8 kHz. It confirms a neat Lamb shape mode travelling along the length of the plate, in line with

modelling.

To make the haptic effect more visible, we placed a small silicon plate on the haptic surface. When applying a unipolar voltage of 100 V (50 V_{AC} + 50 V_{DC}), the haptic device is immediately activated and the small plate slides, as shown in video 1 in [supplementary information](#), indicating a strong haptic effect generated.

Previous studies have demonstrated that the interaction between an ultrasonically vibrating plate and a fingertip causes the fingertip to act as a mechanical damper, altering the resonance frequency of the mode and lowering the displacement. [25–27].

Applying 150 V_{pp} (75 V_{AC} + 75 V_{DC}) can generate nearly 10 μm peak-to-peak displacement. In order to reduce the maximum voltage applied, we further studied the deflection versus DC offset voltage at the resonance, while keeping AC voltage amplitude at 75 V. In Fig. 5, we observe that the displacement stays unchanged with decreasing DC offset (i.e., from unipolar to bipolar). It makes sense because the E_C is 13 kV cm^{-1} , corresponding to a coercive voltage of 100 V (cf. Fig. 3a), which means that applying a bipolar AC voltage within 100 V does not induce domain switching. However, this strategy requires poling PZT initially at a voltage of at least 100 V, corresponding to its coercive voltage.

5. Discussion

The power consumption of one of these actuators is CfU_{rms}^2 , where C , f and U_{rms} are the capacitance at the resonance, the resonant frequency, and the root mean squared voltage, respectively. To achieve the

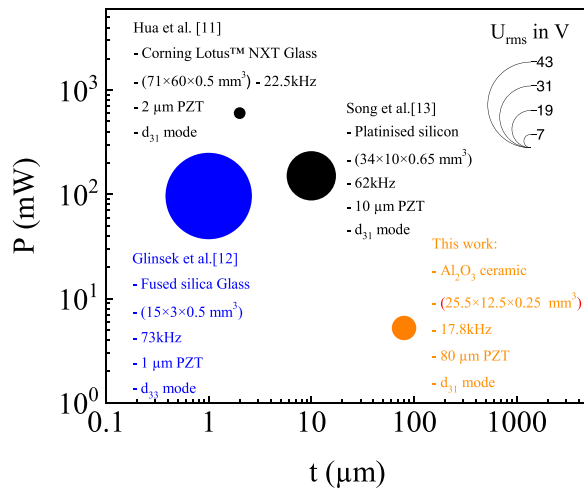


Fig. 6. A comparison of the power consumption of haptic devices and thickness of PZT film reported so far. For a fair comparison, the values of power consumption here are those of haptic devices that generate peak-to-peak displacement of 1 μm . Note that we normalized the actuator's consumption with its width. Diameter of the bubbles represents the applied rms voltage. t represents the film thickness.

specification (1 μm) of a detectable haptic effect, the entire device consumes 5 mW, corresponding to 2.6 mW per actuator at a unipolar voltage of 20 V_{pp}, $U_{rms} = 12.2$ V.

As mentioned earlier, the purpose of using thick film for haptics is to reduce consumption. To evaluate our device, we compared its features with the ones reported in the literatures by normalizing the consumption with the actuators' width, as shown in Fig. 6. If all actuators were 10 mm-wide and if they were driven to reach 1 μm in deflection, the corresponding haptic devices from the relevant literatures would consume respectively 600 mW [Hua],¹¹ 96 mW [Glinsek]¹² and 150 mW [Song]¹³. The consumption of our thick film-based haptic device, limited to 5 mW, is therefore at least 20 times less than the closest state of the art. Note that our device also enables working at low voltage, as shown in Fig. 6.

6. Conclusion

In this work, we developed a haptic device based on 80 μm -thick PZT films deposited by screen printing on an Al₂O₃ ceramic substrate. At 17.8 kHz, a stationary Lamb wave with four nodes equally spaced along its length was generated once a voltage was applied on the PZT actuators. At unipolar voltage of 150 V_{pp} the out-of-plane peak-to-peak displacement reaches up to 9.5 μm . A unipolar voltage of 20 V (10 V_{AC} + 10 V_{DC}, $U_{rms} = 12.2$ V) is enough to obtain a one μm displacement, corresponding to 5 mW in consumption. This is 20 times less than the closest state of the art. The presented results indicate that these thick PZT films not only provide large deflections but also consume much less energy. This could be a game changer for the fabrication of haptic devices, for which one must come up with a solution compatible with collective deposition means and low power consumption.

Declaration of Competing Interest

The authors declare that they have no known competing financial interests or personal relationships that could have appeared to influence the work reported in this paper.

Data availability

Data will be made available on request.

Acknowledgement

The authors acknowledge the Fonds National de la Recherche (FNR) of Luxembourg for supporting this work through the project PRIDE17/12246511/PACE. The authors acknowledge also the Slovenian Research Agency (research core funding P2–0105 and project J2–3058).

Appendix A. Supporting information

Supplementary data associated with this article can be found in the online version at doi:10.1016/j.sna.2023.114346.

References

- [1] T. Watanabe and S. Fukui, A method for controlling tactile sensation of surface roughness using ultrasonic vibration, Proceedings of 1995 IEEE International Conference on Robotics and Automation 1(1995), 1134–1139, <https://doi.org/10.1109/ROBOT.1995.525433>.
- [2] D.A.T. Guzman, Generation and control of tactile feedback with longitudinal ultrasonic vibration and human-in-the-Loop analysis, Université de Lille, 2021, (<https://tel.archives-ouvertes.fr/tel-03674797/>).
- [3] T.H. Yang, J.R. Kim, H. Jin, H. Gil, H. Koo, H.J. Kim, Recent advances and opportunities of active materials for haptic technologies in virtual and augmented reality, Adv. Funct. Mater. 31 (2021) 2008831, <https://doi.org/10.1002/adfm.202008831>.
- [4] C. Basdogan, F. Giraud, V. Levesque, S. Choi, A review of surface haptics: enabling tactile effects on touch surfaces, IEEE T. Haptics 13 (2020) 450–470, <https://doi.org/10.1109/TOH.2020.2990712>.
- [5] Y. Huang, K. Yao, J. Li, D. Li, H. Jia, Y. Liu, C.K. Yiu, W. Park, X. Yu, Recent advances in multi-mode haptic feedback technologies towards wearable interfaces, Mater. Today Phys. 22 (2022), 100602, <https://doi.org/10.1016/j.mphys.2021.100602>.
- [6] M. Biet, F. Giraud, B. Lemaire-Semail, Squeeze film effect for the design of an ultrasonic tactile plate, IEEE Trans. Ultrason. Ferroelectr. Freq. Control 54 (2007) 2678–2688, <https://doi.org/10.1109/TUFFC.2007.596>.
- [7] R.F. Friesen, M. Wiertelowski, M.A. Peshkin, and J.E.E. Colgate, The contribution of air to ultrasonic friction reduction," 2017 IEEE World Haptics Conference (WHC), Jun. 2017. <https://doi.org/10.1109/WHC.2017.7989955>.
- [8] <https://www.hap2u.net/haptic-technology/>.
- [9] <https://product.tdk.com/en/products/sw/piezo/haptic/piezohapt/index.html>.
- [10] S. Glinsek, L. Song, V. Kovacova, M.A. Mahjoub, N. Godard, S. Girod, J.-L. Biagi, R. Quintana, T. Schlee, M. Guedra, M. Rupin, E. Defay, Inkjet-printed piezoelectric thin films for transparent haptics, Adv. Mater. Technol. 7 (2022) 2200147, <https://doi.org/10.1002/admt.202200147>.
- [11] H. Hua, Y. Chen, Y. Tao, D. Qi, Y. Li, A highly transparent haptic device with an extremely low driving voltage based on piezoelectric PZT films on glass, Sens. Actuator A-Phys. 335 (2022), 113396, <https://doi.org/10.1016/j.sna.2022.113396>.
- [12] S. Glinsek, M.A. Mahjoub, M. Rupin, T. Schenk, N. Godard, S. Girod, J.B. Chemin, R. Leturcq, N. Valle, S. Klein, C. Chappaz, E. Defay, Fully transparent friction-modulation haptic device based on piezoelectric thin film, Adv. Funct. Mater. 30 (2020) 2003539, <https://doi.org/10.1002/adfm.202003539>.
- [13] L. Song, S. Glinsek, S. Drnovsek, V. Kovacova, B. Malic, E. Defay, Piezoelectric thick film for power-efficient haptic actuator, Appl. Phys. Lett. 121 (2022) 21290, <https://doi.org/10.1063/5.0106174>.
- [14] H. Ursic, M. Hrovat, J. Holc, J. Tellier, S. Drnovsek, N. Guiblin, B. Dkhil, M. Kosec, Influence of the substrate on the phase composition and electrical properties of 0.65PMN–0.35PT, Thick films, J. Eur. Ceram. Soc. 30 (2010) 2081–2092, <https://doi.org/10.1016/j.jeurceramsoc.2010.04.010>.
- [15] M. Kosec, H. Ursic, J. Holc, M. Hrovat, D. Kuscer, B. Malic, High-performance PMN-PT thick films, IEEE Trans. Ultrason. Ferroelectr. Freq. Control 57 (2010) 2205–2212, <https://doi.org/10.1109/TUFFC.2010.1679>.
- [16] H. Ursic, M. Hrovat, D. Belavic, J. Cilensek, S. Drnovsek, J. Holc, M.S. Zarnik, M. Kosec, Microstructural and electrical characterisation of PZT thick films on LTCC substrates, J. Eur. Ceram. Soc. 28 (2008) 1839–1844, <https://doi.org/10.1016/j.jeurceramsoc.2007.12.029>.
- [17] R. Xu, A. Lei, C. Dahl-Petersen, K. Hansen, M. Guizzetti, K. Birkelund, E. V. Thomsen, O. Hansen, Screen printed PZT/PZT thick film bimorph MEMS cantilever device for vibration energy harvesting, Sens. Actuator A- Phys. 188 (2012) 383–388, <https://doi.org/10.1016/j.sna.2011.12.035>.
- [18] C.C. Hindrichsen, N.S. Almind, S.H. Brodersen, R. Lou-Møller, K. Hansen, E. V. Thomsen, Triaxial MEMS accelerometer with screen printed PZT thick film, J. Electroceram. 25 (2010) 108–115, <https://doi.org/10.1007/s10832-010-9597-4>.
- [19] See <https://accuratus.com/alumox.html>.
- [20] M. Kosec, J. Holc, B. Malic, V. Bobnar, Processing of high-performance lead lanthanum zirconate titanate thick films, J. Eur. Ceram. Soc. 19 (1999) 949, [https://doi.org/10.1016/S0955-2219\(98\)00351-3](https://doi.org/10.1016/S0955-2219(98)00351-3).
- [21] M. Kosec, H. Ursic, J. Holc, M. Hrovat, D. Kuscer, B. Malic, High-performance PMN-PT thick films, IEEE Trans. Ultrason. Ferroelectr. Freq. Control 57 (2010) 2205–2212, <https://doi.org/10.1109/TUFFC.2010.1679>.

- [22] J. Holc, M. Hrovat, M. Kosec, Interactions between alumina and PLZT thick films, *Mater. Res. Bull.* 34 (1999) 2271, [https://doi.org/10.1016/S0025-5408\(99\)00227-5](https://doi.org/10.1016/S0025-5408(99)00227-5).
- [23] ICDD DatabasePDF4+ v4.19 (2019).
- [24] T. Bakarič, B. Malič, D. Kuscer, Lead-zirconate-titanate-based thick-film structures prepared by piezoelectric inkjet printing of aqueous suspensions, *J. Eur. Ceram. Soc.* 36 (2016) 4031–4037, <https://doi.org/10.1016/j.jeurceramsoc.2016.06.038>.
- [25] M. Wiertelwski, V. Hayward, Mechanical behavior of the fingertip in the range of frequencies and displacements relevant to touch, *J. Biomech.* 45 (2012) 1869–1874, <https://doi.org/10.1016/j.jbiomech.2012.05.045>.
- [26] D.A. Torres, B. Lemaire-Semail, C. Giraud-Audine, F. Giraud, M. Amberg, Design and control of an ultrasonic surface haptic device for longitudinal and transverse mode comparison, *Sens. Actuator A Phys.* 331 (2021), 113019, <https://doi.org/10.1016/j.sna.2021.113019>.
- [27] R.F. Friesen, M. Wiertelwski and J.E. Colgate, The role of damping in ultrasonic friction reduction, *IEEE Haptics Symposium (HAPTICS)*, Philadelphia, PA, USA, 2016, 167–172 (2016). <https://doi.org/10.1109/HAPTICS.2016.7463172>.



Longfei Song is a PhD student at the Ferroic Materials for Transducers group in the Materials Research and Technology (MRT) Department of LIST. His research focuses on investigating surface haptic devices based on piezoelectric thin and thick films supervised by Emmanuel Defay and Sebastjan Glinsek.



Sebastjan Glinsek is currently a Senior Research and Technology Associate at Materials Research and Technology Department (MRT) at Luxembourg Institute of Science and Technology (LIST). His previous appointments include CEA-Leti in France, Brown University in USA, and Jozef Stefan Institute in Slovenia. He received his PhD degree in 2012 from Jozef Stefan International Postgraduate School. He is working on electronic oxides, with the focus on their processing via chemical methods and their direct patterning via printing.



Hana Ursic is a tenured researcher associate at Electronic Ceramics Department and an associate professor at the International Postgraduate School. She is the author of 104 scientific publications, 2 review papers, 5 book chapters, and one European, Chinese, and US patent. Her research topics include lead-based and lead-free ferroelectric and piezoelectric ceramics and films, electrocalorics and multicalorics, multiferroics, atomic force microscopy, and aerosol deposition technology. She led 15 national and international projects (and bilateral projects) and was active in the networks EU ERA-NET, KET4, COST. Her work has been cited 2500 times and has an i10 index of 62 and an h-index of 27.



Silvo Drnovsek is a graduate chemical engineer. He has been working at the Electronic Ceramics Department of the Jozef Stefan Institute since 1983. His field of work is synthesis of ferroelectric and piezoelectric materials by classical powder technology and mechanochemical synthesis, sample preparation and characterization. The methods of sample preparation are sintering of bulk ceramics, tape-casting and screen printing of thick films. He is co-author of 42 scientific papers, co-author of 76 published conference abstracts, 36 published conference papers, co-author of 9 patents and many other works.



Matej Sadl is a postdoctoral researcher in the Electronic Ceramics Department at the Jozef Stefan Institute, Ljubljana, Slovenia, where he received his PhD in Sensor technologies in 2022. His research interests include screen-printing and aerosol deposition of ferroelectric ceramic thick films for piezoelectric energy-harvesting, energy storage and electrocaloric applications. He has published 13 scientific papers.



Barbara Malič is Head of Electronic Ceramics Department at Jozef Stefan Institute, Ljubljana, Slovenia, and Professor of Chemistry of Materials at Jozef Stefan International Postgraduate School. Her research topics include lead-based and leadfree ferroelectric and piezoelectric ceramics and thin films, electrocaloric materials, tunable ferroelectric thin films for microwave applications, and patterning of solution derived materials for transparent electronics. She is author or co-author of more than 250 papers, 10 book-chapters, more than 150 technical reports, an EU/US/Chinese patent and 4 Slovenian patents. Recipient of the Zois award (2020) and IEEE 2022 Ferroelectrics Recognition Award.



Emmanuel Defay is the head of the Nanotech Unit and the head of the Ferroic Materials for transducers group at Luxembourg Institute of Science and Technology. His research interests are about materials able to transform one form of energy in another one, and, more specifically, in those related to electrical energy, such as piezoelectric micro-pumps, haptic actuators, mechanical or thermal energy harvesters or electrocaloric solid-state coolers. These topics lie between materials science, engineering and thermodynamics, all of them being required to create innovation in bringing these materials into realistic applications.

Supplementary Material for

Power-Efficient Piezoelectric Haptic Actuators with Large Deflection

Longfei Song,^{1,2*} Sebastjan Glinsek,¹ Hana Ursic,^{3,4} Silvo Drnovsek,³ Matej Sadl,^{3,4}

Barbara Malic,^{3,4} Emmanuel Defay¹

1. Finite element modelling

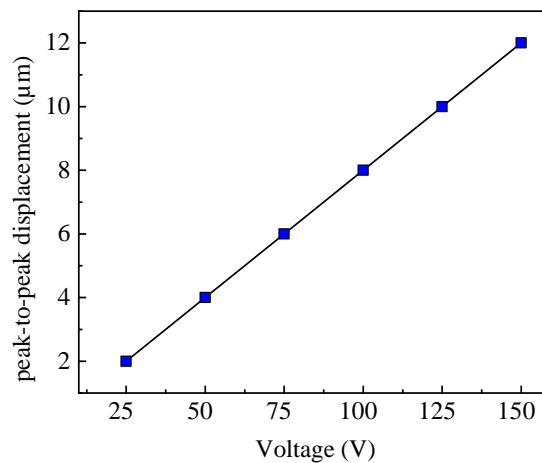


Figure S1 Peak-to-peak displacement versus voltage at the resonance frequency of 19.7 kHz, obtained from finite element modelling.

2. Measurement of piezoelectric coefficient.

To experimentally measure the transverse piezoelectric coefficient $e_{31,f}$, we utilized a cantilever structure method proposed by Mazzalai et. al.¹ The cantilever was deflected using one of the actuators from a fabricated haptic device, as depicted in Figure S2. The electrode dimensions were 1 mm in width and 10 mm in length, and the cantilever was firmly clamped as shown in Figure S3.

Within the region between the clamp at $x = 0$ and the top electrode end at $x_1 = 1$ mm (Figure S2), applying voltage to the cantilever results in a constant curvature. Using a Polytech laser Doppler vibrometer in velocity mode, we measured the displacement at the free end of the cantilever ($w(x_2)$) at $x_2 = 18$ mm.

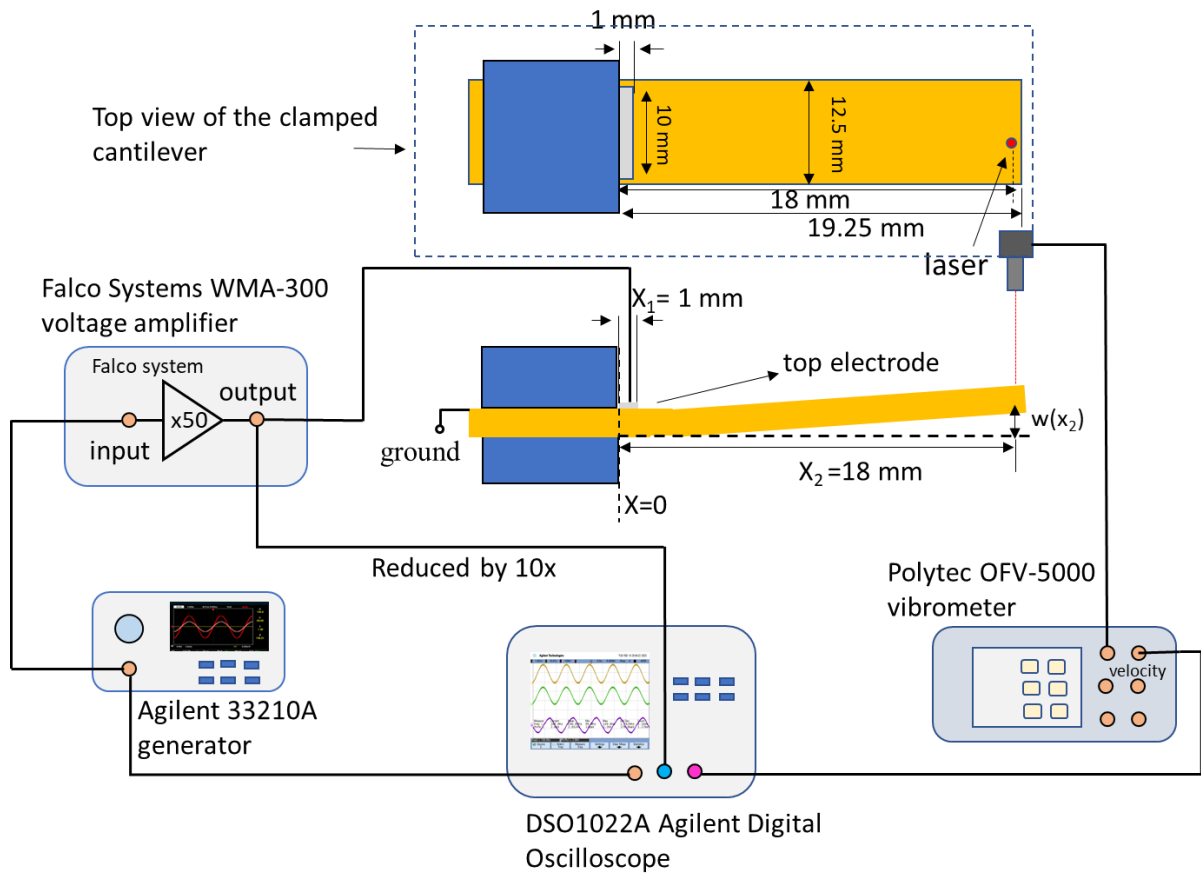


Figure S2 Schematic diagram of the set-up for measuring piezoelectric coefficient using cantilever structure.

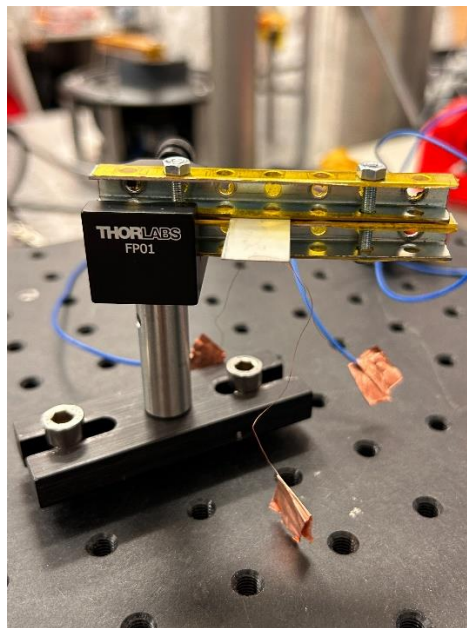


Figure S3 Visual appearance of clamped sample.

In Figure S4, the oscilloscope window displays signals of the source generator, voltage amplifier output (10×CH2), and vibrometer output when a 100 V (unipolar, peak-to-peak) at 100 Hz is applied. Using the vibrometer's measured velocity and the equation $w = Vm / (2\pi f)$, where V is the vibrometer voltage output, m is the velocity range (5 mm/s/V), and f is the frequency, the displacement w can be calculated. At 100 V_{pp} (unipolar, 50 V_{AC} + 50 V_{DC}) and 100 Hz, the peak-to-peak vibrometer output is 225 mV, as shown in Figure S4, corresponding to a peak-to-peak displacement of 1.8 μm ($w(x2)$).

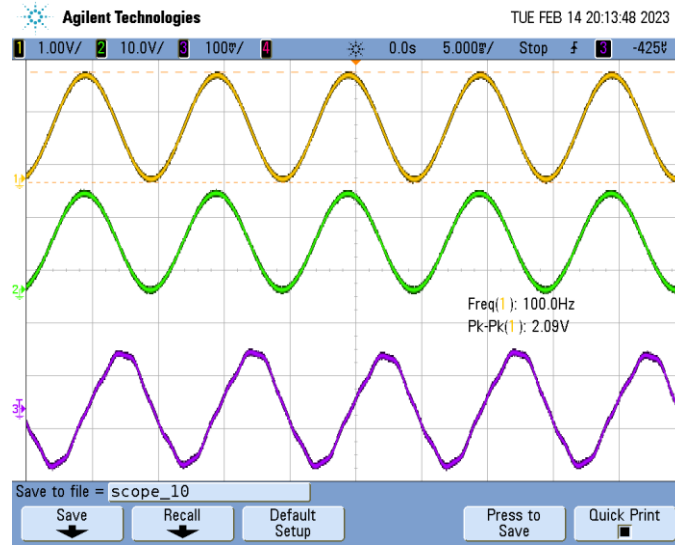


Figure S4 Signals of the source generator (CH1 in yellow, 2 V peak-to-peak, unipolar), voltage amplifier output (CH2 in green, 10 V peak-to-peak, unipolar) and vibrometer output (CH3 in purple). Note that Agilent N2863B oscilloscope passive probe (10:1, 300 MHz) was used to reduce input signal of CH2 by 10x. This means that the voltage amplifier output should be 10 times of the value shown in CH2, namely 100 V peak-to-peak.

Following ref.[1], $e_{31,f}$ can be calculated following the equation:

$$e_{31,f} = -\frac{1}{3} \frac{Y_{sub}}{(1 - \nu_{sub})c_f} [c_f + (1 - c_f)(1 - \nu_{sub})] \frac{w(x_2)}{x_1(2x_2 - x_1)} \frac{t_{sub}^2}{U}$$

where Y_{sub} , ν_{sub} and t_{sub} , are Young's modulus (420 GPa), Poisson ratio (0.2), and thickness of the substrate (0.25 mm), respectively. c_f is the top electrode coverage factor, defined as b_{elec}/b_{cant} , where b_{elec} and b_{cant} are the top electrode width (10 mm) and the cantilever width (12.5 mm), respectively. Therefore, c_f is 0.8. U is the applied voltage, which is 100 V (unipolar, peak-to-peak).

The experimentally obtained $e_{31,f}$ of the printed PZT thick film is -7 C m^{-2} , which is in line with the value extracted from the modelling (-5 C m^{-2}).

It is crucial to avoid measuring $e_{31,f}$ at resonance. Therefore, we conducted a frequency sweep of the vibrometer output from 10 Hz to 1 kHz (see Figure S5) to ensure that the first resonance was observed at 735 Hz, significantly beyond 100 Hz. It indicates that $e_{31,f}$ obtained at 100 Hz is valid.

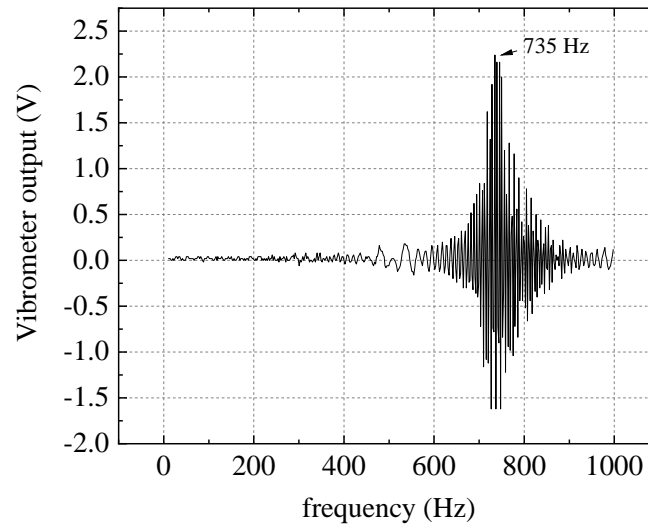
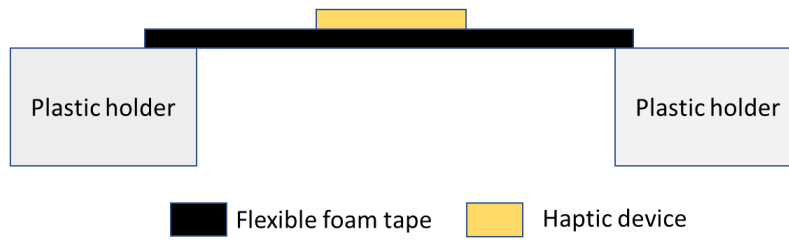


Figure S5 Vibrometer voltage amplitude swept from 10 Hz to 1000 Hz.

3. Set-up for acoustic characterization

In the acoustic measurements, the haptic device was fixed by placing it on double-side flexible foam tape, as shown in Figure S6 and S7 and also in Supplementary Video 1.

Side view of set-up:



Top view of set-up:

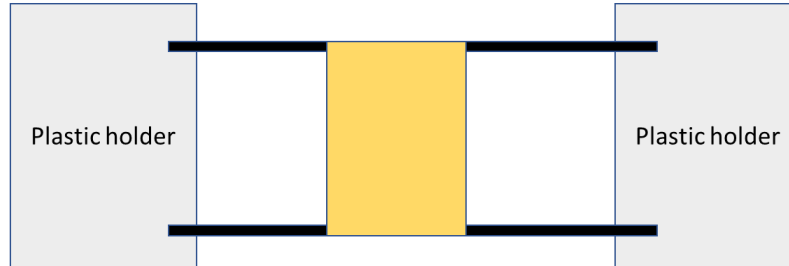


Figure S6 Schematic diagram of set-up built for haptic measurement.

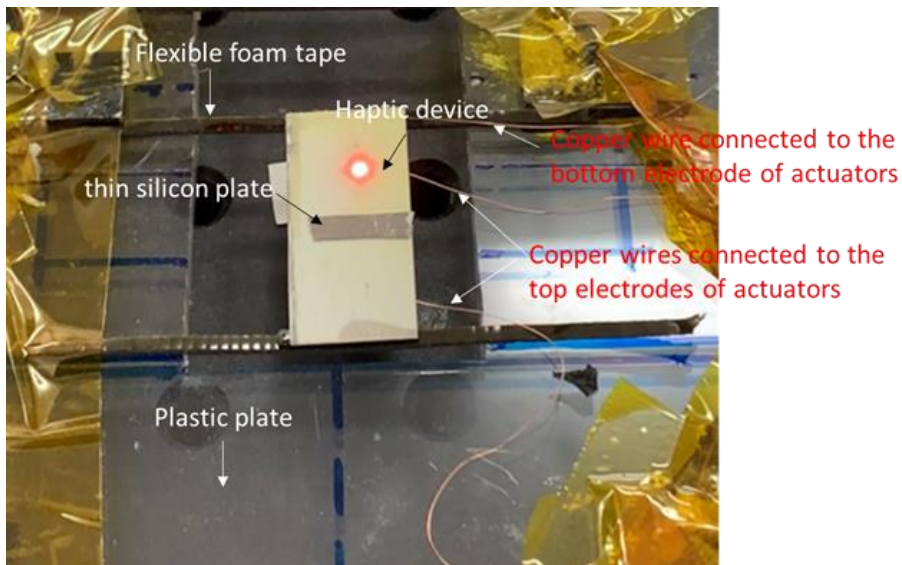


Figure S7 Visual appearance of haptic device fixed on the flexible bars. Note that the thin silicon plate was used to characterize the haptic effect in a visible way, as demonstrated in Video 1 in supplementary material.

4. Comparison between experimental and modelled results

Table 3 Results obtained through experiments and finite element modelling.

	Experimental values	Modelling values
resonance frequency f in kHz	17.8	19.7
peak-to-peak displacement in μm (at 150 V_{pp})	9.5	12
piezoelectric coefficient $e_{31,f}$ in C m^{-2}	-7	-5

References

- 1 A. Mazzalai, D. Balma, N. Chidambaram, R. Matloub and P. Muralt, Journal of Microelectromechanical Systems, 4, 831-838, 2015.

7.3 Challenges

The challenges persist in processing and integrating PZT thick film on haptic surfaces. The sol-infiltration process is suitable for producing dense thick films at a temperature compatible with glass (700 °C) without the need for high-temperature densification or re-crystallization of PZT powders (at 1000 °C). However, this process requires long processing times due to multiple infiltration steps and subsequent annealing. On the other hand, spin coating is not an ideal method for depositing the film as it results in significant waste of PZT powders.

Screen printing is an efficient approach for printing thick films, allowing for deposition of each layer with a thickness exceeding 10 μm while also enabling patterning and wasteless process. However, it requires sintering at very high temperatures (950°C), necessitating the use of a ceramic substrate capable of withstanding such temperatures.

Regardless of the chosen method, the quality of the PZT powder plays a crucial role in producing high-quality PZT thick films.

7.4 Outlook

Combining sol-infiltration with screen printing offers a potential solution to achieve a wasteless process while partially reducing the processing temperature. Furthermore, sol-infiltration can also be implemented through inkjet printing, enabling precise patterning of the film and minimizing waste of PZT powders and solution. Additionally, this approach allows for a computer-controlled process, enhancing process control and efficiency.

Aerosol deposition emerges as a promising technology for depositing thick films at low processing temperatures. Fortunately, during my secondment at Jozef Stefan Institute, I had the opportunity to acquire aerosol-deposited PZT thick films on glass and stainless steel substrates, which will be subject to future investigations. This technique relies on the utilization of fine PZT powders. The thickness achieved in each deposition, using identical parameters, is heavily influenced by the quality of the PZT powders.

Another potential strategy for reducing the processing temperature is the utilization of flash lamp annealing, which allows selective annealing of the film while maintaining a low temperature for the substrate.

Chapter 8

Conclusion and perspectives

8.1 Conclusion

In this thesis, various aspects related to the processing of fabricating surface haptic devices have been studied. Although conclusions have been provided separately in each chapter, this chapter offers a more general conclusion that can be drawn from the current work.

When considering the fabrication process of a surface haptic device on a specific haptic plate, several factors need to be taken into account. These factors include production cost, efficiency, process control, and usage requirements. By considering these factors, several works have been performed:

-Chapter 4: To produce surface haptic devices on glass screens, a flash lamp annealing process has been developed. This process allows for the crystallization of PZT film within a few seconds and in an ambient atmosphere, which can significantly reduce the production cost and simplify the process. The resulting haptic device, fabricated on AF32 glass using flash lamp annealed PZT film, demonstrated an out-of-plane peak-to-peak displacement of 1.5 μm . This displacement meets the threshold required for surface rendering applications.

-Chapter 5: For those requiring metal-insulator-metal haptic actuators with a transparent structure, the use of transparent electrodes becomes essential. In this regard, low-temperature inkjet printed ITO electrodes that are compatible with PZT film have been developed. Inkjet printing was employed as a cost-effective and simplified alternative to the expensive and intricate lithography process. The inkjet printed ITO electrode serves as the top electrode on the PZT film and exhibits comparable ferroelectric properties to those achieved with sputtered ITO and Pt electrodes.

-Chapter 6: Patterning plays a crucial role in integrating haptic devices into microelectronics fabrication. In this context, inkjet printing has been utilized to develop all inkjet printed haptic actuators. Apart from the bottom electrode Pt, the top electrode (ITO), functional PZT film, and nucleation PTO film were deposited and directly patterned using inkjet printing. The printed haptic device, created on platinised silicon, exhibits an out-of-plane peak-to-peak displacement of 1.2 μm at 22 V and 21.23 kHz. This allows a sliding finger to perceive the sensation of a squeezed-air film. The developed all inkjet printing process eliminates the need for lithography or etching, simplifying the production process and reducing costs.

-Chapter 7: For applications that do not require a transparent structure but prioritize low power consumption and larger deflection, PZT thin films may not be the ideal choice. In such cases, PZT ceramic haptic actuators are commonly employed due to their ability to generate significant deflection, thanks to the large piezoelectric coefficient of PZT ceramics. However, these actuators are standalone devices and tend to be expensive. To address these considerations, we have utilized PZT thick film to produce haptic actuators. This approach offers several advantages. Firstly, it can generate comparable deflection at a low voltage, making it more power-efficient. This is possible due to the lower capacitance of thick films. Additionally, thick film actuators have the capability to withstand high voltage, allowing them to generate larger deflection compared to thin film actuators. By selecting PZT thick film, a desirable balance is expected between deflection, power consumption, and cost-effectiveness. This makes it an advantageous choice for applications that do not necessitate transparency.

8.2 Perspectives

Although outlook was provided separately in each chapter, this chapter offers a more general perspective on surface haptics. Surface haptic feedback is a complex interdisciplinary field. The study and application of surface haptic feedback involve multiple disciplines, including mechanical engineering, materials science, electronic engineering, neuroscience, and more. Here, I would like to provide perspectives on the processing for fabricating haptic actuators from the perspective of materials science.

First of all, it is expected that PZT films will play a significant role in upcoming haptic applications because of their low-cost and compatibility with different deposition methods. While bulk ceramic actuators can generate substantial deflection due to their large piezoelectric coefficient, thin-film actuators allow for the development of transparent

actuators that can produce acceptable displacement. Furthermore, thin-film actuators offer the advantage of direct integration onto the haptic surface.

From Chapter 4, we have acquired knowledge about a low-temperature flash lamp annealing process that facilitates the direct deposition of PZT thin films onto glass substrates. The compatibility of flash lamp annealing with large-scale roll-to-roll printing makes it possible to efficiently manufacture PZT films on glass, thereby simplifying the production process. On the other hand, flash lamp annealing can not only be used in thin film fabrication but also in thick film fabrication, which has been previously demonstrated in [128].

From Chapter 5, we have demonstrated the possibility of using ITO as top electrodes on PZT films. In addition to its application in piezoelectric devices, inkjet printed ITO has also been utilized for printing transparent antennas. These antennas have demonstrated comparable performance to those made of the state-of-the-art sputtered ITO. An autonomous IoT communication module based on additively manufactured transparent antenna set to operate at 2.4 GHz was also demonstrated. (Glinsek et al. Autonomous low-energy communication module based on transparent printed antenna, in submission) The promising results suggest that inkjet printed electrodes have the potential to be utilized in various other transparent electronic applications, including thin-film transistors and back contacts in solar cells, and so on.

From Chapter 6, we have known that an all-inkjet printing method allows for the direct patterning of haptic actuators on the haptic surface. However, in this work, the bottom electrodes used are not transparent, resulting in a lack of transparency in the entire actuator. Previous studies have demonstrated that transparent fluorine-doped tin oxide (FTO) can be employed as the bottom electrodes in piezoelectric devices,[129] and it can also be produced using inkjet printing techniques.[130] In the future, there is the potential to develop FTO through inkjet printing, which would allow it to be utilized as bottom electrodes, enabling the creation of fully transparent haptic actuators.

On the other hand, by combining inkjet printing (or screen printing) with flash lamp annealing, it becomes possible not only to efficiently produce PZT films but also to directly pattern them.

From Chapter 7, we have learned that incorporating thick films in haptic actuators offers the advantages of reduced power consumption and the ability to generate acceptable displacement. A combination of screen printing and flash lamp annealing allows for the rapid production of thick films at lower processing temperatures. Since thick films are

not transparent, flash lamp annealing anneals only the PZT film. This approach not only enables the deposition of thick films on special haptic plates like stainless steel which is the one often used in industry, but also facilitates the use of cheaper electrodes such as aluminum instead of platinum.

All the haptic actuators developed in this thesis utilized PZT thin or thick films, which, unfortunately, are not environmentally friendly due to the presence of lead. Therefore, there is a pressing need for the exploration and implementation of lead-free piezoelectric materials in haptic actuator technologies. There have been many studies conducted on the development of printable lead-free films;[\[131–133\]](#) however, these films have not yet been utilized in haptic actuators. The development of such materials would contribute to more sustainable and environmentally conscious approaches in the field of haptic technology.

In the end, I firmly believe that advanced haptic technology that enables subtle haptic feedbacks will be applied to various electronics in the near future, greatly transforming people's lifestyles. This serves as our motivation to continue our studies from the perspective of materials science.

Chapter 9

Publications, Conferences and Activities

Publications

First author and co-first author[†] contributions

[‡] represents the works related to this thesis

Published papers:

1[‡]. **L Song**, S Glinsek, H Ursic, S Drnovsek, M Sadl, B Malic, E Defay, Power-Efficient Piezoelectric Haptic Actuators with Large Deflection, *Sensors and Actuators A: Physical* 2023, 356, 114346.

2[‡]. **L Song**, S Glinsek, S Drnovsek, V Kovacova, B Malic, E Defay. Piezoelectric thick film for power-efficient haptic actuator, 2022, *Applied Physics Letters* 121 (21), 212901.

3[‡]. **L Song**,[†] S Glinsek, E Defay, Toward low-temperature processing of lead zirconate titanate thin films: Advances, strategies, and applications, *Applied Physics Reviews*, 2021, 8 (4), 041315.

4. **L Song**, T Schenk, E Defay, S Glinsek, Highly conductive low-temperature combustion-derived transparent indium tin oxide thin film, 2021, *Materials Advances* 2 (2), 700-705.

5. S Glinsek,[†] **L Song**,[†] V Kovacova, MA Mahjoub, N Godard, S Girod, JL Biagi, R Quintana, T Schlee, M Guedra, M Rupin, E Defay. Inkjet-Printed Piezoelectric Thin Films for Transparent Haptics, *Advanced Materials Technologies*, 2022, 7 (8), 2200147.

Submitted papers:

6[‡]. **L Song**,[†] J Cardoletti,[†] AB Martinez, A Bencan, B Kmet, S Girod, E Defay, S. Glinsek. Low-temperature growth of piezoceramic films on glass, 2023, submitted in Nature Communications and under review now.

7. T Wang,[†] **L Song**,[†] S Gharabeiki, M Sood, A Jean-Claude Mireille Prot, M Melchiorre¹, E Defay, S Glinsek, and S Siebentritt, Shifting the paradigm: a stable passivated hole transport layer for chalcopyrite solar cells, 2023, paper is prepared for submission.

Co-author contribution

8. S Glinsek, **L Song**, M Gerard, O Bouton, S Girod, M El Hachemi, E Defay, T Granzow and J Polesel-Maris, Autonomous low-energy communication module based on transparent printed antenna, paper is under review in Cell Reports Physical Science.

9. P Parimal Biswas, C Milesi-Brault, A Blázquez Martínez, N Aruchamy, **L Song**, V Kovacova, S Glinšek, T Granzow, E Defay, M Guennou, Birefringence induced by antiferroelectric switching in transparent polycrystalline PbZr_{0.95}Ti_{0.05}O₃ film, Physical Review Materials, 2022, 6 (9), L091403.

Patents

1. Longfei Song, Sebastjan Glinsek, Emmanuel Defay, PZT thick film haptics, LU501047, priority date 21/12/2021

Another patent as co-inventor has been also applied with a colleague (Taowen Wang) from the University of Luxembourg in the frame of our PRIDE project (PACE).

Conferences

Oral presentation

1. “Inkjet printed piezoelectric film for transparent haptics” on 2021 International Symposium on Applications of Ferroelectrics (ISAF) conference 2021 in Australia, held by IEEE Ultrasonics, Ferroelectrics, and Frequency Control Society.

2. “All inkjet-printed haptic device” on 2021 8th Piezo-MEMS workshop in Japan.

Poster presentation

1. “All inkjet-printed haptic device” on 2022 PACE Young Scientist Conference in Luxembourg.

2. “All inkjet-printed haptic device” on 2022 IEEE UFFC-S Ferroelectrics School in Lyon, France

Summer school

2022 IEEE UFFC-S Ferroelectrics School

Activities

1. “No more battery, let’s harvest energy!” at Researchers’ days that happened in Rockhal in Luxembourg in November 2022.

2. Organisation of 2022 PACE Young Scientist Conference held by University of Luxembourg and Luxembourg Institute of Science and Technology.

Appendix A

Characterization techniques

In Appendix, various characterization techniques that have been employed in my studies are introduced. These techniques encompass X-ray diffraction, secondary ions mass spectrometry, scanning electron microscopy, and methods for basic electrical measurements. More specifically, the electrical measurement techniques include four-probe conductivity measurement, hysteresis loop measurements of polarization (relative permittivity) versus electric field, and measurements of the converse piezoelectric coefficient. Additionally, I also provided a description and introduction of a homemade set-up utilized for acoustic measurements.

A.1 X-ray diffraction

A.1.1 θ - 2θ and grazing incidence configurations

X-ray diffraction is an analytical method used to study the phase composition of a crystalline thin film. The regular arrangement of atoms within a crystal leads to the formation of an interference pattern for the waves present in an incident X-ray beam. When an X-ray beam contacts a crystal at an incident angle θ , it is reflected from the crystal's atomic planes at the same angle θ . When the X-rays are reflected from atomic planes with a regular distance, they undergo constructive interference. Interference patterns can only arise when the X-rays reflected from different planes interfere constructively. This means, the path length difference between the beams reflecting off two planes must be $n\lambda$ (λ is the wavelength and n is an integer whole number). This can be expressed via the Bragg law: $n\lambda = 2d\sin\theta$, where d is interplanar spacing and θ is the incident angle.

Two typical configurations for XRD (X-ray diffraction) measurements are generally used, namely 2θ configuration and grazing incidence configuration (see Figure A.1). In

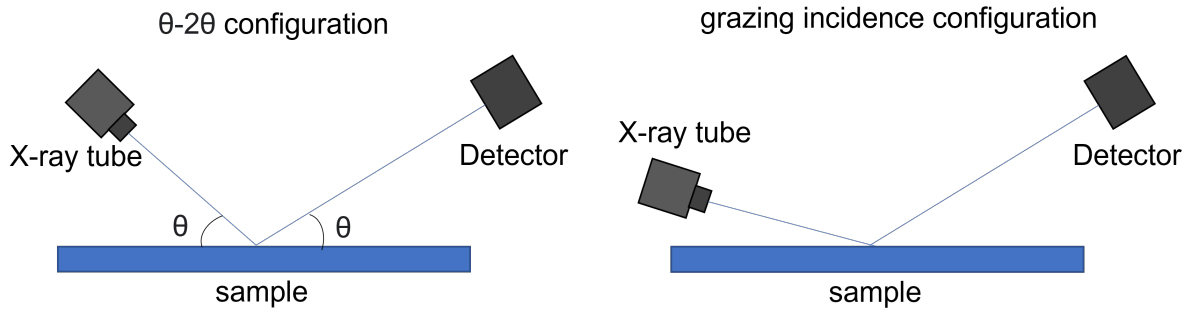


Figure A.1: $\theta/2\theta$ configuration (left) and grazing incidence configuration (right).

the 2θ configuration, the X-ray tube and the detector move symmetrically, allowing for the measurement of crystal planes that are parallel to the surface. In the grazing incidence setup, the X-ray source remains fixed at a small angle, while only the detector moves. This approach enables to measure the surface of the film, excluding the pattern of the substrate. In this thesis, a Bruker D8 Discover diffractometer (Bruker), using Cu-K α radiation, was used to perform XRD measurement.

A.1.2 $\sin^2\Psi$ approach for estimating strain and stress in thin film

A method for estimating strain and stress in thin film involves utilizing a $\sin^2\Psi$ approach. During X-ray diffraction (XRD) analysis, the Φ angle represents the in-plane rotation angle around the surface normal, while the Ψ angle represents the out-of-plane rotation angle that tilts the scattering vector away from the surface normal and into the film plane, as shown in Figure A.2. This technique relies on determining peak positions to calculate the lattice spacing $d_{\Phi,\Psi}$ at specific Φ - and Ψ -rotations.

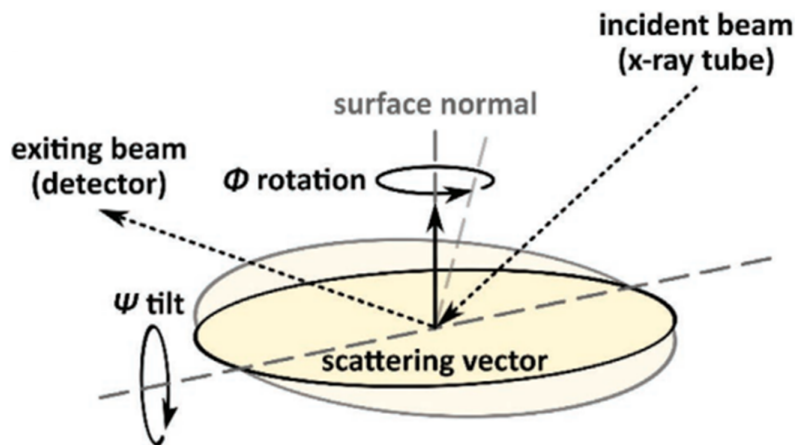


Figure A.2: Schematic diagram of Φ - and Ψ -rotations in XRD.[20]

The strain $\epsilon_{\Phi,\Psi}$ at a Φ and Ψ angle can be calculated via the following equation:

$$\epsilon_{\Phi,\Psi} = \frac{d_{\Phi,\Psi} - d_0}{d_0} = \epsilon_{11}\cos^2(\Phi)\sin^2(\Psi) + \epsilon_{12}\sin(2\Phi)\sin^2(\Psi) + \epsilon_{22}\sin^2(\Phi)\sin^2(\Psi) - \epsilon_{33}\sin^2(\Psi) + \epsilon_{33} + \epsilon_{13}\cos(\Phi)\sin(2\Psi) + \epsilon_{23}\sin(\Phi)\sin(2\Psi) \quad (\text{A.1})$$

where d_0 is reference lattice plane spacing, ϵ_{11} and ϵ_{22} are in-plane stress while ϵ_{33} is out-of-plane strain, ϵ_{12} , ϵ_{13} and ϵ_{23} are shear strain.

The previous study has confirmed that the influence of shear components is negligible, specifically $\epsilon_{12} = \epsilon_{13} = \epsilon_{23} = 0$ [20, 134]. For films exhibiting a uniaxial fiber texture, the recorded XRD patterns are Φ -invariant [135]. Specifically $\epsilon_{11} = \epsilon_{22}$. This way, equation A.1 can be written as:

$$\epsilon_{\Phi,\Psi} = \frac{d_{\Phi,\Psi} - d_0}{d_0} = (\epsilon_{11} - \epsilon_{33})\sin^2(\Psi) + \epsilon_{33} \quad (\text{A.2})$$

To determine the strain without knowing of d_0 , prior research suggests a solution that relies on the assumption that all encountered strain arises solely from bi-axial stress (with the out-of-plane direction being stress-free, as previously established) and that the in-plane elastic constants exhibit isotropic behavior.[20] This way, ϵ_{33} is described as a function of ϵ_{11} :

$$\epsilon_{33} = -\frac{2\nu}{1-\nu}\epsilon_{11} \quad (\text{A.3})$$

where ν is Poisson's ratio. When introduce equation A.3 into equation A.2, it becomes:

$$d_{\Psi} = \frac{1+\nu}{1-\nu}\epsilon_{11}d_0\sin^2(\Psi) + \left(1 - \frac{2\nu}{1-\nu}\epsilon_{11}\right)d_0 \quad (\text{A.4})$$

By plotting d_{Ψ} as a function of $\sin^2(\Psi)$, the slope k is $\frac{1+\nu}{1-\nu}\epsilon_{11}d_0$ while the y-axis intercept y_0 is $\left(1 - \frac{2\nu}{1-\nu}\epsilon_{11}\right)d_0$. This way, ϵ_{11} can be calculated as long as ν is known.

A.2 Secondary ions mass spectrometry

Secondary ions mass spectrometry (SIMS) technology is used to investigate the elemental depth profile. SIMS instruments employ an internally generated primary beam of positive ions (such as Cs) or negative ions (such as O) focused onto a sample surface to generate secondary ions. These secondary ions are transferred into a mass spectrometer via a high electrostatic potential, as schematically illustrated in Figure A.3.

For in-depth elements distribution analysis, dynamic SIMS is needed. Dynamic SIMS instruments utilize primary ion beams of oxygen and cesium to enhance the intensities of both positive and negative secondary ions. As the primary ion dose implanted in the target increases, starting from the surface or going through an interface, the concentration

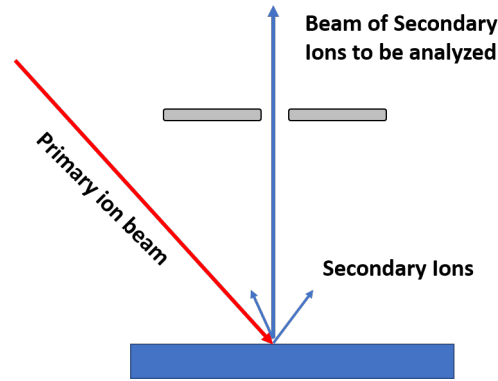


Figure A.3: Schematic diagram of the principle of SIMS.

of the primary species (either oxygen or cesium) will reach an equilibrium state. This equilibrium is dependent on the sputtering conditions and the characteristics of the target material. Once a state of equilibrium is achieved, quantitative analysis can be done by using Relative Sensitivity Factors.

In this thesis, SIMS investigations were done with a CAMECA SC-Ultra SIMS instrument operating with a Cs^+ bombardment at 1 keV. In this technique, the sample under analysis is subjected to bombardment with Cs^+ ions, resulting in the detection of secondary MCs^+ ions instead of M^- ions, where M represents the element that needs to be analyzed.

A.3 Scanning electron microscope

Scanning electron microscope (SEM) was used to study microstructures of the prepared thin films. It generates images by scanning a sample surface with high-energy electron beams. Electrons are emitted at the top of the column, accelerated down, and passed through a combination of lenses and apertures to produce a focused beam of electrons which then scans the surface of the sample (see Figure A.4). When the electrons interact with the sample, they generate secondary electrons, backscattered electrons, and characteristic X-rays. These signals are captured by one or more detectors to create images that are subsequently shown on a computer screen. As the electron beam makes contact with the sample's surface, it penetrates the material to a depth of several microns, which varies based on the accelerating voltage and sample density. This interaction within the sample gives rise to various signals, including secondary electrons and X-rays.

In this thesis, SEM images were obtained through a FEI HeliosNanoLab 650 microscope.

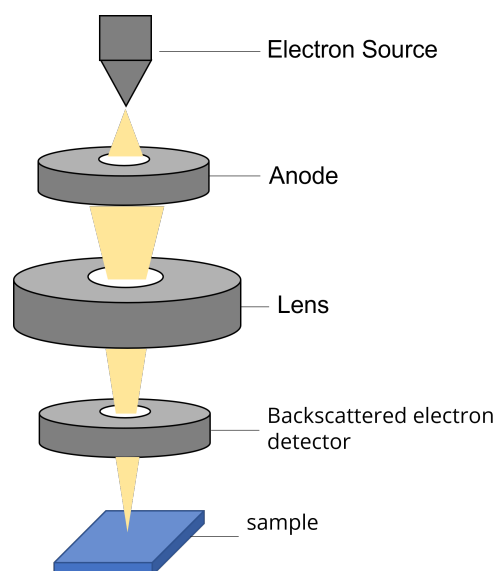


Figure A.4: Schematic diagram of scanning electron microscope.

A.4 Electrical measurements

A.4.1 Four-probe conductivity measurement

The standard method for measuring the sheet resistance (represented as R_s) of TCO (transparent conducting oxide) thin films involves the use of four probes. This method enables the calculation of the resistivity or electrical conductivity of the material. The four probes are equally spaced along a line, as depicted in Figure A.5, and a current is applied through the outer probes while the inner probes measure the resulting voltage. The sheet resistance (R_s) is then determined using the following equation:

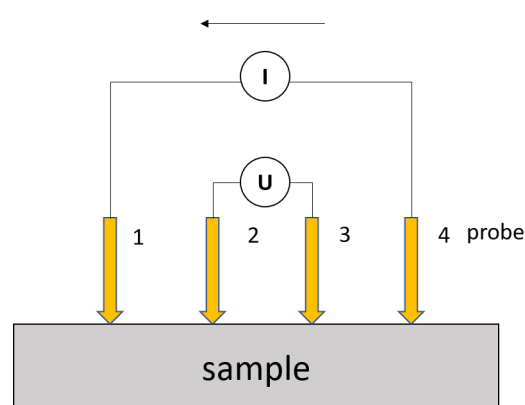


Figure A.5: Schematic diagram of the principle of four-probe conductivity measurement.

$$R_s = k \frac{\Delta V}{I} \quad (\text{A.5})$$

where ΔV is the voltage and I is the applied current, k is a constant that depends on the ratio between lateral dimension (d) and probe spacing (s). k is 4.53 when the lateral

dimension of the sample is more than 40 times the probe spacing, namely $\frac{d}{s} \rightarrow \infty$. If the $\frac{d}{s}$ is smaller than 40, correction factors have to be considered which results in a smaller k .

In our lab, four probes in linear configuration (probe space of 1 mm) with a Keithley 2614B source meter are used to perform sheet resistance measurement, as has been shown in Figure 5.7.

A.4.2 Polarization-electric field hysteresis loop

aixACCT Systems, shown in Figure A.6, are utilized for conducting electrical measurements on ferroelectric thin films.

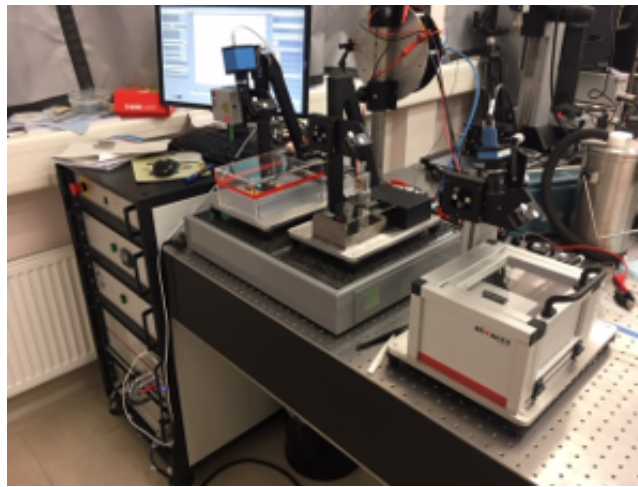


Figure A.6: Photo of aixACCT TF-3000 system (aixACCT Systems GmbH).

The characteristic hysteresis loop of ferroelectric thin films, known as the polarization-electric field (P-E) loop, provides essential parameters such as P_r , P_{max} , and E_c , as previously discussed in Subsection 2.2.1. To obtain the P-E loop, the current $i(t)$ is measured by applying a triangular waveform with a frequency f , as shown in Figure A.7. Polarization value can be calculated based on the following equation:

$$P = \frac{1}{A} \int i(t) dt \quad (\text{A.6})$$

Correspondingly, P-E loop can be obtained. Consequently, current and corresponding

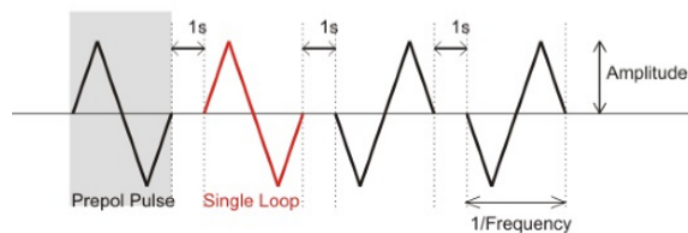


Figure A.7: The applied triangular waveform at a frequency. Source: aixACCT manual

polarization as a function of time is shown in Figure A.8a. The obtained P-E loop is shown in Figure A.8b.

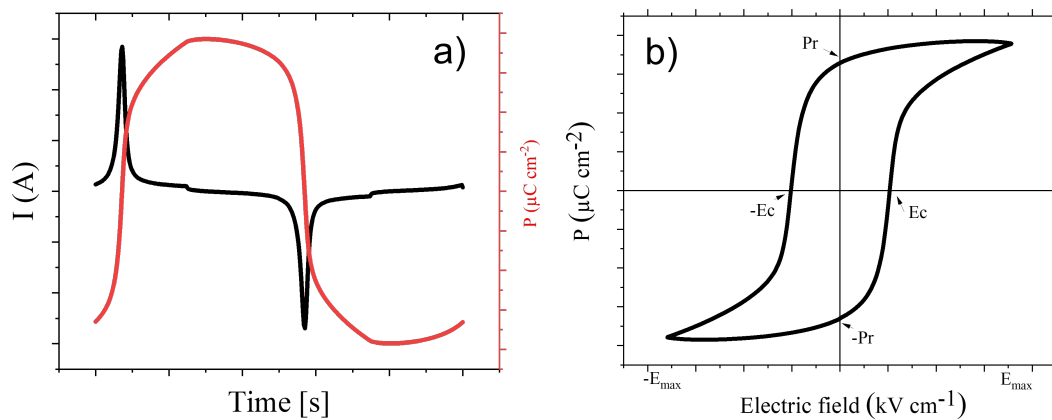


Figure A.8: a) Current and polarization versus time. b) Polarization versus electric field hysteresis loop.

A.4.3 Relative permittivity and loss tangent versus electrical field

The relative permittivity ϵ_r of a capacitor with MIM structure can be calculated via the equation: $C = \epsilon_0 \epsilon_r \frac{A}{d}$, where ϵ_0 is vacuum permittivity constant ($8.85 \times 10^{-12} \text{ F m}^{-1}$), A is the effective area of top electrode of capacitor and d is the film thickness. Typically, a staircase DC bias with a small AC amplitude is applied in the measurement by aixAACT system, as demonstrated in Figure A.9. The capacitance and dielectric loss are derived from the AC small signal current response of the sample measured by the virtual ground.

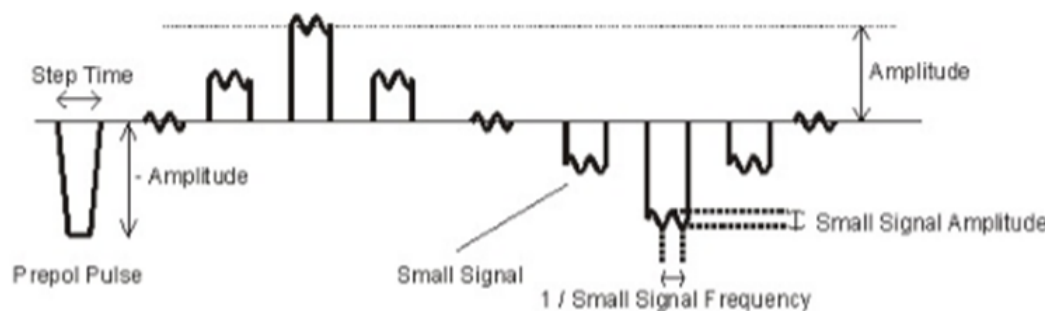


Figure A.9: Measurement of relative permittivity by applying a staircase DC bias with a small amplitude. Source: aixACCT manual

A.4.4 Converse piezoelectric coefficient measurement

The converse piezoelectric coefficient $e_{31,f}$ of thin film can be measured through a cantilever structure, as shown in Figure A.10. The cantilever beam is firmly clamped.

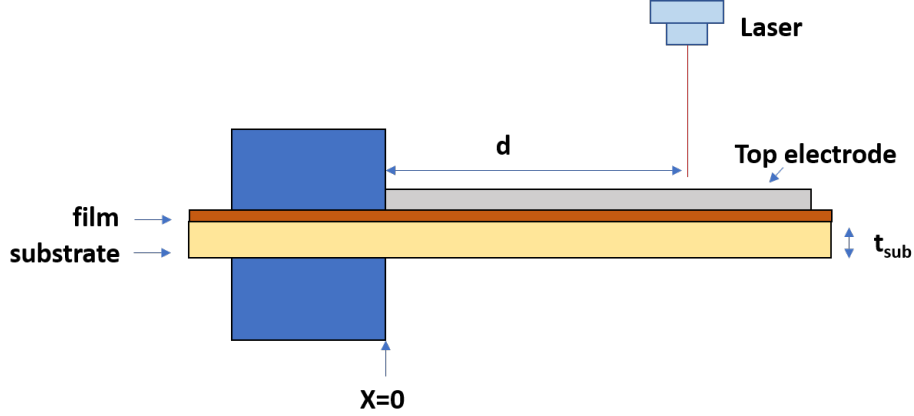


Figure A.10: Cantilever structure for converse piezoelectric coefficient measurement.

When apply a voltage on top electrode, the beam is actuated and bends at a constant curvature. As has been previously reported, the $e_{31,f}$ can be calculated via the following equation:[136]

$$e_{31,f} = -\frac{1}{3} \frac{Y_{sub}}{1 - \nu_{sub}} [c_f + (1 - c_f)(1 - \nu_{sub})] \frac{t_{sub}^2}{d^2} \frac{U}{V} \quad (\text{A.7})$$

where Y_{sub} , ν_{sub} and t_{sub} are Young's modulus, Poisson's ratio and thickness of the substrate, c_f is the electrode coverage factor that is calculated via $\frac{w_{electrode}}{w_{sub}}$ ($w_{electrode}$ and w_{sub} are the widths of electrode and substrate, respectively), U is the deflection at the position of d and at a voltage of U that is typically measured by laser interferometry .

A.5 Setup for Acoustic measurement

The flexible foam tapes were used to support the haptic device, creating a simple supported beam configuration. This setup was placed on a computer-controlled stage that was constructed in-house. To generate an electrical signal, a wave-function generator (Agilent 33210A) was utilized, and the signal was amplified by a factor of 50 using a Falco amplifier (WMA-300). The amplified voltage signal was then employed to operate the haptic device. To measure the out-of-plane displacement of the haptic device, a vibrometer (Polytec OFV-5000) was employed, which captured data from the device's back side. A LabVIEW program (National Instruments) was responsible for controlling both the entire setup and the vibrometer. The whole set-up is schematically shown in Figure A.11

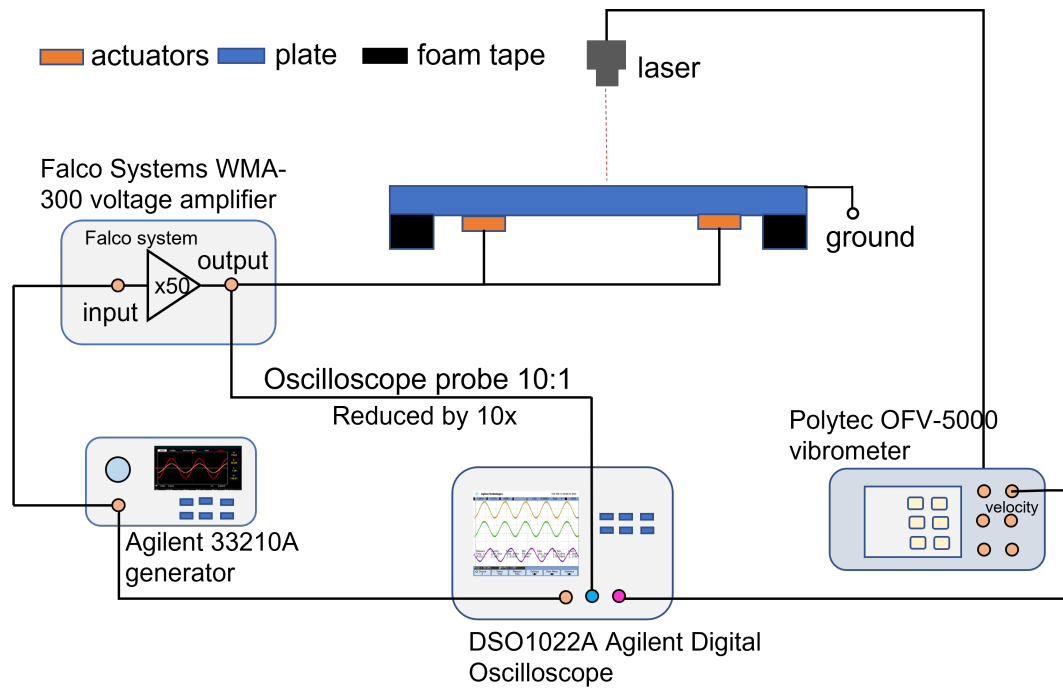


Figure A.11: Schematic diagram of the built set-up used for haptic measurement.

Velocity mode in vibrometer was used to measure the surface displacement (d) of haptic devices, which can be calculated via the equation below:

$$d = \frac{U_{vibro} m}{(2\pi f)} \times 10^6 \quad (\text{A.8})$$

where U_{vibro} is the vibrometer output in V, m is the velocity range in m/s/V, and f is the operation frequency in Hz. This way, the unit of obtained displacement is μm .

Bibliography

- [1] Hui Hua, Youru Chen, Yongchun Tao, Dexing Qi, and Yanzhao Li. A highly transparent haptic device with an extremely low driving voltage based on piezoelectric pzt films on glass. *Sensors and Actuators A: Physical*, 335:113396, 2022.
- [2] Zenghui Liu, Hua Wu, Wei Ren, and Zuo-Guang Ye. Piezoelectric and ferroelectric materials: Fundamentals, recent progress, and applications. *Reference Module in Chemistry, Molecular Sciences and Chemical Engineering; Elsevier: Amsterdam, The Netherlands*, 2022.
- [3] N Setter. Special issue on electroceramics in micro-electro-mechanical systems. *Journal of Electroceramics*, 12(ARTICLE):5–6, 2004.
- [4] Deepak Rajaram Patil, Venkateswarlu Annapureddy, J Kaarthik, Atul Thakre, Jun Akedo, and Jungho Ryu. Piezoelectric thick film deposition via powder/granule spray in vacuum: a review. In *Actuators*, volume 9, page 59. MDPI, 2020.
- [5] Hideo Hosono. Transparent amorphous oxide semiconductors for display applications: Materials, features, progress, and prospects. *Amorphous Oxide Semiconductors: IGZO and Related Materials for Display and Memory*, pages 1–20, 2022.
- [6] Peter P Edwards, Adrian Porch, Martin O Jones, David Vernon Morgan, and R Marc Perks. Basic materials physics of transparent conducting oxides. *Dalton transactions*, 19:2995–3002, 2004.
- [7] Wen-Fa Wu and Bi-Shiou Chiou. Properties of radio-frequency magnetron sputtered ito films without in-situ substrate heating and post-deposition annealing. *Thin Solid Films*, 247(2):201–207, 1994.
- [8] Klaus Ellmer. Past achievements and future challenges in the development of optically transparent electrodes. *Nature Photonics*, 6(12):809–817, 2012.

- [9] Robert M Pasquarelli, David S Ginley, and Ryan O’Hayre. Solution processing of transparent conductors: from flask to film. *Chemical Society Reviews*, 40(11):5406–5441, 2011.
- [10] Brian Derby. Inkjet printing of functional and structural materials: fluid property requirements, feature stability, and resolution. *Annual Review of Materials Research*, 40:395–414, 2010.
- [11] Heather Culbertson, Samuel B Schorr, and Allison M Okamura. Haptics: The present and future of artificial touch sensation. *Annual Review of Control, Robotics, and Autonomous Systems*, 1(1):385–409, 2018.
- [12] Julien van Kuilenburg, Marc A Masen, and Emile van der Heide. A review of fingerpad contact mechanics and friction and how this affects tactile perception. *Proceedings of the Institution of Mechanical Engineers, Part J: Journal of engineering tribology*, 229(3):243–258, 2015.
- [13] Michael J Adams, Brian J Briscoe, and Simon A Johnson. Friction and lubrication of human skin. *Tribology letters*, 26(3):239–253, 2007.
- [14] Jaimie T Shores. Anatomy and physiology of the fingertip. In *Fingertip Injuries*, pages 1–9. Springer, 2015.
- [15] R Fagiani, Francesco Massi, Eric Chatelet, Yves Berthier, and A Sestieri. Experimental analysis of friction-induced vibrations at the finger contact surface. *Proceedings of the Institution of Mechanical Engineers, Part J: Journal of Engineering Tribology*, 224(9):1027–1035, 2010.
- [16] Cagatay Basdogan, Frédéric Giraud, Vincent Levesque, and Seungmoon Choi. A review of surface haptics: Enabling tactile effects on touch surfaces. *IEEE transactions on haptics*, 13(3):450–470, 2020.
- [17] Sebastjan Glinsek, Mohamed Aymen Mahjoub, Matthieu Rupin, Tony Schenk, Nicolas Godard, Stéphanie Girod, Jean-Baptiste Chemin, Renaud Leturcq, Nathalie Valle, Sébastien Klein, et al. Fully transparent friction-modulation haptic device based on piezoelectric thin film. *Advanced Functional Materials*, 30(36):2003539, 2020.

- [18] Mélisande Biet, Frédéric Giraud, and Betty Lemaire-Semail. Squeeze film effect for the design of an ultrasonic tactile plate. *IEEE transactions on ultrasonics, ferroelectrics, and frequency control*, 54(12):2678–2688, 2007.
- [19] Thomas Sednaoui, Eric Vezzoli, Brigida Dzidek, Betty Lemaire-Semail, Cedrick Chappaz, and Michael Adams. Experimental evaluation of friction reduction in ultrasonic devices. In *2015 IEEE World Haptics Conference (WHC)*, pages 37–42. IEEE, 2015.
- [20] Tony Schenk, Chris M Fancher, Min Hyuk Park, Claudia Richter, Christopher Künneth, Alfred Kersch, Jacob L Jones, Thomas Mikolajick, and Uwe Schroeder. On the origin of the large remanent polarization in la: Hfo2. *Advanced Electronic Materials*, 5(12):1900303, 2019.
- [21] V Kovacova, N Vaxelaire, G Le Rhun, P Gergaud, T Schmitz-Kempen, and E Defay. Correlation between electric-field-induced phase transition and piezoelectricity in lead zirconate titanate films. *Physical Review B*, 90(14):140101, 2014.
- [22] Toshio Watanabe and Shigehisa Fukui. A method for controlling tactile sensation of surface roughness using ultrasonic vibration. In *Proceedings of 1995 IEEE International Conference on Robotics and Automation*, volume 1, pages 1134–1139. IEEE, 1995.
- [23] Diana Angélica Torres Guzman. *Generation and control of tactile feedback with longitudinal ultrasonic vibration and human-in-the-Loop analysis*. PhD thesis, Université de Lille, 2021.
- [24] Michaël Wiertlewski, Rebecca Fenton Friesen, and J Edward Colgate. Partial squeeze film levitation modulates fingertip friction. *Proceedings of the national academy of sciences*, 113(33):9210–9215, 2016.
- [25] Isaku Kanno. Piezoelectric mems: Ferroelectric thin films for mems applications. *Japanese Journal of Applied Physics*, 57(4):040101, 2018.
- [26] E Defay, Cyril Millon, Ch Malhaire, and D Barbier. Pzt thin films integration for the realisation of a high sensitivity pressure microsensor based on a vibrating membrane. *Sensors and Actuators A: Physical*, 99(1-2):64–67, 2002.

- [27] Youngoh Lee, Jonghwa Park, Soowon Cho, Young-Eun Shin, Hochan Lee, Jinyoung Kim, Jinyoung Myoung, Seungse Cho, Saewon Kang, Chunggi Baig, et al. Flexible ferroelectric sensors with ultrahigh pressure sensitivity and linear response over exceptionally broad pressure range. *Acs Nano*, 12(4):4045–4054, 2018.
- [28] Seiji Aoyagi, Sho Kumagai, Daiichiro Yoshikawa, and Yuichi Isono. Surface micromachined accelerometer using ferroelectric substrate. *Sensors and Actuators A: Physical*, 139(1-2):88–94, 2007.
- [29] Korbinian Kunz, Peter Enoksson, and Göran Stemme. Highly sensitive triaxial silicon accelerometer with integrated pzt thin film detectors. *Sensors and Actuators A: Physical*, 92(1-3):156–160, 2001.
- [30] Sung Sik Won, Hosung Seo, Masami Kawahara, Sebastjan Glinsek, Jinkee Lee, Yunseok Kim, Chang Kyu Jeong, Angus I Kingon, and Seung-Hyun Kim. Flexible vibrational energy harvesting devices using strain-engineered perovskite piezoelectric thin films (vol 55, pg 182, 2019). *Nano Energy*, 57:924–924, 2019.
- [31] Hong Goo Yeo and Susan Trolier-McKinstry. Effect of piezoelectric layer thickness and poling conditions on the performance of cantilever piezoelectric energy harvesters on ni foils. *Sensors and Actuators A: Physical*, 273:90–97, 2018.
- [32] F Filhol, E Defay, C Divoux, C Zinck, and M-T Delaye. Resonant micro-mirror excited by a thin-film piezoelectric actuator for fast optical beam scanning. *Sensors and Actuators A: Physical*, 123:483–489, 2005.
- [33] Pierre-Henri Cazorla, Olivier Fuchs, Martine Cochet, Sandrine Maubert, Gwenaél Le Rhun, Yves Fouillet, and Emmanuel Defay. A low voltage silicon micro-pump based on piezoelectric thin films. *Sensors and Actuators A: Physical*, 250:35–39, 2016.
- [34] Matthieu Cuffe, Emmanuël Defay, Patrice Rey, Gwenaél Le Rhun, François Peruchot, Christine Ferrandon, Denis Mercier, Frédéric Domingue, Aurélien Suhm, Marc Aïd, et al. A fully packaged piezoelectric switch with lowvoltage actuation and electrostatic hold. In *2010 IEEE 23rd International Conference on Micro Electro Mechanical Systems (MEMS)*, pages 212–215. IEEE, 2010.
- [35] F Casset, JS Danel, C Chappaz, Y Civet, Michel Amberg, M Gorisse, C Dieppedale, G Le Rhun, Skandar Basrour, P Renaux, et al. Low voltage actuated plate for haptic

- applications with pzt thin-film. In *2013 Transducers & Eurosensors XXVII: The 17th International Conference on Solid-State Sensors, Actuators and Microsystems (TRANSDUCERS & EUROSENSORS XXVII)*, pages 2733–2736. IEEE, 2013.
- [36] Longfei Song, Sebastjan Glinsek, and Emmanuel Defay. Toward low-temperature processing of lead zirconate titanate thin films: Advances, strategies, and applications. *Applied Physics Reviews*, 8(4):041315, 2021.
- [37] Nazanin Bassiri-Gharb, Yaser Bastani, and Ashley Bernal. Chemical solution growth of ferroelectric oxide thin films and nanostructures. *Chemical Society Reviews*, 43(7):2125–2140, 2014.
- [38] Yi Qi, Noah T Jafferis, Kenneth Lyons Jr, Christine M Lee, Habib Ahmad, and Michael C McAlpine. Piezoelectric ribbons printed onto rubber for flexible energy conversion. *Nano letters*, 10(2):524–528, 2010.
- [39] Kwi-Il Park, Jung Hwan Son, Geon-Tae Hwang, Chang Kyu Jeong, Jungho Ryu, Min Koo, Insung Choi, Seung Hyun Lee, Myunghwan Byun, Zhong Lin Wang, et al. Highly-efficient, flexible piezoelectric pzt thin film nanogenerator on plastic substrates. *Advanced materials*, 26(16):2514–2520, 2014.
- [40] Iñigo Bretos, Ricardo Jiménez, Aiyong Wu, Angus I Kingon, Paula M Vilarinho, and M Lourdes Calzada. Activated solutions enabling low-temperature processing of functional ferroelectric oxides for flexible electronics. *Advanced Materials*, 26(9):1405–1409, 2014.
- [41] XD Zhang, XJ Meng, JL Sun, T Lin, JH Ma, JH Chu, DY Kwon, and Bog G Kim. Low-temperature preparation of sputter-deposited pb (zr_{0.52}ti_{0.48}) o₃ thin films through high oxygen-pressure annealing. *Journal of crystal growth*, 310(4):783–787, 2008.
- [42] Zhanjie Wang and Jun Ouyang. Low-temperature processing of ferroelectric thin films on si substrates. In *Nanostructures in Ferroelectric Films for Energy Applications*, pages 203–235. Elsevier, 2019.
- [43] Phan Trong Tue, Tatsuya Shimoda, and Yuzuru Takamura. A facile solution-combustion-synthetic approach enabling low-temperature pzt thin-films. *APL Materials*, 8(2):021112, 2020.

- [44] Min-Gyu Kang, Myoung-Sub Noh, Jung Joon Pyeon, Woo-Suk Jung, Hi Gyu Moon, Seung-Hyub Baek, Sahn Nahm, Seok-Jin Yoon, and Chong-Yun Kang. Direct growth of ferroelectric oxide thin films on polymers through laser-induced low-temperature liquid-phase crystallization. *Chemistry of Materials*, 32(15):6483–6493, 2020.
- [45] John F Wager. Transparent electronics. *Science*, 300(5623):1245–1246, 2003.
- [46] Hideo Hosono. 9.4 transparent conducting oxides. *From Magnetic to Bioactive Materials*, page 51, 2022.
- [47] D Ginley, Claes Göran Granqvist, H Hosono, T Kamiya, and G Kiriakidis. Transparent oxides and related materials for electronics and optics: Phys. status solidi a. In *The International Symposium on Transparent Oxide and Related Materials for Electronics and Optics, July, 3-5, 2017, tokyo, Japan*, 2019.
- [48] Hideo Hosono. Recent progress in transparent oxide semiconductors: Materials and device application. *Thin solid films*, 515(15):6000–6014, 2007.
- [49] Hiromichi Ohta and Hideo Hosono. Transparent oxide optoelectronics. *Materials Today*, 7(6):42–51, 2004.
- [50] Sri Venkat and Corey Dunskey. Laser patterning of ito in flat panel display manufacturing. In *Photon Processing in Microelectronics and Photonics V*, volume 6106, pages 8–14. SPIE, 2006.
- [51] Zhao-Hui Li, Eou Sik Cho, and Sang Jik Kwon. Laser direct patterning of the t-shaped ito electrode for high-efficiency alternative current plasma display panels. *Applied Surface Science*, 257(3):776–780, 2010.
- [52] Gregory P Crawford. Flexible flat panel display technology. *Flexible Flat Panel Displays*, pages 1–9, 2005.
- [53] D Zhang, A Tavakoliyaraki, Y Wu, RACMM Van Swaaij, and M Zeman. Influence of ito deposition and post annealing on hit solar cell structures. *Energy Procedia*, 8:207–213, 2011.
- [54] A Valla, P Carroy, F Ozanne, and D Muñoz. Understanding the role of mobility of ito films for silicon heterojunction solar cell applications. *Solar energy materials and solar cells*, 157:874–880, 2016.

- [55] Shui-Yang Lien. Characterization and optimization of ito thin films for application in heterojunction silicon solar cells. *Thin Solid Films*, 518(21):S10–S13, 2010.
- [56] Taemin Lee, Yong Whan Choi, Gunhee Lee, Peter V Pikhitsa, Daeshik Kang, Sang Moon Kim, and Mansoo Choi. Transparent ito mechanical crack-based pressure and strain sensor. *Journal of Materials Chemistry C*, 4(42):9947–9953, 2016.
- [57] Elif Burcu Aydın and Mustafa Kemal Sezgintürk. Indium tin oxide (ito): A promising material in biosensing technology. *TrAC Trends in Analytical Chemistry*, 97:309–315, 2017.
- [58] Kohji Mitsubayashi, Yoshihiko Wakabayashi, Satoshi Tanimoto, Daisuke Murotomi, and Tatsuro Endo. Optical-transparent and flexible glucose sensor with ito electrode. *Biosensors and Bioelectronics*, 19(1):67–71, 2003.
- [59] Young Ho Do, Woo Suk Jung, Min Gyu Kang, Chong Yun Kang, and Seok Jin Yoon. Preparation on transparent flexible piezoelectric energy harvester based on pzt films by laser lift-off process. *Sensors and Actuators A: Physical*, 200:51–55, 2013.
- [60] Franklin Pavageau, Christel Dieppedale, Pierre Perreau, Romain Liechti, Antoine Hamelin, Christophe Licitra, Fabrice Casset, and Gwenaël Le Rhun. Highly transparent piezoelectric pzt membranes for transducer applications. *Sensors and Actuators A: Physical*, 346:113866, 2022.
- [61] Evgeniia Gilshtein, Sami Bolat, Galo Torres Sevilla, Antonio Cabas-Vidani, Frank Clemens, Thomas Graule, Ayodhya N Tiwari, and Yaroslav E Romanyuk. Inkjet-printed conductive ito patterns for transparent security systems. *Advanced Materials Technologies*, 5(9):2000369, 2020.
- [62] Antonis Olziersky, Anna Vilà, and Juan Ramón Morante. Multicomponent oxide thin-film transistors fabricated by a double-layer inkjet printing process. *Thin Solid Films*, 520(4):1334–1340, 2011.
- [63] JeJeong Yu, Sungkoo Lee, Eunhee Lim, TaeHo Kim, and Kyeong K Lee. Preparation of indium tin oxide inks for electrically conductive transparent oxide film with ink-jet printing method. *Molecular Crystals and Liquid Crystals*, 519(1):134–140, 2010.

- [64] Jong-Woong Kim, Sung-Jei Hong, and Min-Gi Kwak. Characteristics of eco-friendly synthesized sio₂ dielectric nanoparticles printed on si substrate. *Microelectronic engineering*, 88(5):797–801, 2011.
- [65] Sung-Jei Hong, Jong-Woong Kim, Jae-Won Lim, Good-Sun Choi, and Minoru Ishiki. Characteristics of printed thin films using indium tin oxide (ito) ink. *Materials transactions*, pages 1008231159–1008231159, 2010.
- [66] MJ Alam and DC Cameron. Optical and electrical properties of transparent conductive ito thin films deposited by sol–gel process. *Thin solid films*, 377:455–459, 2000.
- [67] Seon-Soon Kim, Se-Young Choi, Chan-Gyung Park, and Hyeon-Woo Jin. Transparent conductive ito thin films through the sol-gel process using metal salts. *Thin solid films*, 347(1-2):155–160, 1999.
- [68] Bo-Yuan Su, Sheng-Yuan Chu, Yung-Der Juang, and Han-Chang Chen. High-performance low-temperature solution-processed ingazno thin-film transistors via ultraviolet-ozone photo-annealing. *Applied Physics Letters*, 102(19):192101, 2013.
- [69] Jaehak Shin, Jaemin Kim, Sungmin Park, Soo Jin Kim, Jung Ah Lim, and Sunglim Ko. Low-temperature and rapid photo-annealing process for metal-oxide thin-film transistors using combined excimer deep-ultraviolet and intensely pulsed light irradiation. *Organic Electronics*, 104:106476, 2022.
- [70] Sang Cheol Park, Dongwook Kim, Hyunji Shin, Do Kyoung Lee, Xue Zhang, Jaehoon Park, and Jong Sun Choi. Advanced photo-annealing of indium zinc oxide films for thin-film transistors using pulse uv light. *Journal of Information Display*, 17(1):1–7, 2016.
- [71] Young Jun Tak, Doo Hyun Yoon, Seokhyun Yoon, Uy Hyun Choi, Mardiah Muhamad Sabri, Byung Du Ahn, and Hyun Jae Kim. Enhanced electrical characteristics and stability via simultaneous ultraviolet and thermal treatment of passivated amorphous in–ga–zn–o thin-film transistors. *ACS applied materials & interfaces*, 6(9):6399–6405, 2014.
- [72] Jaakko Leppaniemi, Kim Eiroma, Himadri Majumdar, and Ari Alastalo. Far-uv annealed inkjet-printed in₂o₃ semiconductor layers for thin-film transistors on a

- flexible polyethylene naphthalate substrate. *ACS applied materials & interfaces*, 9(10):8774–8782, 2017.
- [73] Tae-Yil Eom, Chee-Hong Ahn, Jun-Gu Kang, Muhammad Saad Salman, Sun-Young Lee, Yong-Hoon Kim, Hoo-Jeong Lee, Chan-Mo Kang, and Chiwon Kang. Investigation of the evolution of nitrogen defects in flash-lamp-annealed ingazno films and their effects on transistor characteristics. *Applied Physics Express*, 11(6):061104, 2018.
- [74] Adam M Weidling, Vikram S Turkani, Bing Luo, Kurt A Schroder, and Sarah L Swisher. Photonic curing of solution-processed oxide semiconductors with efficient gate absorbers and minimal substrate heating for high-performance thin-film transistors. *ACS omega*, 6(27):17323–17334, 2021.
- [75] Mutsumi Kimura, Takayuki Hasegawa, Keisuke Ide, Kenji Nomura, Toshio Kamiya, and Hideo Hosono. Light irradiation history sensor using amorphous in-ga-zn-o thin-film transistor exposed to ozone annealing. *IEEE electron device letters*, 33(3):384–386, 2012.
- [76] Li Lu, Masahiro Echizen, Takashi Nishida, Yasuaki Ishikawa, Kiyoshi Uchiyama, and Yukiharu Uraoka. Low-temperature fabrication of solution-processed inzno thin-film transistors with si impurities by uv/o₃-assisted annealing. *AIP Advances*, 2(3):032111, 2012.
- [77] Riku Kobayashi, Toshihide Nabatame, Takashi Onaya, Akihiko Ohi, Naoki Ikeda, Takahiro Nagata, Kazuhito Tsukagoshi, and Atsushi Ogura. Comparison of characteristics of thin-film transistor with in₂o₃ and carbon-doped in₂o₃ channels by atomic layer deposition and post-metallization annealing in o₃. *Japanese Journal of Applied Physics*, 60(3):030903, 2021.
- [78] Kwang Hwan Ji, Ji-In Kim, Hong Yoon Jung, Se Yeob Park, Rino Choi, Un Ki Kim, Cheol Seong Hwang, Daeseok Lee, Hyungsang Hwang, and Jae Kyeong Jeong. Effect of high-pressure oxygen annealing on negative bias illumination stress-induced instability of ingazno thin film transistors. *Applied Physics Letters*, 98(10):103509, 2011.
- [79] Se Yeob Park, Kwang Hwan Ji, Hong Yoon Jung, Ji-In Kim, Rino Choi, Kyoung Seok Son, Myung Kwan Ryu, Sangyoon Lee, and Jae Kyeong Jeong. Improvement

- in the device performance of tin-doped indium oxide transistor by oxygen high pressure annealing at 150° c. *Applied Physics Letters*, 100(16):162108, 2012.
- [80] Won-Gi Kim, Young Jun Tak, Byung Du Ahn, Tae Soo Jung, Kwun-Bum Chung, and Hyun Jae Kim. High-pressure gas activation for amorphous indium-gallium-zinc-oxide thin-film transistors at 100° c. *Scientific reports*, 6(1):1–7, 2016.
- [81] You Seung Rim, Wooho Jeong, Byung Du Ahn, and Hyun Jae Kim. Defect reduction in photon-accelerated negative bias instability of ingazno thin-film transistors by high-pressure water vapor annealing. *Applied Physics Letters*, 102(14):143503, 2013.
- [82] Hyo Jin Kim, Byeong Geun Son, Chul-Kyu Lee, So Yeon Je, Ju Yeon Won, and Jae Kyeong Jeong. Effect of nitrous oxide high pressure annealing on the performance of low temperature, soluble-based izo transistors. *IEEE electron device letters*, 35(4):455–457, 2014.
- [83] Myung-Gil Kim, Mercuri G Kanatzidis, Antonio Facchetti, and Tobin J Marks. Low-temperature fabrication of high-performance metal oxide thin-film electronics via combustion processing. *Nature materials*, 10(5):382–388, 2011.
- [84] Xinge Yu, Jeremy Smith, Nanjia Zhou, Li Zeng, Peijun Guo, Yu Xia, Ana Alvarez, Stefano Aghion, Hui Lin, Junsheng Yu, et al. Spray-combustion synthesis: Efficient solution route to high-performance oxide transistors. *Proceedings of the National Academy of Sciences*, 112(11):3217–3222, 2015.
- [85] Jonathan W Hennek, Jeremy Smith, Aiming Yan, Myung-Gil Kim, Wei Zhao, Vinayak P Dravid, Antonio Facchetti, and Tobin J Marks. Oxygen “getter” effects on microstructure and carrier transport in low temperature combustion-processed a-inxzno (x= ga, sc, y, la) transistors. *Journal of the American Chemical Society*, 135(29):10729–10741, 2013.
- [86] Pavan Pujar, Srinivas Gandla, Dipti Gupta, Sunkook Kim, and Myung-Gil Kim. Trends in low-temperature combustion derived thin films for solution-processed electronics. *Advanced Electronic Materials*, 6(10):2000464, 2020.
- [87] Arvind Varma, Alexander S Mukasyan, Alexander S Rogachev, and Khachatur V Manukyan. Solution combustion synthesis of nanoscale materials. *Chemical reviews*, 116(23):14493–14586, 2016.

- [88] Yan Wang, Hong Guo, Jin-ju Chen, Enrico Sowade, Yu Wang, Kun Liang, Kyle Marcus, Reinhard R Baumann, and Zhe-sheng Feng. Based inkjet-printed flexible electronic circuits. *ACS Applied Materials & Interfaces*, 8(39):26112–26118, 2016.
- [89] Junfeng Mei, Michael R Lovell, and Marlin H Mickle. Formulation and processing of novel conductive solution inks in continuous inkjet printing of 3-d electric circuits. *IEEE transactions on electronics packaging manufacturing*, 28(3):265–273, 2005.
- [90] Jongseok Han, Donghyun Ko, Myeongjin Park, Jeongkyun Roh, Heeyoung Jung, Yeonkyung Lee, Yongwon Kwon, Jiho Sohn, Wan Ki Bae, Byung Doo Chin, et al. Toward high-resolution, inkjet-printed, quantum dot light-emitting diodes for next-generation displays. *Journal of the Society for Information Display*, 24(9):545–551, 2016.
- [91] Bo Wu, Haijun Wu, Jiagang Wu, Dingquan Xiao, Jianguo Zhu, and Stephen J Pennycook. Giant piezoelectricity and high curie temperature in nanostructured alkali niobate lead-free piezoceramics through phase coexistence. *Journal of the American Chemical Society*, 138(47):15459–15464, 2016.
- [92] Bernhard R Tittmann, David A Parks, and Shujun O Zhang. High temperature piezoelectrics—a comparison. In *Proceedings of the 13th International Symposium on Nondestructive Characterization of Materials (NDCM-XIII), Le Mans, France*, pages 20–24, 2013.
- [93] Nicolas Godard. *Inkjet-printed piezoelectric films for transducers*. PhD thesis, University of Luxembourg, Esch-sur-Alzette, Luxembourg, 2020.
- [94] B Noheda, DE Cox, G Shirane, JA Gonzalo, LE Cross, and SE Park. A monoclinic ferroelectric phase in the pb (zr 1- x ti x) o 3 solid solution. *Applied physics letters*, 74(14):2059–2061, 1999.
- [95] Nicolas Godard, Patrick Grysan, Emmanuel Defay, and Sebastjan Glinšek. Growth of {100}-oriented lead zirconate titanate thin films mediated by a safe solvent. *Journal of Materials Chemistry C*, 9(1):281–287, 2021.
- [96] GS Wang, Denis Remiens, Caroline Soyer, E Dogheche, and Eric Cattan. The effect of lanio3 bottom electrode thickness on ferroelectric and dielectric properties of (1 0 0) oriented pbzr0. 53ti0. 47o3 films. *Journal of crystal growth*, 284(1-2):184–189, 2005.

- [97] Udo Eckstein, Jörg Exner, Andreja Bencan Golob, Katarina Ziberna, Goran Drazic, Hana Ursic, Haiko Wittkämper, Christian Papp, Jaroslaw Kita, Ralf Moos, et al. Temperature-dependent dielectric anomalies in powder aerosol deposited ferroelectric ceramic films. *Journal of Materiomics*, 8(6):1239–1250, 2022.
- [98] Chen Zhu, Dongliang Guo, Dong Ye, Shan Jiang, and YongAn Huang. Flexible pzt-integrated, bilateral sensors via transfer-free laser lift-off for multimodal measurements. *ACS applied materials & interfaces*, 12(33):37354–37362, 2020.
- [99] Yuki Iga, Kensuke Kanda, Takayuki Fujita, Kohei Higuchi, and Kazusuke Maenaka. A design and fabrication of mems gyroscope using pzt thin films. In *2010 World Automation Congress*, pages 1–4. IEEE, 2010.
- [100] KATO Yoshinori. Fujifilm group’s inkjet printhead and technology. *Fujifilm Research & Development*, 59:27–31, 2014.
- [101] Emmanuel Defay. Integration of ferroelectric and piezoelectric thin films: concepts and applications for microsystems. 2013.
- [102] David S Ginley and John D Perkins. Transparent conductors. In *Handbook of transparent conductors*, pages 1–25. Springer, 2011.
- [103] J Robertson and B Falabretti. Electronic structure of transparent conducting oxides. In *Handbook of transparent conductors*, pages 27–50. Springer, 2011.
- [104] Anna Isabel Hofmann, Eric Cloutet, and Georges Hadziioannou. Materials for transparent electrodes: from metal oxides to organic alternatives. *Advanced Electronic Materials*, 4(10):1700412, 2018.
- [105] Theodor Schneller, Rainer Waser, Marija Kosec, and David Payne. *Chemical solution deposition of functional oxide thin films*. Springer, 2013.
- [106] Dietrich Meyerhofer. Characteristics of resist films produced by spinning. *Journal of Applied Physics*, 49(7):3993–3997, 1978.
- [107] JE Fromm. Numerical calculation of the fluid dynamics of drop-on-demand jets. *IBM Journal of Research and Development*, 28(3):322–333, 1984.
- [108] Nicolas Godard, Sebastjan Glinšek, Aleksander Matavž, Vid Bobnar, and Emmanuel Defay. Direct patterning of piezoelectric thin films by inkjet printing. *Advanced Materials Technologies*, 4(2):1800168, 2019.

- [109] Dongdong Li, Wen-Yong Lai, Yi-Zhou Zhang, and Wei Huang. Printable transparent conductive films for flexible electronics. *Advanced materials*, 30(10):1704738, 2018.
- [110] G.M. Hamilton. Explicit equations for the stresses beneath a sliding spherical contact. *Proceedings of the Institution of Mechanical Engineers, Part C: Journal of Mechanical Engineering Science*, 197(1):53–59, 1983.
- [111] Lisa Skedung, Katrin Danerlöv, Ulf Olofsson, Carl Michael Johannesson, Maiju Aikala, John Kettle, Martin Arvidsson, Birgitta Berglund, and Mark W Rutland. Tactile perception: Finger friction, surface roughness and perceived coarseness. *Tribology International*, 44(5):505–512, 2011.
- [112] Changhyun Choi, Yuan Ma, Xinyi Li, Sitangshu Chatterjee, Sneha Sequeira, Rebecca F Friesen, Jonathan R Felts, and M Cynthia Hipwell. Surface haptic rendering of virtual shapes through change in surface temperature. *Science Robotics*, 7(63):eabl4543, 2022.
- [113] Heinrich Hertz. Ueber die berührung fester elastischer körper. 1882.
- [114] Kenneth L Johnson. One hundred years of hertz contact. *Proceedings of the Institution of Mechanical Engineers*, 196(1):363–378, 1982.
- [115] Alfred Johnsen and Knud Rahbek. A physical phenomenon and its applications to telegraphy, telephony, etc. *Journal of the Institution of Electrical Engineers*, 61(320):713–725, 1923.
- [116] Edward Mallinckrodt, AL Hughes, and William Sleator Jr. Perception by the skin of electrically induced vibrations. *Science*, 118(3062):277–278, 1953.
- [117] Glen Dickson. Tanvas makes inroads with "surface haptics". *Wiley online library*, <https://doi.org/10.1002/msid.0050014>, 2022.
- [118] Kwon Joong Son. A nonlinear rheological model for the ultrasonically induced squeeze film effect in variable friction haptic displays. *Korea-Australia Rheology Journal*, 29:219–228, 2017.
- [119] Farzad Ahmadkhanlou, Gregory N Washington, and Stephen E Bechtel. The development of a five dof magnetorheological fluid-based telerobotic haptic system. In

- Modeling, Signal Processing, and Control for Smart Structures 2008*, volume 6926, pages 31–40. SPIE, 2008.
- [120] Diana Angelica Torres, Betty Lemaire-Semail, Christophe Giraud-Audine, Frederic Giraud, and Michel Amberg. Design and control of an ultrasonic surface haptic device for longitudinal and transverse mode comparison. *Sensors and Actuators A: Physical*, 331:113019, 2021.
- [121] Longfei Song, Juliette Cardoletti, Alfredo Blazquez Martinez, Andreja Benčan, Brigita Kmet, Stephanie Girod, Emmanuel Defay, and Sebastjan Glinsek. Low-temperature growth of piezoceramic films on glass. *arXiv preprint arXiv:2303.13103*, 2023.
- [122] Nabil Fellahi, Mohammed Addou, Amina Kachouane, Mohamed El Jouad, and Zouhair Sofiani. Optical properties of undoped and tin-doped nanostructured In_2O_3 thin films deposited by spray pyrolysis. *The European Physical Journal Applied Physics*, 74(2):24611, 2016.
- [123] Nicolas Godard, Sebastjan Glinsek, and Emmanuel Defay. Inkjet-printed silver as alternative top electrode for lead zirconate titanate thin films. *Journal of Alloys and Compounds*, 783:801–805, 2019.
- [124] Seungjun Chung, Seul Ong Kim, Soon-Ki Kwon, Changhee Lee, and Yongtaek Hong. All-inkjet-printed organic thin-film transistor inverter on flexible plastic substrate. *IEEE electron device letters*, 32(8):1134–1136, 2011.
- [125] Longfei Song, Tony Schenk, Emmanuel Defay, and Sebastjan Glinsek. Highly conductive low-temperature combustion-derived transparent indium tin oxide thin film. *Materials Advances*, 2(2):700–705, 2021.
- [126] Longfei Song, Sebastjan Glinsek, Silvo Drnovsek, Veronika Kovacova, Barbara Malic, and Emmanuel Defay. Piezoelectric thick film for power-efficient haptic actuator. *Applied Physics Letters*, 121(21):212901, 2022.
- [127] Longfei Song, Sebastjan Glinsek, Hana Ursic, Silvo Drnovsek, Matej Sadl, Barbara Malic, and Emmanuel Defay. Power-efficient piezoelectric haptic actuators with large deflection. *Sensors and Actuators A: Physical*, 356:114346, 2023.

- [128] Jing Ouyang, Denis Cormier, Scott A Williams, and David A Borkholder. Photonic sintering of aerosol jet printed lead zirconate titanate (pzt) thick films. *Journal of the American Ceramic Society*, 99(8):2569–2577, 2016.
- [129] Ali Shoghi, Hossein Abdizadeh, Amid Shakeri, and Mohammad Reza Golobostanfard. Sol–gel synthesis of pzt thin films on fto glass substrates for electro-optic devices. *Journal of Sol-Gel Science and Technology*, 93:623–632, 2020.
- [130] Wan Zurina Samad, Muhamad Mat Salleh, Ashkan Shafiee, and Mohd Ambar Yarmo. Transparent conducting thin films of fluoro doped tin oxide (fto) deposited using inkjet printing technique. In *2010 IEEE International Conference on Semiconductor Electronics (ICSE2010)*, pages 52–55. IEEE, 2010.
- [131] Bo Nan, Susana Olhero, Rui Pinho, Paula M Vilarinho, Tim W Button, and José MF Ferreira. Direct ink writing of macroporous lead-free piezoelectric ba_{0.85}ca_{0.15}zr_{0.1}ti_{0.9}o₃. *Journal of the American Ceramic Society*, 102(6):3191–3203, 2019.
- [132] Haibo Zhang, Shenglin Jiang, Jianzhong Xiao, and Koji Kajiyoshi. Low temperature preparation and electrical properties of sodium–potassium bismuth titanate lead-free piezoelectric thick films by screen printing. *Journal of the European Ceramic Society*, 30(15):3157–3165, 2010.
- [133] Wangfeng Bai, Bo Shen, Fang Fu, and Jiwei Zhai. Dielectric, ferroelectric, and piezoelectric properties of textured bzt–bct lead-free thick film by screen printing. *Materials Letters*, 83:20–22, 2012.
- [134] Naveen Aruchamy, Tony Schenk, Veronika Kovacova, Sebastjan Glinsek, Emmanuel Defay, and Torsten Granzow. Influence of tensile vs. compressive stress on fatigue of lead zirconate titanate thin films. *Journal of the European Ceramic Society*, 41(14):6991–6999, 2021.
- [135] T Schenk. *Formation of ferroelectricity in hafnium based thin films*. PhD thesis, Ph. D. Thesis, Technische Universität Dresden, Germany, 2016.
- [136] Andrea Mazzalai, Davide Balma, Nachiappan Chidambaram, Ramin Matloub, and Paul Muralt. Characterization and fatigue of the converse piezoelectric effect in pzt films for mems applications. *Journal of Microelectromechanical systems*, 24(4):831–838, 2014.